

## University of Southampton Research Repository ePrints Soton

Copyright © and Moral Rights for this thesis are retained by the author and/or other copyright owners. A copy can be downloaded for personal non-commercial research or study, without prior permission or charge. This thesis cannot be reproduced or quoted extensively from without first obtaining permission in writing from the copyright holder/s. The content must not be changed in any way or sold commercially in any format or medium without the formal permission of the copyright holders.

When referring to this work, full bibliographic details including the author, title, awarding institution and date of the thesis must be given e.g.

AUTHOR (year of submission) "Full thesis title", University of Southampton, name of the University School or Department, PhD Thesis, pagination

**UNIVERSITY OF SOUTHAMPTON**

**FACULTY OF NATURAL AND ENVIRONMENTAL SCIENCES**

Ocean and Earth Science

**The role of sedimentation rate on the stability of low gradient  
submarine continental slopes**

by

**Morelia Urlaub**

Thesis for the degree of Doctor of Philosophy

January 28, 2013



**Graduate School of the National Oceanography  
Centre, Southampton**

This PhD dissertation by

*Morelia Urlaub*

has been produced under the supervision of the following persons

Supervisors

Dr. Peter J. Talling

Dr. Antonis Zervos

Professor Douglas G. Masson

Chair of Advisory Panel

Professor Jonathan M. Bull

Members of Advisory Panel

Dr. Peter J. Talling

Dr. Antonis Zervos

Professor Douglas G. Masson



UNIVERSITY OF SOUTHAMPTON

ABSTRACT

FACULTY OF NATURAL AND ENVIRONMENTAL SCIENCES

Ocean and Earth Science

Doctor of Philosophy

THE ROLE OF SEDIMENTATION RATE ON THE STABILITY OF LOW  
GRADIENT SUBMARINE CONTINENTAL SLOPES

by Morelia Urlaub

Submarine landslides at open continental slopes are the largest mass movements on Earth and can cause damaging tsunamis. To be able to predict where and when such large landslides may occur in the future requires fundamental understanding of the mechanisms that cause them. Due to the inaccessibility of these features this understanding is based on poorly tested hypotheses. Recent studies have proposed that more landslides occur during periods of sea level rise and lowstand, or during periods of rapid sedimentation. These hypotheses are tested by comparing a comprehensive global data set of ages for large submarine landslides to global mean sea level and local sedimentation rates. The data set does not show statistically significant patterns, trends or clusters in landslide abundance, which suggests that the link between sea level and landslide frequency is too weak to be detected using the available global data base. The analysis also shows no evidence for an immediate influence of rapid sedimentation on slope stability, as failures tend to occur several thousand years after periods of increased sedimentation rates. Large submarine landslides occur on remarkably low slope gradients ( $<2^\circ$ ), which makes them difficult to explain. A widely used explanation for failure of such low angle slopes is high excess pore pressure due to rapid sedimentation and/or focused pore fluid flow to the toe of the slope. If these hypotheses are universal, and therefore also hold for continental margins with comparatively low rates of sediment deposition (where numerous large landslides are observed), is tested in this thesis. Fully coupled 2D stress-fluid flow finite element models are created that simulate the excess pore pressure and drainage response of a continental slope to the deposition of new sediment. Homogeneous models with a wide range of physical-mechanical properties as well as models with an aquifer are loaded by low rates of sediment deposition. All models turn out stable and resulting excess pore pressures are too low to significantly decrease effective stress anywhere along the slope. Hence, factors other than sediment deposition must be fundamental for initiating slope failure, at least in locations with slow sedimentation rates. The results obtained in this thesis not only indicate that failure mechanisms that have previously been considered important may not be universal. They also emphasise the large uncertainties in our current understanding of the occurrence, timing and frequency of large submarine landslides at open continental slopes.



# Contents

<b>Declaration of authorship</b>	<b>xvii</b>
<b>Declaration of co-author contributions</b>	<b>xix</b>
<b>Acknowledgements</b>	<b>xxi</b>
<b>Nomenclature</b>	<b>xxv</b>
<b>Abbreviations</b>	<b>xxvii</b>
<b>1 Introduction</b>	<b>1</b>
1.1 Post-landslide seafloor morphology and inferred characteristics of submarine landslides . . . . .	3
1.2 Causes of submarine landslides . . . . .	6
1.2.1 Sediment deposition as a source of excess pore pressure . . . . .	7
1.3 Climate change and slope stability . . . . .	9
1.4 Downslope evolution of a submarine landslide . . . . .	9
1.5 Rationale . . . . .	10
1.6 Objectives . . . . .	12
1.7 Thesis outline . . . . .	13
<b>2 Timing and frequency of large submarine landslides: Implications for understanding triggers and future geohazard</b>	<b>15</b>
2.1 Introduction . . . . .	16
2.1.1 Aims . . . . .	17
2.1.2 Climate change and slope stability . . . . .	19
2.1.2.1 Deposition rates . . . . .	19
2.1.2.2 Location of depocentres . . . . .	20
2.1.2.3 Stress changes . . . . .	20
2.1.2.4 Isostatic adjustment . . . . .	21
2.1.2.5 Bottom water temperature . . . . .	22
2.1.2.6 Bottom water currents . . . . .	22
2.1.2.7 Groundwater flow . . . . .	22
2.1.2.8 Climate-independent causes . . . . .	23
2.1.3 Dating submarine landslides . . . . .	23
2.1.3.1 <sup>14</sup> C AMS . . . . .	23
2.1.3.2 Oxygen isotopes . . . . .	23
2.1.3.3 Biostratigraphy . . . . .	24
2.1.3.4 Uncertainties due to sample locations . . . . .	24

2.1.3.5	Uncertainties if slide has multiple depositional lobes or headwalls . . . . .	26
2.2	Data and methods . . . . .	26
2.2.1	Criteria for inclusion in the data set . . . . .	26
2.2.2	Real emplacement ages . . . . .	27
2.2.3	Uncertainty estimation for emplacement ages obtained by $^{14}\text{C}$ . . . . .	28
2.2.4	Global sea level as proxy for global climate . . . . .	28
2.2.5	Continental slope accumulation rates . . . . .	29
2.2.6	Data presentation and statistics . . . . .	29
2.2.7	Subdivision into depositional systems . . . . .	31
2.2.8	Limitations . . . . .	31
2.2.8.1	Bias due to limited core penetration . . . . .	31
2.2.8.2	Regional bias . . . . .	32
2.2.8.3	Short term and local climatic events . . . . .	33
2.3	Results . . . . .	33
2.3.1	Field data . . . . .	33
2.3.1.1	Grand Banks . . . . .	33
2.3.1.2	Storegga slide . . . . .	34
2.3.1.3	Trænadjupet slide . . . . .	34
2.3.1.4	Cape Fear slide . . . . .	34
2.3.1.5	Balearic abyssal plain turbidite . . . . .	35
2.3.1.6	Heradotus basin turbidites . . . . .	35
2.3.1.7	BIG95 . . . . .	36
2.3.1.8	South-east Australia . . . . .	36
2.3.1.9	Nyk slide . . . . .	37
2.3.1.10	Hinlopen/Yermak slide . . . . .	37
2.3.1.11	Mauritania slide . . . . .	38
2.3.1.12	Black Shell turbidite . . . . .	38
2.3.1.13	Peach 4 Debrite . . . . .	38
2.3.1.14	Montserrat debris flow . . . . .	39
2.3.1.15	Iberian margin turbidites . . . . .	39
2.3.1.16	Madeira abyssal plain turbidite 'a' . . . . .	40
2.3.1.17	Makran turbidite T2 . . . . .	40
2.3.1.18	Walker-Massingill slump . . . . .	40
2.3.1.19	North-western Nile deep sea turbidite system . . . . .	41
2.3.1.20	Amazon Fan Mass Transport Deposits . . . . .	41
2.3.1.21	Flemish Pass, Canada . . . . .	42
2.3.1.22	Agadir basin turbidites . . . . .	42
2.3.1.23	Cape Blanc slide . . . . .	43
2.3.1.24	Sahara slide . . . . .	43
2.3.2	Data base analysis . . . . .	49
2.3.2.1	Visual evaluation . . . . .	49
2.3.2.2	Statistical analysis of non-biased data (0-30 ka BP) . . . . .	51
2.3.2.3	Timing of failures in different depositional systems . . . . .	52
2.3.2.4	Temporal variations of accumulation rates and the timing of landslides . . . . .	56
2.4	Discussion . . . . .	58

2.4.1	How strong is sea level forcing of landslide frequency? . . . . .	59
2.4.2	The origin of reduced landslide frequency during the modern sea level highstand . . . . .	61
2.4.3	Relevance of preconditioning . . . . .	61
2.4.4	Future geohazard from submarine landslides . . . . .	62
2.5	Conclusions . . . . .	62
<b>3</b>	<b>Methodology</b>	<b>65</b>
3.1	The Finite Element Method . . . . .	66
3.2	Finite Element modelling of a consolidating slope . . . . .	67
3.3	Assessment of slope stability . . . . .	68
3.4	Considerations for modelling of a continental slope . . . . .	69
3.5	Mechanical behaviour of marine sediments . . . . .	70
3.5.1	Porosity-depth profiles and compressibility behaviour . . . . .	72
3.5.2	The effect of carbonate content on physical-mechanical properties .	73
3.5.3	Permeability-porosity relationships and anisotropy . . . . .	73
3.6	The Modified Cam Clay constitutive model . . . . .	74
3.7	Software . . . . .	77
3.8	Hardware . . . . .	77
<b>4</b>	<b>Benchmarking the performances of small strain and finite strain assumptions for the continental slope model</b>	<b>79</b>
4.1	Introduction . . . . .	79
4.2	Methodology . . . . .	80
4.2.1	Implementation . . . . .	80
4.2.2	Model parameters . . . . .	80
4.2.3	Quantification of differences . . . . .	82
4.3	Results . . . . .	82
4.3.1	Pore pressure kinks . . . . .	89
4.4	Discussion and recommendation . . . . .	91
<b>5</b>	<b>How do <math>\sim 2^\circ</math> slopes fail in areas of slow sedimentation? A sensitivity study on the influence of accumulation rate and permeability on submarine slope stability</b>	<b>93</b>
5.1	Introduction . . . . .	94
5.1.1	Aims . . . . .	94
5.1.2	Proto-type Field Location - NW African Margin south of $26^\circ$ N . .	95
5.2	Methodology . . . . .	96
5.2.1	Gibson's (1958) Approach to One-Dimensional Consolidation . . .	96
5.2.2	Finite Element Modelling of Two-Dimensional Slopes . . . . .	96
5.2.2.1	Initial conditions . . . . .	97
5.2.2.2	Key Assumptions . . . . .	98
5.3	Results . . . . .	99
5.3.1	One-Dimensional Consolidation . . . . .	99
5.3.2	Two-Dimensional Consolidation . . . . .	99
5.4	Discussion . . . . .	101

<b>6</b>	<b>The role of sedimentation rate on continental slope stability: Implications for slope failure mechanisms at continental slopes with low sediment input</b>	<b>103</b>
6.1	Introduction . . . . .	103
6.1.1	What triggers large submarine landslides on nearly flat slopes? . .	105
6.1.2	Aims . . . . .	106
6.1.3	Approach . . . . .	107
6.2	Conceptual continental slope model . . . . .	107
6.2.1	Consolidation and slope stability modelling . . . . .	107
6.2.2	FE model geometry of a typical continental slope . . . . .	108
6.2.3	Constitutive model and physical-mechanical properties . . . . .	108
6.2.4	Loading of the slope by asymmetric sediment deposition . . . . .	112
6.2.5	Boundary conditions . . . . .	113
6.2.6	Discretisation . . . . .	113
6.2.7	Initial conditions . . . . .	114
6.2.8	Initial excess pore pressure . . . . .	115
6.2.9	Sand layer . . . . .	116
6.2.10	Choice of models . . . . .	117
6.2.11	Assumptions and limitations . . . . .	120
6.3	Results . . . . .	121
6.3.1	Rapid versus slow sedimentation rates . . . . .	121
6.3.2	Consolidation properties tests (model runs M1 to M8) . . . . .	127
6.3.2.1	Model M1 . . . . .	127
6.3.2.2	Model M2 . . . . .	128
6.3.2.3	Model M3 . . . . .	129
6.3.2.4	Model M4 . . . . .	129
6.3.2.5	Model M5 . . . . .	129
6.3.2.6	Model M6 . . . . .	130
6.3.2.7	Model M7 . . . . .	130
6.3.2.8	Model M8 . . . . .	130
6.3.2.9	Summary and interpretation . . . . .	131
6.3.3	Lateral flow tests (model runs M9-M16) . . . . .	140
6.3.3.1	Model M9 . . . . .	140
6.3.3.2	Model M10 . . . . .	140
6.3.3.3	Model M11 . . . . .	140
6.3.3.4	Model M12 . . . . .	141
6.3.3.5	Model M13 . . . . .	141
6.3.3.6	Model M14 . . . . .	141
6.3.3.7	Model M15 . . . . .	142
6.3.3.8	Model M16 . . . . .	142
6.3.3.9	Summary and interpretation . . . . .	142
6.4	Discussion . . . . .	151
6.4.1	Why do shallow angle slopes in slow deposition areas fail? What is the missing link? . . . . .	152
6.4.1.1	Gas hydrates . . . . .	153
6.4.1.2	Earthquakes . . . . .	153
6.4.2	The role of compressibility . . . . .	153

6.5	Conclusion . . . . .	156
<b>7</b>	<b>Conclusions and future perspectives</b>	<b>157</b>
7.1	Does climate affect continental slope stability? . . . . .	158
7.2	Is slope failure triggered by rapid sedimentation, and how can failure occur in areas of slow sedimentation? . . . . .	160
7.3	How could future studies be directed in order to constrain remaining un- certainties and improve understanding? . . . . .	161
	<b>Bibliography</b>	<b>165</b>



## List of Figures

1.1	Histograms of landslide parameters (headwall height, water depth, slope angle) for events in the Atlantic . . . . .	4
1.2	Morphological features of a translational landslide and their bathymetric expression . . . . .	5
1.3	Time dependent response of sediment to an increase in total stress . . . . .	8
2.1	Different sampling strategies for radiocarbon dating of submarine landslides	18
2.2	Global mean sea level, benthic $\delta^{18}O$ record, and timing of submarine landslides . . . . .	48
2.3	Histogram representation of the timing of submarine landslides . . . . .	50
2.4	Histograms of submarine landslides in the past 30 ky and comparison to Poisson distribution . . . . .	51
2.5	Comparison of the landslide data set to random number sets . . . . .	53
2.6	Histograms for the timing of submarine landslides in different depositional environments . . . . .	54
2.7	Histograms of submarine landslides in river fan systems in the past 30 ky and comparison to Poisson distribution . . . . .	55
2.8	Comparison of the river fan system subset to random number sets . . . . .	56
2.9	Local sedimentation rates and the timing of submarine landslides . . . . .	57
3.1	Rectangular finite elements . . . . .	67
3.2	Model surface fluid flow boundary condition . . . . .	70
3.3	Depth-porosity relationship for marine sediments . . . . .	72
3.4	Optical microscopy image of mudstones with different degrees of anisotropy	74
3.5	Modified Cam Clay constitutive soil model . . . . .	76
4.1	Void ratio - permeability relationship . . . . .	81
4.2	Comparison of small strain and finite strain models: volumetric strain . . . . .	85
4.3	Comparison of small strain and finite strain models: excess pore pressure . . . . .	86
4.4	Comparison of small strain and finite strain models: vertical effective stress	87
4.5	Comparison of small strain and finite strain models: flow velocity . . . . .	88
4.6	Relative differences between excess pore pressure calculated with small strain and finite strain analyses at selected nodes . . . . .	89
4.7	Pore pressure kinks in small and finite strain models . . . . .	90
5.1	Landslide characteristics of three continental margins . . . . .	95
5.2	2D continental slope model geometry with boundary and loading conditions	98
5.3	1D analytical solutions for overpressure ratios with respect to permeability and sedimentation rate . . . . .	100

5.4	2D FE solution for vertical effective stress, overpressure ratio and Factor of Safety . . . . .	101
6.1	Volumes, headwall heights and slope angles for submarine landslides in the Atlantic . . . . .	104
6.2	Sketch of continental slope model geometry, boundary and loading conditions	109
6.3	Initial porosity and permeability distribution with depth . . . . .	114
6.4	Sketch of continental slope model with aquifer . . . . .	117
6.5	Stress paths for models with rapid and slow deposition . . . . .	122
6.6	Temporal evolution of overpressure ratio, vertical permeability and horizontal fluid flow of a model with high as well as low deposition rates . . .	123
6.7	Final state of the model with rapid deposition . . . . .	125
6.8	Final state of the model with slow deposition. . . . .	126
6.9	Stress paths for models M1-M16 . . . . .	127
6.10	FE solutions for model run M1 . . . . .	132
6.11	FE solutions for model run M2 . . . . .	133
6.12	FE solutions for model run M3 . . . . .	134
6.13	FE solutions for model run M4 . . . . .	135
6.14	FE solutions for model run M5 . . . . .	136
6.15	FE solutions for model run M6 . . . . .	137
6.16	FE solutions for model run M7 . . . . .	138
6.17	FE solutions for model run M8 . . . . .	139
6.18	FE solutions for model run M9 . . . . .	143
6.19	FE solutions for model run M10 . . . . .	144
6.20	FE solutions for model run M11 . . . . .	145
6.21	FE solutions for model run M12 . . . . .	146
6.22	FE solutions for model run M13 . . . . .	147
6.23	FE solutions for model run M6 . . . . .	148
6.24	FE solutions for model run M15 . . . . .	149
6.25	FE solutions for model run M16 . . . . .	150
6.26	Conceptual sketch of destructuring . . . . .	155

## List of Tables

1.1	Factors contributing to the initiation of submarine landslides at open continental slopes . . . . .	7
2.1	Approximate lengths of cores recovering turbidites or slide deposits and maximum obtained ages. . . . .	32
2.2	Ages of submarine landslides and their uncertainty intervals as well as sedimentation rates . . . . .	47
2.3	Delay between onset of increased sedimentation on the continental slope and landslide age . . . . .	58
4.1	Modified Cam Clay input parameters . . . . .	81
4.2	Area-weighted root mean square differences between the results of small strain and finite strain analyses . . . . .	83
5.1	Modified Cam Clay input parameters . . . . .	97
6.1	Estimate of initial overpressurisation . . . . .	116
6.2	Input parameters for reference model . . . . .	117
6.3	Input parameters for all models . . . . .	119



## Declaration of authorship

I, *Morelia Urlaub*, declare that the thesis entitled *The role of sedimentation rate on the stability of low gradient submarine continental slopes* and the work presented in the thesis are both my own, and have been generated by me as the result of my own original research. I confirm that:

- this work was done wholly or mainly while in candidature for a research degree at this University;
- where any part of this thesis has previously been submitted for a degree or any other qualification at this University or any other institution, this has been clearly stated;
- where I have consulted the published work of others, this is always clearly attributed;
- where I have quoted from the work of others, the source is always given. With the exception of such quotations, this thesis is entirely my own work;
- I have acknowledged all main sources of help;
- where the thesis is based on work done by myself jointly with others, I have made clear exactly what was done by others and what I have contributed myself;
- parts of this work have been published as: Urlaub et al. (2012). Permission to reproduce this article has been granted by the publisher.

Signed:.....

Date:.....



## Declaration of co-author contributions

Parts of this thesis have been published or will be published as joint author peer-reviewed articles. This section provides details regarding the current state and the contribution of co-authors to each article.

**Chapter 2** entitled "Timing and frequency of large submarine landslides: Implications for understanding triggers and future geohazard" has been submitted for publication to *Quaternary Science Reviews*. Major revisions are required and will be undertaken before re-submission. I confirm that I created the landslide age database, designed the method to calculate uncertainties, conducted the statistical analyses, made all figures and have written all sections of the manuscript. Co-authors Peter Talling and Doug Masson have made substantive intellectual contributions and reviewed the manuscript before submission.

**Chapter 5** entitled "How do  $\sim 2^\circ$  slopes fail in areas of slow sedimentation? A sensitivity study on the influence of accumulation rate and permeability on submarine slope stability" has been published as a book chapter in *Submarine Mass Movements and Their Consequences, edited by Yamada, Y., et al., volume 31 of Advances in Natural and Technological Hazards Research*. I confirm that I created the Finite Element Model, ran the analyses, interpreted the results, made all figures and have written all sections of the manuscript. Co-author Antonis Zervos assisted in the choice of the constitutive model and some model implementations. He reviewed the manuscript before submission. Co-authors Peter Talling and Doug Masson helped with the design of the model geometry and the choice of the type of material. They reviewed the manuscript before submission. Co-author Chris Clayton provided significant intellectual input towards the conceptualisation of the problem.



## Acknowledgements

First and foremost I would like to thank Pete Talling for the mentorship and guidance throughout the past three years, for giving me the freedom and confidence to pursue what has become this thesis, as well as for teaching me the importance of critical thinking and communication. His enthusiasm and attitude towards science have substantially shaped my way of thinking.

My sincere thanks go to Antonis Zervos, who has introduced me to the world of soil mechanics, and has provided all possible help and assistance during my excursions into the depths of numerics. Thanks for the patience, support and encouragement at all times. I have greatly enjoyed the numerous and profound discussions we held on the subject.

I am grateful to Doug Masson for having been a steady critic of my work, and for always providing an open ear to my questions and concerns. His guidance has formed a solid basis for my future scientific ventures.

My dear parents laid the foundation that made all this possible - by giving me both roots and wings. Jacob, thank you for always being with me.



*When you realise there is something you don't understand, then you're generally  
on the right path to understanding all kinds of things.*

*(Jostein Gaarder, The Solitaire Mystery)*



# Nomenclature

## Roman Letters

$C_c$	compression index [ ]
$C_s$	swelling index [ ]
$c$	thickness of virtual layer [m]
$c_v$	coefficient of consolidation [m <sup>2</sup> /s]
$d_{sf}$	distance between radiocarbon sample and failure deposit [m]
$E$	Young's modulus [MPa]
$E_j$	expected number of histogram bins containing $j$ events [ ]
$e$	void ratio [ ]
$e_0$	reference void ratio at an effective stress of unity [ ]
$f$	loading rate [kPa/s]
$G$	shear modulus [MPa]
$g$	gravity acceleration [m/s <sup>2</sup> ]
$h$	element length [m]
$K_g$	bulk modulus [MPa]
$k$	Darcy permeability [m/s]
$k_x$	horizontal Darcy permeability [m/s]
$k_z$	vertical Darcy permeability [m/s]
$k_x/k_z$	permeability anisotropy coefficient [ ]
$k_{vl}$	vertical Darcy permeability of virtual sediment layer [m/s]
$M$	slope of critical state line projected onto the $p'$ - $q$ space [ ]
$m_v$	coefficient of volume compressibility [m <sup>2</sup> /kN]
$N_p$	intercept of the normal compression line in the $\ln p' - q$ space [ ]
$n$	porosity [ ]
$O_j$	observed number of histogram bins containing $j$ events [ ]
$p'$	mean effective pressure [kPa]
$p'_c$	size of yield locus [kPa]
$p'_0$	initial stress state [kPa]
$p$	total pore fluid pressure [kPa]
$p_h$	hydrostatic pore pressure [kPa]
$p_e$	excess pore pressure [kPa]
$p_0$	initial pore pressure [kPa]

## NOMENCLATURE

---

$p_{0vl}$	hydrostatic pore pressure at the top of the virtual layer [kPa]
$q$	deviatoric stress [kPa]
$sr$	sedimentation rate [m/ky]
$T$	total number of histogram bins [ ]
$t$	time [ky]
$u_x$	horizontal displacement [m]
$u_z$	vertical displacement [m]
$v$	specific volume $(e+1)$ [ ]
$v$	total flow velocity [mm/y]
$v_n$	flow velocity normal to seafloor [mm/y]
$v_x$	flow velocity in x-direction [mm/y]
$z$	depth [m]

### Greek Letters

$\gamma$	bulk unit weight [kN/m <sup>3</sup> ]
$\gamma_w$	specific weight of water [kN/m <sup>3</sup> ]
$\lambda^*$	overpressure ratio [ ]
$\lambda$	logarithmic hardening constant [ ]
$\kappa$	elastic logarithmic bulk modulus [ ]
$\nu$	Poisson's ratio [ ]
$\phi'_{crit}$	effective friction angle [°]
$\phi'_{mob}$	mobilised friction angle [°]
$\rho_{dry}$	dry density [kg/m <sup>3</sup> ]
$\sigma'_1$	maximum principle stress [kPa]
$\sigma'_3$	minimum principle stress [kPa]
$\sigma'_v$	vertical effective stress [kPa]
$\sigma_v$	vertical total stress [kPa]
$\epsilon_{vol}$	volumetric shear strain [ ]

## Abbreviations

AD	Anno Domini
AMS	Accelerator Mass Spectrometry
AWRMS	Area-Weighted Root Mean Square
BP	Before Present (before 1950)
CC	Cam Clay
CSL	Critical State Line
FE	Finite Element
FEM	Finite Element Method
FoS	Factor of Safety
GDP	Gross Domestic Product
LGM	Last Glacial Maximum
MAP	Madeira Abyssal Plain
MCC	Modified Cam Clay
mbsf	meter below seafloor



## Chapter 1

### Introduction

Submarine landslides are one of the volumetrically most important processes for transporting sediment across the continental shelf, slope and into the deep ocean (Masson et al., 2006). Moreover, these landslides are a major geohazard as they can cause damaging tsunamis. Submarine landslides are not only much larger than those on land but also can occur on remarkably low gradients ( $1-2^\circ$ ), that are almost always stable on land (Hampton et al., 1996). Their large scale and the fact that they occur on nearly flat slopes, along with the inability to observe them directly, makes submarine landslides more difficult to analyse than many other geohazards. Consequently, they are as yet poorly understood and hazard assessments are problematic, or involve large uncertainties.

Gravity driven downward movement of slope-forming material can occur at all inclined areas of the seafloor, particularly in areas with thick fine grained sedimentary deposits (Masson et al., 2006). Landslides in shallow water ( $<200$  m water depth) can often be linked to cyclic tide or storm wave loading (Prior and Coleman, 1982), whereas fjords are subject to frequent small failures along their steep walls (Jorstad, 1968). Slope failures related to volcanic island flank collapses involve a complex interplay of subaerial and submarine components along steep slopes with high relief (Masson et al., 2002). Canyons at continental slopes have steep margins which frequently collapse and cause comparatively small landslides (Hampton et al., 1996). However, the causes for landslides at open continental slopes at passive margins with typical gradients of less than  $2^\circ$ , without major tectonic stresses, and at water depths too large to be affected by waves ( $>500$  m), are not as obvious. These slopes accommodate some of the largest mass movements on Earth, exceeding volumes of slides on land by up to two orders of magnitude (Korup et al., 2007). The Storegga Slide off the continental slope of Norway is one of the largest submarine landslides to date and mobilised more than  $3,000 \text{ km}^3$  of sediment, enough to bury Scotland to a depth of 80 m (Masson et al., 2010). The Storegga Slide occurred 8,200 years ago and triggered a tsunami that had run-up heights of more than 20 m in the Shetland Islands and up to 6 m in north-east Scotland (Bondevik et al., 2005a). These large landslides are thus potentially highly tsunamigenic. As the likelihood of tsunami

generation varies directly with landslide size (Lee, 2009), these large scale failures at open continental slopes are the focus of this thesis, which focuses on how they are triggered, and hence their frequency. All subsequent descriptions in this thesis refer to landslides at open continental slopes.

The force of gravity is not enough to cause failure of slopes with gradients as low as  $2^\circ$ . Consequently, other factors destabilise a continental slope. In the case of the Grand Banks slide in 1929 an earthquake acted as the trigger (Piper and Aksu, 1987). The link between landslide and trigger is clear in this particular case, as the resultant turbidity current broke several submarine cables sequentially downslope. However, this is a rare exception. In most other cases the relationship between trigger and landslide is not obvious at all, and often earthquakes are used by default to explain large landslides at open low angle continental slopes (e.g. Booth and O’Leary, 1991; Lastras et al., 2004; Kvalstad et al., 2005; Vanneste et al., 2006; Stigall and Dugan, 2010). Submarine landslides are also often linked to climatic and associated environmental changes (Weaver and Kuijpers, 1983). For example, the dissociation of gas hydrates, promoted by a drop in sea level, was initially suspected to be the driver for the Storegga Slide (Mienert et al., 2005). This was later revised, and Kvalstad et al. (2005) suggested that a combination of overpressure due to rapid deposition in glacial times, flow focussing, particularly weak sediment and a large earthquake led to failure. A large number of processes that could cause failure of low angle open continental slopes have been discussed, are listed in Table 1.1 and discussed in more detail below (section 1.2).

Geophysical imaging provides good information about source and depositional areas, from which we can infer where landslides have occurred and how they move downslope. But this data does not allow us to deduce mechanisms and processes that operated before or during collapse of the sediment. Monitoring of submarine landslides is nearly impossible, not only due to the large water depths in which they occur. Landslides are rare on a human time scale and it is difficult to predict when they occur. Even if a landslide happened, any instrumentation will likely be destroyed. Due to this lack of direct observations, potential failure mechanisms (Table 1.1) are difficult to test. It is, however, possible to use field data and numerical techniques to test some of these hypotheses, which will be addressed in this thesis. Comparing the ages of submarine landslides to certain environmental patterns such as sea level, sedimentation rate, atmospheric methane concentration or seismicity, may allow to reject certain trigger mechanisms or emphasise others (Maslin et al., 2004; Owen et al., 2007; Lee, 2009). In addition, the potential of particular failure mechanisms to cause slope failure can be evaluated using numerical models. For example, models can quantify the amount of overpressure generated in a continental slope during consolidation, and the effect this has on the slope’s stability (Dugan and Flemings, 2000; Stigall and Dugan, 2010).

## 1.1 Post-landslide seafloor morphology and inferred characteristics of submarine landslides

Due to the cover of water most submarine landslides occur unobserved. The seafloor morphology that these events leave behind, and which can be mapped using acoustic methods, gives indications of characteristics of these landslides such as their volumes, failure type, and emplacement mechanisms. The following descriptions refer to slides at open continental slopes only, excluding canyon sourced failures.

The headwall represents the upslope part of the rupture surface (Fig. 1.2a). Its height provides information on the depth of failure, although the actual failure area might be covered by displaced material or by post-slide sedimentation. The lateral bounds of the slide's rupture surface are the sidewalls. The surface on which mass is displaced is the rupture surface. If the slide is translational along a bedding plane then the rupture surface is referred to as the glide plane. The toe of the slide (the lower margin of the displaced material that is most distant from the headwall) can be difficult to identify as the displaced mass distributes over large run-out distances from its origin, covering the entire rupture surface. The location of head and sidewalls as well as information on run-out distances allows calculation of the affected area and the volume of sediment that has been mobilised.

Headwalls of submarine landslides at open continental slopes typically dip steeply with inclinations of 15-35° (Bryn et al., 2005; Frey-Martinez et al., 2005; Winkelmann et al., 2008) and average heights of about 100-200 m (Fig. 1.1a, McAdoo et al., 2000; Hühnerbach et al., 2004; Twichell et al., 2009). The majority of slides have headwalls in water depths just under 2,000 m (Fig. 1.1b, Hühnerbach et al., 2004; Twichell et al., 2009). Areas affected by submarine landslides range between 10 and 95,000 km<sup>2</sup> with an approximate mean of 4,000 km<sup>2</sup> (Hühnerbach et al., 2004; Twichell et al., 2009). Volumes of the displaced mass vary over several orders of magnitude from <1 km<sup>3</sup> to >3,000 km<sup>3</sup>, and tend to follow a log-normal distribution (Chaytor et al., 2009; ten Brink et al., 2009). Slope angles in the headwall area as low as 0.4° and up to 9° have been observed (Fig. 1.1c, Hühnerbach et al., 2004; Twichell et al., 2009). The mean slope angle at which submarine slopes fail is ~2°. The Storegga Slide has a 300 km long headwall (Bryn et al., 2005), mobilising about 3,000 km<sup>3</sup> of sediment, affected an area of 95,000 km<sup>2</sup> and had run-out distances of up to 800 km (Haflidason et al., 2004, 2005). This mass movement took place on slope angles less than 1.4°.

Most landslides at open continental slopes are translational and occur along bedding parallel glide planes (Fig. 1.2), rather than rotational failures along rupture surfaces

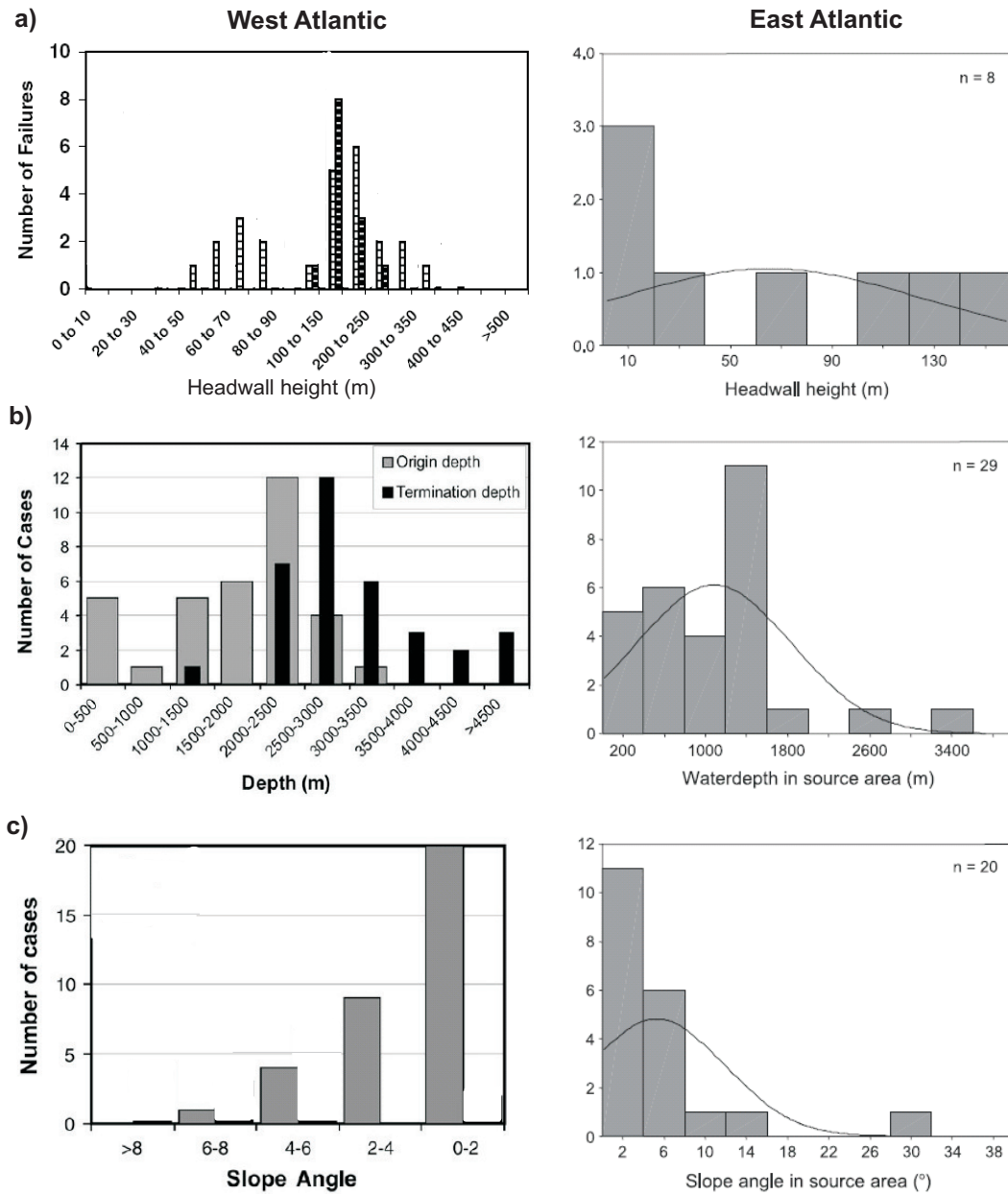


Figure 1.1: Histograms of landslide parameters for events at open continental slopes in the West Atlantic (left column) and the East Atlantic (right column) and adjacent seas, showing (a) headwall height, (b) water depth in the source area, and (c) slope angle in the source area. West Atlantic panels are modified from McAdoo et al. (2000, panel a) and Twichell et al. (2009, panels b and c). East Atlantic panels are taken from Hühnerbach et al. (2004).

(O’Leary, 1991). Such bedding planes have stratigraphic continuity over large areas (Hampton et al., 1996; Masson et al., 2006). Failure can occur on several surfaces parallel to the sediment bedding. Internal headwalls at different water depths document stepwise failure along different glide plains. Fig. 1.2a shows characteristics morphological features of a translational landslide, and how the associated features appear in bathymetric maps of the post-slide seafloor (Fig. 1.2b,c).

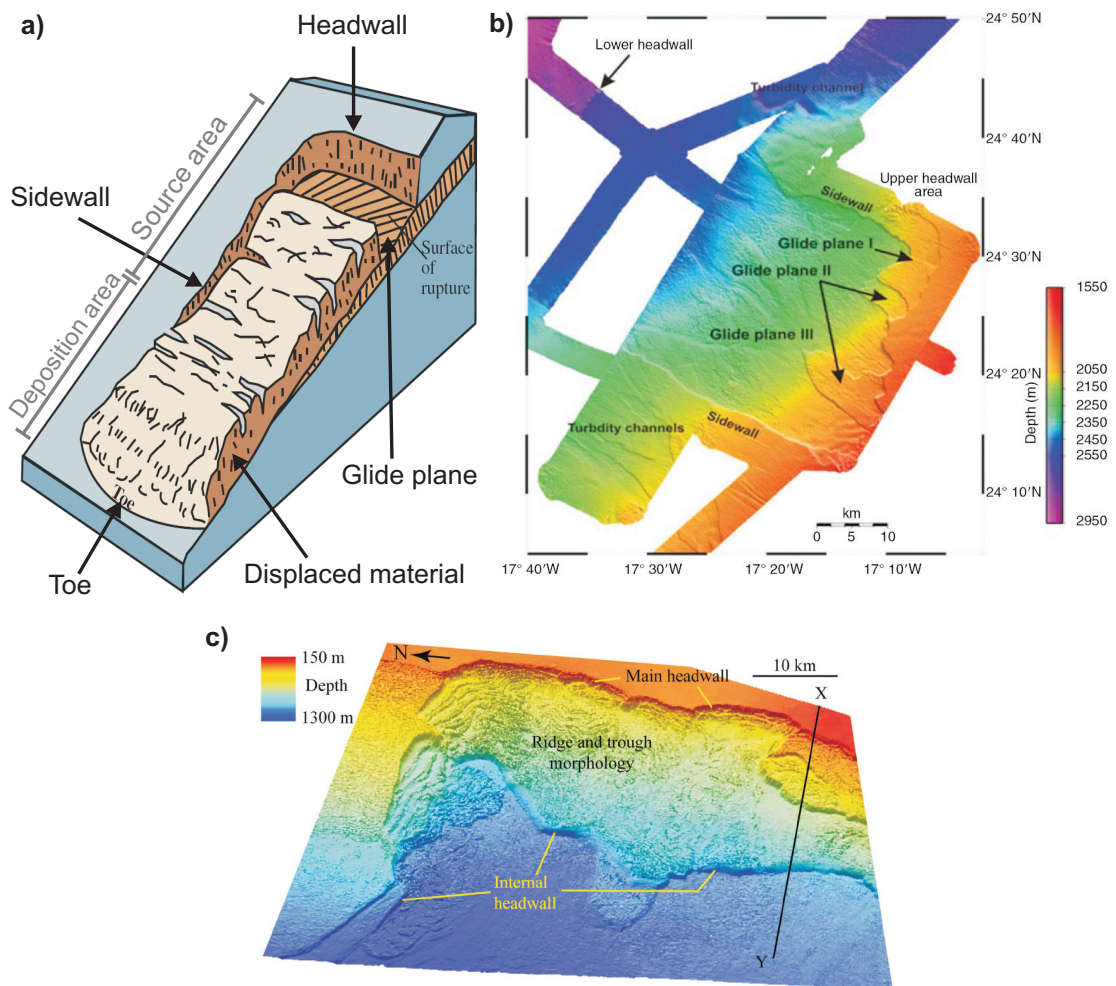


Figure 1.2: (a) Sketch of a translational landslide with typical morphological features (modified after USGS, 2004), which are prominent in bathymetric maps for example of (b) the Sahara Slide at the north-west African margin (Krastel et al., 2012) and (c) the Storegga Slide at the Norwegian continental slope (modified after Masson et al., 2010).

It has been proposed that translational slides may occur in multiple stages (e.g. Lastras et al., 2002; Hafidason et al., 2004; Förster et al., 2010). Such multistage landslides would produce several smaller tsunamis, as opposed to single block slides that would cause a single large tsunami. However, the timing between the different stages is crucial, as superposition of waves can occur (Harbitz et al., 2006). Wave modelling for the tsunami caused by the Storegga Slide showed that the different stages must have been separated by less than a few minutes in order to match run-up heights documented in field data (Bondevik et al., 2005a). Contrary, the presence of thin mud intervals between turbidites associated to individual stages of failure, suggests minimum time intervals of at least several days between each stage in an example of a volcanic island landslide in the Canary Islands (Hunt et al., 2011).

## 1.2 Causes of submarine landslides

For a slope to fail the strength of the sediment must be overcome. Weakening factors are (i) an increase in shear stress, (ii) a decrease in strength or shearing resistance of the slope material, or (iii) a combination of both. In a very low angle slope, such as those at open continental slopes at passive margins, shear stresses are comparatively small. An increase in shear stress for example due to tectonic oversteepening is not expected, although salt diapirism may locally modify slope angles at passive margins. However, to fail such slopes the sediment's shearing resistance must be significantly reduced, for example by pore pressures that greatly exceed hydrostatic pressures (Iverson, 1997; Kvalstad et al., 2005; Locat et al., 2009). Such high excess pore pressures support a large part of the weight of the overlying mass and reduce the effective stress. A broad suite of mechanisms that could cause excess pore pressures has been suggested and Table 1.1 provides a list of these. These weakening processes can broadly be divided into relatively short period events (triggers) and longer term preconditioning factors, which involve aspects of the properties, stratigraphy or depositional processes of the sediment. The most commonly discussed ones are earthquakes (Biscontin et al., 2004) or rapid sediment deposition (Prior and Coleman, 1982).

Specific geological horizons within stratified sequences that act as weak layers are often called upon to explain failure (O'Leary, 1991; Lastras et al., 2004; Wilson et al., 2004; Kvalstad et al., 2005). The weak layer concept fits with the observation that most slides are translational and move along bedding parallel planes. However, it is not clear whether failure spreads in the layer itself, or at an interface between layers of contrasting properties. Water and clay rich contourites were identified as the weak layers along which the Storegga Slide moved (Bryn et al., 2005; Kvalstad et al., 2005). Rapid loading appears to have caused excess pore pressures and reduced the shearing resistance within the contourites. On the other hand, a strong earthquake can generate a water film at the interface between a sand and an overlying clay layer (Kokusho and Kojima, 2002). The reduction in shearing resistance at the interface between these layers caused by the water film has been found sufficient to cause landslides (Kokusho and Kojima, 2002; Locat et al., 2009), and may explain very long run-out distances (Elverhøi et al., 2000; Voight et al., 2012). With the exception of the Storegga Slide, these weak layers are rarely directly sampled as they likely evacuated during failure (Bull et al., 2009; Masson et al., 2010). Our knowledge about the nature, origin and mechanical behaviour of these weak layers is therefore limited.

It is difficult to test the link between submarine landslides and earthquakes. Earthquakes cannot be the default triggers for landslides, as not every major earthquake causes large slope failure. Coring and bathymetric surveys accomplished just after two recent, very

	<b>Mechanism</b>	<b>Example</b>	<b>Field data</b>	<b>Model</b>	<b>Reference of example</b>
Long-term	rapid deposition	Gulf of Mexico	yes	yes	Stigall and Dugan (2010), Flemings et al. (2008)
	flow focussing	New Jersey CM	no	yes	Dugan and Flemings (2000)
	groundwater seepage	Nice Slide	yes	no	Kopf et al. (2010)
	mineral transformation	Antarctic CM	no	no	Volpi et al. (2003)
	sea level change	Madeira Ab. Plain	no	no	Weaver and Kuipers (1983)
	ice (un)loading	Nyk Slide	no	no	Lindberg et al. (2004)
Short-term	earthquake	Grand Banks	yes	no	Piper and Aksu (1987)
	gas hydrate dissociation	Amazon delta	no	no	Maslin et al. (1998)
	<i>oversteepening</i>	Mississippi delta	no	no	Prior and Coleman (1982)
	<i>basal erosion</i>	Angola CM	no	no	Gee et al. (2005)

Table 1.1: Factors that have been suggested for contributing to the initiation of submarine landslides at open continental slopes (CM = continental margin). It is also indicated whether the proposed mechanism has been documented in field data (either by direct observation or through related samples or measurements), and if the proposed scenario is supported by numerical modelling. All factors are sources of excess pore pressure except for those in italic prints.

large earthquakes (the 2004 Boxing Day earthquake on the Sumatran margin and the 2010 Maule earthquake on the Chilean margin) do not show any evidence for large slope failures (Sumner et al., 2010; Völker et al., 2011, respectively). Repeated seismic events that do not lead to failure can even strengthen the sediment by facilitating the consolidation process through rearrangement of grains and dissipation of excess pore pressure (Boulanger and Truman, 1996; Boulanger et al., 1998). How the deposition of sediment may generate high excess pore pressures at continental slopes is explained in the following section.

### 1.2.1 Sediment deposition as a source of excess pore pressure

Consolidation of sediment is the combination of mechanical compaction and fluid flow by which sediments decrease in volume (Terzaghi and Peck, 1948). Consolidation occurs as

an effect of self-weight of the sediment and in response to variations in effective stresses. If a compressive stress acts on the sediment, for example the deposition of new sediment, this load is initially borne almost entirely by the pore water, while the effective stress remains constant. The pore water pressure rises above its equilibrium hydrostatic value and the sediment is underconsolidated. Pore water subsequently dissipates into areas of lower pore pressure, allowing the sediment particles to rearrange and compact. As the excess pore pressure gradually decreases until pore water pressures return to their equilibrium values, the effective stress rises until it bears the entire additional load and the sediment returns into a normally consolidated state (Fig 1.3).

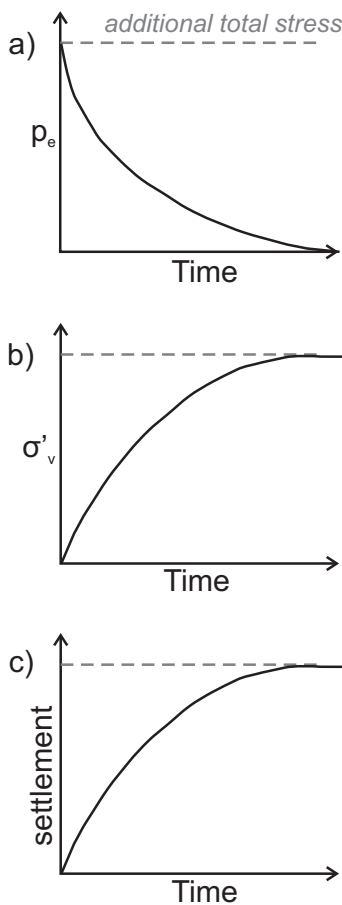


Figure 1.3: Time dependent response of sediment to an increase in total stress: (a) Excess pore pressure,  $p_e$ , (b) vertical effective stress,  $\sigma'_v$ , (c) settlement.

The basic one-dimensional consolidation equation (Terzaghi and Peck, 1948) describing the variation in excess pore pressure over time is:

$$\frac{k}{m_v \cdot \gamma_w} \cdot \frac{\delta^2 p_e}{\delta z^2} = \frac{\delta p_e}{\delta t}, \quad (1.1)$$

where  $k$  is permeability,  $m_v$  is the coefficient of volume compressibility,  $\gamma_w$  is the specific weight of water,  $p_e$  is excess pore pressure,  $z$  is depth and  $t$  time. According to the effective stress principle ( $\sigma_v = \sigma'_v + p_e$ ), an increase in effective stress,  $\frac{\delta \sigma'_v}{\delta t}$ , equals the reduction in excess pore pressure,  $\frac{\delta p_e}{\delta t}$  (Fig.1.3a,b). The rate of settlement is equal to the outward flow rate of pore water (Fig.1.3c).

The magnitude and duration of consolidation depends on the hydromechanical properties of the sediment (compressibility and permeability) as well as on the length of the drainage path that the fluid has to travel to reach areas of less overpressure (Terzaghi and Peck, 1948). Compressibility is a measure of relative volume change in response to stress, and controls the total volume of water to be displaced. Permeability governs the velocity at which pore water flows and the hydraulic gradient is a function of the drainage path. The more pore water has to be displaced and the further the pore water has to travel at low velocities, the longer a sediment takes to consolidate.

Deposition of new sediment is a temporally continuous process. If the rate at which the sediment deposits exceeds the rate at which the sediment consolidates, excess pore pressures build up and the sediment is in a disequilibrium state (Gibson, 1958). Excess pore pressure generation during rapid burial of low permeable sediments is a well-known process in sedimentary basins and has been documented extensively (Bredehoeft and Hanshaw, 1968; Smith, 1971; Bethke and Corbet, 1988; Audet and Fowler, 1992; Wangen, 1992, 1997). Recent drilling in the Gulf of Mexico as part of the International Ocean Drilling Programme (IODP Leg 308) confirmed that high excess pore pressures also prevail at continental slopes (Flemings et al., 2006, 2008). Consolidation behaviour and sedimentation rate thus control the stress state (and consequently stability) in areas where sediment deposition is the major source of pressure. This is the case at continental slopes along passive margins, where large lateral tectonic stresses are absent. It is therefore important to include consolidation when addressing continental slope stability.

### 1.3 Climate change and slope stability

Changes in global climate such as the transitions between ice- and greenhouse worlds are believed to have affected slope stability (Maslin et al., 2004; Owen et al., 2007; Lee, 2009; Leynaud et al., 2009). Such drastic climate transitions go along with numerous changes in environmental conditions that can affect continental slopes globally, for example:

- Sea level or water temperature changes could affect the stability of gas hydrates (Kvenvolden, 1993).
- Changes in the amount and type of sediment that reaches the slopes as well as shifts in the location of depocentres alter the slope's stress state.
- Removal of ice increases the seismicity due to isostatic rebound of the lithosphere (Bungum et al., 2005).

Knowing whether past landslides coincided with major climatic events, or were more frequent during particular climatic stages (glacials, interglacials, warming or cooling phases), can therefore potentially provide a test for failure mechanism hypotheses. Understanding any correlation of the timing of submarine landslides and climate changes would also aid in the evaluation of future hazards.

### 1.4 Downslope evolution of a submarine landslide

Remarkable features of many submarine landslides are their long run-out distances which are considerably longer than on land (Hampton et al., 1996). The slid material often

travels distances of far more than 100 km on nearly flat slopes ( $\sim 0.1^\circ$ ). Frictional forces between the landslide mass and the seafloor must be low, possibly as a result of high excess pore pressures involved in the whole landslide process (Norem et al., 1990; Mohrig et al., 1998).

On its downslope journey, the slid mass itself remains intact, breaks up into distinct blocks or deforms internally. In some cases the mass disintegrates as it moves downslope along the failure plane due to turbulence and water intake. A cloud of suspended particles forms and divides into a debris flow at the bottom and a turbidity current on top (Mohrig and Marr, 2003). The debris flow travels faster on steeper portions of the slope but stops eventually due to frictional forces, whilst the turbidite can travel very long distances until turbulence decreases below a critical value (Iverson, 1997). The potential of a slide to transform into these sediment flows as well as the flow's intensity and run-out distances depend on a number of factors, e. g. the density of the failed material, its initial excess pore pressure, whether the material is contractive or dilational and its sensitivity, i. e. the amount of shear strength that is lost when the material fails (Hampton et al., 1996). This aspect of slide movement is not focus of this thesis, which rather considers how they are triggered.

### 1.5 Rationale

Due to increasing awareness, improved acquisition techniques and broader data coverage the number of submarine landslides observed at the seafloor has drastically increased in the past decade (Locat and Lee, 2002; Masson et al., 2006). Most continental slopes around the globe are affected by landsliding to some degree, independently of latitude, level of seismicity or depositional environment (Canals et al., 2004; Hühnerbach et al., 2004; Masson et al., 2006; Lee, 2009).

Considering the abundance of submarine landslides, it is evident that these events play an important role in the evolution of the submarine landscape of continental margins (Masson et al., 2006). The sediment flows that landslides generate can transport masses of sediment that exceed the annual discharge of all the rivers in the world combined (Talling et al., 2007), and are therefore vital in the redistribution of sediments into the deep ocean.

It has been suggested that large submarine landslides affected climate in the past (Maslin et al., 2004), and possibly will in the future (Maslin et al., 2010). Large volumes of methane, an important greenhouse gas, are stored as gas hydrates in continental margin sediments (Kvenvolden, 1993). Slope failure removes sediment and reduces pressure from

overlying sediment. The new pressure conditions can cause hydrate dissociation and a sudden release of large amounts of methane with possible consequence for global climate (the 'clathrate gun hypothesis', Maslin et al., 2004, 2010).

Submarine landslides at open continental slopes are not only of specific academic interest, but also of socioeconomic relevance. The sudden mobilisation and redistribution of large amounts of slope material associated with submarine landslides can cause far-reaching tsunamis. The tsunami triggered by the Storegga Slide off Norway 8,200 years ago had run-up heights of more than 20 m in the Shetland Islands and up to 6 m in north-east Scotland (Bondevik et al., 2005a). Examples of more recent landslide-triggered tsunamis are:

- The Grand Banks tsunami in 1929 with wave heights of up to 7.5 m and 29 fatalities (Fine et al., 2005).
- The great 1946 Aleutian tsunami that killed 167 people and reached a local run-up of 42 m (Okal et al., 2003; Fryer et al., 2004).
- The 1964 Valdez tsunami that reached local wave height of 67 m, destroyed several coastal communities and left 82 dead (Lee et al., 2007).
- The devastating Papua New Guinea tsunami with 10-15 m maximum wave height triggered by a slump in 1998 (Tappin et al., 2001). The tsunami caused 2,200 fatalities.

Although on a global scale landslide tsunamis are comparatively infrequent, they can have serious social and economic impacts and classify therefore as "high impact-low frequency" events (Nadim, 2012).

Undersea cables carrying telephone, Internet and other data traffic across the oceans are vulnerable to submarine landslides and turbidity currents. Such cable breaks can disrupt communications to entire regions and cause significant economic loss. In 2006, a submarine landslide broke almost all telecommunication cables off Taiwan and severely affected communication within the entire south-east Asian region for 12 hours (e.g. Su et al., 2012). Business losses are estimated to amount to a substantial part of the region's daily GDP, which approximates \$7.56 billion. Landslides are also a threat to oil production platforms. An increasing proportion of the world's hydrocarbon resources are now recovered from deep-water sites, with associated infrastructure exposed to submarine mass movements. In the Gulf of Mexico landslides have repeatedly destroyed or destabilised foundations of hydrocarbon exploration structures (e.g. Bea, 1971; Sterling and Strohbeck, 1973).

Global temperature is expected to increase by about 3° C in the next century (Meehl et al., 2007), accompanied by an associated rise in sea level between 0.9 and 1.3 m (Grinsted et al., 2010). These environmental changes could potentially affect the stability of continental slopes and cause more landslides (Owen et al., 2007; Maslin et al., 2010). Such an increase in landslide frequency would have important impacts on future hazard assessments and would need to be considered.

Given the direct and indirect damage that large submarine landslides could cause, there is a need to understand where and when landslides may occur in the future. A prerequisite for such forecasting is to understand what causes underwater slope failures. Traditional geotechnical slope stability methods, as used for stability predictions on land, fail to explain landslides in the marine realm. This is mainly due to the very low slope gradients (in many cases less than 1 or 2°; Hühnerbach et al., 2004) at which marine slope failures occur. Numerous hypotheses have been put forward as to what mechanisms could cause failure of nearly flat slopes, including earthquakes, gas hydrate dissociation or the presence of weak layers (Table 1.1). However, these hypotheses are difficult to test in the real world due to the inaccessibility, a lack of direct observations and in situ monitoring. The reason(s) for large scale failure of low angle submarine slopes are therefore contentious. This lack of consensus over landslide triggers makes hazard assessment more difficult than for other geohazards.

## 1.6 Objectives

This thesis aims to contribute towards an improved understanding of the mechanisms that control the occurrence, timing and frequency of submarine landslides. Only large slides at open continental slopes that occurred on slope angles of 2° and less are considered.

A better understanding of the way in which climate-related environmental changes influence (or do not influence) the stability of continental slopes could help to constrain possible failure mechanisms. To test whether and how climate change affects continental slope stability the first part of this thesis (chapter 2) aims to answer the following questions:

- What are the uncertainty ranges to given landslide ages?
- Including these uncertainties, is there an association between sea level and the timing of large seafloor failures on a global scale?

- Do landslides happen when deposition rates are high?
- What are the implications for the understanding of failure mechanisms and future geohazard?

The second part of the thesis focuses on the hypothesis that excess pore pressures or complex drainage patterns due to rapid sedimentation can cause landslides. Pore pressures that greatly exceed hydrostatic pressures are necessary to initiate failure of low gradient slopes. Rapid deposition and underconsolidation of soft sediments could be the source of such high pressures (Leynaud et al., 2007; Schneider et al., 2009; Stigall and Dugan, 2010). Complex drainage patterns may also contribute to the generation of high pore pressures (Dugan and Flemings, 2000, 2002). However, submarine landslides occur at all continental margins irrespective of sedimentation rates. Therefore, can excess pore pressure generation due to sediment deposition be a universal failure mechanism, that explains the occurrence of submarine landslides at low angle slopes globally? More specifically, the thesis aims to answer the following questions:

- Do low rates of sedimentation produce sufficiently high excess pore pressures to initiate failure?
- How else can high excess pore pressures be generated in areas of slow ( $<0.2$  m/ky) sedimentation?
- What are the key physical-mechanical properties capable to reduce slope stability with respect to excess pore pressure generation?
- What other processes that act on a global scale may contribute to the overpressurisation and failure of continental slopes?

The obtained results will be placed in the context of the current understanding of the global occurrence, timing and frequency of submarine landslides at open continental slopes. The final aim is to identify the remaining uncertainties. How could future studies be directed in order to constrain remaining uncertainties and improve understanding?

## 1.7 Thesis outline

The main body of the thesis contains three individual chapters (2, 5 and 6) in a stand-alone research article format. The papers have been published by, submitted to, or are in preparation for publication in international peer-reviewed journals.

Chapter 2 addresses a possible link between climate and landslide frequency. Ages of past submarine landslides are collated within a new data base, which is the most comprehensive of its kind and the only one to include uncertainty intervals to individual age estimations. The entries in the data base, either as a whole or divided into subsets, are compared to global mean sea level curves and local sedimentation rates as proxies for climatic changes, using statistical techniques.

Chapter 3 gives a description of the methodology used in the subsequent chapters. A general introduction to the Finite Element Method is followed by more specific sections on the modelling of consolidation and slope stability, and how these techniques are used to simulate a continental slope under continuous sediment deposition. General aspects about the mechanical behaviour of marine sediments are discussed in the light of appropriate constitutive modelling.

Chapter 4 describes a benchmark study that was conducted to evaluate two types of analyses of the same model with respect to computational performance and errors. The models used in this thesis capture a continental slope to its full extent, and are considerably large. Using a less expensive type of analysis is therefore beneficial, but requires the assessment of errors, and if these are tolerable.

In chapter 5, I apply numerical modelling to assess the stability of a continental slope subjected to low rates of sediment deposition. The simulations use average physical-mechanical properties for hemipelagic sediment predominant at continental margins with low sediment input. This chapter has been published as Urlaub et al. (2012).

Chapter 6 is an extension of the modelling done in the previous chapter. The sensitivity of the continental slope model towards excess pore pressure generation is tested under consideration of a wide range of physical-mechanical properties. Key parameters for slope stability are identified. In addition, the effect of lateral pore fluid flow on slope stability is analysed under low sedimentation rates.

The thesis ends with a synthesis of the main conclusions of this study and suggestions for future research directions in chapter 7.

## Chapter 2

# Timing and frequency of large submarine landslides: Implications for understanding triggers and future geohazard <sup>1</sup>

### Abstract

Large submarine landslides can have serious socioeconomic consequences as they have the potential to cause tsunamis and damage seabed infrastructure. It is important to understand the frequency of these landslides, and how that frequency is related to climate-driven factors such as sea level or sedimentation rate, in order to assess their likely frequency in the future. Recent studies have proposed that more landslides occur during periods of sea level rise and lowstand, or during periods of rapid sedimentation. In this contribution we test these hypotheses by analysing the most comprehensive global data set of ages for large ( $>1 \text{ km}^3$ ) late Quaternary submarine landslides that has been compiled to date. We include the uncertainties in each landslide age that arise from both the dating technique, and the typically larger uncertainties that result from the position of the samples used for dating. Contrary to the hypothesis that continental slope stability is linked to sea level change, the data set does not show statistically significant patterns, trends or clusters in landslide abundance. If such a link between sea level and landslide frequency exists it is too weak to be detected using the available global data base. It is possible that controlling factors vary between different geographical areas, and their role is therefore hidden in a global data set, or that the uncertainties within the dates is too great to see an underlying correlation. Our analysis also shows that there is no evidence for an immediate influence of rapid sedimentation on slope stability as failures tend to occur several thousand years after periods of increased sedimentation rates. The results imply that there is not a strong global correlation of landslide frequency with sea level changes or increases in local sedimentation rate, based on the currently available ages for large submarine landslides.

---

<sup>1</sup>This chapter has been submitted for publication in *Quaternary Science Reviews* with co-authors Peter J. Talling and Douglas G. Masson.

## 2.1 Introduction

Submarine landslides include the largest mass flows on Earth and can be far larger than slope failures on land (Hampton et al., 1996). For instance, the Storegga slide offshore Norway has a volume of over  $3000 \text{ km}^3$ , and covers an area larger than Scotland (Haffidason et al., 2004). For comparison, collapse of the Mt St Helens volcano in 1980 involved  $\sim 3 \text{ km}^3$  (Voight et al., 1985), whilst the annual global flux of sediment from rivers into the ocean is  $\sim 11 \text{ km}^3$  (Milliman and Syvitski, 1992; Talling et al., 2007). Perhaps the most remarkable aspect of large submarine landslides is not their scale but the fact that they can occur on remarkably low ( $< 2^\circ$ ) seafloor gradients, which are almost always stable on land. Submarine landslides can generate damaging tsunamis and therefore pose a significant geohazard. The Storegga slide produced a tsunami that locally ran up for up to 20 m around the North Sea coasts, 8200 years ago (Bondevik et al., 2005a). A slump containing 5-10  $\text{km}^3$  of sediment triggered a tsunami that killed 2200 people in Papua New Guinea in 1998 (Tappin et al., 2001). The landslides themselves can damage seafloor infrastructure, such as that used to recover oil and gas, or seafloor telecommunication cables that carry more than 95% of the global internet traffic. Such cables were broken by a large submarine landslide and the flow of sediment it generated off Grand Banks, Canada, in 1929 (Piper and Aksu, 1987). Numerous hypotheses have been put forward for what causes large submarine landslides on shallow gradients, including earthquakes, rapid deposition or gas hydrate dissociation (e.g. Maslin et al., 1998; Stigall and Dugan, 2010; Masson et al., 2011). These hypotheses are poorly tested, and even less is known about the effect of other preconditioning factors such as fluid flow focussing in the slope (Dugan, 2012).

It has been proposed that future climatic change and ocean warming may increase the frequency of large submarine landslides, such as through triggering by gas hydrate dissociation (Maslin et al., 1998; Tappin, 2010). It is therefore important to know if past large landslides coincided with major climatic events, or were more frequent during periods of global warming. It is also important to understand the timing of large submarine landslides to document their frequency and assess the hazard they pose, and to constrain the factors that precondition and trigger slope failure. The timing of landslides and factors such as sea level or sedimentation rate can potentially provide a test for failure mechanism hypotheses.

Comparisons of landslide frequency with sea level have been undertaken previously by Maslin et al. (2004), Owen et al. (2007), Lee (2009), and Leynaud et al. (2009), who used compilations of between 16 and 43 large submarine failures. All studies suggest an increased landslide occurrence during periods of glaciation and/or during glacial to interglacial transitions. Several other authors report an increased recurrence interval of

submarine mass failures from various geographical locations worldwide during sea level lowstand and during sea level rise (e.g. Paull et al., 1996; Prins et al., 2000; Piper et al., 2003; Lebreiro et al., 2009; Henrich et al., 2010; Lee et al., 2010). These studies are purely qualitative as they are not supported by any statistical analysis. Importantly, they do not take fully into account uncertainties in the determination of landslide ages. These uncertainties can be large, as illustrated by changes in understanding of the age(s) of the Storegga slide. Early studies were based on three cores containing turbidites deposited in an adjacent depositional basin that had no physical connection to the Storegga slide scars. The slide was interpreted as a three-phase event, one of which was older than 30 ka (Bugge et al., 1988). This was then revised by later work that used a more extensive (> 90) core data set (Hafidason et al., 2005), to show that the slide was one main event that occurred 8.2 ka BP. This significant change in age of the Storegga slide is cautionary, as many other slides are dated using small core data sets comparable to that originally used to date Storegga and similar scientific approaches to obtain landslide ages (e.g. Pearce and Jarvis, 1992; Wynn et al., 2002).

Moreover, the age of a landslide is always accompanied by an uncertainty interval as the accurate age determination is complicated by a number of factors. The main uncertainty is typically related to the location of samples, and it is not the uncertainty in the radiocarbon dates themselves. Samples for dating submarine slides can originate from the slide deposit as well as from the slide scar. They can be taken above, below or within a deposit or scar (Fig. 2.1a-d). These dates usually provide minimum or maximum emplacement ages, rather than exact ages. Their proximity to the exact age depends strongly on sedimentology. For instance, the time gap between landslide and sample age will be large if erosion has taken place or the boundary between pre- and post-failure sedimentation is disturbed by bioturbation (Fig. 2.1g).

### 2.1.1 Aims

This contribution assembles a data set of ages for 62 large volume submarine landslides, of which 61 are previously published. These ages are derived by dating of the landslide itself, or by dating of the turbidite generated by a landslide. Only landslides (or turbidites) with volumes in excess of 1 km<sup>3</sup> are included in this study. Each data point underwent a critical review to avoid interpretation errors and is assigned an individual uncertainty interval.

The first aim is to address the following questions. Given the available ages for these landslides, and taking into account uncertainties in these ages, is there an association between sea level and the timing of seafloor failure? Does landslide frequency vary significantly with sea level, or could the pattern of landslide ages be random and unrelated

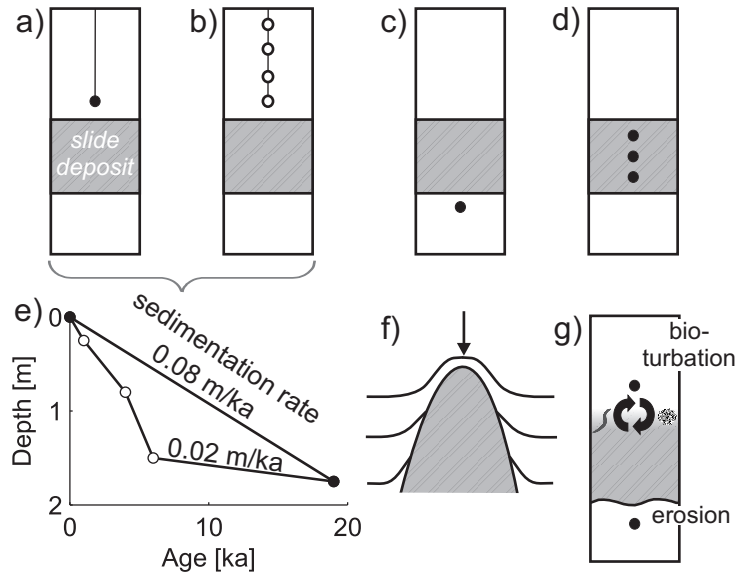


Figure 2.1: Different sampling strategies for radiocarbon dating of submarine mass failures. The rectangles represent sediment cores with hemipelagic background sedimentation (white) and a mass failure deposit (grey). Open and filled black circles indicate the position of the sample. A minimum age is obtained by taking one (a) or several samples (b) from the hemipelagic unit above the mass failure deposit. A maximum age is obtained when samples are either taken from the hemipelagic unit below (c) or within (d) the failure deposit. A linear average sedimentation rate for the core based on one sample can be significantly different from actual temporary sedimentation rates (e), which can be calculated when several samples between the top of the core and the top of the failure deposit are available. Samples above the deposit can give an age too young if located on a local high (f) and bioturbation on the top as well as erosion at the base of the failed deposit (g) are possible sources of uncertainty to the estimated ages.

to sea level? We apply basic statistics to the data set and assess whether the impact of sea level cycles on landslide timing is as strong as previously suggested (Maslin et al., 2004; Owen et al., 2007; Lee, 2009).

The data set is then subdivided to consider the frequency of landslides in different settings that comprise (i) glaciated margins, (ii) river-dominated systems, (iii) sediment-starved margins, and (iv) the north-west African margin where there is an unusually extensive data set. This is done to accomplish the second aim. Is there a significant association between landslide timing and sea level in particular subsets of the data?

We then document available information on changes in sedimentation rate in the vicinity of these large volume landslides. Our third aim is to determine whether there is an association between periods of rapid sedimentation and the timing of landslides, and we analyse the temporal relation of peak sedimentation rates and nearby large scale slope failure. This analysis aims to understand whether there is a strong causal link between

periods of rapid sedimentation and slope failure, as has been predicted by some previous models (e.g. Coleman and Prior, 1988; Leynaud et al., 2007; Stigall and Dugan, 2010).

We conclude with a summary of the implications of this work for predicting the likely hazard posed by landslides (and landslide-tsunamis) in the future as sea level rises rapidly.

### 2.1.2 Climate change and slope stability

A variety of factors has been proposed to impact on the stability of continental slopes. One of these factors is sea level change associated with glacial-to-interglacial climatic cycles (Mulder and Moran, 1995; Maslin et al., 1998; Vanneste et al., 2006; Owen et al., 2007; Leynaud et al., 2009; Lee, 2009). Here, we analyse the direct and indirect links between eustatic sea level and slope stability. The eustatic (global) sea level curve is used, rather than local sea level curves for individual areas, because local sea level curves are not available for some areas. Eustatic sea-level may also be a better proxy for large-scale climate changes, including changes in ocean temperature and circulation.

#### 2.1.2.1 Deposition rates

One factor often assumed as the driving mechanism for submarine landslides is high rates of deposition that cause overpressure in the sediment (e.g. Stigall and Dugan, 2010). This is because rapid sedimentation favours the retention of pore fluid, and development of high excess pore pressures. The amount of terrestrial sediment that is transported into the ocean is mainly controlled by weathering patterns in the hinterlands, which are subjected to glacial-interglacial shifts of climate belts. The interplay with many other factors, for example a regional time delay between climate-driven onshore changes and offshore deposition (e.g. Métiver and Gaudemer, 1999; Castelltort and VanDenDriessche, 2003) make the sedimentation rate histories of different continental margins variable (e.g. Nittrouer, 2007; Covault and Graham, 2010).

In high latitudes terrestrial sediment input is highest during glacial periods due to erosion at the base of ice sheets which then extend to the shelf edge (Vorren et al., 1998; Weaver et al., 2000; Rørvik et al., 2010). Across-shelf oriented ice streams drain the ice sheets and therewith provide effective transport of eroded material. Consequently, large depocentres of glacial sediments (trough mouth fans) develop in front of these ice streams. This process stops as soon as ice sheets retreat, leaving a minor terrestrial input to the ocean by meltwater and a significantly smaller sedimentation rate (Dowdeswell and Elverhøi, 2002; Rørvik et al., 2010). Mulder and Moran (1995) suggest that not only elevated deposition rates at glaciated margins during glaciations but also the weight of

the ice sheet causes excess pore pressure in the sediment.

During glacial periods in moderate latitudes the ice was concentrated inland and did not reach the shelves (Clark et al., 2009). Large amounts of sediments locked up in these ice sheets are released by meltwater discharge pulses during deglaciation (Lebreiro et al., 2009; Toucanne et al., 2012). At most mid-latitude continental margins deposition rates are thus highest at the end of a glacial, i.e. during the onset of sea level rise (e.g. Ducassou et al., 2009; Lebreiro et al., 2009; Bourget et al., 2011). This is also when most of the big river systems experience highest discharge rates (Covault and Graham, 2010). Contrary, in some cases the rising sea level may also hamper the sediment coming off the shelf and sedimentation rates decrease (e.g. Nelson, 1990; Rothwell et al., 2000; Reeder et al., 2002).

In low latitudes weathering rates in the hinterland change with climate shifts. River systems may be active or not depending on precipitation rates. The “Wet Sahara” is one example, which describes short pluvial phases with active river systems in an otherwise arid area (e.g. Pachur and Kröpelin, 1987).

Hemipelagic sedimentation is generally highest during glacials regardless of latitude. Biological primary production benefits from strong winds during glacials caused by increased land-sea temperature gradients, which input important nutrients to the ocean (Berger and Wefer, 1991).

### **2.1.2.2 Location of depocentres**

Not only the amount of terrestrial sediment delivered to the continental margin changes from glacials to interglacials, but also the location of its deposition (Lee, 2009). In periods of low sea level large areas of the continental shelves are exposed and sediment deposition shifts seaward and towards the continental toe (Posamentier et al., 1992). This is critical as, when loaded, a slope has a higher potential to fail due to prevailing shear stresses than a nearly flat shelf where shear stresses are absent. During high sea level shelves are flooded and continental slopes are disconnected from rivers or ice streams, limiting direct delivery of sediment to the continental slope and promoting deposition on the flat shelf (Covault and Graham, 2010; Rørvik et al., 2010).

### **2.1.2.3 Stress changes**

Previous work has suggested that sea level fluctuations impact on slope stability directly (Weaver and Kuijpers, 1983; Lee et al., 1996; Antobreh and Krastel, 2007), as they alter

the stress regime at the seafloor. It is important to understand that sea level fluctuations change hydrostatic pore water pressure (the weight of all the water above). This directly affects the total stress (the total load experienced at a point), which is the sum of the effective stress and the pore water pressure. The fraction of the applied load that is borne by the pore fluid is given by the loading efficiency  $\alpha$ . For shallow marine sediments  $\alpha = 0.97$  (Liu and Flemings, 2009), i.e. a change in total stress is almost entirely borne by the pore pressure (97%) and the effective stress changes only slightly (3%). Therefore, from a geomechanical point of view, the direct impact of changing sea level on slope stability is likely to be minimal.

Free gas is affected more strongly by a change in sea level as it depends on total stress. If gas is present in the pore space during sea level fall, the pore pressure drops less than the total stress due to the high compressibility of gas and overpressure develops (Liu and Flemings, 2009). Contrarily, the effective stress increases in gas bearing sediments when sea level rises.

#### **2.1.2.4 Isostatic adjustment**

When ice sheets retreat the Earth's crust responds elastically to the loss of weight by isostatic rebound. This uplift is most rapid where the ice was thickest, such as in the centre of the continent, and gradually declines towards the continental margin (e.g. Milne et al., 2001), thereby causing steepening of continental slopes and decreasing their stability. However, this slope gradient increase is small; e.g. in the order of  $0.1^\circ$  for the Norwegian continental margin. We calculate this using the total uplift of 0.76 km in the past 13 ka at the centre of uplift at the Swedish Baltic coast (Mörner, 1979), and a distance of about 400 km to the Norwegian continental slope, where the uplift is nearly zero.

The crust also responds in a brittle manner to crustal stress changes by generation of earthquakes (Bungum et al., 2005). Seismic shaking can cause an increase in pore pressure as well as a decrease in the sediment's strength and is therefore capable of triggering a submarine slide (Biscontin et al., 2004). However, repeated seismic events that do not lead to failure can also strengthen the sediment by facilitating the consolidation process through rearrangement of grains and dissipation of excess pore pressure (Boulanger and Truman, 1996; Boulanger et al., 1998). Earthquake-induced shear stresses are less significant in deep sediments (>100 m below seabed) as they quickly decrease with depth (Leynaud et al., 2004).

### **2.1.2.5 Bottom water temperature**

A change in global surface temperature is followed by a gradual and slow temperature change of the bottom water in the oceans and at the seafloor (e.g. Clark et al., 2009). A bottom water temperature increase leads to a downslope shift of the gas hydrate stability zone and will cause dissociation of hydrates at the base of the hydrated layer (Kvenvolden, 1993). If this layer is thick the released gas will migrate back into the stability zone to form hydrate again. If the layer is thin the free gas will cause pore pressures in excess of hydrostatic and decrease the strength of the sediment, promoting slope instability. This especially affects shallow hydrates at water depths <600 m because here the gas hydrate stability zone is relatively thin. Deep hydrates at water depths >1000 m will remain stable as the gas hydrate stability zone is thick and its top lies well above the seafloor due to high hydrostatic pressure at these depth (Reagan and Moridis, 2008).

During the retreat of ice sheets, hydrate destabilisation due to a temperature increase is counterbalanced by an increase in pressure due to sea level rise. Nevertheless, this stabilising effect is small and can only delay a release of methane, especially in shallow water (Kvenvolden, 1993; Reagan and Moridis, 2008).

### **2.1.2.6 Bottom water currents**

Strong intermediate and deep water bottom currents can erode sediment at the toe of the slope and therewith undercut and destabilise the slope (Hampton et al., 1996). A climate-ocean circulation link is widely accepted (e.g. Rahmstorf, 2002) and glacial-interglacial variability of bottom current strengths has been reported from various locations (e.g. McCave et al., 1995; Gröger et al., 2003). However, the way in which bottom current strengths is affected is complex and spatially variable, i.e. during glacials bottom currents can be stronger (e.g. Revel et al., 1996) or weaker (e.g. McCave et al., 1995; Gröger et al., 2003).

### **2.1.2.7 Groundwater flow**

Groundwater seepage may contribute to excess pore pressures within a continental slope (Locat and Lee, 2002). Drainage patterns depend on head differences between continental groundwater and sea level, which increase during sea level fall (Lee, 2009). In addition, DeFoor et al. (2011) show evidence that ice sheet meltwater infiltrated into the continental groundwater, and was discharged as submarine groundwater in the Greenland Shelf. The authors report a twofold increase in discharge rate during the Last Glacial Maximum compared to ice-free conditions.

### 2.1.2.8 Climate-independent causes

Seismicity is generally controlled by tectonics and thus assumed independent of climate, unless associated with glacial loading or rebound. A trigger mechanism such as an earthquake would be expected to produce randomly distributed landslides. Exceptions are glaciated regions, where seismicity is controlled by a retreat of the ice sheet. Oversteepening due to salt doming or other tectonic activities as well as a stress-related collapse of mechanically weak layers are other climate-independent failure mechanisms.

### 2.1.3 Dating submarine landslides

Several approaches can be used to date the timing of submarine slope failures. The most appropriate strategy is to determine the age of the hemipelagic sediment that is immediately overlying and/or underlying the landslide in sediment cores. Three methods are widely used for the age determination of hemipelagic sediment. The uncertainties involved with each dating method are firstly described, followed by (often larger) uncertainties arising from the location of the sediment samples within the core.

#### 2.1.3.1 $^{14}\text{C}$ AMS

$^{14}\text{C}$  AMS dating of microfossil shells is the most widely used tool to determine the absolute age of marine sediments younger than 50 ka (e.g. Thomson and Weaver, 1994). This method can date sediments to an age of up to 50 ka with typical measurement uncertainties of  $\pm 100$  years. A calibration (e.g. Reimer et al., 2009) as well as a reservoir correction for conversion to calendar years is necessary (Lassey et al., 1990). These corrections vary both temporally and locally and are the main reasons for the typical uncertainty for calibrated dates in marine sediments of  $\pm 100$  years.

#### 2.1.3.2 Oxygen isotopes

Oxygen isotope stratigraphy is the preferred method for dating marine sediments older than 50 ka (Prell et al., 1986). The amount of  $^{18}\text{O}/^{16}\text{O}$  in hand picked calcareous shells of microorganisms is measured in a mass spectrometer and the resulting isotope record has a dominant glacial-interglacial signal (Shackleton and Opdyke, 1973). The relationship of this isotope record to age is obtained by orbital tuning (e.g. Imbrie et al., 1984). The isotope content is measured preferably on benthic foraminifera as, while alive, they were subjected to a much smaller range of temperature due to relatively stable deep water temperatures (Shackleton and Opdyke, 1973).

Uncertainties in this method may arise from bioturbation that mixes foraminifera up or down the core. For instance, Hutson (1980) reports a 4.5 ky uncertainty for oxygen isotope stratigraphy due to bioturbation at oxygen isotope stage boundaries. Uncertainties will be higher for cases with relatively low abundance or variations in abundance of the species on which the isotopes are measured (Hutson, 1980). Differences within one species, as well as physiological differences between different species, may also result in different  $^{18}\text{O}/^{16}\text{O}$  ratios. Moreover, below a certain water depth (typically between 3-5 km), the carbonate in foraminifera shells begin to dissolve (Berger, 1972). At ages older than the  $^{14}\text{C}$  range (50 ka) the isotope record is tied in to absolute ages by orbital tuning which can introduce maximum errors of about 5 ky (Martinson et al., 1987). If an uncertainty range is not given in the original publication, information on the data in such detail that would allow to estimate the individual uncertainty range is often not provided either. Thus, there is a need for a uniform uncertainty range which takes into account all possible uncertainties named above. We thus assume uncertainties involved with oxygen isotopes to be about 5 ky for the period 0-50 ka, and about 10 ky for older samples. This is a trade-off between conservative and consistent uncertainty estimation, as especially for dates younger than about 5 ky the uncertainties can be lower.

### 2.1.3.3 Biostratigraphy

Biostratigraphic methods are indirect dating methods based on the identification of micro- or nanofossils in the sediment. A biozone (interval of geological strata) is assigned according to the prevailing taxons. The identification of fossils for biostratigraphy is subjective and thus poses a source of uncertainty, along with reworking of fossils (Sadler, 2004) and uncertainties at zone boundaries resulting from diffuse transitions between biozones (Jasko, 1984). The length of the uncertainty interval strongly depends on the frequency of individual species in the sediment and thus can vary largely between sites. Therefore, no universal error can be estimated and we use the uncertainties assigned by the original authors. One example method is calcareous nanofossil stratigraphy suggested by Weaver (1994) which is based on the analysis of ratios of different species of coccoliths. Used in conjunction with oxygen isotope stratigraphy the author suggests an accuracy of a few thousand years.

### 2.1.3.4 Uncertainties due to sample locations

By far the largest source of uncertainty originates from the positioning of the sample in the sediment core relative to the mass movement deposit or erosional hiatus. Ideally, samples are taken from hemipelagic background sediment deposited after (Fig. 2.1a, b) as well as before the event (Fig. 2.1c) to provide a time bracket for the maximum and minimum landslide ages, respectively. The sample is preferably taken very close to the slid mass whilst at the same time avoiding sediment mixing by bioturbation or bottom

currents (Fig. 2.1g). This method is favoured by rapid sedimentation rates, and is more problematic in areas with low sedimentation rates. The time interval between deposition of the sediment from which the sample is taken and the actual event should be calculated based on local sedimentation rates and added or subtracted to the estimated age of the sample. Uncertainties arising from this interpolation can be large, especially when accumulation rates are low or unknown (Fig. 2.1e), but can be reduced by taking several samples to better constrain the sedimentation rate history (Fig. 2.1b, e).

Samples taken above the deposit (Fig. 2.1a) can give an age that is too young if the samples are located on a local high within a geometrically irregular deposit. Post-failure sedimentation on a local high in a hummocky deposit can result in a local reduction in sedimentation rate, or even a hiatus (Fig. 2.1f). Samples taken above the slide deposit can also return an age older than the actual emplacement age. This occurs if the slide deposit carries abundant microfossils and if the sample lies within an area affected by bioturbation and reworking of this deposit (Fig. 2.1g). On the contrary, if the slide deposit has low carbonate content, the contamination by bioturbation is less important. It is generally best to obtain multiple dates in the sediment that drapes a landslide, such that the accumulation rate can be used to extrapolate a more precise age for the upper surface of the landslide (Fig. 2.1b, e).

Samples taken below the slide deposit (Fig. 2.1c) can return much older ages than the emplacement age. This is because the base of the slide is likely to erode underlying background sediment, and the uncertainty depends on the depth of erosion.

Dating the slid mass itself (Fig. 2.1d) gives a maximum age for the failure. However, the uncertainty can be large due to reworking of the failed material, because the landslide can contain relatively old material.

Uncertainties resulting from the relative position of samples and slid mass in the sediment are relatively difficult to quantify. It can be reduced by extrapolating accumulation rates using multiple dates in the drape above a landslide, especially in locations with rapid sedimentation, or by having samples from many cores (e.g. Haffidason et al., 2005, for the Storegga slide). Ages that are consistent with multiple dating techniques may also be considered to be more robust.

### **2.1.3.5 Uncertainties if slide has multiple depositional lobes or headwalls**

Depositional lobes characterise the downslope ends of many submarine landslides (O’Leary, 1991). In some cases several lobes are mapped which could have been created successively during one event, as in the Storegga slide (Hafliðason et al., 2005). However, they could have also been emplaced at longer time intervals and thus represent several separate events (Georgiopoulou et al., 2009; Förster et al., 2010). It is therefore important to take cores from all lobes in order to correctly interpret the timing of the events and to understand their temporal evolution. This is not always the case and increases the level of uncertainty. For instance, four depositional lobes are observed in the Trænadjupet slide area (Laberg et al., 2002b). Although radiocarbon ages have only been determined for one of the lobes, the slide has been interpreted as one single event (Laberg et al., 2002a,b). The same principle holds if the slide area shows multiple headwalls. Ideally, cores need to be taken from all scars to constrain the timing between single events.

These error sources are not predictable and are therefore not included in any error estimations. Consequently, uncertainties for submarine landslide ages are always conservative.

## **2.2 Data and methods**

A new data base is established based on published and unpublished field data. We calculate actual emplacement ages from the available data and develop a methodology to determine uncertainty intervals for ages obtained with the  $^{14}\text{C}$  method. The methodology used to analyse the data base is explained in this section.

### **2.2.1 Criteria for inclusion in the data set**

The data set only contains mass failures worldwide for which relatively reliable ages are available. Only open continental slopes are within the scope of this paper. Volcanic island failures are omitted because they may involve subaerial material and have specific failure mechanisms (Masson et al., 2002). Only case studies in which ages were obtained by radiocarbon  $^{14}\text{C}$  AMS measurements or by applying a combination of several methods (e.g. biostratigraphy and oxygen isotopes or bio-, magneto- and seismic stratigraphy) were accepted.

The data base also includes large turbidites with volumes  $>1\text{ km}^3$ , which increases the size of the data base significantly. Large volume turbidite deposits in deep sedimentary basins are proxies for landslides on the adjacent continental slope (Talling et al., 2007). Moving down the continental slope a submarine landslide may undergo progressive disintegration and can eventually turn into a density flow that is deposited several hundred kilometres

away from the source (e.g. Masson et al., 2006). The 1929 Grand Banks event, where a seismically triggered landslide evolved into a turbidite, is a seminal example (Piper and Aksu, 1987). Nevertheless, density flows can also be initiated by flood discharges from rivers (Mulder and Alexander, 2001). These flows are usually small, considering that the mean annual discharge of all rivers worldwide is  $2 \cdot 10^{13}$  kg (Milliman and Syvitski, 1992), or about  $11 \text{ km}^3$ , assuming a density of  $1800 \text{ kg/m}^3$  (Baas and Best, 2002). Canyon levee system turbidites (e.g. Lebreiro et al., 2009; Henrich et al., 2010) are likely dominated by river input and are thus omitted here. Other turbidite systems such as in the Ulleung basin (Lee et al., 2010) had to be excluded from the data set despite their well constrained ages as no volume estimates are available. Turbidites in the Canadian abyssal plain involve large uncertainties due to heavy bioturbation and limited material for radiocarbon sampling (Grantz et al., 1996) and therefore are omitted.

### 2.2.2 Real emplacement ages

Ages obtained from radiocarbon dating of material above (Fig. 2.1a, b) or below (Fig. 2.1c) the mass transport deposits does not provide the real emplacement date as the sample is usually taken at some distance from the failed material. Hemipelagic sedimentation rates at the location of the specific core are needed to interpolate the sample age to the age of emplacement.

The emplacement age equals  $\text{radiocarbon\_age} + \frac{d_{sf}}{sr}$ , where  $d_{sf}$  is the distance in the core between the radiocarbon sample and the failure deposit and  $sr$  is the sedimentation rate. In the case of a single radiocarbon age obtained below the mass transport deposit sedimentation rates have to be inferred elsewhere, e.g. from other cores nearby or regional rates, and the emplacement age is calculated by  $\text{radiocarbon\_age} - \frac{d_{sf}}{sr}$ . The age obtained assumes no erosion during emplacement. If measurements from several cores are available and the ages are similar, then the arithmetic mean of all samples is used in order to average out uncertainties. However, in the case of considerably different ages, the oldest date for samples above the slide and the youngest for samples below the slide are used. If uncalibrated  $^{14}\text{C}$  ages are published we use the Marine09 calibration curve (Reimer et al., 2009) for conversion.

For landslide ages obtained by oxygen isotope stratigraphy it is not necessary to calculate the real emplacement age as the isotope curve ideally is a series of closely spaced measurements that interpolates ages down to the landslide deposit. In the case of biostratigraphy the assignment of real emplacement ages is generally not possible because biozones rather than absolute ages are determined.

### 2.2.3 Uncertainty estimation for emplacement ages obtained by $^{14}\text{C}$

As the technical error with the  $^{14}\text{C}$  method is small, the main uncertainty in dating submarine failures arises from estimating sedimentation rates needed to calculate real emplacement ages. Sedimentation rates are usually obtained by linear interpolation between two  $^{14}\text{C}$  ages, i.e. dividing the distance by the age difference between these two samples, or between a  $^{14}\text{C}$  age and the seafloor with an age of zero. Ideally, several radiocarbon ages are available in the hemipelagic sediment above the slide deposit (Fig. 2.1b) as the sedimentation history can be determined with a higher resolution and changes in sedimentation rates can be detected (Fig. 2.1e, open circles). If these values vary significantly, the sedimentation rate from the interval closest to the failure deposit is chosen. If only one age above the deposit is available (Fig. 2.1a), a linear sedimentation rate from the seafloor to the sample must be assumed (Fig. 2.1e, filled circles). Consequently, both the errors for the  $^{14}\text{C}$  measurements and an uncertainty due to simplification of sedimentation rate propagate into the final sedimentation rate that is used for the age estimate of a submarine landslide. Errors can be especially large when time and distance for the interpolation are large and sedimentation rates change within short periods (Fig. 2.1e). We take these uncertainties into account by assuming that sedimentation rates may vary by a factor of four. Accordingly, if the radiocarbon sample was taken above the failure deposit, the minimum age, i.e. the lower bound of the uncertainty interval, is calculated by  $\text{radiocarbon\_age} + \frac{d_{sf}}{sr \cdot 4}$ , and the maximum age, i.e. the upper bound of the uncertainty interval, correspondingly by  $\text{radiocarbon\_age} + \frac{d_{sf}}{4}$ .

This method is applied to case studies in which minimum radiocarbon ages were available, such that the sample was taken from above the slide deposit. If additional maximum ages were measured either from material within or below the slide deposit and the results provide an age younger than the maximum age determined by the method described above, the latter age is discarded and the measured age accepted. If more than one age estimate is available the maximum and minimum ages for each age estimate are calculated. The overall uncertainty interval and the emplacement age for the particular event is then obtained by taking the arithmetic mean of all samples.

### 2.2.4 Global sea level as proxy for global climate

The global mean sea level is used here as an analogue of global climate and environmental changes. The sea level curve used here is based on benthic foraminifera isotopic records (mean ocean  $\delta^{18}\text{O}$ ) and displayed relative to present sea level (Waelbroeck et al., 2002).

### 2.2.5 Continental slope accumulation rates

Accumulation rates are not only important for dating marine slope failures but may also directly impact on slope stability (Stigall and Dugan, 2010). Therefore we compare the timing of submarine landslides to pre-failure sedimentation rates from the continental slopes where the slides originate. Sedimentation rate estimates are not always available from ideal locations proximal to the headwall. Cores used to determine these rates may originate from different locations on the slope and thus record different rates of sediment input. We acknowledge the uncertainties in these estimates of accumulation rates near the landslides. However, the values show whether the margin is subject to high ( $> 5$  m/ky), intermediate (0.5-5 m/ky) or low ( $< 0.5$  m/ky) sedimentation rates. Relative trends in sedimentation rates such as increases and decreases are likely to be synchronous across and are likely to affect the whole continental slope so that correlation of changes in sedimentation rates to timings of landslides within one region are still relevant.

### 2.2.6 Data presentation and statistics

Large and irregular uncertainty intervals along with a bias towards younger ages limit a statistical analysis of landslide ages. We therefore analyse the data set both qualitatively and by using basic statistical tests.

The frequency distribution of the data is shown by histograms. We found that the duration of the histogram bins (e.g. 1 ky, 2 ky, or 5 ky) is important because it may change the shape of the histogram. It is not clear what duration of bin to use. Histogram bins must be long enough to cater for uncertainties in the data. However, shorter bins are needed to see if landslides occur during shorter lived fluctuations in sea level. We therefore analyse histograms with a range of bin durations, which are 5 ky, 2 ky and 1 ky.

For each bin duration, two histograms are calculated. One histogram is based on the best estimate age and ignores the uncertainty in that 'best guess' of landslide age. The second histogram is calculated by taking into account the uncertainty interval and ignoring the best estimate age. It is assumed that the probability of the slide is evenly distributed over the uncertainty interval, regardless of the best estimate age. This process is illustrated by considering an event with an uncertainty interval ranging between 3-7 ka BP, and a bin duration of 2 ky. The landslide will be assigned as 0.25 to the 2-4 ka bin, 0.5 to the 4-6 ka bin and 0.25 to the 6-8 ka bin.

One aim is to test if the data set is randomly distributed through time or if it has any statistically significant peaks, clusters or trends. A model of randomness is provided by

the Poisson distribution. The  $\chi^2$  test can be used to assess the goodness of fit of the data set to the Poisson distribution. As a temporal process is tested, the data is split into time intervals of certain lengths (identical to histogram bins as described above) and the number of bins containing a certain number of landslides ( $j=0\dots 10$ ) is counted ( $O_j$ ). We then calculate the expected number of bins ( $E_j$ ) containing certain numbers of landslides ( $j$ ) according to a Poisson model with the same total number of events ( $n$ ) and histogram bins ( $T$ , the ratio of the total length of the data set [ky] and the bin size [ky]) as in the landslide data set:

$$E_j = T \cdot e^{-\frac{n}{T}} \cdot \frac{(\frac{n}{T})^j}{j!} \quad (2.1)$$

We thus obtain an expected number of histogram bins ( $E_j$ ) with  $j = 1\dots 10$  landslides (also termed class), which can be compared to those numbers observed in the landslide data set using the  $\chi^2$  test. The  $\chi^2$  test is not valid if  $E_j$  is small. There is no general convention on the minimum  $E_j$  in one class but a value of five is often used (Swan and Sandilands, 1995). Classes with  $E_j < 5$ , can be eliminated by combining two or more classes together. The resulting number of valid classes  $k$  is used in the  $\chi^2$  test:

$$\chi^2 = \sum_{j=1}^k \frac{(O_j - E_j)^2}{E_j}. \quad (2.2)$$

As the Poisson distribution has one parameter, the number of degrees of freedom  $\nu$  is given by  $k - 2$ . If the resulting value of  $\chi^2$  is small, the observed number of histogram bins containing  $j = 1\dots k$  landslides is close to the expected number. Thus, if the critical  $\chi_{crit}^2$  value within a 5% or 10% level of significance exceeds the resulting  $\chi^2$  then the data set resembles a Poisson distribution. The test is only conducted for histogram bin lengths of 2ky and 1ky because calculations for 5ky bins fail the  $E_j \geq 5$  criterion. Furthermore, this analysis can only be applied to a data set that is free from sampling bias.

We also visually test if peaks and clusters in the landslide frequency are significantly different to those obtained in random distributions. As a measure for outstanding peaks we analyse the maximum number of slides in a bin. The maximum difference in number of slides between two neighbouring bins will provide information about whether these large peaks cluster within sets of high peaks, i.e. describing a trend, or if they occur as single peaks surrounded by bins containing comparatively small numbers of slides. The number of neighbouring bins containing more than the average number of slides in a bin is used as a measure of clustering in the data. The average numbers are calculated by dividing the number of total events by the number of histogram bins, i.e. there will be six 5ky bins within a 30ky long data set. A comparison of these characteristics to those of a randomly distributed sample allows a judgement of the significance of these different

characteristics. To do so, probabilities for each characteristic are computed using 1000 sets of computer generated random numbers with the same sample size and time frame as in the original landslide data base.

### 2.2.7 Subdivision into depositional systems

In addition to analysing the entire data set we further investigated subgroups that are characterised by fundamental differences in their depositional environment. The reason for the subdivision is that changes in sea level and climate are likely to impact different depositional environments in different ways.

Glaciated margins are thought to be strongly influenced by climatic cycles due to the direct influence of a growing and shrinking ice sheet and a significantly higher sediment input during glacials (Owen et al., 2007; Lee, 2009). In contrast, most river deltas experience the highest sediment input during deglaciation (sea level rise) or lowstands (Covault and Graham, 2010). As rivers effectively transport terrestrial sediment (Milliman and Syvitski, 1992) this subset of river fan systems is also characterised by generally high deposition rates ( $> 1$  m/ky). A third subset comprises all those continental margins that are not affected by ice sheet coverage, are located away from major rivers and experience rather low sediment deposition. This subset, referred to here as 'sediment-starved continental margins' includes for instance the north-west African, the south-east Australian and US east coast margins. However, there might be an element of the river fan systems subset in this group, as rivers are dynamic systems and highly influenced by local climate in the hinterland. Although virtually no rivers are known from the Sahara today, there is strong evidence for the existence of paleorivers (e.g. Pachur and Kröpelin, 1987). Data from the north-west African margin is also taken as a separate group. This data set is unusually extensive and contains several very large slides mapped at the continental slope as well as turbidites from the same sediment-starved area.

### 2.2.8 Limitations

#### 2.2.8.1 Bias due to limited core penetration

In some cases scientific drill cores provide information about old buried slides (e.g. Maslin et al., 1998), although only few slides haven been drilled. Therefore, the majority of submarine mass failures in the data set are sampled by box, piston or gravity corers. These devices have a limited penetration depth ( $< 30$  m) which strongly depends on the nature and fabric of the sediment. Thus, the material obtained only covers a short time interval, especially in areas of high sedimentation rates such as in river fans. In many cases the

core does not penetrate the entire failed mass, so that deeply buried mass transport deposits are not sampled. Cores in turbidite systems sometimes recover several sequences of mass failures (Table 2.1 and references therein), but even then the recovery is limited. Table 2.1 summarises the age limits and maximum penetration depths for several turbidite studies. This data shows that in most cases the cores date back no further than  $\sim 30$  ka BP, which corresponds roughly to the onset of the Last Glacial Maximum (LGM). It is therefore possible that fewer or a larger number of mass failures occurred before the LGM, which are not represented in the data set simply because they were not recovered and thus not dated appropriately.

Area	Max core length [m]	Max age [ka]	Reference
Balearic abyssal plain	36.0	<50.0	Rothwell et al. (1998)
Heradotus basin	26.0	28.8	Reeder et al. (2000)
Iberian margin	4.4	23.0	Gracia et al. (2010), Masson et al. (2011)
Nile	29.0	120.0	Ducassou et al. (2007)
Makran	33.0	21.6	Bourget et al. (2011)

Table 2.1: Approximate lengths of cores recovering turbidites or slide deposits and maximum obtained ages.

Due to the bias towards younger slides, we use a cut-off age of 30 ka. We assume that landslides younger than 30 ka are in most cases unaffected by this sampling bias (Table 2.1). Exceptions may occur in environments with rapid deposition of coarse sediment, such as trough mouth fans, where cores rarely penetrate beyond  $\sim 15$  ka (e.g. King et al., 1998; ÓCofaigh et al., 2001; Laberg et al., 2002b), contributing to a regional bias (as discussed below). The 30-0 ka BP period covers parts of the last sea level fall (30-22 ka BP), the lowstand during the LGM (22-18 ka BP), the rapid sea level rise (18-6 ka BP) as well as the modern highstand (6-0 ka BP).

### 2.2.8.2 Regional bias

Continental slopes in the different subsets may be scientifically investigated to varying levels of detail. This can be due to difficulties in accessibility, for example in regions that are permanently covered by ice. Large parts of the Antarctic continental slope and the margins surrounding the Arctic Ocean remain unexplored. River deltas are often close to good infrastructure on land and host hydrocarbon reservoirs, so the data base for these settings may be relatively good.

### 2.2.8.3 Short term and local climatic events

Whereas global and local climate changes are often reconstructed to annual resolution based on ice cores, tree rings, lake varves, etc., hardly any submarine landslide has a comparable resolution. The timing of the Storegga slide coincides with a local temperature drop of 3°C that lasted no more than 100 years (Dawson et al., 2011). However, when taking into account the uncertainty interval of the Storegga event, which is as low as 100 years (Dawson et al., 2011), we cannot determine whether the slope failed during the temperature fall, the temperature low or the subsequent temperature rise. Thus, even the age of the best dated slide in the world is not good enough to allow comparison to short term climate fluctuations. Local sea level curves can also differ significantly in magnitude (Raymo and Mitrovica, 2012) as well as in phase (Owen et al., 2007) from the global mean sea level. The analysis presented here only takes into account global sea level changes and ignores local and short term climatic fluctuations.

## 2.3 Results

### 2.3.1 Field data

The following section provides a brief summary of the data on which each landslide age is based on, how uncertainty intervals were obtained for individual failures, and sedimentation rates in the vicinity of the respective failure. For events dated by the  $^{14}\text{C}$  method, the given ages are calculated following the method described above. For slides dated using other methods, brief explanations of the respective uncertainty is provided. All slides in the data set are also listed in Table 2.2 with minimum, maximum and most likely age rounded to the nearest ten years, as well as local accumulation rates.

#### 2.3.1.1 Grand Banks

The Grand Banks slide occurred immediately after the Grand Banks earthquake in 1929 (Piper and Aksu, 1987). The slide turned into a turbidity current which broke several deep sea cables, thereby allowing exact timing, and caused a tsunami.

Huppertz and Piper (2009) estimate a sedimentation rate on the Grand Banks slope of 0.1 m/ky since  $\sim 26$  ka BP based on seismic profiles and cores. During the antecedent glacial the rate was slightly higher (0.15 m/ky).

### **2.3.1.2 Storegga slide**

The Storegga slide is the best-studied submarine slide in the world (Hafliðason et al., 2005; Masson et al., 2006; Dawson et al., 2011) as its age was determined based on almost 200 sediment cores, 90 of which were chronologically analysed by  $^{14}\text{C}$  AMS dating (Hafliðason et al., 2005). The Storegga slide is interpreted as one main event that occurred between 8.1 and 8.2 ka BP (Hafliðason et al., 2005; Dawson et al., 2011). Numerous radiocarbon samples from plant microfossils within the sediments deposited by the tsunami in Norway (Bondevik et al., 1997) and on the Shetland Islands (Bondevik et al., 2005b) support this.

Sedimentation rates on the Norwegian slope varied greatly through time. In the immediate proximity of the slide Hjelstuen et al. (2004) report a maximum of 36 m/ky between 18.9 and 18.6 ka BP at the margin, followed by rates of 27 m/ky between 18.6 and 17.8 ka BP. Holocene sedimentation rates are much lower (0.1 m/ky).

### **2.3.1.3 Trænadjupet slide**

Two cores were taken from within the slide area near the headwall. Each core has two  $^{14}\text{C}$  AMS dates above the failed material indicating an age older than 4 ka (Laberg et al., 2002b). Sedimentation rates can be calculated for the time period between the dates and including a fourfold uncertainty the minimum time of emplacement is 4.3 ka BP and the maximum emplacement time is 7 ka BP. The slide was most likely emplaced 4.84 ka BP. The slide deposit shows four depositional lobes in geophysical data which may indicate that the slide happened in four stages. Only one sediment core from one of the lobes was dated, confirming a minimum age of 4 ka (Laberg et al., 2006). However, the ages of the other lobes remain unknown.

Rørvik et al. (2010) reconstruct the sedimentation history proximal to the former Vestfjorden-Trænadjupet ice stream based on sediment from the Lofoten Contourite Drift. Sedimentation rates were high during the LGM (2.2 m/ky) and significantly decreased during deglaciation (0.18 m/ky).

### **2.3.1.4 Cape Fear slide**

At least five major headwalls can be identified at the Cape Fear slide complex, offshore the south-eastern United States (Hornbach et al., 2007). The water depths of the headwalls range from 890 m to 2300 m for the main headwall. Paull et al. (1996) report the results of  $^{14}\text{C}$  AMS dating from nine gravity cores within 50 km of the main headwall.

All cores penetrate through the sole and a maximum age of 33.1 ka is obtained from hemipelagic sediment below the slide deposit. Several nearby sediment cores reveal hiatuses during the last glacial sea level lowstand (14-25 ka BP), indicating that the age of the slide is probably closer to the samples taken above the slide deposit. We therefore use this maximum age as a broad constraint but give preference to the maximum age based on sediment rate uncertainty. According to Paull et al. (1996) samples taken 0.05 to 0.5 m above the failed material yield ages ranging from 9.67 to 17.12 ka. As no more details of the samples are given, we calculate the uncertainty interval based on the given age of 17.12 ka and a distance of 0.05 m between the radiocarbon sample and the mass transport deposit. The minimum age is 13.48 ka, the maximum age is 20.10 ka and the most likely emplacement age is 15.10 ka.

The regional sedimentation rate has been fairly constant at an average of 0.2 m/ky (Paull et al., 1996).

#### 2.3.1.5 Balearic abyssal plain turbidite

Five piston cores recovered and penetrated the megaturbidite deposited in the western Mediterranean Sea (Rothwell et al., 1998). The deposit in the different cores was correlated via geochemical analysis.  $^{14}\text{C}$  AMS dates were taken from above and below the turbidite in each core and the pelagic layers were dated using biostratigraphy. Sedimentation rates averaged from the top of the cores to the radiocarbon date above the turbidite are 0.3-0.8 m/ky. We calculate a mean minimum age of 20.4 ka, a mean maximum age of 21.49 ka and a mean age of 20.52 ka.

The submarine landslide that resulted in this turbidite had its origin on the north-western Mediterranean margin (Rothwell et al., 1998), where three major river fan systems are present; the Var, Rhône and Ebro fans. Pleistocene sedimentation rates at the upper slopes were around 1 m/ky. Higher rates of up to 1.5 m/ky were dominant just after the LGM and were lower ( $\sim 0.1$  m/ky) in the Holocene (Nelson, 1990; Dennielou et al., 2009).

#### 2.3.1.6 Heradotus basin turbidites

Reeder et al. (2000) found 16 turbidite deposits in five cores from the Heradotus basin. Ten have volumes in excess of 1 km<sup>3</sup> and eight have  $^{14}\text{C}$  AMS age estimates following the method of Thomson and Weaver (1994). The source areas are the Nile Cone (for turbidites 'b', 'd', 'e', 'g') as well as the Mediterranean Ridge and the surrounding continental slopes or shelves (Reeder et al., 2002). The main focus was put on the 'n' event as

it is the largest turbidite in this system, the emplacement age of which is constrained by four samples above the mass transport deposit. Neither Reeder et al. (2000) nor Reeder et al. (2002) give the distance between sample and turbidite deposit so that it is impossible to calculate minimum and maximum ages and the original age and uncertainty assigned by the authors has to be used.

Accumulation rates for the Nile Cone are given in the Nile section.

#### **2.3.1.7 BIG95**

The BIG95 event is the largest submarine landslide on the Ebro margin in the north-western Mediterranean Sea (Canals et al., 2004). Four  $^{14}\text{C}$  AMS dates were retrieved from a piston core from the source and one  $^{14}\text{C}$  AMS date was taken from a core from the distal area (Lastras et al., 2002, 2004). All samples were taken from the hemipelagic layer on top of the flow deposit. Averaging over the three samples taken nearest to the debrite ( $< 0.05\text{ m}$ ) and taking into account a fourfold sedimentation rate uncertainty, the minimum time of deposition is 11.26 ka BP and the maximum deposition time is 13.44 ka BP. The event most likely took place 12.00 ka BP.

One sediment core immediately upslope the main scar indicates a Holocene sedimentation rate of 0.09-0.12 m/ky (Lastras et al., 2004). Nelson (1990) reports a higher sedimentation rate of 1.01-1.65 m/ky during the Pleistocene on the continental slope.

#### **2.3.1.8 South-east Australia**

Clarke et al. (2012) analysed three slides from the upper south-east Australian passive continental margin. Dating is based on one gravity core from each slide. From each core two samples for  $^{14}\text{C}$  AMS dating were taken from above the inferred slide plane boundary, allowing the calculation of site-specific sedimentation rates (0.05 m/ky, 0.12 m/ky and 0.06 m/ky for slides 1, 2 and 3, respectively). The three slides yield highest likelihood ages of 21.95 ka, 20.64 ka and 16.81 ka.

Due to a lack of major rivers modern and ancient deposition rates at the continental slope have been low (Boyd et al., 2010). Information is limited but few biostratigraphic age models in sediment cores suggest a rate of 0.05 m/ky over the last 11 ka and slightly higher rates of up to 0.16 m/ky in the Pleistocene (Jenkins and Keene, 1992, and references therein).

### 2.3.1.9 Nyk slide

The Nyk slide underlies and is partly buried by the Trænadjupet slide (Lindberg et al., 2004). The area near the headwall is exposed and shows extensional as well compressional features which Lindberg et al. (2004) interpret to belong to a single event. However, as the depositional area downslope is buried and therefore cannot be mapped, a multistage event cannot be excluded. Two gravity cores were taken with one  $^{14}\text{C}$  AMS dating above the slide (0.05 m and 0.08 m) in each core (Laberg et al., 2001). Linear sedimentation rates from the top of the core to the depth of the sample yield 0.03 m/ky and 0.1 m/ky. Our minimum and maximum emplacement ages are 16.53 ka and 21.55 ka. The slide most likely has an age of 17.53 ka.

The slide's glide plane lies inside the Nyk drift body which was deposited at 1.2 m/ky (Laberg et al., 2001). Hemipelagic background sedimentation rates are lower (see Trænadjupet slide). Between 25.9 and 17.8 ka BP this part of the Norwegian margin was also strongly influenced by high-frequency irregular ice sheet fluctuations which is possibly reflected in accumulation rates (Dahlgren and Vorren, 2003). Consequently, the uncertainty arising from sedimentation rates are particularly high for this slide.

### 2.3.1.10 Hinlopen/Yermak slide

The Hinlopen slide is one of the largest slides worldwide and occurred as one main event followed by several smaller scale failures (Vanneste et al., 2006). Winkelmann et al. (2008) collected four samples from a kastenlot core that penetrated the marginal turbidite of the main event. Three samples were taken above and one below the turbidite, providing site-specific sedimentation rates and an additional maximum age constraint (45 ka). The rate of hemipelagic sedimentation following the slide event for this core is 0.04 m/ky, resulting in an age of 32.2 ka based on a sample taken about 0.1 m above the debris flow (uncertainty interval 30.5-39 ka). An additional sample from the hemipelagic drape 0.12 m above the main slide debris comes from a gravity core close to the sidewall with a linear sedimentation rate from the top to the depth of the sample of 0.04 m/ky. The calculated emplacement age is 32.23 ka with an uncertainty interval from 30.1-40.76 ka. Both ages from the turbidite as well as the main slide are consistent, indicating that the main slide event occurred around 32 ka BP.

Situated directly at Hinlopen Trough Mouth Fan, deposition is expected to be highly variable with periodically very high sedimentation rates related to glacial sediment transport by ice streams (Vanneste et al., 2006). From the same kastenlot core as mentioned above post-slide rates vary between 0.04 and 0.2 m/ky.

#### **2.3.1.11 Mauritania slide**

The Mauritania slide complex is a result of a multiple stage failure (Henrich et al., 2008). An estimate of emplacement age is available only for the youngest event. Age models are based on percentage of carbonate and elemental data (Wien et al., 2007) as well as oxygen isotope and  $^{14}\text{C}$  AMS dating (Henrich et al., 2008; Förster et al., 2010). Four radiocarbon dates from the hemipelagic layer deposited directly after the emplacement were taken (Henrich et al., 2008) as well as one radiocarbon date from the underlying hemipelagic sediment (Förster et al., 2010). Two cores originate from mid-slope locations whereas the other two cores were taken downslope from the edge of the debris flow deposit. Using linear sedimentation rates we calculate 11.95 ka BP for the timing of the youngest failure with upper and lower uncertainty limits of 8.8 and 24.6 ka BP. The radiocarbon age below the debrite gives a maximum emplacement age of 28 ka. The result from Wien et al. (2007) suggests 13.7 ka as the youngest emplacement age and is in good agreement with the age range obtained from radiocarbon dating.

The source area is the north-west African continental slope for which sedimentation rates can be estimated from ODP site 658. The rates in an area of focused deposition, due to the presence of an upwelling cell causing high primary productivity, vary from 0.07 to 0.15 m/ky (Ruddiman et al., 1988).

#### **2.3.1.12 Black Shell turbidite**

The Black Shell turbidite covers a large area of the Hatteras abyssal plain at the north-east American continental margin. Elmore et al. (1979) dated three samples from the basal sand of the turbidite from two cores with the  $^{14}\text{C}$  method. It should be noted that repeated measurements of the same samples gave inconsistent values with variations of up to 21 ka. The youngest radiocarbon age must be the maximum age of the slide, which is 18.65 ka.

The turbidite was initialised from a slump at the Cape Hatteras shelf. Holocene sedimentation rates at the shelf were 0.12 m/ky and 0.24 m/ky during glacials (Balsam, 1981).

#### **2.3.1.13 Peach 4 Debrite**

This is the youngest mass failure deposit in the Peach debris flow complex. A single vibrocore from the debrite area, taken for paleoclimate purposes, is well-dated by six  $^{14}\text{C}$  AMS dates (Kroon et al., 2000). This core, however, does not recover the debrite

so that the oldest radiocarbon date provides a minimum age (14.68 ka at a core depth of 4.3 m). Seismic lines in the proximity of the core suggest a depth of the Peach 4 debris flow of 4-8 m (Owen, personal communication). The sedimentation rate between the two oldest radiocarbon dates is 0.8 m/ky. Using this rate, the maximum age of the slide is then given by the age of the oldest sample (14.68 ka) plus the maximum distance between this sample and the slide (3.7 m) divided by a fourth of the nearest sedimentation rate ( $\frac{1}{4} \cdot 0.8 \text{ m/ky}$ ), resulting in 33.18 ka. Owen et al. (2010) suggest emplacement before 19 ka BP based on the observation that the slide cut the ice-scour marks, indicating a slide age no older than the onset of the deglaciation.

Sedimentation rates on the Barra Fan varied between 0.4 and 2 m/ky during the LGM (Knutz et al., 2002). Post-slide sedimentation rates calculated from radiocarbon dates are also highly variable and range between 0.1 and 4.3 m/ky with a peak between 13 and 11 ka BP.

#### 2.3.1.14 Montserrat debris flow

A bioclastic mass flow adjacent to the volcanic island of Montserrat in the Caribbean originates from the shelf of one of the neighbouring islands Antigua or Redonda (Trofimovs et al., 2010). The failure is not associated with a major volcanic eruption as the slid material contains only a small fraction of volcanic material ( $< 5\%$ ). The emplacement age of 14 ka is unusually well constrained by biostratigraphy, stable isotopes and several  $^{14}\text{C}$  AMS dates above and below the deposit. The maximum  $^{14}\text{C}$  measurement error ( $2\sigma$ ) is  $\pm 327$  years, which we use as uncertainty range.

Around Montserrat sediment accumulates at rates of 0.01-0.1 m/ky (Reid et al., 1996). During interglacial periods these rates were lower.

#### 2.3.1.15 Iberian margin turbidites

The active south-west Iberian continental margin is the source for a number of large turbidites that are observed in the adjacent Tagus and Horseshoe abyssal plains. Earthquakes are likely triggers for these failures (Gracia et al., 2010; Masson et al., 2011). From these authors we picked 12 widespread events with direct age control, i.e. a radiocarbon measurement directly above or below the turbidite, and adopted the labelling scheme from Gracia et al. (2010). The authors' original uncertainty ranges are used.

Sedimentation rates at the upper south-west Portuguese continental slope have been relatively low (0.2 m/ky), but constant over the past 20 ka (Baas et al., 1997). However,

some turbidites in the Tagus abyssal plain may originate from canyon levee failures (Masson et al., 2011). Canyons provide pathways for much larger amounts of sediments, especially during the last sea level lowstand. Lebreiro et al. (2009) report sedimentation rates of 0.56 m/ky prior to  $\sim 15$  ka BP from the canyon walls.

#### **2.3.1.16 Madeira abyssal plain turbidite 'a'**

Thomson and Weaver (1994) evaluate their method of dating turbidites on the youngest deposit in the Madeira abyssal plain. From three  $^{14}\text{C}$  AMS measurements on three box cores they obtain ages of 1.12, 0.73 and 0.87 ka. The authors apply a weighted mean to get a mean emplacement time of  $930 \pm 76$  years BP. As no information on the radiocarbon sampling in the cores is given we use 0.73 ka and 1.12 ka as the lower and upper uncertainty interval.

#### **2.3.1.17 Makran turbidite T2**

The Makran turbidite system in the Oman abyssal plain is bounded by the Oman margin, the Pakistan/Iran continental shelf and the Murray Ridge. T2 is by far the largest turbidite that has been penetrated and recovered (Bourget et al., 2011). Three  $^{14}\text{C}$  ages are available from two cores (Bourget et al., 2011) and were taken below the turbidite. We calculate an emplacement time of 1.68 ka BP with an uncertainty range from 1.53 to 1.72 ka BP.

Bourget et al. (2011) provide sediment accumulation rates at the mouth of two of the large canyon systems. One canyon yields Late Pleistocene rates around 1.65 m/ky and Holocene rates around 1.3 m/ky whereas the other canyon shows Holocene rates of 0.9 m/ky. The accumulation rates remained largely constant and seem independent of sea level changes.

#### **2.3.1.18 Walker-Massingill slump**

This is the only previously unpublished landslide age in the data base. The Walker-Massingill slump is a large slump on the Mississippi Fan associated with the head of the Mississippi Canyon and the adjacent shelf edge (Walker and Massingill, 1970). The slump comprises two lobes of different deposit thickness. We retrieved one sample of  $\sim 1000$  handpicked foraminifera (*Globigerinoides ruber* and *Globigerinoides sacculifer*) for radiocarbon analysis from the base of the hemipelagic mud that overlies the Walker-Massingill slump in a core taken by R/V Vema. This old core from one of the lobes is heavily sampled so that only a thin veneer of hemipelagic drape remained which did not

allow to take more than one sample. Sedimentation rates thus cannot be estimated. The radiocarbon age was dated by the AMS method at the National Environmental Research Council radiocarbon facility and calibrated with the Marine09 calibration curve (Reimer et al., 2009). An open ocean marine reservoir correction of 400 years was used as the marine reservoir database contained relatively few samples from the Mississippi Delta region. The hemipelagic drape gives an age of 6.46 ka (6.369-6.588 ka,  $2\sigma$ ). Accordingly, the slump was deposited around 6.5 ka BP. As only one of the depositional lobes was dated it remains unclear whether the two lobes were deposited as a result of one event or during multiple stages.

Sedimentation rates in the Mississippi Fan are highly variable, reflecting for example the growth and decay of the Laurentide ice-sheet with high rates during lowstand and rising sea level (Suter and Berryhill, 1985; Kolla and Perlmutter, 1993). In the Ursa basin at some distance from the Mississippi Canyon and its levees high rates of 12 m/ky prevailed between 24-16 ka BP, decreasing to 4 m/ky between 16-11 ka and 1 m/ky during the Holocene (Flemings et al., 2006).

#### **2.3.1.19 North-western Nile deep sea turbidite system**

Garziglia et al. (2008) mapped seven mass transport deposits in the western part of the Nile delta, of which three were recovered in sediment cores (SL2, SL6, SL7). Ducassou et al. (2007) established a detailed ecostratigraphic scheme for the Nile Fan based on planktonic foraminifera distribution, oxygen isotope stratigraphy, tephro- and sapropel chronology as well as radiocarbon data and suggest an error of  $\pm 2$  ky. Taking into account this uncertainty, this scheme was applied to date the turbidites in the north-western Nile fan. SL2 has occurred between 103-119 ka BP, SL6 between 7-12 ka BP and SL6 between 6.94-12 ka BP.

The rates of sediment accumulation in the western Nile cone are also constrained by the ecozone stratigraphy and on the upper slope reached 0.1 m/ky between 127-70 ka BP, 0.03 m/ky between 70-25 ka BP, 0.02 m/ky during the LGM, 0.2 m/ky between 14.8-12 ka BP and 1.5 m/ky between 12-8 ka BP (Ducassou et al., 2007). Modern rates do not exceed 0.3 m/ky.

#### **2.3.1.20 Amazon Fan Mass Transport Deposits**

Seismic and core data reveal four large mass failures in the Amazon Fan, two of which are near-surface and two buried. However, only the three recovered in sediment cores are included in this study. Analysis of benthic foraminifera shows that the failed material

originates on the continental slope (Maslin et al., 2005). The stratigraphy of the Amazon Fan is well established by a number of different stratigraphic methods. The emplacement ages are estimated by bio- and magnetostratigraphy supported by radiocarbon data and sedimentation rate constrains (Maslin et al., 1998) based on ODP drill cores (Leg 155) and gravity cores. One radiocarbon date ( $\sim 13$  ka) exists from a hemipelagic layer more than 5 m above the shallowest debris flow. The bed in between the debris flow and the sample shows evidence of very rapid deposition. The younger of two ages from the debris corresponds to  $\sim 21$  ka. Accordingly, the debris flow was emplaced between 13 and 21 ka BP, with the real age more likely to be closer to the younger age. Maslin et al. (2005) give an age range of 35-37 ka for the 'Deep Eastern' mass transport deposit and 41-45 ka for the 'Deep Western' deposit. The authors declare that the range is a result of sedimentation rate uncertainties which are needed for the interpolation from the last datable horizon. They do not provide information on how the sedimentation rates and their level of uncertainty were determined forcing us to use the uncertainty intervals suggested by the authors.

During the LGM sedimentation rates at the Amazon Fan were 4.4 m/ky and only a tenth of this during the Late Pleistocene between 33.9-104.8 ka BP (Mikkelsen et al., 1997).

### **2.3.1.21 Flemish Pass, Canada**

Huppertz and Piper (2009) present a regional stratigraphy for the Flemish Pass basin on the Eastern Canadian continental margin based on high resolution seismic stratigraphy, correlation of more than 60 cores with  $^{14}\text{C}$  AMS dates, oxygen isotope records and tephrochronology. 22 mass failure deposits were tied in to this stratigraphy and uncertainty intervals are given by the authors and adapted in this study. The uncertainty intervals vary between 5 and 30 ka and are a function of sedimentation rates and the stratigraphic position of the horizon.

From their seismic stratigraphy Huppertz and Piper (2009) calculate upper slope sedimentation rates of 0.1 m/ky in the past 28 ky, 0.2 m/ky between 28-50 ka BP, 0.18 m/ky between 50-105 ka BP and 0.5 m/ky between 105-165 ka BP.

### **2.3.1.22 Agadir basin turbidites**

The turbidite sequences in the Agadir basin are a part of the Moroccan turbidite system on the north-west African continental margin, which also feeds into the Seine and the Madeira abyssal plains. A large number of cores allow extensive mapping and correlation of turbidites across all three basins. We concentrate on the Agadir basin because it has

the best core controls (Wynn et al., 2002; Hunt, 2012). The stratigraphic framework is based on oxygen isotope records, coccolith ratios (Wynn et al., 2002) and high resolution carbonate content analysis (Hunt, 2012). In addition to oxygen isotopes, carbonate percentage in this region provides another proxy for sea level. We estimate an uncertainty of  $\pm 5$  ky for events at stage boundaries and younger than 50 ka as well as  $\pm 10$  ky for events within stages and younger than 50 ka. For turbidites older than 50 ka the stage boundary uncertainty is  $\pm 10$  ky and  $\pm 20$  ky within stages.

#### **2.3.1.23 Cape Blanc slide**

Wien et al. (2007) use geochemical data (elemental and total carbonate) measured on several reference cores to correlate and indirectly date the emplacement of the Cape Blanc slide off north-west Africa. Only one of the reference cores is dated by oxygen isotopes. Both the uncertainty for oxygen isotope stratigraphy ( $\pm 10 - 20$  ky) and the propagation of this uncertainty must be considered. We therefore conservatively suggest an uncertainty interval of  $\pm 20$  ky. The authors propose an age of 155 ka. Considering the uncertainty interval the minimum age of the Cape Blanc slide is 135 and the maximum age 175 ka.

#### **2.3.1.24 Sahara slide**

Georgiopoulou et al. (2010) provide evidence for emplacement of the Sahara slide between 50 and 60 ka BP, just after the isotope stage 3 to 4 glacial to interglacial transition. The authors analysed coccolith ratios on one gravity and nine piston cores from the slide area. The microfossil stratigraphy is supported by oxygen isotope record on one core and seismic stratigraphy. Due to the extensive data set and the use of various dating methods we estimate the uncertainty of  $\pm 5$  ky and thus use the age range of 50-60 ka BP proposed by Georgiopoulou et al. (2010).

Event	Age [ka]			Reference	V [km <sup>3</sup> ]	Group	Accumulation rate [m/ky]	Reference
	min	max	best					
Agadir basin	A3	35.00	45.00	40.00	Wynn et al. (2002) (Hunt, 2012)	4		Ruddiman et al. (1988)
	A5	54.00	64.00	59.00		20		
	A7	75.00	85.00	80.00		9		
	A10	95.00	115.00	105.00		2		
	A11	105.00	125.00	115.00		8		
	A12	120.00	130.00	125.00		9		
	A13	120.00	140.00	130.00		2		
Amazon shallow deep E deep W	W	13.00	21.00		Maslin et al. (2005)	1500		Mikkelsen et al. (1997)
	E	35.00	37.00	36.00		610		4.41 (34-10 ka) 0.45 (105-34 ka)
	W	41.00	45.00	43.50				
Balearic plain	abyssal	20.40	21.49	20.52	Rothwell et al. (1998)	500		0.33 (50-21 ka), 3.50 (21-20 ka), 0.27 (< 20 ka)
BIG95*		11.26	13.44	12.00	Lastras et al. (2004)	26		1.00 (> 22 ka), 1.75 (22-18 ka), 1.00 (18-11 ka), 0.63 (< 11 ka)
Black Shell			18.65		Elmore et al. (1979)	100		0.12 (< 12 ka), 0.24 (glacials) Balsam (1981)
Cape Blanc		135.00	175.00		Wien et al. (2007)	20		< 0.15 Ruddiman et al. (1988)
Cape Fear*		13.48	20.10	15.10	Paull et al. (1996)	300		0.20 Paull et al. (1996)

Flemish Pass (Ca)		Huppertz and Piper (2009)	Huppertz and Piper (2009)	Huppertz and Piper (2009)
1	128.50	143.80	136.00	0.70 (> 122 ka), 0.18 (122-50 ka), 0.21 (50-26 ka)
2	81.70	118.10	102.00	G
3	78.50	115.10	99.00	G
4	59.10	116.80	83.70	G
5	56.10	117.00	74.00	G
6	57.20	115.10	80.30	G
7	57.20	72.10	64.30	G
8	56.10	70.90	63.40	G
9	30.00	44.80	37.20	G
Grand Banks	0.07	0.07	0.07	0.10 (< 26 ka)
Heradotus basin*				
b	6.50	9.50	7.50	0.05 (> 28 ka), 2.00 (28-17 ka), 1.00 (17-6 ka), 0.15 (6-0 ka)
d	9.50	11.62	10.56	R(N)
e	11.62	12.22	11.92	R(N)
g	13.11	16.64	14.87	R(N)
h	16.64	20.06	17.49	R
k	20.06	25.43	21.40	R
m	20.06	25.43	24.74	R
n ('megaturbidite')	25.40	28.83	27.13	R
Hinlopen*	30.10	40.00	32.20	0.04-0.20
				Winkelmann et al. (2008)
				Winkelmann et al. (2008)



Peach 4*	14.68	19.00	Owen et al. (2010)	135	G	0.40-2.00 (26-19ka)	Knutz et al. (2002)
Sahara	50.00	60.00	Georgiopoulou et al. (2010)	600	O	< 0.15	Ruddiman et al. (1988)
SE Australia*	1	21.01	25.70	21.95	Clarke et al. (2012)	1-20	Jenkins and Keene (1992)
	2	20.27	22.10	20.64			0.05 (34-25 ka), 0.16 (25-11 ka),
	3	16.05	19.83	16.81			0.05 (<11 ka)
Storegga	8.01	8.21	8.11	Dawson et al. (2011)	2800	G	1.40 (> 18.8 ka), 36.00 (18.8-18.6 ka), 27.00 (18.6-17.8 ka), 0.10 (< 17.8 ka)
Trænadjupet*	4.30	7.00	4.84	Laberg et al. (2002b)	900	G	0.70 (26-21 ka), 1.10 (21-19 ka), 2.20 (19-18 ka), 0.18 (18-0 ka)
Walker-Massingill	6.46	11.66	6.50	this paper	1000	R	5.00 (42-24 ka), 12.00 (24-16 ka), 4.00 (16-11 ka), 1.00 (< 11 ka)

Table 2.2: List of submarine mass failures with reliable ages used for analysis in this paper in alphabetical order. The minimum age (*min*) is the lower bound of the uncertainty interval, the maximum age (*max*) is the upper bound and *best* is the best estimate age. *V* is the minimum volume of the slide deposit and *Group* refers to distinct depositional environments (G = glaciated margins, R = river fan systems, O = sediment-starved margins). References for ages as well as for sedimentation rates at the respective continental slope are given. All ages are shown in calibrated calendar ages. Heradotus basin turbidites depicted with (N) are sourced from the Nile Delta. An asterisk indicates that the uncertainty ranges were calculated according to the method described in the text. MAP: Madeira Abyssal Plain.

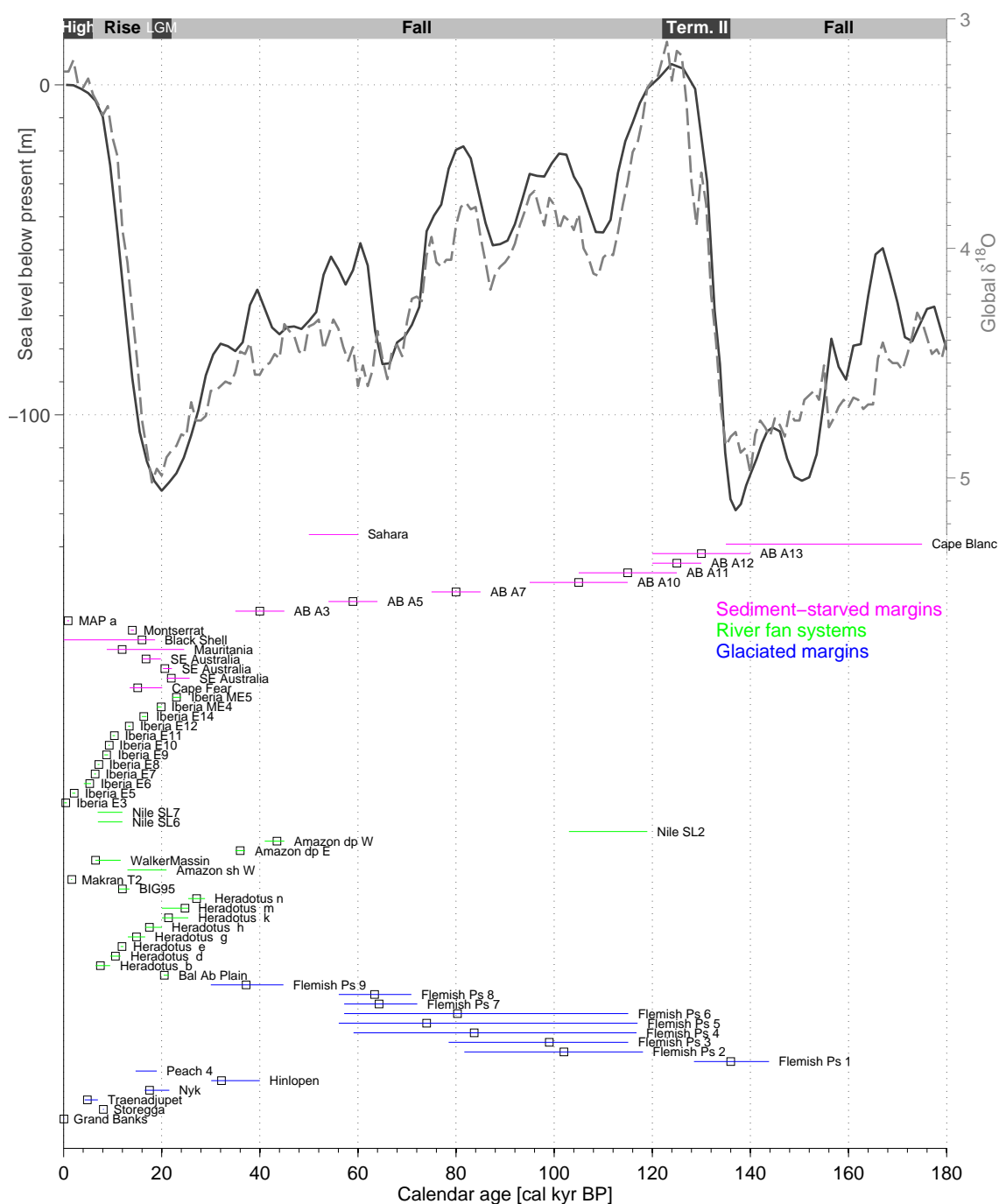


Figure 2.2: Global mean sea level (dark grey curve, Waelbroeck et al., 2002) and global stack of benthic  $\delta^{18}O$  records (light grey curve, Lisiecki and Raymo, 2005) plotted in the upper part of the figure. The lower part shows all submarine mass failures listed in Table 2.2 with their individual uncertainty intervals. If available, the age with highest probability is shown by a grey square. The colour of the uncertainty line indicates the sedimentary environment (river fan systems with high terrestrial input, glaciated margins and sediment-starved margins). The grey time line at the top of the figure indicates the sea level patterns: Sea level fall and lowstand from 180-136 ka BP, sea level rise and highstand during Termination II (136-122 ka BP), sea level fall (122-22 ka BP), the Last Glacial Maximum (LGM) from 22-18 ka BP followed by a sea level rise (18-6 ka BP) and the modern sea level highstand (6-0 ka BP). MAP = Madeira Abyssal Plain; AB = Agadir Basin.

### 2.3.2 Data base analysis

The age constraints for 62 submarine mass failures with volumes  $>1\text{ km}^3$  were found suitable for subsequent analysis (Table 2.2, Fig. 2.2). The most recent slide in the data base is the Trænadjupet slide (4.84 ka), while several turbidites are younger, e.g. the Grand Banks event that happened in 1929 AD. The oldest event is the Cape Blanc slide off north-west Africa (135-175 ka). Out of the total 62 slides in the data set, 33 occurred since the LGM and 40 in the past 30 ka. The data base contains predominantly younger slides because of the 50 ka limit of radiocarbon dating as well as the limited availability of long cores that sample deeply buried mass transport deposits. We determine the quality of the age estimate for a slide by taking into account the number of samples and cores as well as the methodology based on which the age was determined, the quality of the sedimentation rates and the number of existing lobes and headwalls that were sampled. In this data base two slides have a good age control, 41 have an intermediate age control and 19 have a low quality age control. The age range between minimum and maximum ages, i.e. the uncertainty interval, can be large (up to 61 ky). The average uncertainty interval for all entries in the data base is 10.4 ky and 3.8 ky for those younger than 30 ka.

#### 2.3.2.1 Visual evaluation

We separate the sea level curve shown in Fig. 2.2 into five intervals: Sea level rise and highstand during termination II (136-122 ka BP), sea level fall (122-22 ka BP), sea level lowstand during the LGM (22-18 ka BP), sea level rise after the LGM (18-6 ka BP) and the modern highstand (6-0 ka BP). Taking uncertainties into account, 23 events lie fully within a period of rising sea level. Six events can be assigned to sea level fall and five events occurred during sea level highstand. Almost half of the ages in the data set (29) have uncertainties that span over one or more sea level transitions and therefore cannot be attributed to a particular sea level stand. When uncertainties are ignored and the best estimate ages are used, the data set contains three entries for the 14 ky long penultimate period of sea level rise (frequency of 0.21 failures/ky), 21 entries for the 100 ky long period of overall falling sea level (0.21 failures/ky), five entries during the 4 ky long LGM (1.25 failures/ky), 25 entries for the 12 ky period of sea level rise after the LGM (2.08 failures/ky) and seven entries for the last 6 ky (1.17 failures/ky).

Fig. 2.3 shows a histogram representation of the data set with a histogram bin length of 5 ky. The number of slides older than the LGM ( $> 25$  ka) is comparatively low and three mass failures occur within a 5 ky bin at most. As uncertainties are high for old landslides we analyse the uncertainty histogram (open bars) and find that histogram peaks coincide with sea level lowstand (140-135 ka, 115-105 ka BP), highstand (125-120 ka, 45-35 ka BP) or rising sea level (85-80 ka, 65-60 ka BP). For the past 30 ka uncertainties are

generally smaller and the analysis is based on the histogram using best estimate ages. The histogram is nearly bell-shaped with a maximum of ten events within 5 ky during the maximum rate of sea level rise. During the preceding sea level lowstand as well as the following modern highstand less failures occurred.

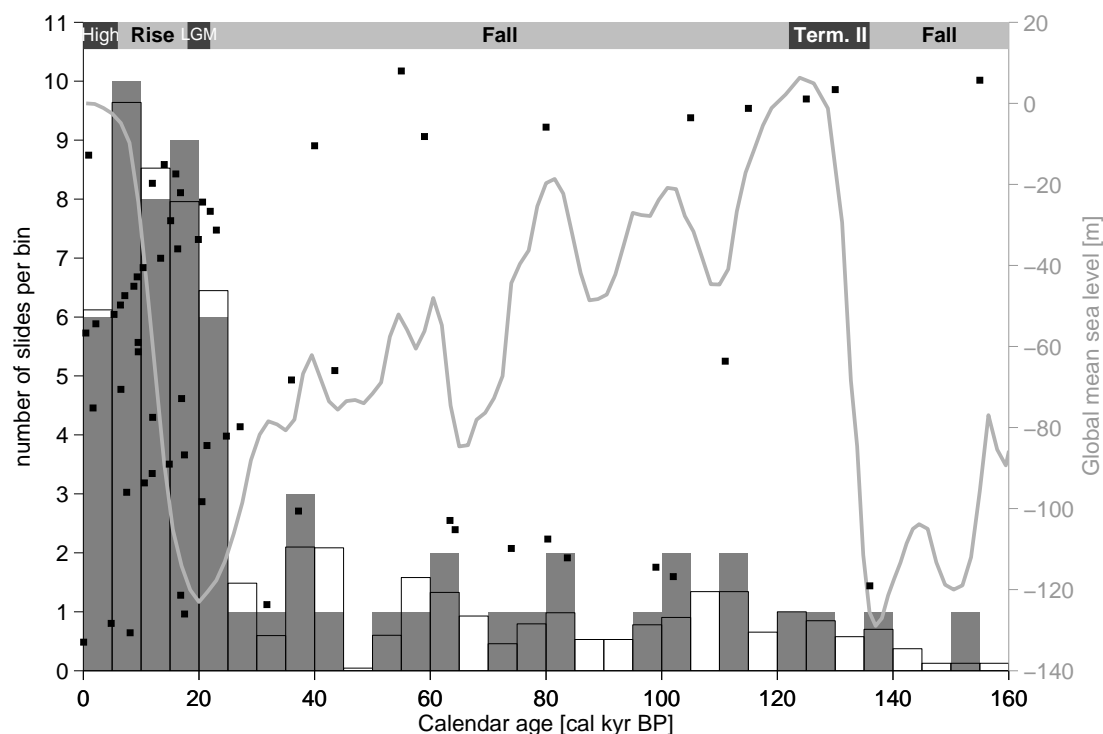


Figure 2.3: Global mean sea level (light grey) and time line (top) as in Fig. 2.2 and histogram representation of submarine mass failures based on the most likely ages (dark grey bars) as well as taking into account the uncertainty interval, assuming an evenly distributed probability along this interval (open bars with black edges). The bin width is 5 ky. Black markers show the 'best estimate' (highest likelihood) age. Where no 'best estimate' age is provided, the mean of the uncertainty bar is assigned.

Figs. 2.4a and 2.4b represent the same data base with smaller histogram bin lengths of 2 ky and 1 ky, respectively. This representation is particularly useful for the past ~ 30 ka as the data base is more comprehensive, age errors are smaller and the sea level changed rapidly. A quiet period in terms of landslide occurrence can be identified when sea level rise comes to a halt with only four slides during 6-1 ka BP. The bell-shaped curve covering a large part of the period of sea level rise since the LGM seen in Fig. 2.3 appears not as a curve with one maximum but rather with two maxima during early sea level rise (18-16 ka BP) and when sea level rise was in full progress (11-9 ka BP). During the early stages of the LGM (22-20 ka BP) a comparatively high number of four slides occurred, followed by a drop to only one slide in the 20-18 ka interval.

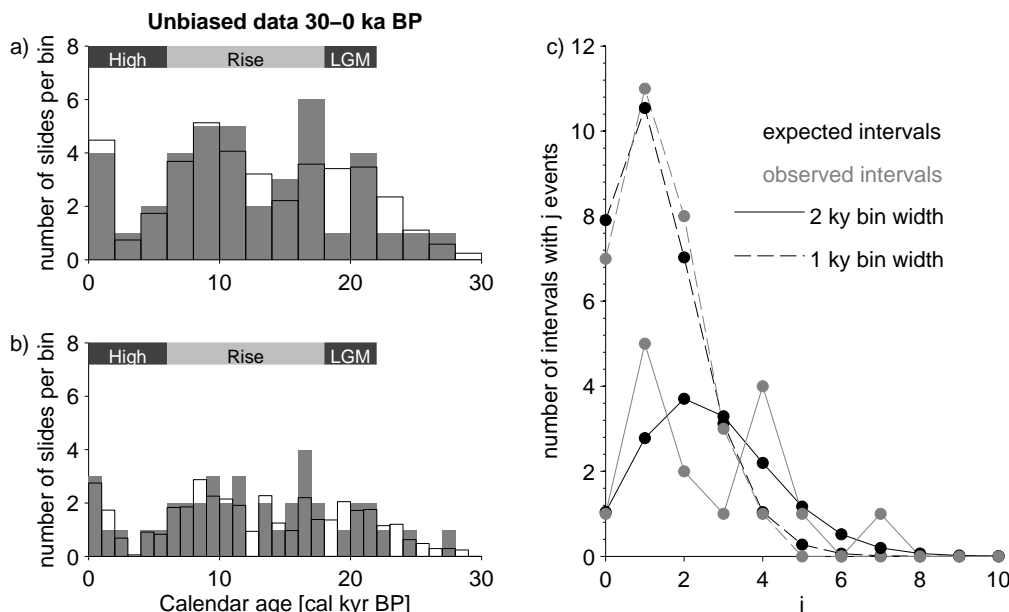


Figure 2.4: Histograms of the assumed non-biased part of the data set plotted with bin widths of 2 ky (a) and 1 ky (b) following the same notation as in Fig. 2.3. Panel c) shows the number of histogram bins expected to have  $j = 0 - 10$  events ( $E_j$ ) according to the Poisson model (black lines and dots) as opposed to the observed number of histogram bins with  $j$  landslides from the landslide data set (grey lines and dots). The continuous lines represent a 2 ky bin width whilst the dashed lines show the results for 1 ky bins.

### 2.3.2.2 Statistical analysis of non-biased data (0-30 ka BP)

The data base including the past 30 ka is assumed free of sampling bias (see section 2.2.8.1). The 30-0 ka BP period comprises 40 events. Because no bias is involved, at least in terms of core depth penetration, this subset can undergo statistical tests.

The data set's fit to a Poisson model is tested using a  $\chi^2$  test. The Poisson model describes a frequency distribution of random data. The  $H_0$  hypothesis states that the landslides in the data set fit the Poisson model and thus are randomly distributed through time, which is accepted when the calculated value for  $\chi^2$  is smaller than the critical  $\chi^2$  value. The number of histogram bins that contain 0 to 10 landslides are counted (grey lines in Fig. 2.4c) and compared to the number of expected bins for a Poisson distributed sample (black lines in Fig. 2.4c). This is done for bin lengths of 1 and 2 ky. The 1 ky binned landslide data (dashed lines in Fig. 2.4c), in particular, is in good agreement with the artificial data, which follows the Poisson distribution. The 2 ky bin landslide data has more spikes than the smoother artificial sample. The  $\chi^2$  test returns values of 1.0458 and 0.1466 for 2 ky and 1 ky binned landslide data, respectively. These are well below the critical values of 3.841 and 5.991 (5% significance with one and two degrees of freedom, respectively). Increasing the level of significance to 10% yields critical values of

2.706 and 4.605. Even with such a high level of significance, the critical values exceed the calculated  $\chi^2$ . Therefore, the  $H_0$  hypothesis is accepted and the timing of landslides follows a Poisson distribution, i.e. the occurrences of landslides over time are very similar to randomly distributed data.

Fig. 2.5 shows the probability for the maximum numbers of slides that can occur within one histogram bin (Fig. 2.5a, d, g), the maximum difference in numbers of slides between two neighbouring bins (Fig. 2.5b, e, h) and the number of neighbouring bins containing more than seven (Fig. 2.5c), four (Fig. 2.5f) and three (Fig. 2.5i) events in randomly distributed samples in bins of 5 ky (Fig. 2.5a-c), 2 ky (Fig. 2.5d-f) and 1 ky (Fig. 2.5g-i). The arrows mark the position of the landslide data set. The maximum number of landslides in the data base agrees very well with the maximum number of events that are likely to occur in random distributions (Fig. 2.5a, d, g). The maximum difference in the numbers of landslides between neighbouring histogram bins in the data set also conforms with those expected in random distributions (Fig. 2.5b, e, h). Therefore, the height of peaks in the original data set is not significant. Their appearance in clusters or single peaks could also originate from a random distribution. Only the number of neighbouring bins containing more than average slides in the landslide data set exceeds the most likely number by one (Fig. 2.5c, f, i). However, the probability of these higher values is still larger than 20% and the occurrence is comparatively likely.

In summary, the temporal distribution of landslides resembles a Poisson distribution and is relatively easily reproduced by a random number generator. Therefore, any observed peaks and clusters as identified from Fig. 2.3 are not statistically significant.

### 2.3.2.3 Timing of failures in different depositional systems

Fig. 2.6 shows histograms of the data set divided into three sets of different sedimentation environments (Fig. 2.6a-c) as well as one regional subset (Fig. 2.6d) representing slides off the north-west African coast. The histogram bin length is 5 ky in all plots.

Out of the total 62 mass failures 15 occurred at glaciated continental margins (Fig. 2.6a). The single events are nearly evenly scattered from 140 ka BP to recent without any periods of significantly increased landslide frequency or outstanding peaks. This is evident in both the histogram based on best estimate ages and the histogram that includes uncertainties. Landsliding seemed to have occurred during all sea level conditions.

The relationship between landslide frequency and sea level is different for mass failures in river fans and systems with large sedimentary input (Fig. 2.6b). The 30 events in this

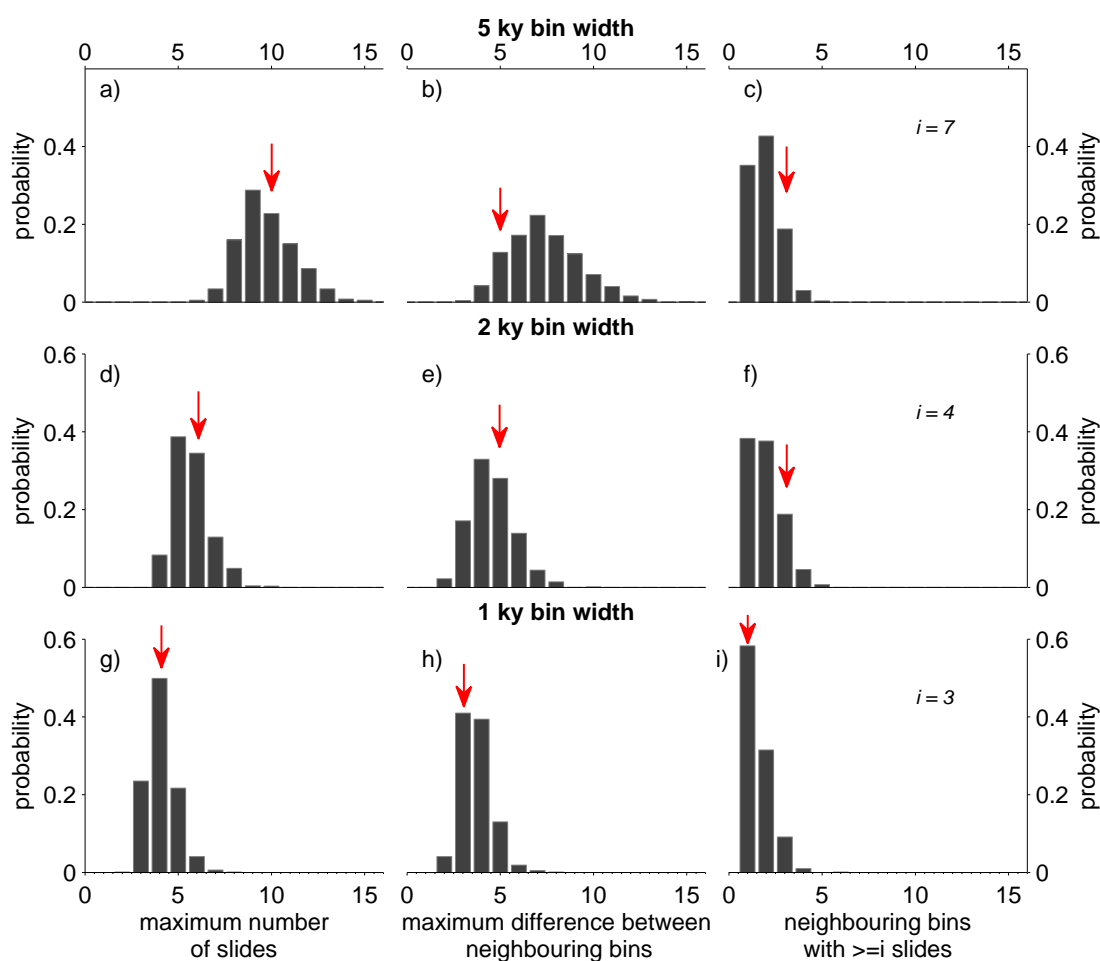


Figure 2.5: Probabilities for the maximum number of slides in one histogram bin (a), maximum difference in number of slides between two neighbouring bins (b) as well as the number of neighbouring bins with more than the average number of slides,  $i$ , (c) for randomly distributed samples and a histogram bin size of 5 ky. Probabilities for the same characteristics are also shown for histogram bin sizes of 2 ky (d, e, f) and 1 ky (g, h, i). The arrows indicate the numbers observed in the landslide data base.

group span over a period from 115 ka BP to recent, although only one event is older than 45 ka. The highest abundance of nine landslides was between 10-5 ka BP coinciding with a high rate of sea level rise. This peak was preceded by a gradual increase in abundance from one slide between 30-25 ka BP during falling sea level, to eight slides during sea level lowstand (25-15 ka BP). The 10-5 ka BP maximum is followed by a steep drop to only three slides in the past 5 ka. These features are nearly identical when uncertainties are included (open bars). However, in a 2 ky bin size representation (Fig. 2.7a) the outstanding peak reduces to three neighbouring moderate peaks and is even less pronounced in a 1 ky bin size histogram (Fig. 2.7b).

Fig. 2.6c shows a histogram of landslides at sediment-starved margins with comparatively

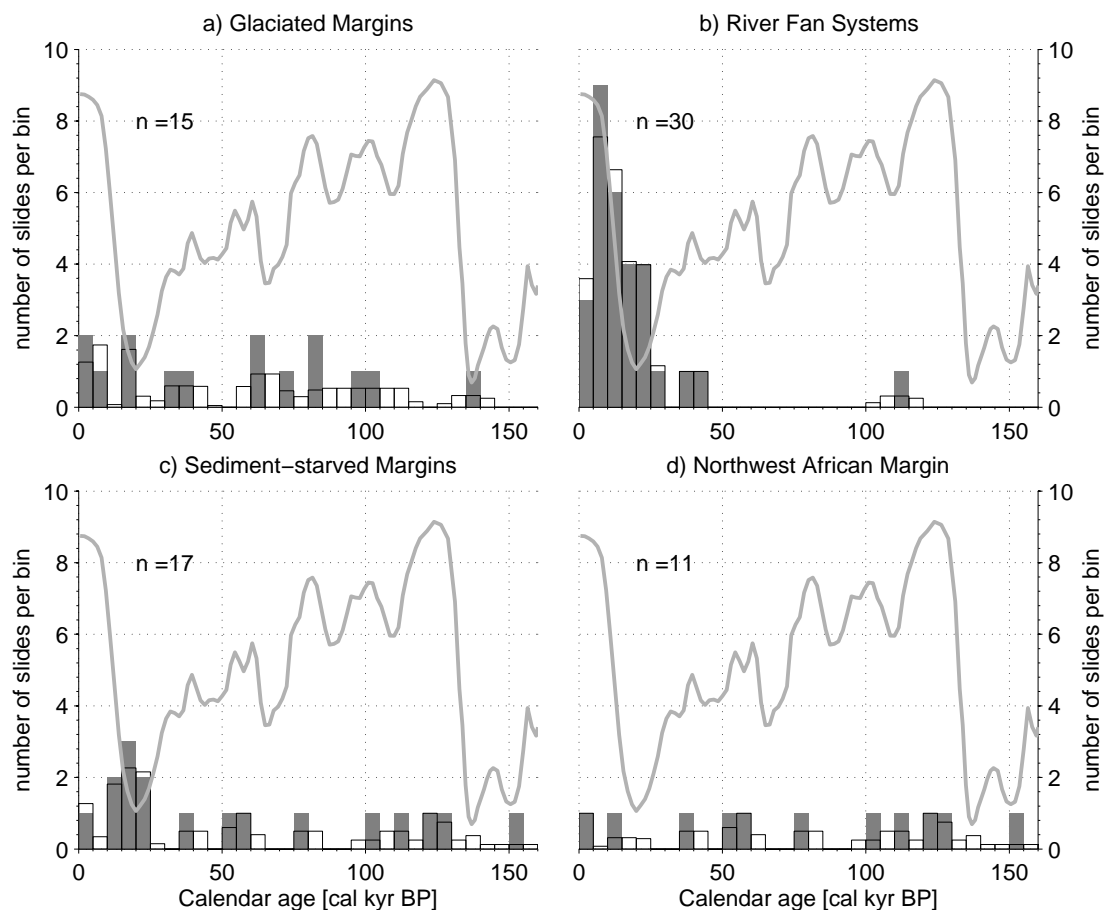


Figure 2.6: Histogram representation as in Fig. 2.3 for subsets of the landslide data set (notation identical to Fig. 2.3): (a) glaciated margins, (b) river fan systems with large sediment input, (c) sediment-starved margins and (d) failures off the coast of north-west Africa. The grey curves depict global mean sea level (Waelbroeck et al., 2002) and  $n$  is the number of landslides in the respective subset.

little terrestrial sediment input, i.e. at moderate to low latitudes and away from rivers. This group includes failures at the north-west African continental margin, although these are also represented individually in Fig. 2.6d. The histogram shows a scattered distribution of nine events between 155-25 ka BP. Eight slides are younger than 25 ka giving a slightly denser histogram distribution with seven slides clustering at sea level lowstand and early rise during and just after the LGM (25-10 ka BP). Only one slide is younger than 10 ka.

The landslide record on the north-west African continental margin (Fig. 2.6d) resembles the glaciated margin subset. All 11 data points are nearly evenly distributed over the entire time frame without any clustering or increased frequency.

For the largest of these subgroups, the river fan system group, we apply the same test for Poisson distribution as applied to the undivided data. The result is shown in Fig. 2.7c with the same notation as in Fig. 2.4c. The curves for expected and observed intervals resemble each other and the  $\chi^2$  test for 2 and 1 ky bins returns values of 1.0151 and 0.8583, respectively. Both values are well below the critical 3.841 and 5.991 with 5 % significance with one and two degrees of freedom. The calculated  $\chi^2$  values are also below the critical values with 10 % significance (2.706 and 4.605). As for the main data set, the river fan systems subset follows a Poisson process and could be essentially random.

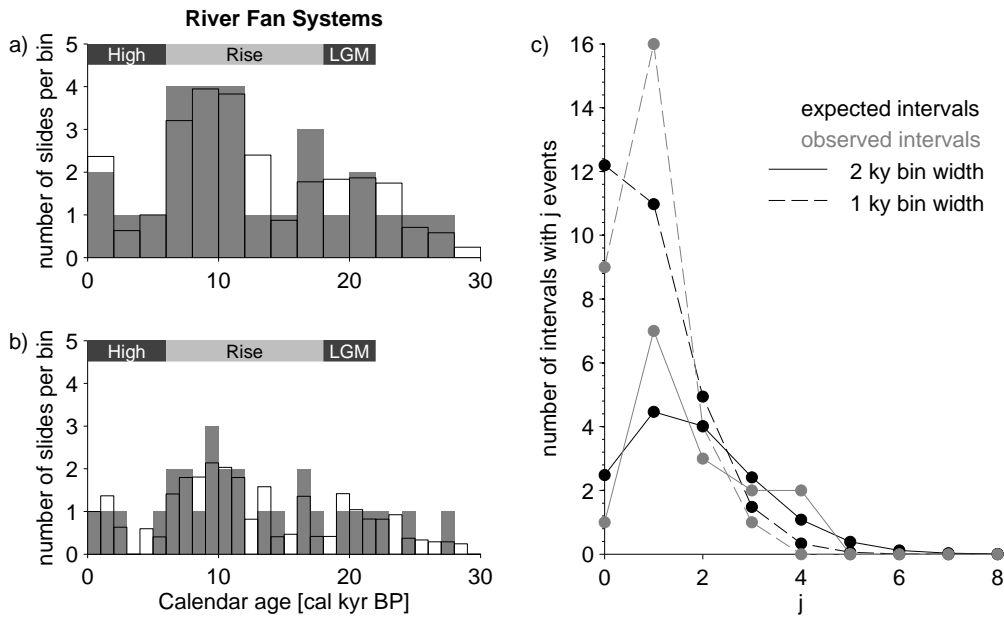


Figure 2.7: Histograms of the river fan systems subset (Fig. 2.6b) plotted with bin widths of 2 ky (a) and 1 ky (b) following the same notation as in Fig. 2.4. Panel (c) shows the number of histogram bins expected to have  $j = 0 - 8$  events ( $E_j$ ) according to the Poisson model (black lines and dots) as opposed to the observed number of histogram bins with  $j$  landslides from the landslide data set (grey lines and dots). The continuous lines represent a 2 ky bin width whilst the dashed lines show the results for 1 ky bins.

The river system subset's peaks and cluster identified in Fig. 2.6b were analysed in the same way as for the main data set and the results are displayed in Fig. 2.8, following the notation used for Fig. 2.5. Independent of the bin size all characteristics of the landslide data set locate at comparatively high probabilities. Accordingly, peaks and clusters are not significant and can easily be reproduced by random numbers.

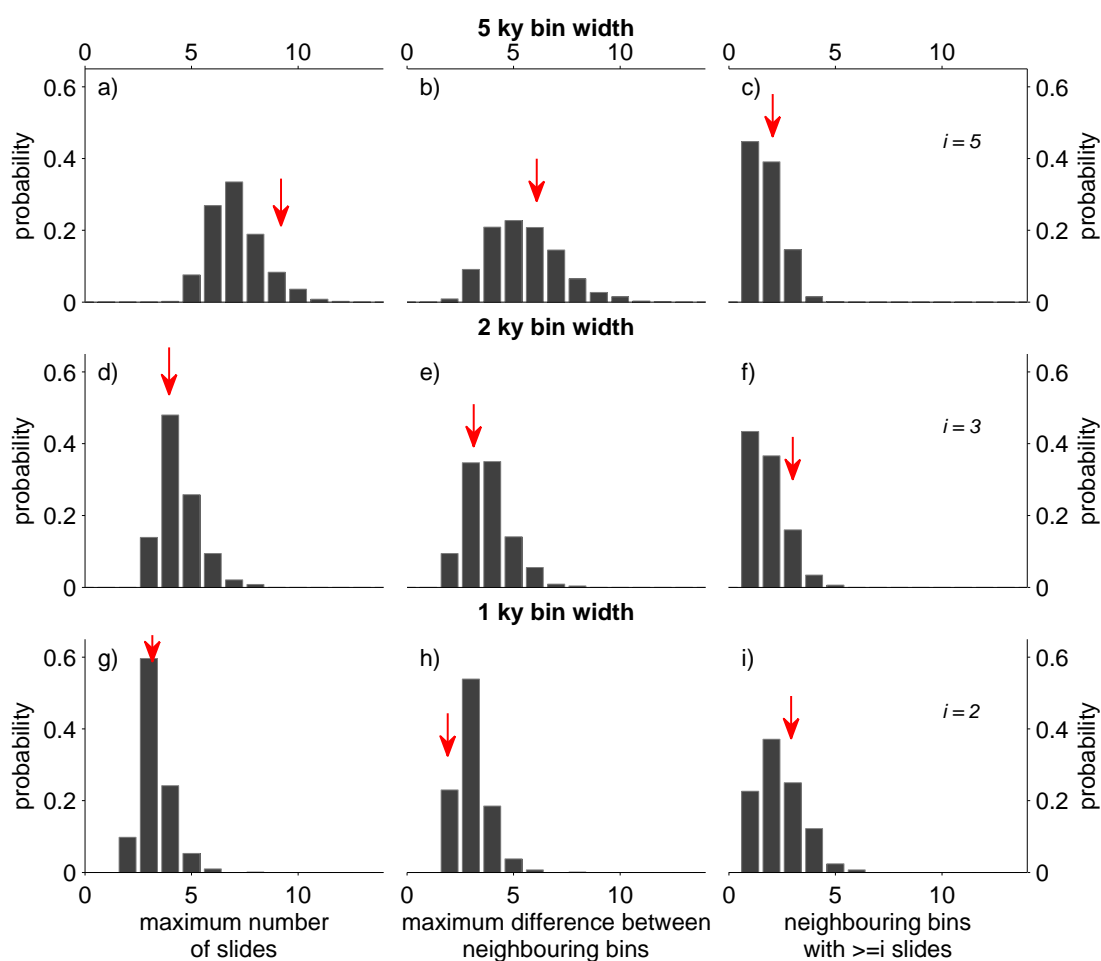


Figure 2.8: Probabilities of various characteristics for randomly distributed samples with the same sample size as the river fan systems subset, following the notation of Fig. 2.5. The arrows highlight the numbers observed in the river fan systems subset.

### 2.3.2.4 Temporal variations of accumulation rates and the timing of landslides

Fig. 2.9 shows the timing of submarine landslides and typical accumulation rates in their source areas, for those sites where changes in accumulation rates have been documented. For simplification and consistency the slide names are given rather than the name of the source area, i.e. for the slide named BIG95 sedimentation rates typical for the Ebro margin in the western Mediterranean Sea are documented. For a clearer visualisation the figure is separated into three subplots. Note the logarithmic y-scale in Fig. 2.9a. All sedimentation rates are also given in Table 2.2.

Peak accumulation rates were highest in the Storegga slide area (36 m/ky), followed by the large river fans of the Mississippi (12 m/ky) and Amazon (4 m/ky). All systems in

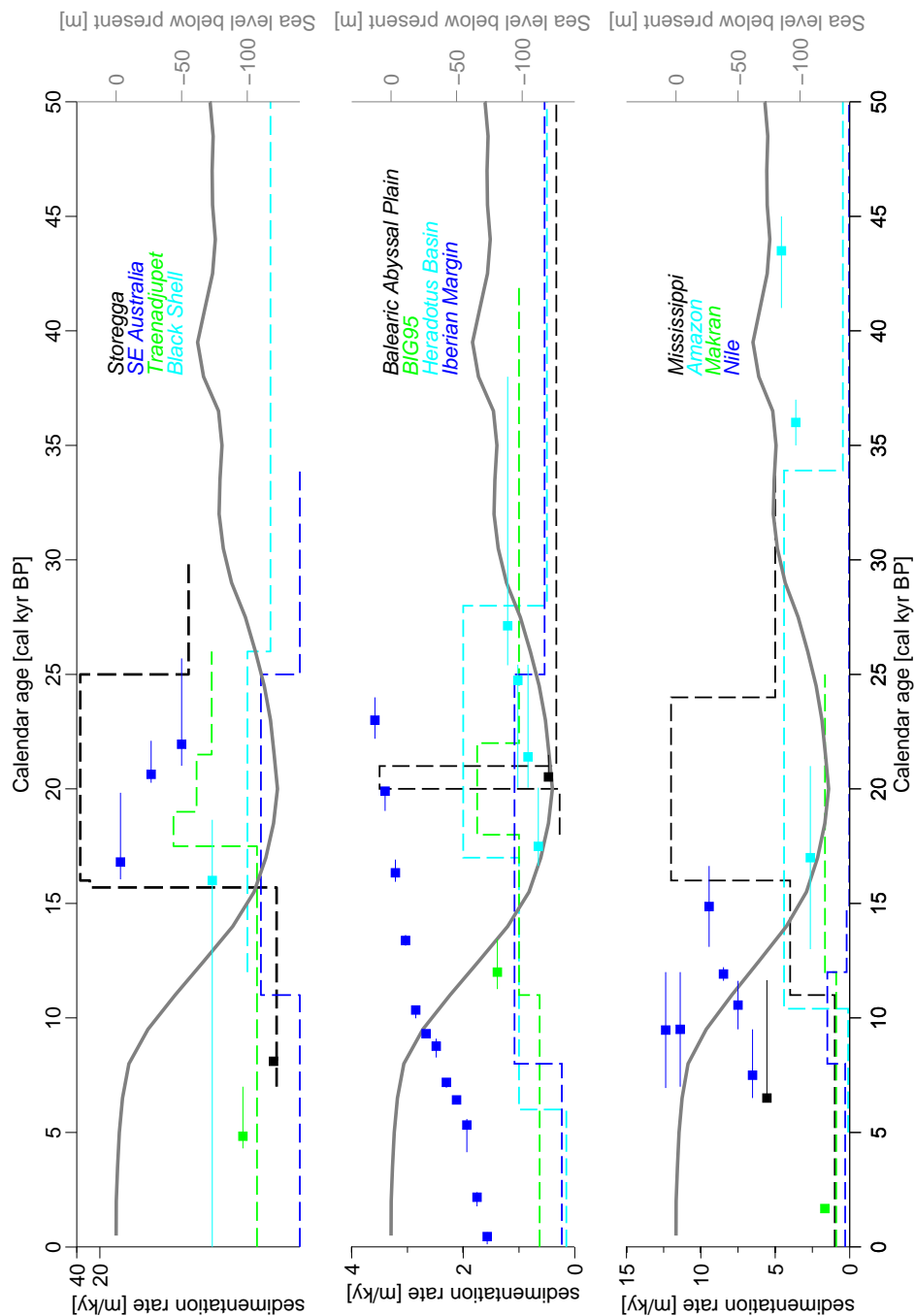


Figure 2.9: Sea level curve (grey) after Waelbroeck et al. (2002), timing of submarine landslides (squares) with uncertainty intervals (thin solid lines) and local accumulation rates over time (dashed lines). Note the logarithmic scale in the uppermost panel.

Fig. 2.9 show increased sediment accumulation during the LGM with the exception of the Nile, where deposition rates were low until about 14 ka BP and increase while sea level was rising. The onset of rapid deposition in the Amazon Fan at about 34 ka BP is earlier than for the other margins. The length of high accumulation intervals differ and for depositional systems like the Amazon and Mississippi fans, and the Iberian,

Makran and south-east Australian margin these periods extend well into the onset of deglaciation. However, as the global sea level rises to almost modern level (6 ka BP) sedimentation rates at all margins decrease significantly. Through time the sediment accumulation rates changed by up to a factor of four (Makran, BIG95, Iberian margin, Heradotus basin, south-east Australia), about an order of magnitude (Trænadjupet, Mississippi/Walker-Massingill, Balearic abyssal plain, Amazon) or even more (Storegga, Nile).

Slope failures tend to happen during or after a period of increased deposition, except for two old slides in the Amazon Fan. The delays between the onset of high accumulation rates and actual failure vary between  $< 1$  ky to as long as 23 ky (Table 2.3). The delay times summarised in Table 2.3 involve all the uncertainties of landslide age estimates as well as uncertainties with respect to the determination of sedimentation rates. Consequently, large errors are possible and the data should be treated with caution.

Failure	Delay [ky]	Max delay [ky]	Min delay [ky]
Walker-Massingill	18	18	13
Amazon	17	21	13
Makran	23	23	23
Iberian margin	$>2$	$>2$	$>2$
BIG95	11	12	10
Heradotus	1-10	3-11	0-8
Balearic abyssal plain	$<1$	1	0
Trænadjupet	14	15	12
Storegga	8	8	8
Nile	0-4	2-5	0-3
SE Australia	3-9	4-9	3-8

Table 2.3: Delay between onset of increased sedimentation on the continental slope and best estimate age, minimum and maximum age of slope failures for examples shown in Fig. 2.9.

## 2.4 Discussion

The new data set of ages of submarine landslides contains 62 large mass failures at continental margins worldwide, and is significantly larger than previously published data sets (Maslin et al., 2004; Owen et al., 2007; Lee, 2009; Leynaud et al., 2009). For a large part of the data base uncertainty in ages is significant and dating is of low quality. Nearly half of the failures in the data base have too large uncertainty intervals to be assigned to a particular sea level condition. Using a purely qualitative approach as was done in similar studies (e.g. Owen et al., 2007; Lee, 2009; Leynaud et al., 2009), and by choosing a sufficiently large histogram bin size (5 ky), the landslide time series seems to contain

several peaks, trends and clusters when compared to the global sea level curve. The highest frequency of submarine slope failure in a global average was during periods of rising sea level after the LGM (25 failures). The second highest frequency was while sea level was lowest during the LGM (five failures). The landslide frequency has significantly reduced in the past 6 ka (seven failures) when the rate of sea level rise declined. Dividing the data set into subsets of different depositional environments results in substantially different temporal distributions in the subset. Failures at the north-west African continental slope as well as at glaciated margins are regularly spaced over time. The latter is interesting, as it has been suggested previously that the stability of glaciated margins is heavily affected by climatic changes owing to the direct impact of ice sheet advances and retreats or surging of glaciers (Owen et al., 2007; Tappin, 2010) as well as catastrophic floods during glacial-interglacial transition (Piper and Normark, 2009). The frequency of landslides at sediment-starved margins increases slightly towards the end of the LGM. Failures at river fan systems cluster in the past 30 ka which is most likely an artifact of sampling bias considering high sedimentation rates usually involved in river dominated systems. The highest frequency is reached towards the end of sea level rise (12-6 ka BP) with two slides per thousand years.

However, patterns such as peaks and clusters appear rather diffuse and are less prominent when the data set is plotted with smaller histogram bin sizes (compare Figs. 2.3 and 2.4a, b as well as Figs. 2.6b and 2.7a, b). This apparent bin size dependence is cautionary and, depending on which bin size is chosen, can manipulate any visual interpretation. This should be avoided by statistically testing the data set for appropriate distributions.

#### 2.4.1 How strong is sea level forcing of landslide frequency?

The data set is very similar to randomly distributed artificial data. Our results show that landslide timings are distributed according to a Poisson distribution, i.e. could be essentially random, and do not show any significant trends, peaks or clusters. No statistically significant peaks can be found when splitting up the data set into groups of distinct depositional environments, either. These results stand in contrast to the conclusions of previous studies on the timing of submarine landslides by Maslin et al. (2004), Owen et al. (2007) and Lee (2009), who all suggest that the dominant factor for the timing of landslides is glacial-interglacial cyclicity.

Four factors can be responsible for the timing of landslides being random:

1. There is no forcing such as sea level or climate change that controls the timing of submarine landslides.

2. The forcing is weak and the data base is too small to resolve the signal. As opposed to a strong forcing, a weak forcing requires a large data set to show up as a significant signal.
3. Affects of sea level or climate change on slope stability are not uniform and every margin responds differently, resulting in inconsistent signals.
4. The landslide ages are not sufficiently accurate or even incorrect - as Storegga's age once was.

If climate does not have any influence on slope stability, or if the forcing is weak, climate-independent processes must be dominant factors causing submarine slope failure. Seismicity is generally controlled by tectonics and thus assumed independent of climate. Earthquakes as triggers would likely produce randomly distributed events in a global data set. An exception are glaciated regions, where seismicity is also a function of isostatic rebound and is highest when ice sheets retreat and sea level is rising (Bungum et al., 2005). The potential of earthquakes to cause slope failure is evident from field observations (Piper and Aksu, 1987) and lab testing (Biscontin et al., 2004). However, not every earthquake causes slope failures, independent of their magnitude (Sumner et al., 2010; Völker et al., 2011). The majority of landslides in the data base originate from passive continental margins with generally low levels of seismicity. We therefore suggest that earthquakes may invoke or initiate slope instability, but are possibly not the unique mechanism for many large submarine slope failures.

Oversteepening due to salt doming or other tectonic activities as well as a stress-related collapse of mechanically weak layers are other climate-independent failure mechanism. Contourite deposits forming mechanically weak layers have been repeatedly discussed as failure mechanisms, especially for but not limited to failures at glaciated margins (e.g. Lindberg et al., 2004; Bryn et al., 2005; Laberg and Camerlenghi, 2008).

Separate analyses for individual margins can help in explaining if and how climate affects regional or local slope stability. We attempted this for the north-west African continental margin. Unfortunately, the data is sparse and only ages for eleven slope failures along an entire margin within a period of 150 ka are available. However, visually the data set does suggest a random distribution. It is also unclear on what spatial scales these climatic effects vary, i.e. along a continental margin, within individual depositional basins or at even smaller scales.

### 2.4.2 The origin of reduced landslide frequency during the modern sea level highstand

A prominent pattern in the data base is that significantly fewer events occur in the past 6 ka (seven events) than during the sea level rise since the LGM (25 events). The 6-1 ka BP period is particularly quiet with only four failures. This observation is certainly robust, as any bias due to core lengths would tend to increase the number of younger events. Global sea level was at a similar level towards the end of Termination II (125-120 ka BP), but as these old ages involve large uncertainty intervals and the data base is generally sparse this cannot be used as an analogue for the modern sea level highstand. During sea level highstand shelves are flooded and disconnected from rivers so that less sediment reaches the slopes. The level of post-glacial seismicity decreases and the stress conditions in the sediment equilibrate. Continental slopes are thus expected to stabilise during a high but stable sea level. Mechanisms causing slope failure under these conditions are likely independent of sea level. Indeed, two of the three failures between 6-1 ka BP occurred at the Iberian margin (turbidites E5 and E6) and Masson et al. (2011) present evidence that earthquakes triggered the corresponding landslides. The Trænadjupet slide off the Norwegian continental margin is the third failure in this otherwise quiet period. Laberg et al. (2003) suggest that a contourite underlying the Trænadjupet slide acted as a mechanically weak layer. With this evidence for earthquakes and weak layers, we suggest that during stable and high sea level potential failure mechanisms are limited to those independent of sea level and therefore less failures may be expected. If over all climatic stages only climate independent failure mechanisms act, the data would be distributed uniformly and such a drop in frequency as observed during the modern highstand would not exist. This supports reasons 2 and 3 discussed above, i.e. that climate forcing may be weak and variable across different margin settings.

### 2.4.3 Relevance of preconditioning

Sedimentation rates at most continental margins are highest during the LGM or shortly after (Fig. 2.9) and thus are tightly linked to global sea level. As we do not observe a significant correlation of landslide timings with global climate or sea level, rapid sedimentation rates do not seem to be important as a direct cause for slope failure. However, an indirect impact on the stability of continental slopes is possible. Excess pore pressure develop as a result of rapid loading which decrease the strength and 'precondition' the slope for failure (e.g. Stigall and Dugan, 2010). An external trigger, most likely a climate-independent one such as an earthquake may then be necessary to eventually cause failure. Hence, although preconditioned by a climate-controlled process, the landslide can occur at any time irrespective of sea level.

Rapid deposition may allow for, accommodate, or enhance other processes capable of destabilising a slope, such as fluid flow to areas of less rapid deposition where the corresponding effective stress reduction is more critical (Dugan and Flemings, 2000; Leynaud et al., 2007). A delay time is necessary for the fluid migration to take place which mainly depends on the permeability of the sediment as well as the distance the fluid has to travel, and may involve several thousand to a million years (Dugan and Flemings, 2000; Dugan, 2012). This may explain the observed variations in delay times between the onset of rapid deposition and the timing of the failure (Table 2.3) and supports reason 3 discussed above. 2D numerical modelling of excess pore pressure generation due to fluid flow for well-constrained case studies as for the Storegga slide (Leynaud et al., 2007) and the New Jersey continental margin (Dugan and Flemings, 2000) can help to test this hypothesis.

#### 2.4.4 Future geohazard from submarine landslides

Global temperature is expected to increase by about 3° C in the next century (Meehl et al., 2007). Recent modelling based on this assumption predicts an associated rise in sea level between 0.9 and 1.3 m in the next 100 years (Grinsted et al., 2010), which equals the rate at which sea level rose after the LGM. The absolute amount of modern sea level rise of about 0.3 m (Grinsted et al., 2010), however, is low when compared to 120 m after the LGM. Our work suggests that, at least during the last 30 ka, there has not been a strong linkage between the frequency of major ( $>1 \text{ km}^3$ ) landslide and rapid sea level rise. The linkage is sufficiently weak that it is not statistically significant in our data set, which we acknowledge has uncertainties and has a limited number of examples.

## 2.5 Conclusions

A data set with ages of 62 submarine mass failures at open continental slopes with volumes  $>1 \text{ km}^3$  has been compiled. This data base is the most comprehensive one to date and is the only one considering uncertainty intervals to the age estimates, and to include changes in local sedimentation rates.

Based on this data set we do not find statistical evidence for a climate control on the timing of large submarine landslides, as these resemble a Poisson distribution in which events are essentially random. One reason could be that the sample size is too small and/or the forcing too weak to be statistically significant. Another explanation is that the impact of climate on factors promoting slope instability is not uniform and margins respond differently to an external climate forcing, thus resulting in an inconsistent signal. For example fluid flow within the slope may act as an important factor controlling the

timing of failure. However, there does not appear to be a very strong linkage between sea level and landslide frequency.

A time lag of several kiloyears between periods of rapid deposition and slope failure implies that in most cases rapid deposition does not immediately cause failure. Rapid deposition may well weaken the slope due to excess pore pressures locked in low permeable sediment, or due to fluid migration within layers of high permeability towards areas far away from the excess pore pressure initiation area.

About half of the slides in the data base have uncertainties that are too large to attribute them to a particular sea level stand. To confidently reject or confirm any climate dependence an unbiased data set that covers one full sea level cycle is necessary. This means that sediments and buried slides as old as 130 ka need to be recovered which in many locations is only possible by scientific deep sea drilling.



## Chapter 3

# Methodology

This chapter describes how the Finite Element Method (FEM) is applied to assess the stability of a continental slope over time. The slope is subjected to continuous sediment deposition, which causes consolidation of the slope material and controls the stress state of the slope. Using the FEM allows the determination of stresses and pore pressures over time, as well as their use to assess the stability of the slope during consolidation.

The first part of this chapter describes the modelling approach (sections 3.1 - 3.4). A brief outline of the FEM is followed by a specific description of the implementation of the consolidation process. Different ways of assessing the stability of the slope are explained and key points that need to be considered when modelling a continental slope are summarised. The second part gives an overview of the general mechanical behaviour of marine sediments (sections 3.5 - 3.6), how they differ from soil on land, and how these sediments may be modelled.

Soil is the term that geotechnical engineers use for the "unbonded, granular material which covers much of the surface of the Earth" (Powrie, 2002), whereas a geologist uses the expression sediment. In the following, both terms are used interchangeably. Furthermore, engineering disciplines use void ratio,  $e$ , as a measure of the voids (filled by air or water) in a material, whereas porosity,  $n$ , is common in geology. Conversion between the two parameters is as follows:

$$e = \frac{n}{1 - n}; \quad n = \frac{e}{1 + e}. \quad (3.1)$$

As this thesis integrates aspects from both disciplines, it is inevitable that both terms are used.

### 3.1 The Finite Element Method

In the Finite Element Method the solution of a differential equation is approximated as a continuous function over a discrete number of elements of finite size. The problem of determining, for example, the displacement field in a body is reduced to determining the displacement components at a finite number of nodes that connect the elements. Displacements within elements are approximated using nodal values and shape functions. Shape functions describe mathematically how the interpolated fields (e.g. displacement) vary within each element and should provide displacement continuity between elements (compatibility) in order to avoid the development of gaps and overlaps. Stresses and strains also exist within an element and are approximated using derivatives of shape functions. Shape functions should therefore also satisfy the 'completeness' requirement, i.e. the requirement for an element to take on uniform strain (within this element but not overall).

The most common solution approach is the displacement formulation, which considers displacements as the primary unknowns. From the law of equilibrium, the sum of internal and external forces on a node must equal zero, and the displacement must be chosen accordingly. The relationship between nodal displacements and forces is given by the stiffness matrix  $[K]$ :

$$[K] \cdot D = F \quad (3.2)$$

where  $D$  is the vector of displacement degrees of freedom and  $F$  is the force vector. Once the stiffness matrix for each of the elements has been assembled into a global stiffness matrix, standard direct or iterative solvers can solve this single matrix equation. The solution must satisfy equilibrium, compatibility, material constitutive behaviour and boundary conditions. From the resulting nodal displacements the displacement field within each element can be approximated using the shape functions. The stiffness matrix is then generated by numerical integration on integration points inside the element using the Gauss quadrature. The exact location of these Gauss or integration points are chosen to optimise the accuracy of the numerical integration. Finally, stresses can then be calculated through the constitutive equation.

The FEM is an approximate method and the accuracy of the approximation depends on the choice of element types and mesh. Typical shapes of 2D elements are triangles and rectangles (Fig. 3.1). The corresponding shape functions are polynomial and can be linear or quadratic for the elements shown in Fig. 3.1. A linear rectangular element has four nodes with four Gauss points (Fig. 3.1a), whilst a quadratic rectangular element has eight nodes with nine Gauss points (Fig. 3.1b). In the case of reduced integration the number of Gauss points reduces to one in a linear rectangular element and four in a

quadratic rectangular element.

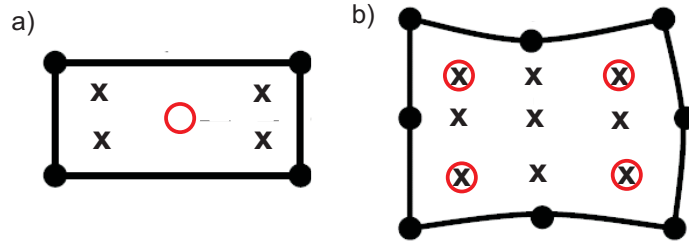


Figure 3.1: Two-dimensional linear (a) and quadratic (b) rectangular elements with node points (black dots) and integration points for full (black crosses) and reduced integration (red circles).

The choice of the element type, polynomial order of the shape functions and integration type depends on the type of analysis. Generally, the larger the number of nodes and integration points the better the accuracy and the longer the running time. The mesh itself should be fine where steep gradients are expected. A coarse mesh is adequate in areas of reasonably low rates of change or that are not of the user's interest.

### 3.2 Finite Element modelling of a consolidating slope

No analytical solution for two-dimensional consolidation of a slope exists, so that a numerical approximation is required. Consolidation is modelled as fully saturated flow through porous media by coupling mechanical (stress and strain) and pore pressure diffusion effects. The coupling is based on the effective stress principle (Terzaghi and Peck, 1948), which assumes that the total stress at each point is the sum of an 'effective stress' (carried by the soil skeleton) and a pore pressure in the fluid permeating the soil. This fluid pressure can change with time if external conditions change, and any pore pressure differences from hydrostatic pressures will cause the fluid to flow. Fluid flow is governed by Darcy's law, which relates flow velocity to hydraulic gradient. For modelling flow in a porous medium the soil particles and the pore water are assumed incompressible.

The consolidation problem can be formulated using a 'small strain' or a 'finite strain' analysis. In the former analysis the kinematic relationships are linearised and the model is geometrically linear, i.e. elements remain in their initial nodal coordinates. The latter analysis is geometrically nonlinear and includes large displacement effects, and elements are formulated using current nodal positions. A comparison of both types of analyses as well as their advantages and disadvantages are investigated in greater detail in chapter 4.

In a transient nonlinear analysis, such as consolidation, the solution is found by subdividing the simulation into a number of time increments. The equilibrium configuration is approximated at the end of each of these time increments. To determine an acceptable approximation several iterations may be necessary within one time increment. However, there is a lower limit on the time increment that is related to the element size:

$$\Delta t \geq \frac{\gamma_w}{6 \cdot E \cdot k} \cdot \left(1 - \frac{E}{K_g}\right)^2 \cdot (\Delta h)^2. \quad (3.3)$$

$\Delta t$  is the time increment,  $\gamma_w$  is the specific weight of water,  $E$  is Young's modulus of the soil,  $k$  is permeability of the soil,  $K_g$  is the bulk modulus of the solid grains and  $h$  is the typical element length. If time increments are smaller, spurious oscillations may appear in the solution. These nonphysical oscillations may cause problems if pressure-sensitive plasticity is used to model the porous medium.

### 3.3 Assessment of slope stability

Traditional geotechnical slope stability analyses include limit equilibrium methods (e.g. Bishop's or Morgenstern's method), limit analysis, or the slip line method. These methods are based on comparison of forces that cause and those that resist instability. Typical soil models used in these analyses are Mohr-Coulomb or Tresca. More recently, and with rapidly increasing computer capacities, the use of nonlinear FE modelling has become popular (Griffiths and Lane, 1999). Important advantages over the traditional approaches are that no failure mechanism needs to be assumed, advanced soil models can be used and complex loading and boundary conditions can be applied. Moreover, information on deformation can be obtained and progressive failure up to total failure can be monitored. The greatest advantage, in particular for the application here, is the possibility of transient assessment of slope stability. The stability of the sediment can be assessed at any time and any location during the consolidation process.

The FE method detects failure of the slope naturally by non-convergence of the solution (Zienkiewicz and Taylor, 1989). If the algorithm is unable to find a stress redistribution that satisfies global equilibrium, a dramatic increase in nodal displacement results. When these large displacements exceed tolerance levels the solution stops converging. However, it is often equally important to assess the state of stability of an as yet unfailed slope and two ways of doing this are explained in the following.

The state of stability of a slope is commonly expressed via the Factor of Safety (FoS). In a partially drained problem, such as consolidation, the FoS is defined on soil strength

and gives the ratio of mobilised shearing strength to the available shearing strength. The mobilised strength  $\phi'_{mob}$  is the strength required to maintain the stability of the slope and is given by

$$\sin \phi'_{mob} = \frac{\sigma'_1 - \sigma'_3}{\sigma'_1 + \sigma'_3}. \quad (3.4)$$

The available strength is the material strength given by the critical state friction angle  $\phi'_{crit}$ . An FoS value  $< 1$  indicates that the required strength exceeds the available strength, and the slope is unstable.

Another way to assess the state of stability of the slope is by using the overpressure ratio  $\lambda^*$ , which characterises the relationship between pore pressure and vertical stress. This is particularly useful for low gradient slopes where high excess pore pressures are likely to initiate slope failure by decreasing the shearing resistance of the soil. The overpressure ratio is given by the ratio of excess pore pressure to the vertical effective stress corresponding to hydrostatic conditions. When  $\lambda^*=0$  there is no overpressure, and when  $\lambda^*=1$  the pore pressure equals the overburden stress. In the latter case vertical effective stresses are zero and the soil collapses. The overpressure ratio as well as the Factor of Safety can be calculated for any element at any time of the simulation.

### 3.4 Considerations for modelling of a continental slope

The aim of the modelling is to assess the stability of a submerged continental slope under continuous sedimentation. The modelling approach taken here is to start with a body of sediment which has attained a state of gravitational equilibrium under its own weight and has zero excess pore pressure. This body is then loaded anew to undergo further consolidation.

The problem is clearly not one-dimensional, as a slope is involved and fluid may flow sideways. In a real slope stress and strain are 3D tensors, but the length of a continental margin is much greater than the width and depth of its slope. The strains associated with continental margin length ( $y$ -direction) are therefore small compared to the cross-sectional strains ( $x$ - and  $z$ - directions). The continental slope analysis can therefore be seen as a plane problem with zero strain in the  $y$ - direction. The stress in  $y$ -direction is considered as a dependent variable, which is forced to adopt whatever value is necessary to comply with the imposed zero strain condition. In a coupled displacement - pore pressure plane strain analysis each node therefore has two displacement degrees of freedom.

Pore pressures can be accounted for by excess or total pore pressure formulation. The latter requires the definition of sea level (i.e. water depth) in order to prescribe water

pressures. Care is then required for boundary and loading conditions at the seafloor, where water pressure is high and effective stresses are low.

Gravity needs to be applied in the continental slope model. In addition to its fundamental role in slope failure, gravity forces are also important in consolidation. Consolidation due to self-weight becomes especially important when soil is soft or thick or both, and neglecting gravity will seriously underestimate displacement and effective stresses (e.g. Mei, 1985).

The consolidation - slope stability model does not take into account sedimentation. The accumulation of new sediment is not physically modelled but simulated as a vertical load on the original seafloor. Consequently, the model is not capable of simulating failure within this interval of newly deposited sediment. Not simulating the new sediment also has implications for the fluid flow boundary condition at the surface of the model. The sediment drains freely through the seafloor, and pore pressures at the seafloor are hydrostatic.

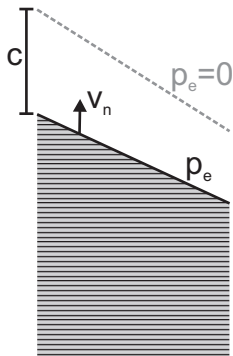


Figure 3.2: Drainage boundary condition at the model's surface. The black solid line represents the model surface and the grey dashed line shows the 'new' seafloor.

As the deposition of sediment (loading) starts, what has been the seafloor originally, is now being buried and pore pressures may differ from hydrostatic. Drainage is restricted by overlying sediment, and fluid flow is a function of the pore pressure gradient in and the permeability ( $k_{vl}$ ) of the overlying sediment (Fig. 3.2). The flow speed at which pore water drains vertical to the model surface is calculated according to:

$$v_n = \frac{k_{vl}}{\gamma_w \cdot c}(p_e) \quad (3.5)$$

with  $c$  as the thickness that the sediment would have at a given time and location. The seafloor now is the model surface plus  $c$ , where excess pore pressures are zero (Fig. 3.2).

### 3.5 Mechanical behaviour of marine sediments

The main type of sediment at continental margins with low sedimentation rates is hemipelagic mud. Hemipelagite is a mixture of biogenic particles settling out from the water column (nano- or microfossil ooze) and particles of terrigenous origin that were

delivered by wind, rivers, icebergs, and/or glaciers into the ocean (siliciclastic clay or silt). The carbonate and clay contents vary highly and depend on the ratio of biogenic to terrigenous material. Clay to silt grain sizes are dominant. Predominant clay minerals in hemipelagic sediment are smectite, illite and chlorite (Poulos, 1988). Organic matter can reach up to 7% (e.g. Keller, 1982). Mass transport deposits from turbidity currents or debris flows are often interbedded, but in most cases comprise the same hemipelagic sediment from further up the slope or shelf.

Information on the mechanical behaviour of marine sediments is mostly limited to a few metres below seafloor, or the maximum penetration depth of gravity or piston cores. Moreover, it is complicated by the comparatively large logistical effort (Locat and Lee, 2002). It is extremely difficult to obtain undisturbed samples that are needed for a thorough geotechnical analysis, especially in the deep ocean. Most coring devices have a thin diameter of <10 cm, so that the penetration shock will affect all retrieved material and part of the sediment's fabric will likely be destroyed. For example, Long et al. (2011) noted that core disturbance can result in measured compressibility values at a given void ratio that are lower than those of intact rock. Box corers are the only devices with which geotechnical samples can be properly taken (Locat and Lee, 2002), but their penetration is limited to about 0.5 m. Even with this device deformation cannot be fully excluded. The variation of core quality with various degrees of disturbance makes data synthesis complicated (Bryant et al., 1981).

Hemipelagic sediments are generally soft, highly sensitive, and fit within the critical state framework developed for natural soils on land (Maltman and Bolton, 2003; Baudet and Ho, 2004; Brandes, 2010). However, the high pressure-low temperature environment in which marine sediments are formed may have important effects on sediment microstructure. Sedimentation through salt water at typically very low rates allows more flocculated and weaker microstructures to form (Brandes, 2010). As a result, deep-sea sediments are generally more compressible than soils on land (refer to section 3.5.1) and have a much higher sensitivity (Baudet and Ho, 2004). The strength characteristics of fine grained marine sediments are similar to those of fine grained sediment onshore, i.e. lower particle density results in higher effective friction angles (Poulos, 1988). Cementation or bonding therefore increase the shearing resistance. The majority of geotechnical experiments on marine sediments suggest that sediments in the deep sea are non-cohesive (e.g. Poulos, 1988; Dugan and Flemings, 2000). Marine sediments are usually normally consolidated as due to the long time scales involved with their deposition (Poulos, 1988).

### 3.5.1 Porosity-depth profiles and compressibility behaviour

In traditional soil mechanics the relative volume change of the sediment is a linear function of exponential stress change, and is typically plotted as specific volume ( $v = 1 + \text{void ratio}$ ) against the natural logarithm of mean effective stress ( $p' = (\sigma'_1 + \sigma'_2 + \sigma'_3)/3$ ) as shown in Fig. 3.5a. The compressibility is highest at high specific volumes and decreases with increasing effective stresses. The slope of this normal compression line,  $\lambda$ , is a measure for the compressibility of the sediment. However, it has been noted that this approach does not capture well the very high porosity loss that is observed within the upper  $\sim 100$  m the seafloor (Fig. 3.3 Brandes, 2010; Long et al., 2011). Long et al. (2011) therefore suggest that  $\lambda$  decreases linearly with effective stress, following a concept developed by Butterfield (1979, 2011). This can be implemented in a conventional constitutive model by a linear variation of  $\lambda$  with void ratio, as opposed to a constant value for  $\lambda$ .

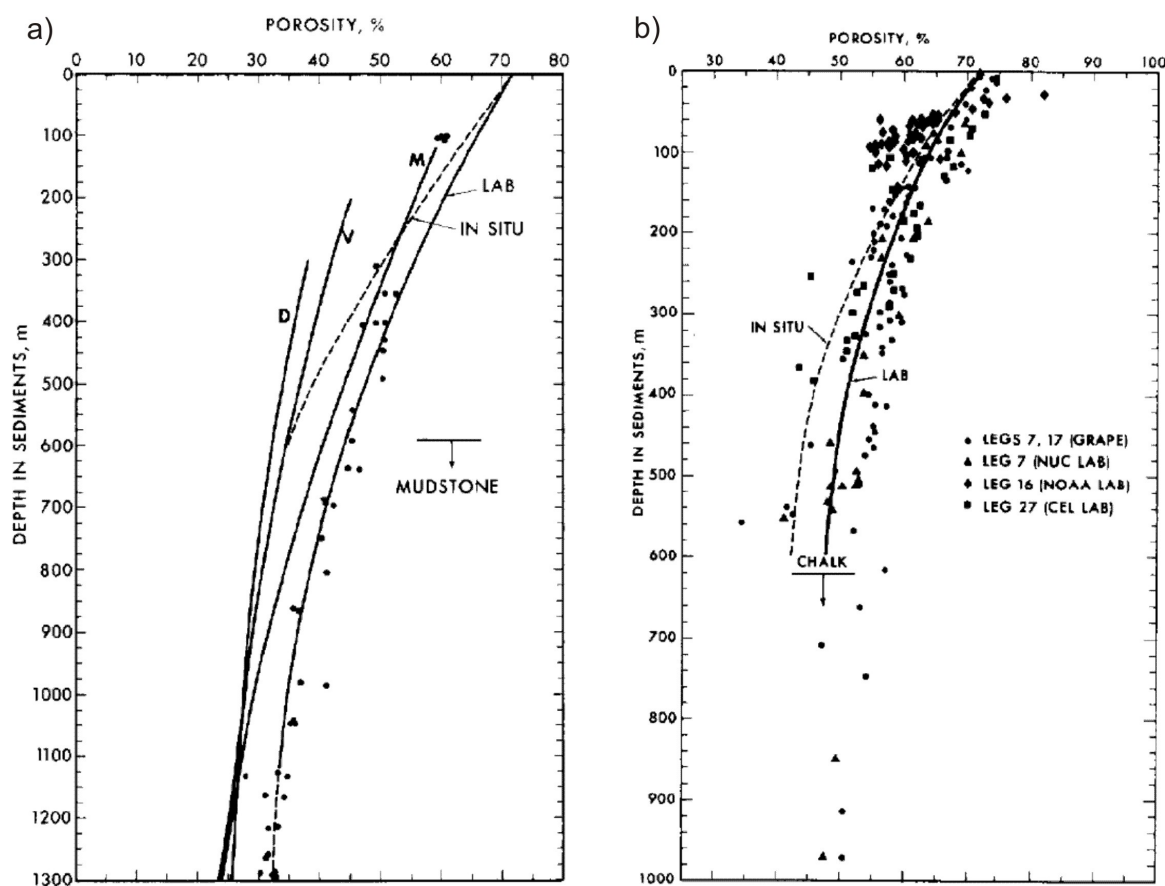


Figure 3.3: Depth-porosity relationship for a) siliciclastic and b) carbonate rich sediments, modified after Hamilton (1976).

### 3.5.2 The effect of carbonate content on physical-mechanical properties

It has been noted that carbonate content has a significant influence on the physical-mechanical properties of a sediment (e.g. Bryant et al., 1981; Bartetzko and Kopf, 2007). A higher shear strength is observed with higher carbonate content (Bryant et al., 1981). Moreover, carbonate rich sediments often have unusually high overconsolidation ratios without any evidence of erosion of the overburden. Such 'apparent' overconsolidation along with higher shearing resistance is attributed to early bonding or cementing (Bryant et al., 1981). This early diagenesis can also explain the observation that carbonate rich sediments are comparably stiff (Masson, personal communication), and do not consolidate to as low porosities as siliciclastic clays (Fig. 3.3, e.g. Hamilton, 1976; Bryant et al., 1981).

### 3.5.3 Permeability-porosity relationships and anisotropy

The permeability,  $k$ , of fine grained sediments decreases over several orders of magnitude with increasing depth. The dominant factor of permeability is porosity,  $n$ . Therefore, permeability of marine sediments is often expressed as an exponential function of porosity of the form

$$k = A \cdot e^{Bn} \quad (3.6)$$

with lithology-dependent constants  $A$  and  $B$  (Long et al., 2008; Binh et al., 2009; Flemings et al., 2012). These constants are determined in the laboratory using permeameters or during oedometer tests. Pump tests to measure in situ permeability of deep sea sediments are hardly realisable at deep sea sites, and were attempted at a limited number of sites only (Boutt et al., 2012). Alternatively, an estimated in situ permeability from laboratory-based porosity-permeability relationship and in situ porosities is often provided.

Where available, in situ permeability exceeds laboratory measured permeability often by more than one order of magnitude (Rowe, 1968; Boutt et al., 2012). This discrepancy is explained by larger scale in situ fluid pathways that are not captured by laboratory-size samples. Fissures and fractures provide such additional fluid pathways, or permeability anisotropy that supports lateral drainage. Marine sediments are likely to have a high ratio of horizontal to vertical permeability due to their sedimentation and compaction history (Bennett et al., 1989). Compaction during burial causes reorientation of solid particles in alignment perpendicular to the principal effective stress (Fig. 3.4). Fluid flow is easier along the direction of aligned particles than across. In the case of absence of horizontal tectonic stresses, the alignment is horizontal.

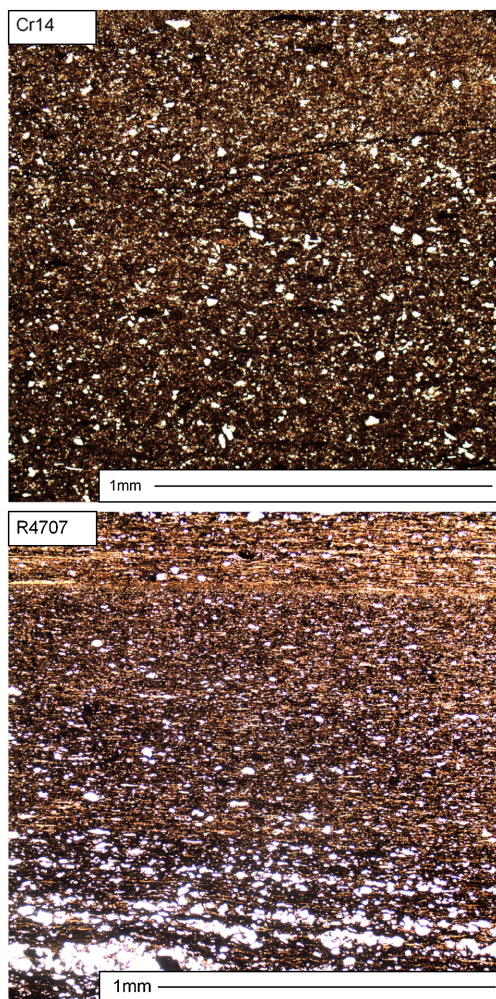


Figure 3.4: Optical microscopy images of two mudstones with low (upper panel) and high (bottom panel) degrees of anisotropy (Day-Stirrat et al., 2010).

### 3.6 The Modified Cam Clay constitutive model

Soil (or sediment) consists of a heterogeneous mixture of fluids and particles and therefore has a complex and highly nonlinear mechanical behaviour. Constitutive models are fit empirically to experimental measurements. The critical state theory is the most appropriate for modelling fine grained marine sediments (Maltman and Bolton, 2003; Baudet and Ho, 2004; Brandes, 2010). Critical state theory links the shear strength not only to stress variations, but also to specific volume, the current value of stress and its path, and is known to realistically predict volume changes. The Modified Cam Clay (MCC) constitutive model (Roscoe and Burland, 1968) is therefore used throughout the thesis.

Critical state theory defines the stress state of a sediment by the effective mean stress,  $p'$ , the mean stress difference,  $q$ , and its specific volume,  $v=e+1$ . The current strength

of the sediment depends on these state variables. A certain combination of the state variables defines the critical state, in which the sediment cannot take more load and continues distorting at constant effective stress. Critical stress states are illustrated by the critical state line (CSL), which parallels the normal compression line in a  $\ln p' - v$  plane (Fig. 3.5a) and follows a straight line in a  $p' - q$  plane (Fig. 3.5b). The CSL intersects the yield surface at the point at which the maximum value of  $q$  is attained. The yield surface represents the boundary between elastic and plastic states in a three-dimensional space of stresses. In MCC it has an elliptic shape.

At very small strains the behaviour of a sediment is purely elastic and lies inside the yield surface. Elastic behaviour is described by a nonlinear isotropic porous-elastic model, in which the change in volume of the material is proportional to the logarithm of the mean effective stress. When the stress state lies on the yield surface, the stress-strain behaviour changes to plastic behaviour, i.e. the material is said to yield. The yield surface changes its size according to the volumetric strain so that the current stress state lies always on the yield surface. The flow rule defines the direction of the plastic strain increment vector. In MCC, the vector is normal to the yield surface and the flow rule is associated. Accordingly, for a stress state to the right of the centre of the yield locus ('wet side', Fig. 3.5b), plastic strains are compressive and the material hardens as it deforms plastically. If the stress state lies on the left ('dry') side, the material dilates and softens. Failure occurs when the stress path intersects the critical state line as the deviator stress increases and the sediment reaches critical state.

The main difference between the Modified and the original Cam Clay (CC) models is the shape of the yield surface. Due to its elliptic shape MCC correctly predicts volumetric strains only and no shear strains during isotropic compression, while CC also imposes shear strains. This discontinuity of the yield surface can cause numerical instability and therefore makes MCC the preferred constitutive model, especially in numerical analyses.

MCC requires five parameters (Fig. 3.5):

- the slope of the elastic path;  $\kappa$
- the slope of the normal compression line and critical state line on a graph of  $v$  against  $\ln p'$ ;  $\lambda$
- the slope of the critical state line on a graph of  $q$  against  $p'$ ;  $M$
- the shear modulus;  $G$ , or the Poisson's ratio;  $\nu$
- the intercept of the normal compression line at  $\ln p'=0$  on a graph of  $v$  against  $\ln p'$ ;  $N_p$ .

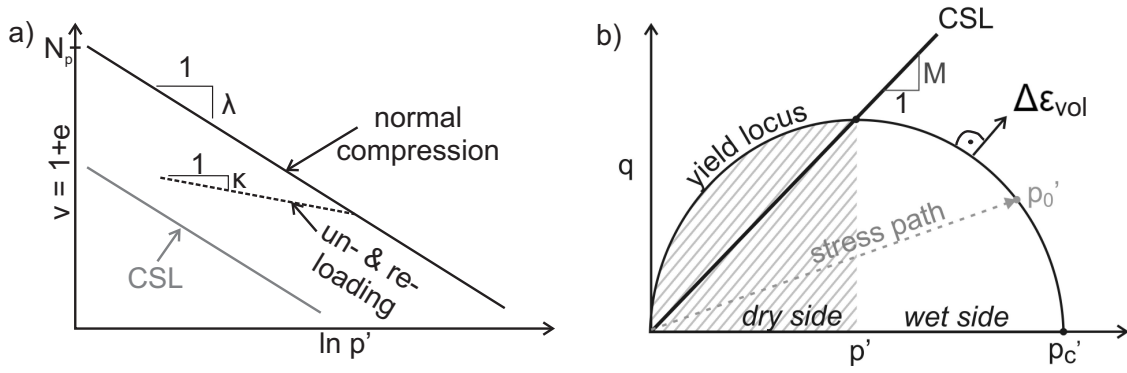


Figure 3.5: Modified Cam Clay constitutive model: a) representation of the compression and critical state lines in the  $\ln p' - v$  space; b) yield locus in the  $p' - q$  space. CSL is the critical state line,  $p_0'$  is the initial stress state and  $p_c'$  is the size of the yield locus. The volumetric strain vector ( $\Delta \epsilon_{vol}$ ) is perpendicular to the yield surface for an associated flow rule.

The parameters  $\lambda$  and  $\kappa$  are obtained from consolidation experiments, such as one-dimensional compression tests in an oedometer. Often, the results are expressed as compression and swelling indices,  $C_c$  and  $C_s$ . The MCC parameters  $\lambda$  and  $\kappa$  can be calculated from  $C_c$  and  $C_s$ , respectively, by dividing each by  $\ln 10$  (Powrie, 2002). The stress ratios ( $q/p'$ ) at the end of a series of triaxial tests define the critical state line with slope  $M$ . Because  $M$  is a measure of the ratio of shear to normal effective stress at failure, it is related to the friction angle,  $\phi'_{crit}$ , of the material by:

$$M = \frac{\sin \phi'_{crit} \cdot 6 \cdot \sqrt{1 - b + b^2}}{3 + \sin \phi'_{crit} \cdot 2 \cdot b - \sin \phi'_{crit}} \quad (3.7)$$

with  $b = 0.5$  for plane strain conditions (Powrie, 2002). Analysis of Mohr circles of stress from triaxial tests provides  $\phi'_{crit}$ .

The model formulation does not impose any condition on the elastic shear response so that either the shear modulus  $G$  or the Poisson ratio  $\nu$  can be specified. Prescribing a constant  $\nu$ , which is acceptable for marine sediments even at large depths (Karig and Hou, 1992), results in a stress dependent shear modulus  $G$ :

$$G = \frac{3(1 - 2\nu)(1 + e_0)}{2(1 + \nu)\kappa} p' \quad (3.8)$$

where  $e_0$  is a reference void ratio.

For slope stability modelling purposes it is more convenient to specify the initial size of the yield locus,  $p_c'$  in the  $p' - q$  plane (Fig 3.5b), rather than  $N_p$ . The position of the stress state of a material point relative to the yield locus determines the overconsolidation

ratio. If the stress state lies on the yield locus, whose shape is given by

$$\frac{q^2}{p'^2} + M^2 \cdot \left(1 - \frac{p'_c}{p'}\right) = 0, \quad (3.9)$$

then the material is normally consolidated. If the stress state lies within the yield locus, it is overconsolidated. Because the degree of overconsolidation directly affects the sediment's mechanical behaviour, the stress initialisation at the beginning of the analysis is a critical point.

A significant disadvantage of the classic MCC formulation is that its hardening law predicts total closure of pore space for very large strains. This means that void ratios are predicted to become negative under high pressures. To avoid the risk of negative void ratios, the parameter  $\lambda$  (the slope of the normal compression line) can be defined as a function of the void ratio. The value of  $\lambda$  approaches zero at very low void ratios, as used in the approach discussed in section 3.5.1.

Due to the shape of the yield locus when compared to the critical state line, MCC can significantly overestimate failure stresses on the left ('dry') side of the yield locus (Gens and Potts, 1988). For yielding on the dry side, incremental plastic volumetric strains are dilatant and softening behaviour results. Therefore, care needs to be taken when dilatant volumetric strains occur.

## 3.7 Software

The software package ABAQUS is used for the creation and solution of consolidation-slope stability models (ABAQUS, 2009). ABAQUS/CAE, an interactive graphical environment, allows to create finite element models and evaluate results. The general-purpose finite element program ABAQUS/Standard uses the FEM to solve the differential equation system. MATLAB is used for post-processing and graphical representation of the numerical results.

## 3.8 Hardware

For the calculations of all FE models shown in the thesis a standard desktop computer with a Linux RedHat v2.16.0 operating system is used. The machine has two 4 · 1.6 GHz quadcore processors and 12.29 GB of available physical memory in addition to practically unbounded virtual memory. ABAQUS is capable of multithreading and parallel

computing. Using four processors in multithread mode, the solution of a model with about 1.76 million degrees of freedom that is run for 2 million years takes about four hours.

## Chapter 4

# Benchmarking the performances of small strain and finite strain assumptions for the continental slope model

### 4.1 Introduction

Terzaghi's classical consolidation equation (Terzaghi and Peck, 1948) assumes that strains are infinitesimal, such that it suffices to consider equilibrium of the body in the undeformed configuration. Translated into Finite Elements this means that the stiffness matrix is determined for the initial nodal coordinates throughout the analysis. The internal forces are linear functions of displacement and the external forces do not depend on displacements at all. This so called small strain analysis can be used confidently when strains are comparatively small.

However, for soft soils strains can be large so that this assumption does not hold. For this reason Gibson et al. (1967) first implemented the finite strain analysis into the analytical consolidation equations which takes into account the deformed configuration of a body. In the Finite Element Method, the inclusion of this geometric nonlinearity requires the element stiffness matrices to be formulated anew for each increment, using the most recent nodal coordinates. The internal forces are nonlinear functions of displacement and the external forces may also depend on displacement, such as the external pressure acting on a deformed surface.

Gibson et al. (1981), Schiffman (1982) and Schiffman et al. (1984) compared the solutions of small and finite strain analyses for 1D consolidation of a clay layer to field data. While both types of analyses reliably reconstruct final displacements, the paths to reach this final displacement over time differ. Moreover, the solution for excess pore pressure calculated by small strain analysis overpredicts the excess pore pressures observed in the

field data. The magnitude of this overestimation varies with time and depth.

For the consolidation of very soft marine sediments, and considering also the shear strains that develop due to loading on a slope, large strains are expected, especially near the surface. It is therefore better to use finite strain analysis. However, owing to the recalculation of the stiffness matrices and loading conditions at every numerical increment, finite strain analyses are computationally much more expensive. It is therefore worth to carefully evaluate whether a finite strain analysis is necessary, or if the problem can be simulated using the less expensive small strain analysis. If small strain analyses are to be used, it is also important to quantify the error for the specific model setting used here over time and space. To estimate this error, two models of submarine slopes with identical geometries, sediment properties, boundary and initial conditions are calculated, the first one using finite strain and the second one using small strain assumptions. The solutions are compared and their differences over time and space analysed.

## 4.2 Methodology

### 4.2.1 Implementation

The software ABAQUS allows geometrical nonlinear analysis for nearly all provided element types. Due to limitations in the software (conflicting surface flow boundary condition) the geometrically nonlinear analysis has to be conducted using excess pore pressure formulation. Implementing excess pore pressure formulation in a consolidation analysis involves a further complication. The body force representing gravity acts only on the particles in the matrix. As porosity changes during consolidation, so does the weight of the sediment body, but the software does not take this into account. Therefore, the body force defined on each element must be updated to the current porosity continuously via subroutines. This increases the already high computational costs involved with finite strain assumptions. Moreover, the calculations are done within subroutines, that do not support parallel computation. Therefore, the computationally expensive finite strain analysis cannot be solved in parallel, which is an important disadvantage.

### 4.2.2 Model parameters

The model set up, mesh, geometry, boundary and initial conditions are identical to those used and described for later models. In order to avoid repetition, the reader is referred to the previous chapter 3 as well as the methodology section in the following chapter 6.2.

Permeability is isotropic and changes as a function of void ratio (Fig. 4.1). For higher void ratios (between 0.7 and 3.0) the permeability decrease is more rapid than for smaller void ratios (between 0.1 and 0.7). The initial permeability is  $10^{-8}$  m/s at the seafloor (at a void ratio of 3.0), decreases to  $10^{-11}$  m/s at a depth below seafloor of about 1600 m (void ratio of 0.7) and a minimum of  $10^{-12}$  m/s at a void ratio of 0.1. All other physical-mechanical parameters are given in Table 4.1.

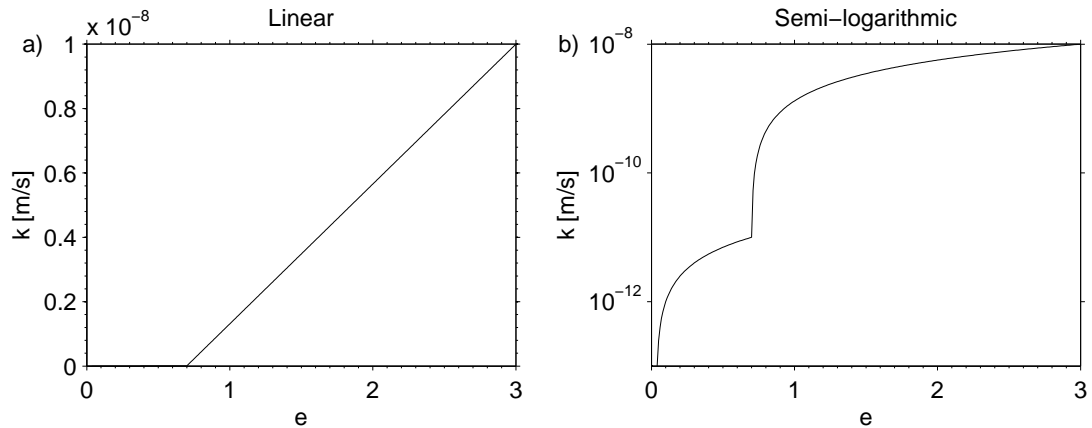


Figure 4.1: Relationship between void ratio,  $e$ , and permeability,  $k$ , for the models used here. The same relationship is shown a) in a linear plot, and b) in a semi-logarithmic plot.

A vertical load at the top surface is increased continuously from 0 kPa at the start of the simulation ( $t=0$ s) to a maximum load of 36000 kPa after 2,000 ky at the shelf (left side of the model). This corresponds to a rate of sediment deposition of 1.5 m/ky. The load magnitude decreases exponentially with increasing distance from the origin just as described in equation 6.7 in chapter 6. The models were run for 2 million years with automatic time incrementation.

Notation		Value	Reference
$\kappa$	Swelling index	0.027	Valent et al. (1982); Demars (1982)
$\nu$	Poisson ratio	0.3	Karig and Hou (1992)
$\lambda$	Compression index	0.28	Valent et al. (1982); Demars (1982)
$\phi'_{crit}$ [°]	Friction angle	28	Valent et al. (1982)
$M$	Slope of critical state line	0.87	
$\gamma_w$ [kN/m <sup>3</sup> ]	Specific fluid weight	10.24	
$g$ [m/s <sup>2</sup> ]	Gravity	9.81	

Table 4.1: Spatially and temporally constant input parameters used in the models of this section.

### 4.2.3 Quantification of differences

Important variables for slope stability analyses are excess pore pressure and effective stress. In addition, fluid flow and strains are key parameters in understanding and interpreting pore pressure and effective stress fields. These four variables are therefore chosen for a detailed analysis of the differences between the linear and the nonlinear model. The development of excess pore pressure, vertical effective stress, fluid flow velocity and total volumetric strain over time are output at 15 selected nodes. These nodes are chosen for five x-coordinates distributed evenly along the length of the model (node n1 at x=10 km, node n2 at x=30 km, node n3 at x=60 km, node n4 at x=80 km and node n5 at x=110 km). To quantify variations with depth, information for each horizontal location is provided at three different depths (z=0 m, z=90 m and z=200 m). Stresses are interpolated from integration points to nodal values using shape functions.

For an overall estimation and quantification of the differences between two models, the area-weighted root mean square (AWRMS) differences in excess pore pressure, total volumetric strain, fluid flow velocity and vertical effective stress between the linear and nonlinear models are calculated for the entire model area at various points in time (411 ky, 684 ky, 1026 ky and 2000 ky). The AWRMS takes into account the area which one node (or integration point) 'covers' in the model ( $a_i$ ) and is obtained according to:

$$AWRMS = \sqrt{\frac{\sum_{i=1}^k (m1_i - m2_i) \cdot a_i}{a_t}}, \quad (4.1)$$

where  $k$  is the number of nodes (integration points),  $a_t$  is the total area of the model,  $m1_i$  is the value of the specific variable at the same node (integration point)  $i$  for one model and  $m2_i$  is the value of the specific variable at node (integration point)  $i$  for the second model. Weighing the squared difference of the two models by their nodal (elemental) area is necessary here, because element sizes within the model vary over several orders of magnitude.

## 4.3 Results

The finite strain model (circular markers in Figs. 4.2 - 4.5) requires a much larger number of increments than the small strain model (cross markers) due to its higher degree of nonlinearity. Computing times are about 3 hours for small strain and just over 11 hours for finite strain analysis.

Solutions of both models for volumetric strains,  $\epsilon_{vol}$ , are nearly identical for all selected nodes at the model surface (Fig. 4.2a), at 90 m below the model surface (Fig. 4.2b) as well as at 200 m below the model surface (Fig. 4.2c). The AWRMS difference between the linear and the nonlinear geometry formulations at the end of the analysis ( $t=2,000$  ky) is 0.006 (Table 4.2). To give some idea of what the error means in terms of relative accuracy, the AWRMS value of the small strain analysis at the 250,000 elements considered was 0.166. The ratio of AWRMS difference to AWRMS value of the small strain analysis is 0.039, or 3.9%. The percentage is about similar at the other time steps given in Table 4.2, indicating that differences in volumetric strains between the two analyses are less than 6%, which can be considered as a satisfactory match.

Time	Variable	<i>AWRMS</i> difference	<i>AWRMS</i> $S_{ref}$	<i>AWRMS</i> difference [%]
411 ky	$\epsilon_{vol}$ [ ]	0.004	0.070	5.93
	$p_e$ [kPa]	589	1421	41.48
	$\sigma_{v'}$ [kPa]	365	27592	1.32
	$v$ [mm/y]	0.019	0.076	24.97
684 ky	$\epsilon_{vol}$ [ ]	0.004	0.092	4.29
	$p_e$ [kPa]	958	2959	32.38
	$\sigma_{v'}$ [kPa]	371	28789	1.29
	$v$ [mm/y]	0.017	0.066	25.73
1026 ky	$\epsilon_{vol}$ [ ]	0.004	0.114	3.24
	$p_e$ [kPa]	1102	4920	26.98
	$\sigma_{v'}$ [kPa]	385	30290	1.43
	$v$ [mm/y]	0.016	0.074	21.28
2,000 ky	$\epsilon_{vol}$ [ ]	0.006	0.166	3.39
	$p_e$ [kPa]	3145	9165	34.31
	$\sigma_{v'}$ [kPa]	989	36557	2.71
	$v$ [mm/y]	0.018	0.091	19.78

Table 4.2: Area-weighted root mean square (AWRMS) differences between the results of small strain and finite strain analyses for total volumetric strain,  $\epsilon_{vol}$ , excess pore pressure,  $p_e$ , vertical effective stress,  $\sigma_{v'}$  and fluid flow velocity,  $v$ , at several times during the analysis. To provide an estimate of the relative accuracy of these differences, the AWRMS value for the more accurate finite strain analysis ( $AWRMS_{ref}$ ) and the percentage of *AWRMS* differences to  $AWRMS_{ref}$  are listed as well.

Large differences are obvious in the pore pressure solutions of the two models (Fig. 4.3), especially from about 800 ky onwards at the buried nodes (Fig. 4.3b,c). Node n1 near the shelf edge, where rates of deposition are highest, shows a kink towards rapid rates of increase, followed a few hundred kiloyears later by nodes n2, n3 and n4. This kink in the pore pressure development seems to occur only in the small strain analysis, although, a certain steeper pore pressure increase is also seen for node n1 at  $z=200$  m of the finite strain solution (blue circular markers in Fig. 4.3c). The pore pressure increase, however, occurs about 600 ky later and is less steep compared to the corresponding node in the

small strain solution. A closer look at these kinks in excess pore pressure as well as their effect on the AWRMS error is taken in the following subsection. The total AWRMS difference at the end of the analysis ( $t=2,000$  ky) is 3145 kPa (Table 4.2) suggesting that small strain analysis overestimates excess pore pressures by about 34 %. In the early stages of the modelled time period these differences are larger than 40 %, before they decrease to less than 30 % at  $t=1026$  ky. The absolute difference to the finite strain solution varies over time and space, and therefore no general assumptions about the magnitude of the error introduced by small strain analysis can be made.

Vertical effective stresses are nearly identical for both analyses for the selected nodes (Fig. 4.4). This is also reflected in the low overall AWRMS relative difference of less than 2 % during and at the end of the simulations (Table 4.2).

For the Darcy flow velocity the relative AWRMS varies between 20-25 %. No constant pattern can be observed at the selected nodes (Fig. 4.5). Initially, fluid flow rate calculated with small strain analysis is higher than flow calculated with finite strain. This changes towards the end of the analysis. Node n1 at  $z=200$  m in Fig. 4.5c shows a positive peak at about  $t=800$  ky in the small strain, and a peak at about  $t=1200$  ky in the finite strain solutions. A similar 'delay' occurs for node n2 with a negative peak at about 1000 ky (small strain) and 1600 ky (finite strain).

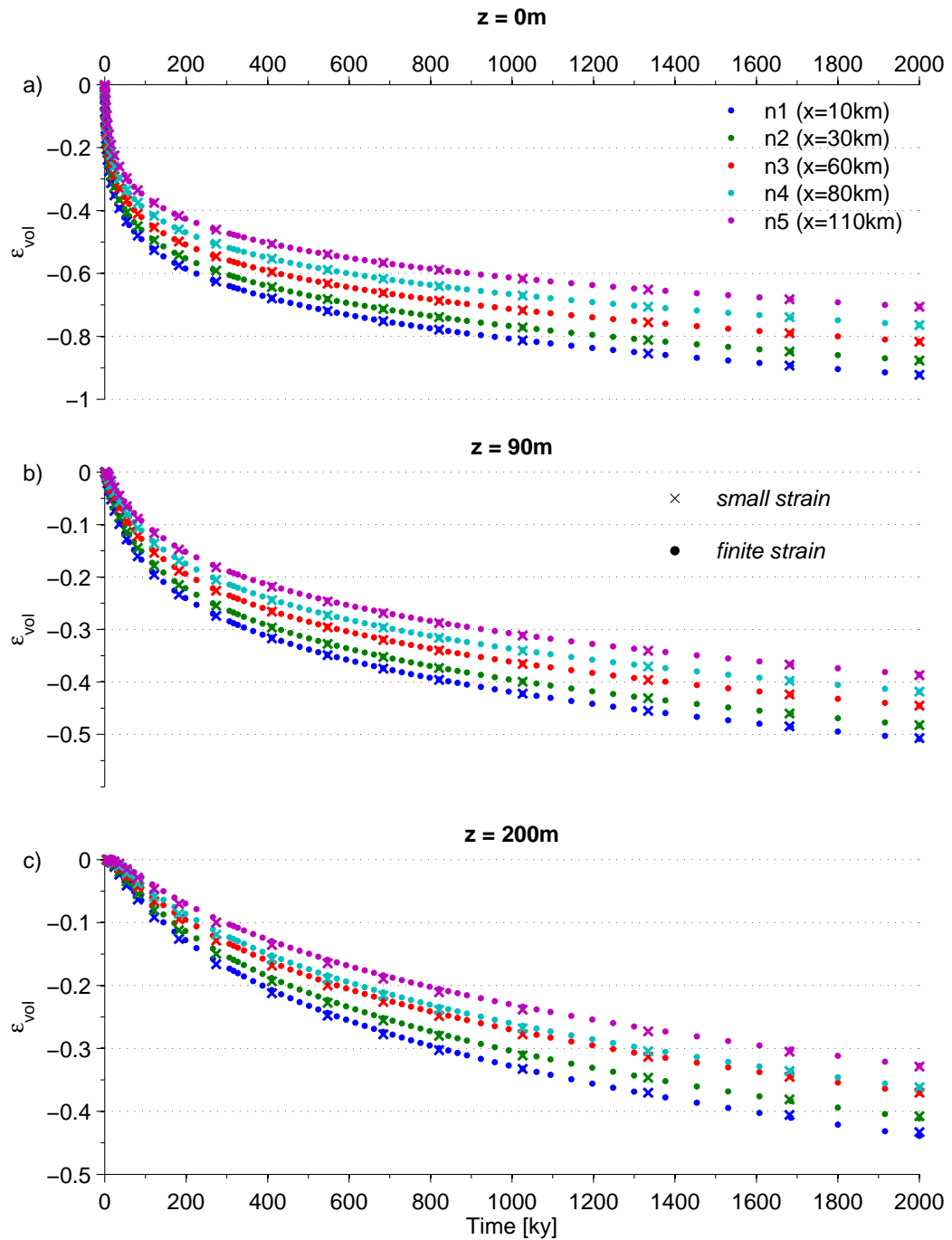


Figure 4.2: Total volumetric strain,  $\epsilon_{vol}$ , over model time for selected nodes at (a) the model surface, (b) 90 m below the model surface and (c) 200 m below the model surface. The same model is solved using small strain analysis (cross markers) as well as finite strain analysis (circular markers).

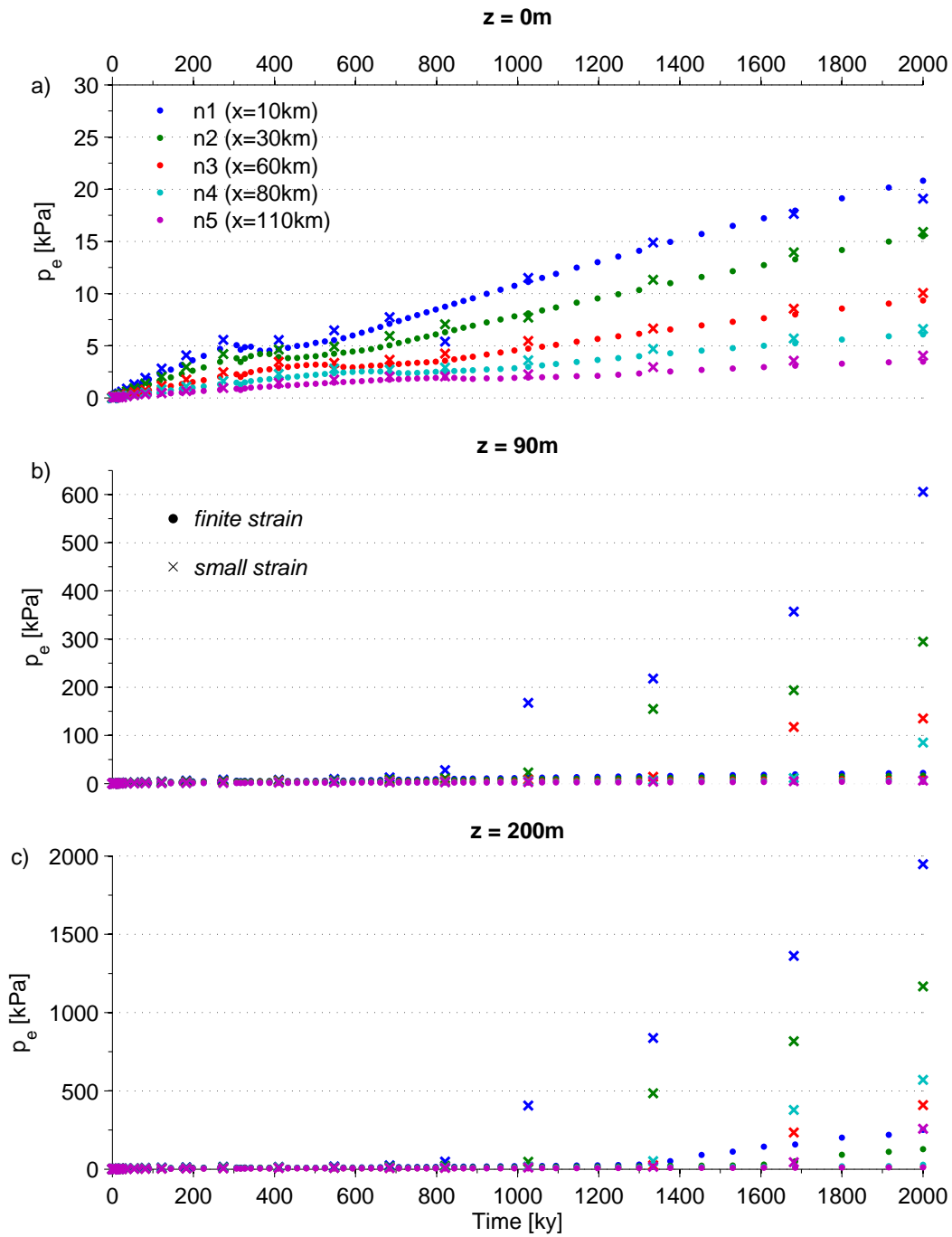


Figure 4.3: Excess pore pressure,  $p_e$ , over model time for selected nodes at (a) the model surface, (b) 90 m below the model surface and (c) 200 m below the model surface. The same model is solved using small strain analysis (cross markers) as well as finite strain analysis (circular markers).

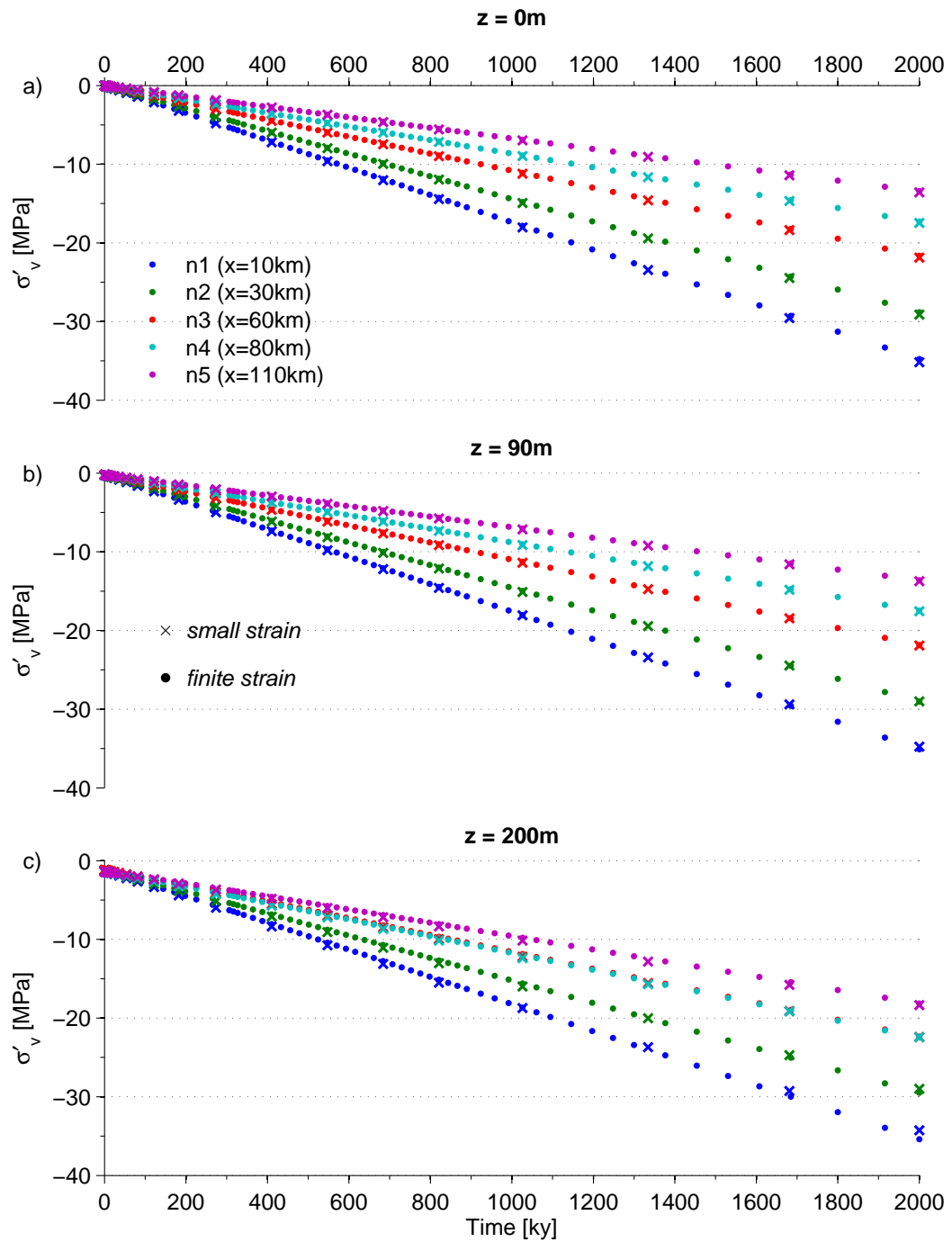


Figure 4.4: Vertical effective stress,  $\sigma'_v$ , over model time for selected nodes at (a) the model surface, (b) 90m below the model surface and (c) 200m below the model surface. The same model is solved using small strain analysis (cross markers) as well as finite strain analysis (circular markers).

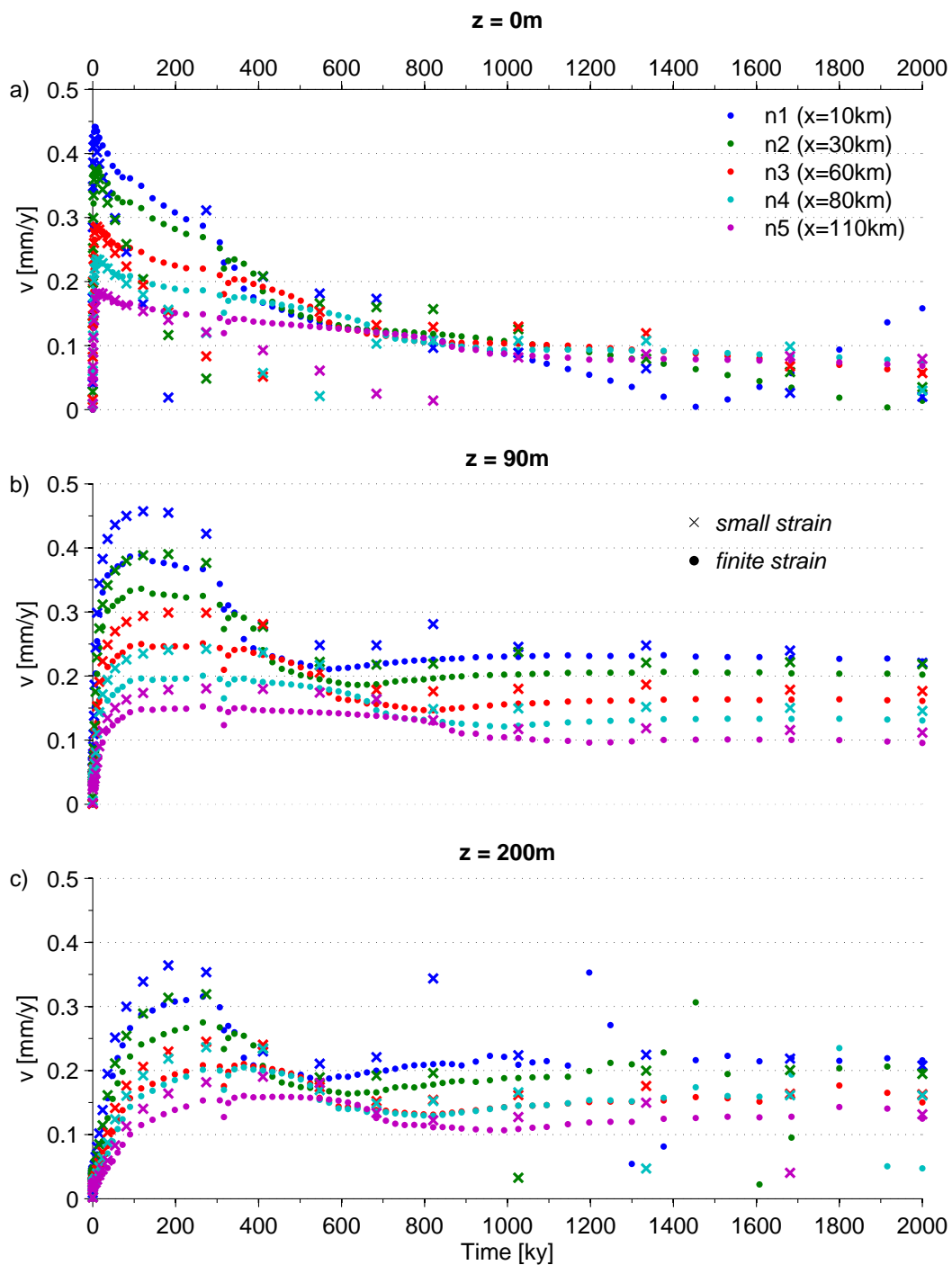


Figure 4.5: Total fluid flow velocity,  $v$ , over model time for selected nodes at (a) the model surface, (b) 90 m below the model surface and (c) 200 m below the model surface. The same model is solved using small strain analysis (cross markers) as well as finite strain analysis (circular markers).

### 4.3.1 Pore pressure kinks

The differences between excess pore pressure calculated by small and finite strain models for some selected nodes become very large after some time of loading, while deviations for other nodes remain near the suggested overall AWRMS difference (Fig. 4.6). These large differences can be attributed to a kink in the temporal evolution of excess pore pressure in the small strain consolidation analysis as described above, that is not seen in the finite strain solution. Accordingly, the AWRMS error estimate is only valid if none of the nodes in the specific area of interest has reached the kink in excess pore pressure.

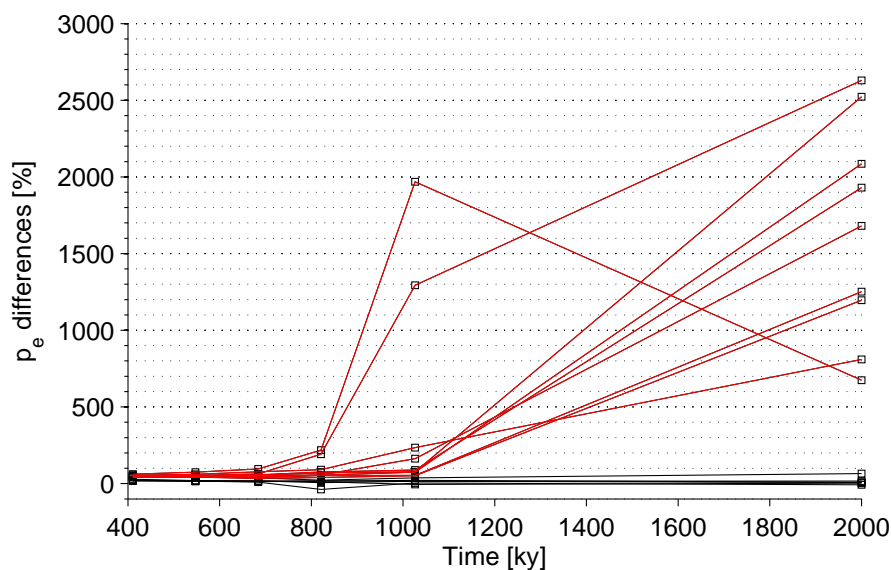


Figure 4.6: Relative differences between excess pore pressure calculated with small strain and finite strain analyses at selected nodes shown in Fig. 4.3. Red lines indicate nodes for which a kink in excess pore pressure of the small strain solution is observed in Fig. 4.3

For a closer examination of these excess pore pressure kinks, Fig. 4.7 shows excess pore pressure, void ratio and permeability for nodes along the model at depths of 90 m and 200 m, where the kinks are observed. Due to asymmetric exponential loading the rate of loading is highest at node n1, where the kink is observed first. As loading continues, nodes in areas with lower loading rates are also effected. In the finite strain solution, a pattern that may be interpreted as a pore pressure kink similar to what is observed earlier in the small strain analysis occurs in nodes n1 and n2 at  $z=200$  m, but at a much later stage. It is also less steep (Fig. 4.7a-c). It seems likely, that some stress related mechanism must be responsible for this sudden rapid pore pressure increase.

Void ratio,  $e$ , decreases with increasing effective stresses according to the exponential hardening constant,  $\lambda$ . Due to its exponential nature the void ratio decrease is most rapid at low effective stresses (Fig. 4.7b, e). It is notable that void ratios calculated

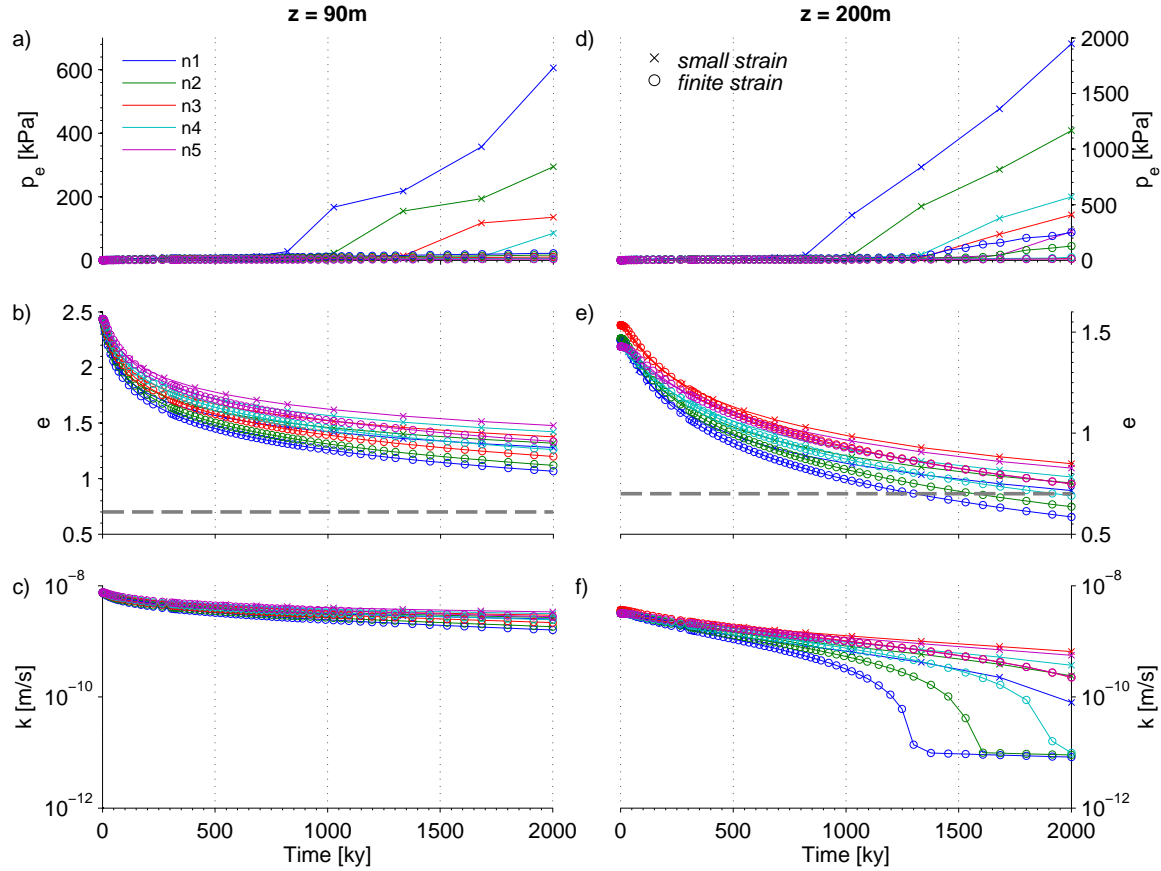


Figure 4.7: Excess pore pressure,  $p_e$ , void ratio,  $e$  and permeability,  $k$ , over time for selected nodes at different model depths at  $x=10$  km (a-c) and  $x=30$  km (d-f). Cross markers give the solutions of the small strain consolidation analysis and circular markers represent finite strain consolidation analysis solutions. Grey dashed lines in panels b) and f) indicate  $e = 0.7$ .

by small strain analysis are consistently higher than those calculated using finite strain analysis.

Void ratio controls permeability,  $k$ , through a linear void ratio-permeability relationship as shown in Fig. 4.1. Permeability declines until very low values are reached at  $e = 0.7$ . This threshold (marked in Fig. 4.7b and e by a grey dashed line) is overcome by some of the selected nodes in the finite strain analysis only, and is reflected clearly by a steep drop to low permeability (compare Fig. 4.7e and f). Crossing the void ratio threshold as well as the drop to low permeabilities both coincide with the kink in excess pore pressure (compare Fig. 4.7d-f). Furthermore, the rate at which permeability decreases is particularly high immediately before the pore pressure kink appears (Fig. 4.7f). The pore pressure kink may therefore be caused either by crossing a critical void ratio or by a fast rate of change of permeability ( $\frac{\delta k}{\delta t}$ ). Hence, continuous stress increase due to loading causes a continuous void ratio decrease, which in turn leads to a decrease in permeability. At certain pressures (depending on the void ratio - permeability relationship)

permeability becomes too low to effectively drain the excess pore fluid and pressures rise rapidly.

However, this mechanism cannot explain the occurrence of pore pressure kinks in the small strain solution, as void ratios and consequently permeability do not decline to as low values as in the finite strain solution. The rate of permeability decrease with time ( $\frac{\delta k}{\delta t}$ ) does not change significantly either. There is no obvious mechanical process that may explain the steep pore pressure kinks in the small strain analysis.

## 4.4 Discussion and recommendation

The aim of this exercise was to characterise and quantify the differences between using small strain and large strain analysis for simulating the consolidation process on a slope. Stresses and strains are nearly identical in small strain and finite strain analyses, differing by less than 6%. Small strain analysis continuously overestimates excess pore pressures at an average of about 35% over the entire model. Fluid flow velocity differences are about 20-25% of the total velocity but a general estimate of the difference cannot be made.

Although relative errors may be up to 40%, important patterns of stresses, strains, pore pressure and fluid flow are reliably simulated by small strain consolidation analysis. However, excess pore pressure errors much larger than 40% can appear in specific model areas at higher stresses. The onset of these differences is characterised by a sudden steep increase in excess pore pressure in small strain analysis, which cannot be explained by a mechanical process (such as a sudden drop in permeability) and which is not observed in finite strain analysis. If small strain analysis is to be used, it is therefore safer to monitor nodes in the area of interest, and discard any modelling results subsequent to the appearance of a kink in excess pore pressure.

It is evident that a finite strain consolidation analysis offers a potentially more accurate alternative to a small strain analysis (Gibson et al., 1981; Schiffman, 1982), especially with respect to excess pore pressure. However, the problems approached in this thesis relate to fundamental processes and mechanisms, and are investigated for a completely generic setting and parameter sets. Therefore, the exact prediction of pore pressure or fluid flow is not of such importance as it would be for studies related for example to the design of tailings impoundments. A disadvantage of finite strain consolidation analysis clearly is the disability to be run in parallel and the about four times higher computing time. The latter is important when large numbers of models have to be calculated for

example in sensitivity studies. Another disadvantage related to the FE software used in this thesis, is the software's inability to use a total pore pressure formulation in finite strain analyses.

Based on the results of the experiments in this section, it was considered that the solutions of small strain consolidation analyses can be used with confidence, if the excess pore pressure development at a series of nodes in the area of interest is monitored. If one of the nodes shows a kink in the excess pore pressure path the subsequent results shall be rejected and calculations repeated using finite strain analysis. In addition, the possibility that excess pore pressures are overestimated by about 30 % and that fluid flow velocity can have errors of about 25 % will be taken into account.

## Chapter 5

# How do $\sim 2^\circ$ slopes fail in areas of slow sedimentation? A sensitivity study on the influence of accumulation rate and permeability on submarine slope stability <sup>1</sup>

### Abstract

Overpressure generation due to rapid sediment deposition can result in low effective stresses within the sediment column. It has been proposed that these large overpressures are the main preconditioning factor for causing large-scale submarine slope failure on passive continental margins, such as those in the Gulf of Mexico and offshore Norway. The rate of overpressure generation depends on the sedimentation rate, sediment compressibility and permeability. The Gulf of Mexico and the Norwegian continental slope have experienced comparatively high sediment input, but large-scale slope failure also occurs in locations with very low sedimentation rates such as the Northwest African continental margin. Here we show results from 2D numerical modelling of a  $2^\circ$  continental slope subjected to deposition rates of 0.15 m/ka. These results do not indicate any evidence for significant overpressure or slope instability. We conclude that factors other than overpressure must be fundamental for initiating slope failure, at least in locations with slow sedimentation rates.

---

<sup>1</sup>This chapter has been published as **Urlaub**, M., Zervos, A., Talling, P.J., Masson, D.G., and Clayton, C.I. (2012). How do  $\sim 2^\circ$  slopes fail in areas of slow sedimentation? A sensitivity study on the influence of accumulation rate and permeability on submarine slope stability. In Yamada, Y., Kawamura, K., Ikehara, K., Ogawa, Y., Urgeles, R., Mosher, D., Chaytor, J., and Strasser, M., editors, *Submarine Mass Movements and Their Consequences*, volume 31 of *Advances in Natural and Technological Hazards Research*, pages 277-287. Springer Netherlands.

## 5.1 Introduction

Submarine landslides that occur on the open slopes of passive continental margins represent the largest submarine mass flows on our planet. Perhaps the most remarkable feature of huge continental slope failures is that they occur in locations worldwide on gradients of just  $\sim 2^\circ$ . Such low gradient slopes are almost always stable on land. We are yet to monitor one of these huge underwater landslides in action, and the reason(s) for such large-scale failure on such low gradients are contentious.

IODP Leg 308 drilling in the Gulf of Mexico recently confirmed that high excess pore pressures can be generated in areas of rapid sediment accumulation (Flemings et al., 2008). Low permeability prevents sufficiently rapid dewatering and excess pore pressures are produced that are up to 70 % of the lithostatic weight. Numerical models using these IODP results suggest that a combination of rapid (up to 30 m/ka) sediment deposition caused by Mississippi River discharge and lateral fluid flow can generate slope failures (Flemings et al., 2008; Stigall and Dugan, 2010). Similarly high sedimentation rates are likely to occur offshore from many major rivers and thereby cause large-scale slope failures. Sediment deposition at the margins of ice streams can also be very rapid and lead to excess pore pressures. Sedimentation rates of up to 36 m/ka occurred near the Storegga Slide headwall at the end of the last glaciation (Leynaud et al., 2007), although eventual failure of the Storegga Slide occurred  $\sim 7$  ka after this peak sedimentation.

It might therefore be proposed that rapid sediment accumulation generating high excess pore fluid pressures are a major reason for large-scale continental slope failure on low ( $\sim 2^\circ$ ) gradients. However, large-scale slope failures also occur on continental margins with much slower sediment accumulation rates, such as off the coast of Northwest Africa south of  $26^\circ$  N (Wynn et al., 2000). Deposition rates in this area do not exceed 0.15 m/ka, measured over the last 3.6 Ma (Ruddiman et al., 1988). Landslides in this area have a similar bedding-parallel slab-like morphology to failures like those in the Gulf of Mexico and the Storegga Slide (Haffidason et al., 2005; Twichell et al., 2009; Krastel et al., 2012), suggesting a common failure mechanism. Failure of the NW African slope has been attributed to overpressure (e.g. Antobreh and Krastel, 2007) but a detailed analysis of how such overpressure might build up was not undertaken. Some key information and relationships of the three considered continental margins is given in Figure 5.1.

### 5.1.1 Aims

Here we undertake a sensitivity analysis of how sediment accumulation rate and permeability influence the stability of low-angle continental slopes, starting with a one-dimensional column followed by a two-dimensional slope profile. The models are meant

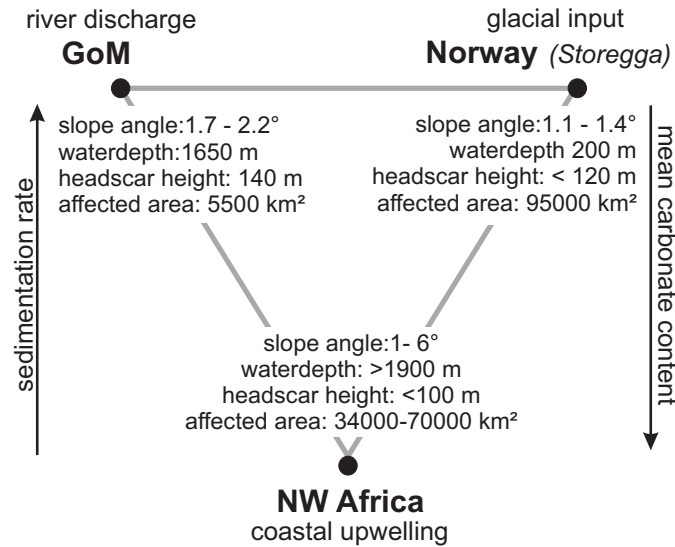


Figure 5.1: Landslide characteristics (mean values) and important aspects of the three continental margins discussed in this study (GoM = Gulf of Mexico).

to be generic and broadly representative of the NW African type of continental margin. Our aims are to identify the situations in which particularly high excess pore fluid pressures might be generated, and whether slow sedimentation rates can produce high excess pore pressures that bring a slope close to failure, for reasonable values of sediment permeability. If we are unable to initiate slope failure through build up of high excess pore fluid pressures in this way, then slope failure in low sedimentation rate settings is more likely due to other factors such as internal sediment structures.

### 5.1.2 Proto-type Field Location - NW African Margin south of 26° N

The NW African continental margin is relatively uniform over long distances and is disrupted only by widely-spaced canyons. Pelagic and hemipelagic background sedimentation is dominant and originates from a continuous upwelling cell that produces large quantities of biologic material and is located at the upper slope (Sarnthein et al., 1982). Sediment cores recover thick sequences of fine-grained carbonate rich marls and oozes consisting mainly of planktonic shell fragments and terrigenous dust (e.g. Henrich et al., 2008). Sediment accumulation decreases offshore, with rates of up to 0.15 m/ka at the upper slope, and 0.01 m/ka at the mid and lower slope (Ruddiman et al., 1988; Henrich et al., 2008).

## 5.2 Methodology

### 5.2.1 Gibson's (1958) Approach to One-Dimensional Consolidation

Gibson's (1958) theory of 1D (vertical column) consolidation under constant deposition is a simple approach to estimate overpressure within a continuously growing clay layer. Key variables are sedimentation rate, time, Darcy's permeability  $k$  [m/s], stiffness  $E$  [kPa] and the unit weight of the pore fluid  $\gamma_w$  [kPa]. We solve Gibson's theory for sedimentation rate/permeability pairs that result in an overpressure ratio  $u^* = 0.7$  in a generic, very soft marine clay.  $u^*$  [ ] is the excess pore water pressure at the base of the sediment column normalised to effective stress due to overburden (submerged weight of the overlying sediment).  $\gamma_w$  is  $10.24 \text{ kN/m}^3$  and a stiffness  $E$  of  $480 \text{ kPa}$  is assumed, which represents the lower limit for very soft clay suggested by USACE EM 1110-1-1904.

### 5.2.2 Finite Element Modelling of Two-Dimensional Slopes

A 2D plane strain nonlinear elastoplastic coupled pore pressure-deformation model was developed using the finite element (FE) software package ABAQUS. We use the Modified Cam Clay model (Roscoe and Burland, 1968) with isotropic nonlinear elasticity and constant Poisson's ratio  $\nu$ . The slope of the critical state line  $M$  [ ] is a constant and is calculated from the friction angle  $\phi'_{crit}$  [°] by

$$M = \frac{\sin\phi'_{crit} \cdot 6 \cdot \sqrt{1 - b + b^2}}{3 + \sin\phi'_{crit} \cdot 2b - \sin\phi'_{crit}} \quad (5.1)$$

where  $b = 0.5$  for plane strain conditions (Potts and Zdravkovic, 2001). Strain hardening is exponential. Void ratio changes due to effective stress changes are controlled by the logarithmic bulk modulus (or compression index)  $\lambda$  [ ]. The sediment is cohesionless and its coefficient of earth pressure  $K_0$  [ ] equals  $1 - \sin\phi'_{crit}$ . Table 5.1 lists the constants that define the constitutive model consistent with a calcareous marine clay as typically found off NW Africa.

A simplified continental margin geometry is adopted based on the morphology of the NW African margin and is shown in Figure 5.2. The entire continental margin is modelled as one layer without abrupt material changes and only vertical (not lateral) density and permeability gradients. The model domain is partitioned into region 1, which comprises the upper 500 m of the seafloor and region 2, which covers the deeper part. The mesh consists of 76,050 rectangular plane strain elements and 238,347 nodes (compare Figure 5.4a). Elements have a size of  $10 \times 10 \text{ m}$  at the seafloor, whilst a coarser mesh size ( $100 \times 100 \text{ m}$ ) was adopted at 500 m below the seafloor as changes in mechanical properties are less pronounced at these deeper levels (Hamilton, 1976; Karig and Hou, 1992). Element sizes further increase towards the model's bottom as well as towards side

Notation		Value	Reference
$\kappa$	Swelling index	0.027	Valent et al. (1982); Demars (1982)
$\nu$	Poisson ratio	0.3	Karig and Hou (1992)
$\lambda$	Compression index	0.28	Valent et al. (1982); Demars (1982)
$\phi'_{crit}$ [°]	Friction angle	28	Valent et al. (1982)
$M$	Slope of critical state line	0.87	eq. 5.1, $b = 0.5$ , Potts and Zdravkovic (2001)
$\gamma_w$ [kN/m <sup>3</sup> ]	Specific fluid weight	10.24	
$g$ [m/s <sup>2</sup> ]	Gravity	9.81	

Table 5.1: Spatially and temporarily constant input parameters used in the Modified Cam Clay constitutive model.

boundaries at the shelf and the foot of the slope.

Boundary conditions are given in Figure 5.2. Sedimentation is simulated by progressively adding a vertical surface load that decreases from the shelf edge towards the abyssal plain. At the shelf the rate is uniform. The exponential rate of decrease ( $e^{-0.032x}$ , where  $x$  [km] is the distance from the shelf edge) is based upon thinning rates of seismic sequences in (Antobreh and Krastel, 2007). A unit weight,  $\gamma=12$  kN/m<sup>3</sup> was assumed for the newly deposited fully saturated sediment corresponding to a dry density of 670 kg/m<sup>3</sup>. The peak sedimentation rate at the shelf edge is 0.15 m/ka.

### 5.2.2.1 Initial conditions

Seafloor sediments are considered normally consolidated and have an initial void ratio of 3.0 (75 % volume porosity). Sediment porosity  $\phi$  and void ratio  $e$  are related by  $\phi = \frac{e}{1+e}$ . In the interval 0 to 500 m below the seafloor (region 1)  $\phi$  is defined by

$$\phi = 0.75 \cdot 0.987z + 0.83z^2 \quad (5.2)$$

where  $z$  [km] is the depth below the seafloor after Hamilton (1976) for calcareous sediments. In region 2 porosity decreases linearly from 40 % at 500 m below the seafloor, to 10 % at 5000 m below the seafloor (Velde, 1996).

Permeability depends linearly on void ratio and is anisotropic, as measured for pelagic clay (Kawamura and Ogawa, 2004). The horizontal sediment permeability  $k_x$  at the seafloor before burial (where  $e=3.0$ ), is  $10^{-8}$  m/s based on oedometer measurements of calcareous sediments compiled by Demars (1982). Yang and Aplin (2010) found vertical

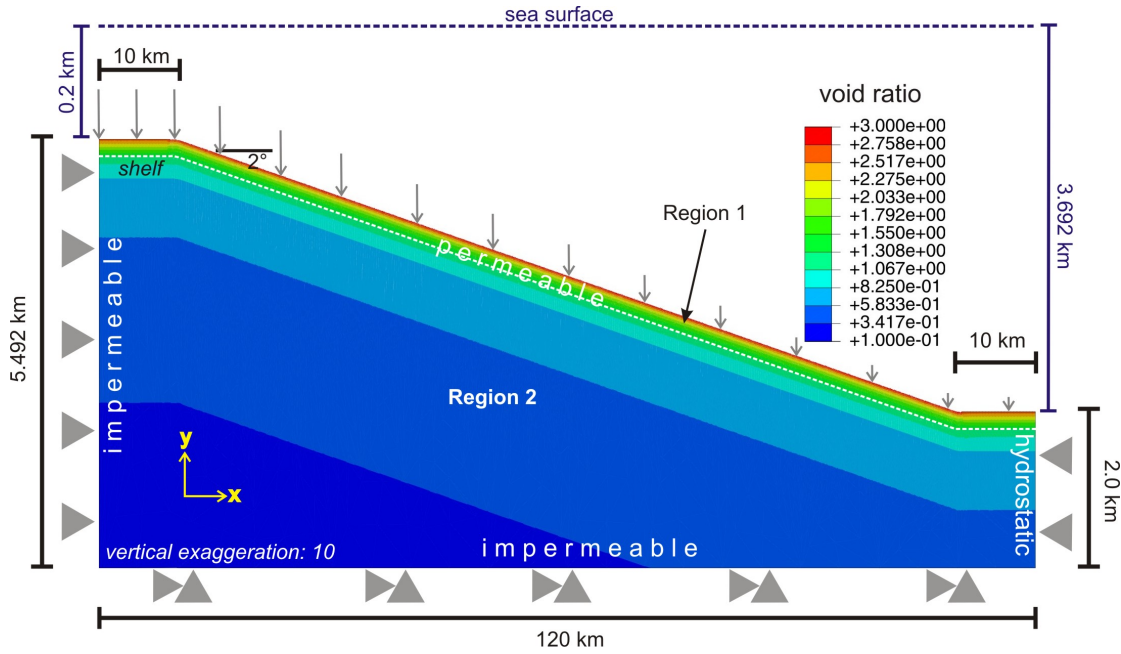


Figure 5.2: 2D slope model geometry (not to scale) with boundary and loading conditions. Pore pressure at the right boundary is hydrostatic so that flow into or out of the model is allowed. As deposited sediment is simulated as a surface load at the seafloor, the flow normal to the surface is governed by the pore pressure gradient and the vertical permeability. The seafloor is free to move in any direction whereas the side boundaries are fixed in the  $x$  direction and the bottom is fixed in both directions. The water column is represented as a hydrostatic pressure load on the seafloor, such that there is zero effective stress at the seafloor. Sedimentation decreases from the shelf edge towards the abyssal plain (grey vertical arrows). Colours represent the initial void ratio on which permeability and density depend linearly.

permeability  $k_y$  as low as  $10^{-13}$  m/s for mudstones with 40% porosity, which we use as the lower limit for vertical permeability variations. Below 500 m (region 2)  $k$  is isotropic and constant ( $k = 10^{-13}$  m/s). In our models we keep the permeability at the seafloor constant and varied  $k$  at 500 m as well as the anisotropy coefficient in order to explore model sensitivity.  $k_y$  can be up to one order of magnitude smaller than  $k_x$ . Sediment at the seafloor has a dry density of  $670 \text{ kg/m}^3$  ( $\gamma=12 \text{ kN/m}^3$ ) that increases linearly to  $1400 \text{ kg/m}^3$  at 500 m depth ( $\gamma=20 \text{ kN/m}^3$ ). Sediment more than 500 m below the seafloor has constant density of  $2400 \text{ kg/m}^3$  ( $\gamma=26 \text{ kN/m}^3$ ).

### 5.2.2.2 Key Assumptions

The continental margin is simulated as one layer (no abrupt property changes) to investigate whether failure could occur without the need for weak layers or glide planes. This effectively assumes spatially uniform deposition of the same material in space and time. Geotechnical properties have not been measured on deep sediments off NW Africa. Those properties used in this model are thus based on a literature review for calcareous

pelagic and hemipelagic sediments measured elsewhere (Hamilton, 1976; Velde, 1996; Yang and Aplin, 2010, and references in Table 5.1). The FE model is comparatively simple; it does not include geometric nonlinearity and the deposited sediment is simulated by a surface load. The latter is important because it means that the added sediment is not a source of fluid, and possible failure within the additional sediment thickness cannot be modelled. However, this model serves to explore the general relationships between sediment accumulation rates and permeability in a continental slope with a geometry broadly similar to that of the NW African margin, Gulf of Mexico or Norwegian margin.

## 5.3 Results

### 5.3.1 One-Dimensional Consolidation

High sedimentation rates for prolonged periods of time, and low permeability and stiffness, tend to result in high overpressure. Our 1D modelling indicates that a significant overpressure ratio of  $u^* = 0.7$  does indeed build up in settings with rapid sediment accumulation, such as the Gulf of Mexico (after sedimentation periods of about 50 ka) and the Norwegian continental slope after 10 ka (Figure 5.3 Leynaud et al., 2007; Flemings et al., 2008). When sedimentation is  $\sim 500$  times slower (0.15 m/ka) as in the case of the NW African margin, the permeability must be lower than  $10^{-12}$  m/s and continuous sedimentation must go on for long periods ( $> 1.5$  Ma) to generate significant overpressure ratio. Such low values of permeability have been measured perpendicular to bedding for mudstones with clay content  $> 50\%$  and porosities  $< 30\%$  (Yang and Aplin, 2010). However, the average clay content of sediment at the NW African margin is about 25% and the porosity at 300 m depth below seafloor is 50% (Ruddiman et al., 1988). The occurrence of permeabilities  $< 10^{-12}$  m/s in a sediment as found off NW Africa is thus unlikely, but cannot be fully excluded as clay mineral accumulation may peak locally. Due to sparse data coverage, especially at greater depths, this is not well constrained and requires further investigation. With a higher but more realistic permeability of  $10^{-9}$  m/s (Demars, 1982), the overpressure ratio is negligible and the slope is not close to failure.

### 5.3.2 Two-Dimensional Consolidation

Several numerical experiments with different vertical permeability gradients and anisotropy ratios were run for 1 Ma. Slope stability is evaluated by analysing vertical effective stresses,  $\sigma'_v$ , overpressure ratios,  $u^*$ , and Factors of Safety (FoS, ratio of the critical state friction angle to the mobilised friction angle). In summary, all models are stable. All simulations show an expected increase in vertical effective stress and pore pressure due to the overburden. Fluid flow patterns vary within the different models and lateral flow

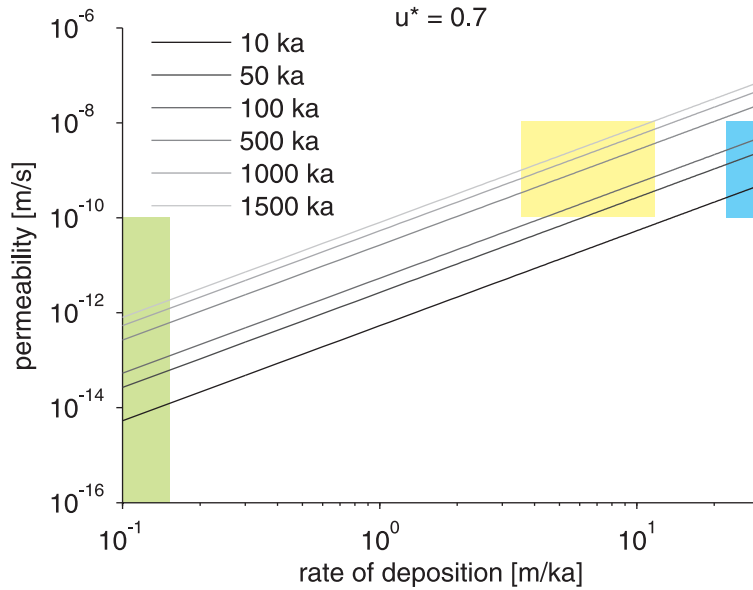


Figure 5.3: Log-log plot of combinations of permeability and sedimentation rate that result in an overpressure ratio  $u^*=0.7$  at the base of a consolidating layer for time periods of 10 ka to 1.5 Ma. Calculations are based on (Gibson, 1958). All parameters are assumed constant and the bottom boundary is impermeable. Shaded backgrounds highlight typical sedimentation rate ranges off Northwest Africa (green) as well as sedimentation rate and permeability ranges at continental margins in the Gulf of Mexico (yellow) and off Norway (blue). A stiffness of 480 kPa is used throughout the calculations.

is observed in the models with permeability anisotropy but does not generate significant overpressure ratios at the lower slope. Where permeability is isotropic, fluid flow is purely vertical.

To give an example, Figure 5.4 shows the model with lowest permeability ( $k_x$  decreasing from  $10^{-8}$  to  $10^{-12}$  m/s at 500 m depth,  $k_x/k_y = 10$ ) and a sedimentation rate of 0.15 m/ka at the shelf. The  $\sigma'_v$  contour lines are not parallel to the slope; with higher values at the shelf and lower values towards the foot of the slope (Figure 5.4a). This is due to asymmetric loading.  $\sigma'_v$  does not show any abnormal pattern and is nowhere near zero.

The maximum overpressure ratio  $u^*$  is 0.074 near the shelf edge and at a sub-seafloor depth of about 1500 m (Figure 5.4b). However, in the top 500 m  $u^*$  is significantly lower. Fluid flow has a small component towards the foot of slope but is predominantly vertical (as shown by black vectors in Figure 5.4b). The FoS is as low as 1.2 below the shelf edge, coinciding with a high overpressure ratio, and at the abyssal plain (Figure 5.4c). The FoS contour lines along the slope converge towards the lower slope indicating that the lower slope is less stable than the upper slope. Nevertheless, FoS is  $>1$  everywhere in the model and so no failure mechanism could be identified.

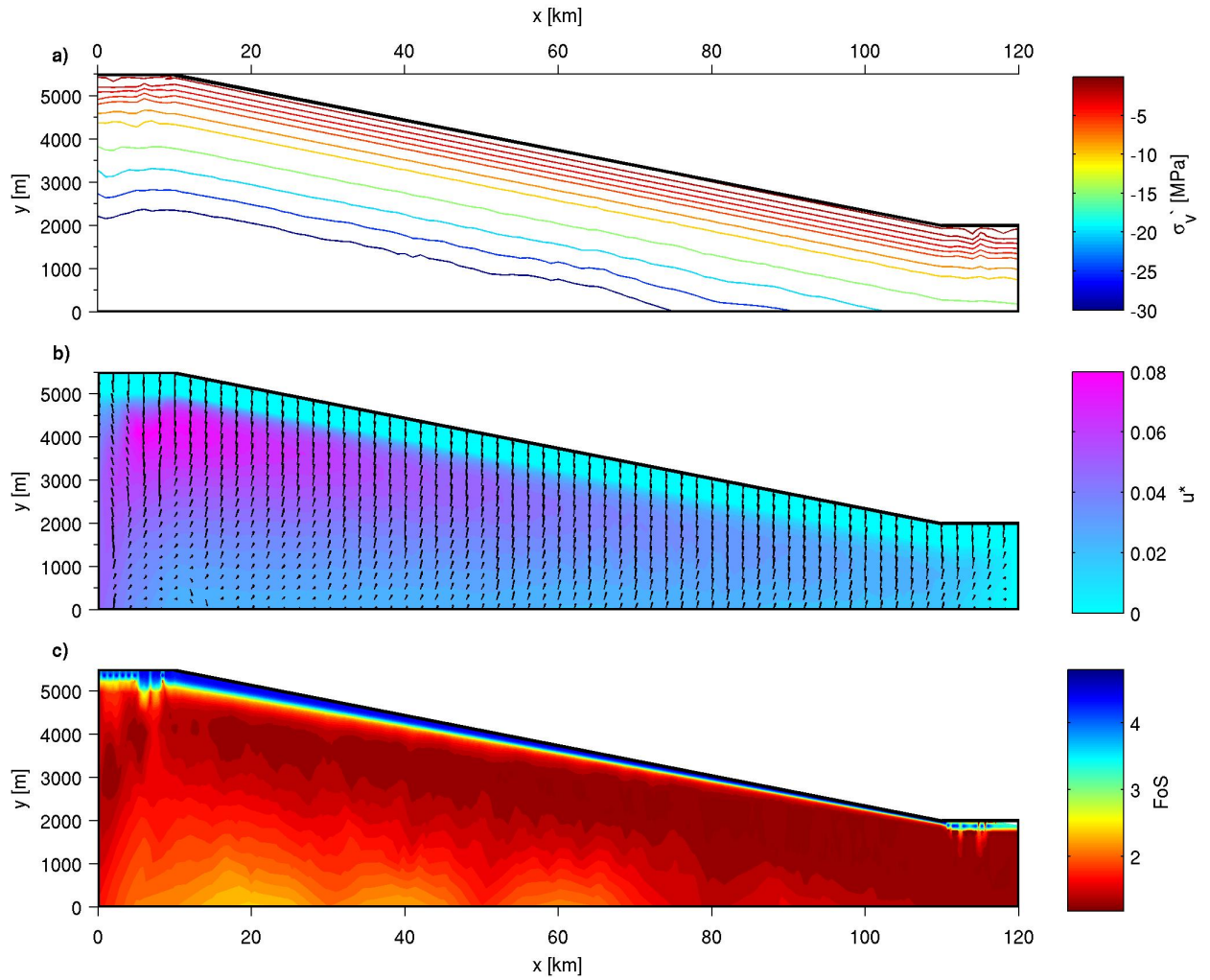


Figure 5.4: 2D FE solution for (a) vertical effective stress  $\sigma'_v$ , (b) overpressure ratio  $u^*$  with flow velocity vectors normalised to their absolute magnitude, and (c) Factor of Safety calculated at each node after continuous loading with 0.15 m/ka for a period of 1 Ma. Vertical exaggeration is 5.

## 5.4 Discussion

Previous 1D and 2D slope modelling suggests that rapid (peaking at  $\sim 30$  m/ka) and prolonged (several ka) sediment deposition from river discharges or ice streams can generate sufficiently high over-consolidation ratios ( $u^* > 0.7$ ) to make a continental slope unstable (Leynaud et al., 2007; Flemings et al., 2008). However, our modelling suggests that such large pressurisation ratios are not generated in locations such as the NW African margin where sedimentation rates are much lower (0.01 to 0.15 m/ka), for reasonable values of initial permeability and changes of permeability with depth.

Our work therefore suggests that large-scale failures of slope made of homogeneous low-permeability sediment are in at least some cases not generated by rapid sediment loading alone (perhaps with lateral fluid flow to the toe of slope). It appears that layers of anomalously low permeability that prevent fluid migration, or high permeability layers that allow more rapid lateral fluid flow would be needed. Alternatively, weak layers must be present, all of which are not included in our modelling.

If weak layers are needed for low angle slope failure in areas of slow sedimentation, what are those weak layers? It has been suggested that dissociation of gas hydrates could produce weak layers in a number of ways including rapid removal of cement to leave sediment under-consolidated, formation of voids (gas bubbles) and fractures, and freshening of pore fluids leading to quick clay behaviour (e.g. Bull et al., 2009). All three margins considered here show evidence for gas hydrate occurrence (Sager et al., 1999; Bouriak et al., 2000; Davies and Clarke, 2010). However, slide headscars in the Gulf of Mexico and off NW Africa are located at water depths well below the gas hydrate stability zone (Wynn et al., 2000; Twichell et al., 2009). Shifts of the upper end of the gas hydrate stability zone therefore are unlikely to affect sediments near the headscars. We therefore conclude that gas hydrates as a trigger can be excluded. It appears that some other mechanism is capable of producing weak layers in locations offshore NW Africa, and potentially also in other locations where sedimentation rates are greater.

### **Acknowledgements**

Sebastian Krastel kindly provided reflection seismic lines offshore NW Africa. Brandon Dugan, Peter Flemings and Derek Sawyer are thanked for their encouragement to address these problems. We also thank the reviewers C. Berndt and A. Kopf for their constructive reviews.

## Chapter 6

# The role of sedimentation rate on continental slope stability: Implications for slope failure mechanisms at continental slopes with low sediment input

### 6.1 Introduction

Submarine landslides at open continental slopes are the largest mass flows on Earth and can be up to two orders of magnitude larger than the largest landslides on land (Korup et al., 2007). The Storegga Slide involved more than 3,000 km<sup>3</sup> of sediment and affected an area similar to that of Scotland (Hafliðason et al., 2004). Submarine landslides play an important role in the Earth's sedimentary budget and are important in shaping continental margins, as they transport large amounts of sediment from the continental shelf and slope into the deep ocean (Masson et al., 2006). While nearly all large landslides on land occur on the steepest parts of the Earth's land surface (Korup et al., 2007), submarine landslides are not restricted to areas of steep slopes. Remarkably, the largest slides occur on continental slopes with gradients of 2° or less (Fig. 6.1, Hühnerbach et al., 2004), and these often have very long run outs of several hundreds of kilometres. At these low gradients, slopes on land are almost always stable.

Submarine landslides pose a geohazard to society as they can cause damaging tsunamis. For example, the Storegga Slide off Norway dated at 8,200 years BP produced a tsunami that locally ran up for 20 m around the North Sea coasts (Bondevik et al., 2005a). More recently, a slump off Papua New Guinea triggered a tsunami that killed 2,200 people in 1998 (Tappin et al., 2001). The landslides themselves can damage telecommunication cables or seafloor infrastructure, such as that used for hydrocarbon exploration. They may also generate longer run-out sediment flows called turbidity currents that break cables, as occurred offshore from the Grand Banks, Canada, in 1929 (Piper and Aksu, 1987).

Submarine mass movements occur at active and passive continental margins, glaciated margins, volcanic island flanks, submarine canyon walls, in fjords and river fan systems (Masson et al., 2006). However, this study focuses on open continental slopes at passive margins, because they accommodate some of the largest submarine landslides, that occurred on slope angles  $< 2^\circ$ . Almost all passive continental margins are affected by submarine landslides, irrespective of depositional environment, tectonic activity or sedimentation rates (Hühnerbach et al., 2004). Some of the largest landslides occur on passive continental margins away from major sediment input by rivers or ice streams. Examples include landslides on the north-west African continental margin (Wynn et al., 2000), the US east coast (Twichell et al., 2009), the south-east Australian margin (Boyd et al., 2010), and the south-east Brazilian continental slope (Kowsmann et al., 2002). This is surprising, as conventional slope stability concepts predict slopes with higher rates of sediment loading to be less stable (e.g. Duncan and Wright, 2005).

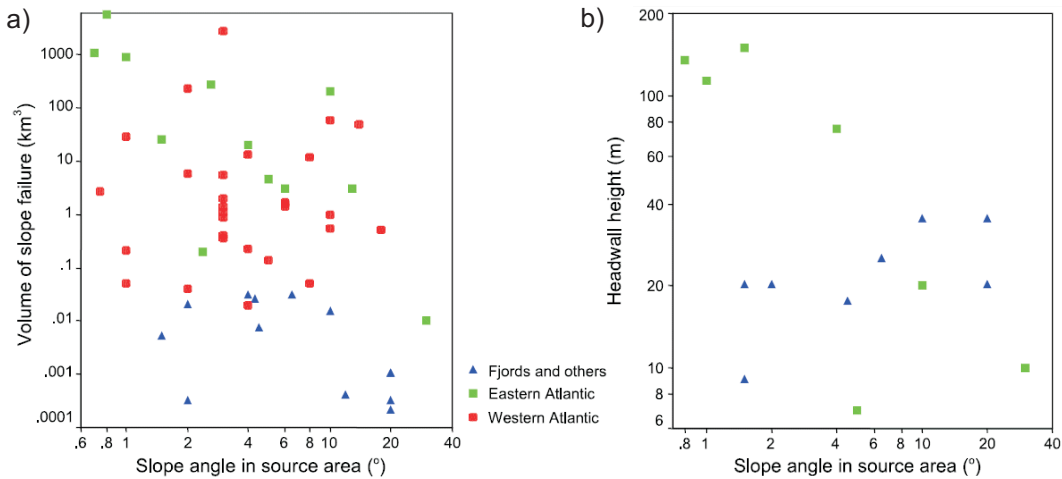


Figure 6.1: Log-log plots of a) landslide volume and b) headwall height against slope angle for submarine landslides in the North Atlantic and adjacent seas (modified after Hühnerbach et al. (2004)).

Seabed and sub-seafloor geophysical imaging provides a clear picture of the morphology produced by seafloor failure. Large landslides at open continental slopes often produce similar morphologies (Masson et al., 2010). Failure is usually translational and occurs along a bedding plane parallel surface. This plane lies between sub-seafloor depths of several 10 m to several 100 m, and in most cases it occurs at about 100 m below the pre-landslide seafloor (Fig. 6.1). Extensive lateral continuity of bedding type and sediment composition are typical characteristics of many passive continental margins. Once initiated, failure can spread far without hitting obstacles, which could explain the large dimensions of submarine landslides (Masson et al., 2010). Most of these large landslides originate at the middle and lower slope in water depths of 1,500 to 2,500 m (Hühnerbach et al., 2004; Twichell et al., 2009).

### 6.1.1 What triggers large submarine landslides on nearly flat slopes?

Due to their potential as a geohazard it is important to understand what causes large submarine landslides, to be able to understand where and when future landslides might occur. Numerous hypotheses have been put forward to suggest mechanisms that could have the capability of triggering failure of nearly flat slopes, including earthquakes, gas hydrate dissociation or the presence of weak layers. However, the reason(s) for large scale failure of low angle submarine slopes are contentious and their understanding is complicated by the lack of direct observations and in situ monitoring. This lack of consensus over landslide triggers makes risk assessment more difficult than for other geohazards.

The morphological similarity of many large landslides suggests a similar failure mechanism, and possibly also similar geotechnical and rheological properties of the failed material (Locat and Lee, 2002). The failure of slopes with inclination of  $< 2^\circ$  is difficult to explain, as this is well below typical friction angles for any type of soil. Mechanically, the most plausible way to overcome the sediment's shearing resistance and to cause failure at such low slope angles is by high pore pressures (or overpressures) that greatly exceed the hydrostatic pressure. High pore pressures can also be an explanation for extremely long run-outs on nearly flat seafloor (e.g. Elverhøi et al., 2000).

Overpressure has been documented in a number of sedimentary basins and at continental slopes worldwide (e.g. Osborne and Swarbrick, 1997; Flemings et al., 2008). Recent studies have identified a number of processes that effectively generate high pore pressures in marine sediments over long time scales. These include:

- Loading of continental slopes by sedimentation can cause excess pore pressures. Excess pore fluid cannot dissipate quickly enough due to long drainage paths, low permeability and stiffness of the sediment (e.g. Gibson, 1958; Leynaud et al., 2007).
- Consolidation properties of marine sediments favour the generation and retention of excess pore pressures (Binh et al., 2009; Schneider et al., 2009; Long et al., 2011). Fine grained deep sea sediments typically show a very rapid porosity decrease with burial (e.g. Hamilton, 1976; Long et al., 2011), causing rapid volume change, along with low permeability ( $< 10^{-9}$  m/s, e.g. Bryant et al., 1981), preventing drainage of excess pore fluid.
- Lateral pore fluid flow and pressure redistribution due to lateral pore pressure gradients can generate excess pore pressures in areas that are otherwise unaffected by overpressure generating mechanisms (Yardley and Swarbrick, 2000; Flemings et al.,

2002). At a continental slope, this can be due to rapid asymmetric deposition, with rate usually increasing towards the shoreline. Pore fluid flows laterally towards the lower slope, where the resulting excess pore pressure effectively decreases the sediment's shearing resistance and potentially causes instability (Dugan and Flemings, 2000; Flemings et al., 2002).

Modelling has shown that excess pore pressures generated by rapid (peaking at  $\sim 30$  m/ky) and prolonged (several kiloyears) deposition or lateral fluid flow can cause failure of low angle continental slopes (Dugan and Flemings, 2000; Leynaud et al., 2007; Stigall and Dugan, 2010). These modelling efforts are, however, limited to open continental slopes with relatively high sediment input, such as the Norwegian continental margin or the Gulf of Mexico. Simple 1D modelling predicts that the generation of excess pore pressure is small when sedimentation rates are low (Gibson, 1958; Urlaub et al., 2012). Detailed modelling of excess pore pressure generation when the deposition is slow has not yet been undertaken, although some of the largest submarine landslides have occurred at continental margins with low sedimentation rates (Wynn et al., 2000; Twichell et al., 2009; Krastel et al., 2012). It is as yet unknown whether slow sediment deposition alone can cause submarine slope failure, or if an additional factor such as the presence of a weak layer is necessary.

### **6.1.2 Aims**

This study therefore aims to investigate whether sedimentation alone can cause failure of continental slopes with low sediment input. Two possible mechanisms are taken into account that could cause failure. The first mechanism is failure due to retention of high levels of excess pore pressure in the sediment. The main factors controlling the generation of excess pore pressure are the permeability and compressibility of the sediment, and the length of the drainage path (which is directly related to sedimentation rate). Can the mechanical properties of the sediment preserve excess pore pressures effectively enough to make up for a comparatively short drainage path associated with slow deposition? What properties are critical? The second mechanism is failure due to lateral transfer of pore fluid into areas of low overburden. Is the lateral pressure transfer high enough to significantly decrease effective stresses and cause instability away from the depositional centre? Ultimately, if sedimentation as the only pressure source is not sufficient to cause failure, what other processes that act on a global scale may contribute to the overpressurisation and failure of continental slopes?

### 6.1.3 Approach

I use the Finite Element (FE) Method to simulate consolidation of a typical continental 2° slope from shelf to abyssal plain. Consolidation occurs as a result of self weight and a continuous, spatially varying load (Fig. 6.2). First, the results for a homogeneous model with average consolidation properties subjected to rapid ( $\sim 15$  m/ky) as well as to slow deposition ( $\sim 0.15$  m/ky) are compared. As expected, rapid deposition causes failure due to high excess pore pressures, while the model with slow deposition is stable. I then analyse the sensitivity of overpressure generation to various consolidation properties, such as compressibility and permeability. In a second set of numerical experiments, scenarios that favour lateral transfer of pore fluid, for example in a layer of high permeability, are modelled.

Numerical methods have been used previously to address consolidation effects and submarine slope stability (Dugan and Flemings, 2000, 2002; Binh et al., 2009; Hustoft et al., 2009; Stigall and Dugan, 2010). These previous models are capable of simulating 2D fluid flow, but are limited to 1D deformation, vertical stresses and strains. The modelling approach used here differs, as I use fully coupled plane strain fluid flow and stress analysis, which also takes into account lateral stresses, strains and deformations. This is particularly useful when modelling consolidation of slopes as shear strains and horizontal displacement can be expected. In addition, the FE Method has a number of advantages over traditional slope stability analyses (e.g. Duncan, 1996). No failure mechanism needs to be assumed, complex loading conditions can be applied, advanced soil models can be used, information on deformation can be obtained and progressive failure up to total failure can be monitored.

## 6.2 Conceptual continental slope model

### 6.2.1 Consolidation and slope stability modelling

I use a fully coupled transient 2D pore fluid diffusion and stress analysis to model the flow of a single phase through porous media. The porous medium is modelled by attaching the FE mesh to the solid phase. The fluid can flow through the mesh, and is governed by Darcy's law. The mechanical part of the model is based on the effective stress principle (Terzaghi and Peck, 1948). Gravity is considered and pore fluid pressure is formulated in terms of total pore pressure. The elastoplastic Modified Cam Clay (Roscoe and Burland, 1968) model accounts for compaction caused by stress-induced deformation of the sediment matrix and fluid flow. The sediment is assumed fully saturated with a single incompressible pore fluid (sea water). Non-convergence of the solution defines failure (Zienkiewicz and Taylor, 1989). Both failure and numerical non-convergence occur

simultaneously as they are characterised by a dramatic increase in nodal displacement. The commercial software package ABAQUS is used for the FE calculations (ABAQUS, 2009). All calculations are conducted on a desktop PC.

### 6.2.2 FE model geometry of a typical continental slope

I use the north-west African continental slope as a proto-type field location for the model construction as it can be regarded as a typical passive continental margin with low sediment input (Weaver et al., 2000). Off north-west Africa the break of the essentially flat shelf is at a water depth of 100-200 m (Wynn et al., 2000). The continental slope is between 50-250 km long and slope angles vary between  $1 - 6^\circ$ . Typical gradients of the continental rise are  $0.1 - 1^\circ$  at water depths between 1500 and 4000 m. At continental slopes globally, scars of submarine landslides are observed at all parts of the slopes, from the shelf edge to the toe, affecting sediment from the seafloor to a maximum of 500 metres below seafloor (mbsf) (Hühnerbach et al., 2004). The area of interest of this study therefore concentrates on the upper 500 m within the sediment from the shelf break to the continental rise.

Fig. 6.2 shows a sketch of the model outline. It is 120 km long in x-direction. Although the main focus is on the slope itself, the shelf and abyssal plain are each 10 km wide in order to avoid boundary effects. Water depth is 200 m at the shelf break and 3700 m at the abyssal plain. The slope is 100 km long at an angle of  $2^\circ$  including both continental slope and rise. The model depth in z-direction is 5500 m at the shelf and 2000 m at the abyssal plain (not including water). Although the area of interest is defined as the upper 500 m of sediment, large overall model depths are necessary to avoid boundary effects. The sediment is assumed homogeneous without interfaces of abrupt changes in sediment properties, except for one model which introduces a layer of higher permeability to act as an aquifer.

The water column is not modelled as such but represented by a pressure load corresponding to the hydrostatic pore pressure at the seafloor. Most passive continental margins are uniform over large distances so that two-dimensional modelling is adequate.

### 6.2.3 Constitutive model and physical-mechanical properties

Hemipelagic clays alternating with mass transport deposits are the dominant sediment type at continental margins with low sediment input, i.e. away from big rivers or ice streams (e.g. Doyle et al., 1979; Weaver et al., 2000). I model the entire sediment column as one material with gradual downward property changes, given that these mass

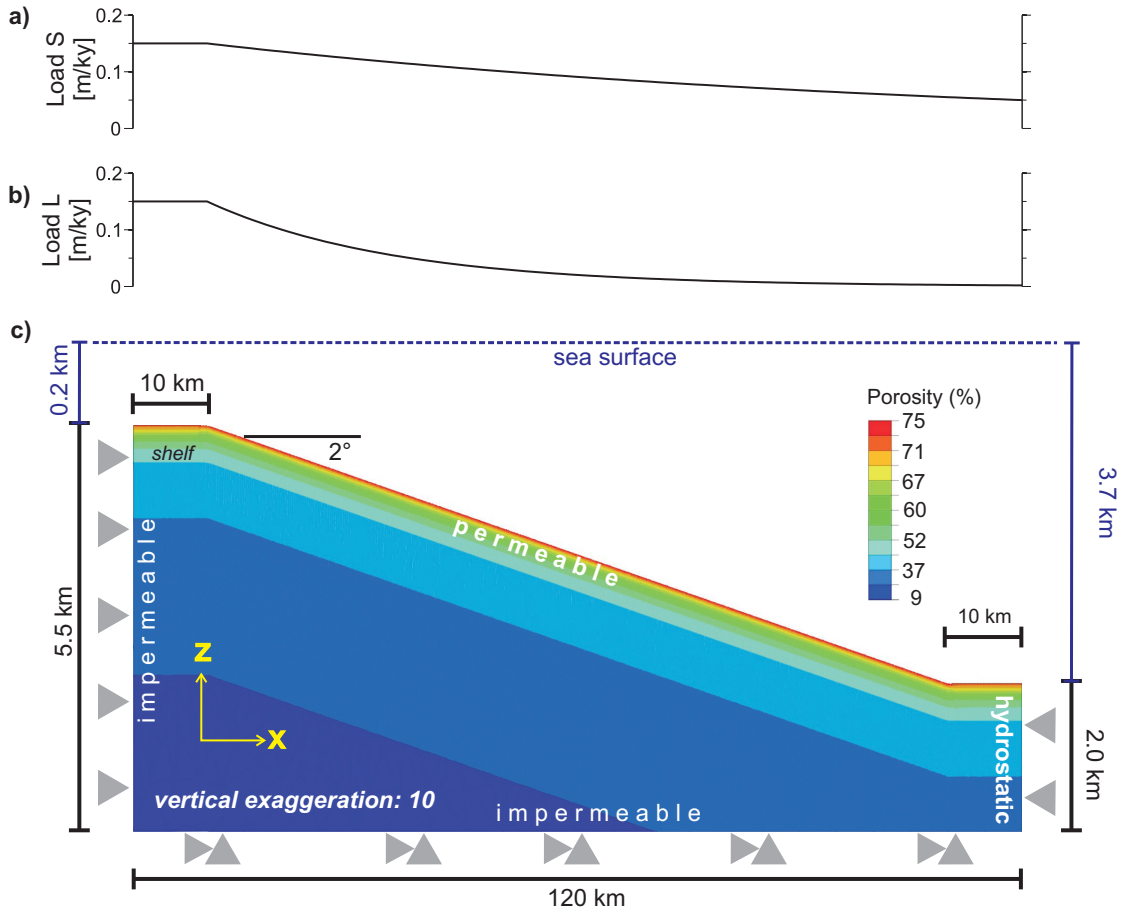


Figure 6.2: Continental slope model geometry (not to scale) with boundary and loading conditions. Displacement boundary conditions are represented by grey arrows (e.g. the base is fixed against movement in both x- and z- direction). Fluid flow boundary conditions are annotated. Colour coding represents the initial porosity distribution. Upper panels show asymmetric loading rate distributions: a) the smoothly decaying load distribution  $S$  (Eq. 6.7) and b) the rather localised load distribution  $L$  (Eq. 6.8).

transport deposits are also composed of hemipelagic sediments, remobilised from further up the slope or shelf. Hemipelagic sediments are generally soft, highly sensitive, and fit within the critical state framework (Baudet and Ho, 2004; Brandes, 2010). I therefore choose Modified Cam Clay (Roscoe and Burland, 1968) as an appropriate plasticity model. The change in size of the yield locus is determined by the amount of inelastic volume change according to an exponential strain hardening theory. The plastic strain rate is defined by an associated flow assumption. The elastic behaviour is modelled with a nonlinear, isotropic porous elastic constitutive model. Nonlinear permeability is implemented as a function of porosity. Cohesion is zero for normally consolidated clays and silts (Lambe and Whitman, 1979; Powrie, 2002).

Mechanical and physical properties for fine grained hemipelagic sediments are taken from the available literature. It has to be noted that in almost all cases the samples on which

mechanical properties are measured for scientific purposes, come from the upper 10 mbsf. It was not until 2006 that recent research efforts have made available well-constrained mechanical properties of deeper sediments from drill cores in the Gulf of Mexico, which has received large amounts of terrestrial sediment input from the Mississippi (Flemings et al., 2006, 2012). Although the sediments are mainly of terrigenous origin, I also use these data as, to my knowledge, it is the only reliable and publicly available information of geotechnical behaviour of fine grained sediments at larger depths.

The slope of the critical state line in the  $p'$ - $q$  plane,  $M$ , remains constant during the analysis. Because  $M$  is a measure of the ratio of shear to normal effective stress at failure, it is related to the effective friction angle,  $\phi'_{crit}$  by:

$$M = \frac{\sin\phi'_{crit} \cdot 6 \cdot \sqrt{1-b+b^2}}{3 + \sin\phi'_{crit} \cdot 2 \cdot b - \sin\phi'_{crit}} \quad (6.1)$$

with  $b = 0.5$  for plane strain (Powrie, 2002). The effective friction angle of hemipelagic deep sea sediments is often given as about  $30^\circ$  (Valent et al., 1982; Kayen and Lee, 1991; Baraza et al., 1992; Dugan and Germaine, 2008), which I adopt in most of the models. However, shear strength can be highly variable and lower values have been reported (e.g. Dugan and Germaine, 2008) so that  $\phi'_{crit} = 15^\circ$  will also be used in one model.

The slope of the critical state line when projected onto the  $(e+1) - \ln p'$  [ $kPa$ ] space,  $\lambda$ , determines the compressibility. Values for  $\lambda$  are highly variable, ranging from as low as 0.08 (Baudet and Ho, 2004) to a maximum of 0.88 (Busch and Keller, 1982; Hattab and Favre, 2010). However, the upper  $\lambda$  limits reported from a significant number of consolidation tests on hemipelagites as well as sediments of terrigenous origin cluster around 0.24 to 0.28 (Valent et al., 1982; Demars, 1982; Bayer and Wetzel, 1989; Leynaud et al., 2007; Dugan, 2008; Schneider et al., 2009). Accordingly,  $\lambda = 0.28$  is used, which is constant throughout the analysis. In contrast to a constant  $\lambda$ , Brandes (2010) and Long et al. (2011) found that a linear decrease of  $\lambda$  with increasing effective stress describes the rapid porosity decrease typically observed in shallow marine sediments more adequately than a constant  $\lambda$  value. After Long et al. (2011)  $\lambda$  depends on porosity according to

$$\lambda = 0.68 \cdot n + 0.01. \quad (6.2)$$

Considering the initial porosity distribution in the model, the relationship proposed by Long et al. (2011) corresponds to initial values of  $\lambda = 0.52$  at the model surface and  $\lambda = 0.08$  at a model depth of 5.5 km. I extend this for maximum surface-near compressibility of 0.88 giving a steeper decline in  $\lambda$  with effective stress:

$$\lambda = 1.23 \cdot n - 0.04. \quad (6.3)$$

Therefore, in models where compressibility is a function of the effective stress,  $\lambda$  is not constant and changes accordingly during the analysis.

The elastic logarithmic bulk modulus,  $\kappa$ , is commonly estimated as 1/10 of  $\lambda$  (Powrie, 2002). I therefore use  $\kappa = 0.028$  in all models. I define Poisson's ratio  $\nu = 0.3$ , so that elastic shear stiffness  $G$  increases as the sediment compacts.

Permeability,  $k$ , is a function of porosity,  $n$ , and therefore varies temporally as well as spatially during compaction. Due to a lack of permeability values for hemipelagic sediments at depths larger than about 10 mbsf, I use the porosity-permeability relationships given by Flemings et al. (2012) for mud of terrigenous origin:

$$k_z = 10^{-15.48} m/s \cdot 10^{9.4 \cdot n} \quad (6.4)$$

as well as those suggested by Binh et al. (2009) for silty clay

$$k_z = 7 \cdot 10^{-15} m/s \cdot e^{14.61 \cdot n} \quad (6.5)$$

and hemipelagic sediment

$$k_z = 10^{-15} m/s \cdot e^{18.93 \cdot n}. \quad (6.6)$$

A higher horizontal ( $k_x$ ) than vertical permeability ( $k_z$ ) is often observed in marine sediments and anisotropy ratios of 10 or 100 have been measured on mudstone samples from the Gulf of Mexico (Schneider et al., 2009; Binh et al., 2009). Rowe (1965, 1968) finds that in situ permeability is generally higher than permeability measured in the laboratory. He attributes this finding to the presence of fabric, fissuring or fracturing that allow for sideways drainage but which are not captured in size limited laboratory samples. Clayton et al. (1995) compare in situ and laboratory values for consolidation coefficients (a function of permeability and compressibility) of identical materials and find that in situ values can be up to 1000 times larger than those obtained on small samples. This highlights the importance of in situ geotechnical testing and justifies the use of  $k_x/k_z = 1000$ , in addition to  $k_x/k_z$  ratios of 10 and 100 as measured in laboratory experiments.

The sediment's clay content typically increases downslope (e.g. Lee et al., 1993). Together with slow deposition and settling rates this results in a decrease in permeability towards the toe of the slope. The models therefore also take into account a horizontal permeability gradient, in addition to a vertical one. The initial permeability ( $k_x$  as well as  $k_z$ ) linearly decreases by one order of magnitude from the top to the base of the slope. This means that the initial permeability of a material point at a given depth below seafloor at  $x=120$  km is one tenth of the initial permeability of a material point at the

same depth at  $x=0$  km.

Dry density is a linear function of porosity ( $\rho_{dry} = -2.6 \cdot n + 2.6$ ), and remains constant during the analysis. The sediment is fully saturated.

#### 6.2.4 Loading of the slope by asymmetric sediment deposition

Sediment deposited at the shelf and continental slope can have various origins. The main inputs are from rivers transporting eroded material from the hinterland, the detritus of biogenic production in the water column, and aeolian input, as well as from mass wasting of these sediments. Therefore, rates of deposition vary spatially and are usually highest at the shelf and the upper slope. Downslope and towards the deep ocean, these rates decrease exponentially, as clearly expressed in the shape of a continental margin. At the proto-type field location off north-west Africa, Ruddiman et al. (1988) document maximum sedimentation rates of 0.15 m/ky at the upper slope and 0.1 m/ky at the mid-slope during the past 6 Ma. The rate of decrease from the shelf break to the toe of the slope is calculated from thinning rates of seismic sequences at various locations off north-west Africa based on seismic data from Antobreh and Krastel (2007).

Sedimentation as such is not implemented in the model. The newly added sediment itself is not physically modelled but simulated by an equivalent vertical vector load on the seafloor that increases linearly over time. The conversion of sedimentation rate (thickness per unit time; m/ky) into a loading rate (pressure per unit time; kPa/ky) is based on the porosity and dry density equal to that of seafloor sediments ( $n = 75\%$ ,  $\rho_{dry} = 670 \text{ kg/m}^3$ ). The rate of loading is highest along the shelf. The thinning rates are converted into two exponential equations that prescribe the load distribution along the slope. The first load distribution describes a smooth decay and is termed load distribution S hereafter (Fig. 6.2a):

$$S = f \cdot e^{-0.01 \cdot x[km]} \quad (6.7)$$

with  $f$  as the maximum loading rate and  $x [km]$  as the distance from the shelf break. The second load is a localised load distribution (hereafter referred to as load distribution L) that decays more rapidly with increasing distance from the shelf (Fig. 6.2b):

$$L = f \cdot e^{-0.04 \cdot x[km]}. \quad (6.8)$$

### 6.2.5 Boundary conditions

The lateral boundaries of the model are fixed against movements in the horizontal direction, but are free to move vertically. The base of the model is fixed in both vertical and horizontal directions. The upper boundary, or seafloor, is free to move in either vertical or horizontal direction. The landward boundary of the model (left side, Fig. 6.2) is impermeable, but pore fluid is allowed to flow through the abyssal plain boundary (right side). The landward boundary is impermeable because loading due to sedimentation to both sides of this boundary is assumed equal and purely vertical flow is therefore expected. No flow takes place through the basal boundary as sediments at this depth are highly lithified and virtually impermeable (Skempton, 1970).

The surface flow boundary condition is a mixed boundary condition. Although it does not physically exist in the model, the newly deposited sediment needs to be taken into account, as flow out of the surface cannot take place freely after deposition has started. Hereafter, the newly deposited sediment is referred to as "virtual layer" and its top is the "new seafloor". Flow velocities at the model surface are restricted depending on the permeability of the overlying sediment as well as the pore pressure gradient in the virtual layer. The pore pressure at the top of the virtual layer (new seafloor) is hydrostatic. The pore pressure gradient between the the model surface and the new seafloor is assumed linear. The fluid flow velocity normal and out of the model surface ( $v_n$ ) is calculated according to

$$v_n = \frac{k_{vl}}{(\gamma_w \cdot c)} \cdot (p - p_{0vl}), \quad (6.9)$$

where  $c$  is the thickness of the virtual layer,  $p$  is the current pore pressure at the model surface and  $p_{0vl}$  is the hydrostatic pore pressure at the new seafloor. As  $c$  is a function of time (constant and continuous sedimentation) as well as space (sedimentation rate decreases exponentially downslope),  $v_n$  varies spatially and temporally and therefore needs to be recalculated for every surface element at every time increment.  $k_{vl}$  is the average vertical permeability in the virtual layer.  $k_{vl}$  equals the vertical permeability at the model surface and decreases accordingly over time due to compaction.

### 6.2.6 Discretisation

The mesh is finest within the upper 100 m of the model with 10 m long and 10 m wide elements. Between model depths of 100 m and 500 m the element size gradually increases to 100 m length and width. Outside the area of interest, at model depths larger than 500 m, the elements increase in size up to 1000 m at the model's basal boundary. The total number of elements amounts to  $\sim 250,000$ . I use 8-node biquadratic displacement and bilinear pore pressure elements. Calculations are done on reduced integration points

and the number of degrees of freedom is about 1.76 million. A typical runtime for such a model is about four hours.

### 6.2.7 Initial conditions

Before loading by sediment deposition begins, all stresses are in equilibrium with the gravitational load ( $g = 9.81m/s^2$ ), and pore pressures are hydrostatic throughout the model. The state of consolidation of the sediment depends strongly on the rate of deposition and the length of the drainage path (Terzaghi and Peck, 1948). As only slow deposition is considered in this study, the sediment in the model is initially normally consolidated with an overconsolidation ratio of 1. The initial size of the yield surface is determined such that the stress state lies on the yield surface.

The initial porosity in the upper 500 mbsf decreases quadratically from 75% at the surface to 45% according to the relationship for calcareous hemipelagic sediment suggested by Hamilton (1976). At larger depths the decrease in porosity is linear, reaching a minimum porosity of 10% (Velde, 1996). Fig. 6.2c shows the spatial initial porosity distribution, while Fig. 6.3a depicts the decrease of porosity with depth in greater detail. Initial permeability is derived from the initial porosity distribution according to the corresponding porosity-permeability relationships (Fig. 6.3b).

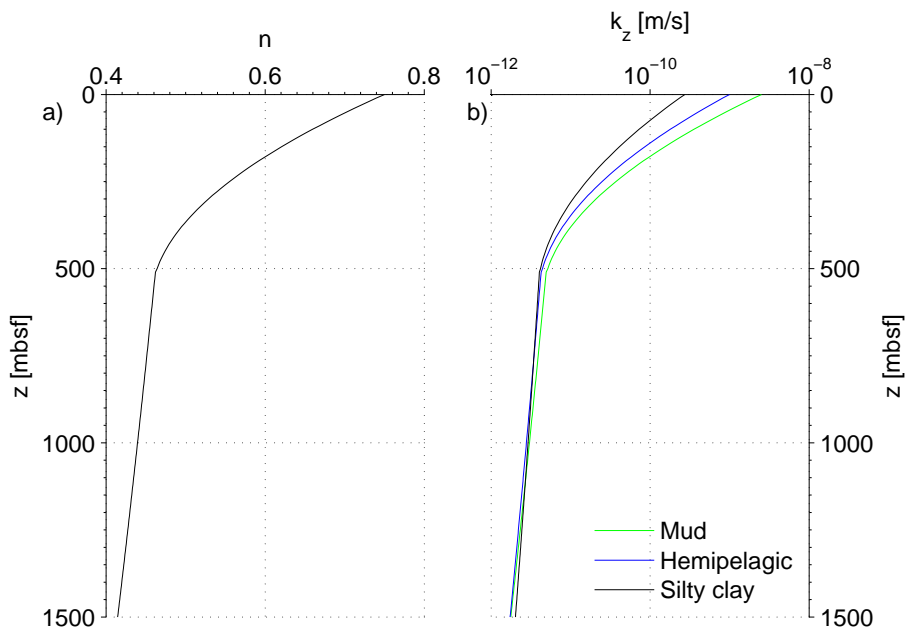


Figure 6.3: (a) Initial porosity distribution with depth after Hamilton (1976) and Velde (1996). (b) Initial permeability distribution with depth for three different porosity-permeability relationships (Binh et al., 2009; Flemings et al., 2012) used in this study.

### 6.2.8 Initial excess pore pressure

At the beginning of the simulations, pore pressures are assumed hydrostatic. However, as mentioned above and as I show in the subsequent modelling, consolidation of soft marine sediment favours the generation of excess pore pressures that are retained in the sediment. It is therefore likely, that the slope is overpressured already, before the simulation starts. The assumption that initial pore pressures within the modelled slope would be hydrostatic is therefore incorrect, and the modelling results will underestimate excess pore pressure. It is therefore necessary to broadly quantify these initial pore pressures, so that they can be added to the resulting pore pressures at the end of the model runs. To estimate the degree of initial overpressurisation, I perform a simple and quick 1D consolidation analysis following the approach of Gibson (1958). This simple analysis neglects lateral flow, assumes constant permeability and stiffness, and tends to overestimate excess pore pressures (Gibson et al., 1981; Schiffman et al., 1984). However, it will provide a broad estimate of the degree of initial overpressurisation with depth when sedimentation rates are low.

Young's modulus is assumed to be 50 MPa, which is representative for silty clay (United States Army Corps of Engineers guidelines). The bulk unit weight is 20 kN/m<sup>3</sup> for the sediment, and 10.24 kN/m<sup>3</sup> for the pore water. As this simple consolidation analysis assumes that permeability does not change with depth, I calculate results three times using different vertical permeabilities. The first vertical permeability ( $k_{z1} = 10^{-9}$  m/s) represents the shallow sediment (0-50 mbsf). The second vertical permeability ( $k_{z2} = 10^{-10}$  m/s) simulates sediment between 50 and 300 mbsf. The third vertical permeability ( $k_{z3} = 10^{-11}$  m/s) is used for sediment deeper than 300 mbsf (compare Fig. 6.3b). I use a sedimentation rate of 0.15 m/ky, and run the model for 333,000 years with  $k_{z1}$ , 2 million years with  $k_{z2}$ , and 20 million years with  $k_{z3}$  to build up a sediment column that is 50 m, 300 m, and 3000 m thick. The results are given in terms of overpressure ratio,  $\lambda^*$ , the ratio of excess pore pressure to vertical effective stress corresponding to hydrostatic conditions:

$$\lambda^* = \frac{p_e}{\sigma_v - p_h}. \quad (6.10)$$

This simple analysis shows that the initial excess pore pressures within the continental slope can be assumed not to exceed 20 % of the hydrostatic vertical effective stress (Table 6.1). As most submarine failures occur within the upper 300 m of sediment, it is more likely that initial excess pore pressures are considerably less, i.e. < 0.2 % of the hydrostatic pressure (Table 6.1).

z [mbsf]	$\lambda^*(k_{z1})$	$\lambda^*(k_{z2})$	$\lambda^*(k_{z3})$
0	0.0000	0.0000	0.0000
10	$4 \cdot 10^{-5}$	0.0028	0.2256
20	$4 \cdot 10^{-5}$	0.0028	0.2252
40	$3 \cdot 10^{-5}$	0.0027	0.2245
60		0.0026	0.2230
80		0.0025	0.2222
100		0.0024	0.2204
150		0.0021	0.2186
200		0.0019	0.2074
500			0.1888
1000			0.1512
2000			0.1135
3000			0.1135

Table 6.1: Estimate of initial overpressure ratio,  $\lambda^*$  (Eq. 6.10), in a sediment column deposited at low rates. Values are given at various depths below seafloor,  $z$ , and were calculated according to Gibson (1958) for three different permeabilities ( $k_{z1} = 10^{-9}$  m/s,  $k_{z2} = 10^{-10}$  m/s,  $k_{z3} = 10^{-11}$  m/s).

### 6.2.9 Sand layer

The assumption that the whole continental slope consists of a homogeneous material may not hold for all continental margins. Changes in the type of terrestrial sediment supply, for example due to climate changes in the hinterland or a change in dominant transport processes, can cause abrupt differences in lithology across the adjacent continental slope. This may be expressed in the form of beds or single lenses of coarser material, which may be laterally extensive and could act as fluid pathways (Rowe, 1965, 1968).

To account for such a fluid pathway, a high permeability layer can optionally be added to the existing model set up (Fig. 6.4). The layer is 20 m thick and is parallel to the seafloor at a depth of 40 m below initial seafloor. The material's mechanical behaviour is that of sand and is simulated with a nonlinear, isotropic porous elastic constitutive model. The elastic bulk modulus,  $\kappa$ , is 0.05 and Poisson's ratio,  $\nu$ , is 0.3. Dry density is constant throughout the layer at 1,100 kg/m<sup>3</sup>. The initial porosity of models with this layer is identical to models without a layer. The permeability of the material within the layer is constant and anisotropic with  $k_x/k_z = 10$ . Vertical permeability,  $k_z$ , of the sand layer is  $10^{-8}$  m/s and uniform in one scenario. In another scenario  $k_z$  decreases laterally from  $10^{-8}$  m/s (at  $x=0$  km) to  $10^{-9}$  m/s (at  $x=100$  km, Fig. 6.4). Both the upper and lower boundaries of the sand layer are permeable so that fluid can flow freely across the clay/sand interface. As the permeability of this sand layer is significantly higher than that of the surrounding sediment it is also referred to as an aquifer in the following.

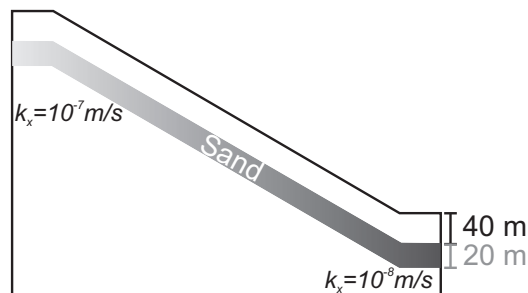


Figure 6.4: Sketch of model with sand layer (aquifer) whose permeability decreases linearly from the top to the bottom of the slope (not to scale).

### 6.2.10 Choice of models

A total of 18 model runs are performed. In a first approach an identical model is subjected to rapid as well as to slow sedimentation. This first model has average physical-mechanical properties for fine grained marine sediments (Table 6.2). The sediment body is homogeneous without layers or interfaces of abrupt property changes. Two model runs are conducted; with high ( $< 15$  m/ky) and low ( $< 0.15$  m/ky) sedimentation rates. The rate of sedimentation decreases exponentially away from the shelf edge according to load  $S$  (Fig. 6.2a). All subsequent models are identical to the first model, with one parameter varied at a time in order to analyse the model's sensitivity to that specific parameter.

	<b>Notation</b>	Value
$\kappa$	Swelling index	0.027
$\nu$	Poisson ratio	0.3
$\lambda$	Logarithmic bulk modulus	0.28
$\phi'_{crit}$ [°]	Friction angle	30
$M$	Slope of critical state line	0.87
$k_z$	Vertical permeability	Eq. 6.4
$k_x/k_z$	Permeability anisotropy ratio	10
$\gamma_w$ [kN/m <sup>3</sup> ]	Specific fluid weight	10.24
$g$ [m/s <sup>2</sup> ]	Gravity	9.81

Table 6.2: Input parameters used in the first (reference) model.

The initial eight sets of model runs (M1 to M8) are designed to investigate the influence of consolidation properties on the generation of excess pore pressures (Table 6.3). The model's sensitivity to compressibility is tested in model runs M1 and M2. Both models include a linear decrease in the exponential hardening constant,  $\lambda$ , with decreasing porosity. In model run M1 the relationship proposed by Long et al. (2011) is used and  $\lambda$  decreases from 0.52 (for  $n=75\%$ ) to 0.08 (for  $n=10\%$ ). In model run M2 the shallow sediment is softer ( $\lambda=0.88$  for  $n=75\%$ ), and the decrease of  $\lambda$  is consequently steeper. I assess the influence of permeability-porosity relationships on overpressure generation in models M3 and M4 by using two permeability-porosity relationships that differ from the

first model. The relationships developed by Binh et al. (2009) for hemipelagic sediment as well as for silty clay are used in model runs M3 and M4, respectively. In order to assess the sensitivity to absolute values of permeability in model run M5, the porosity-permeability relationship of model M1 is used, but all permeabilities are one order of magnitude lower. Changes in the nature of the sediment through time are possible, and the newly deposited sediment can be less permeable than the underlying sediment. If the newly deposited sediment has a lower permeability than the sediment at the original seafloor it acts as a 'cap', possibly leading to excess pore pressures as vertical drainage is hindered. Model M6 takes this into account by simulating newly accumulated sediment which is an order of magnitude less permeable than the underlying sediment. The sediment in model run M7 has a critical friction angle of  $15^\circ$ , representing an internally weak material. In model run M8 I combine the parameters that are likely to favour the generation of excess pore pressures: high compressibility, low permeability and a sediment 'cap'.

A second set of model runs aims to identify factors that drive fluid laterally into areas of low overburden, where a rise in pore pressure decreases the effective stress (Table 6.3, M9 to M16). Firstly, I calculate models with strong permeability anisotropy (M9 with  $k_x/k_z = 100$ ; M10 with  $k_x/k_z = 1000$ ). I then introduce a gradual lateral decrease in permeability by one order of magnitude along the entire slope (M11). Model 12 is a combination of the permeability anisotropy ( $k_x/k_z = 1000$ ) as in model run M10, and lateral decrease in permeability as in model run M11.

A third set of model runs (M13 to 16) then include a 20 m thick layer of higher permeability material (sand layer). The permeability within the 20 m thick layer is horizontally constant (M13 and M14) or decreases downslope (M15 and M16). To identify whether the shape of the load impacts on lateral fluid flow the sediment is loaded with load S (M13, M15) and the rather localised load L (M14, M16). Load L (Fig. 6.2b) has a stronger exponential decrease away from the shelf edge than load S (Fig. 6.2a).

All models are set to run for 2 million years under continuous loading. After loading has started the model's surface will not represent the seafloor any more, but a buried bedding plane. The depth of burial depends on the rate and shape of asymmetric loading. After 2 million years with load S (Fig. 6.2a), 300 m of 'virtual' sediment will have deposited at the shelf and 100 m at the downslope end. For load L (Fig. 6.2b) the burial depth at the toe of the slope is 5 m.

$\lambda$	$k_z$	$k_x/k_z$	$k_z/k_{vt}$	$M$	Load	Layer	Fig.	Comment	
M1	<i>Eq. 6.2</i>	mud (Eq. 6.4)	10	1	0.87	S	no	6.10	depth-dependent compressibility
M2	<i>Eq. 6.3</i>	mud	10	1	0.87	S	no	6.11	depth-dependent compressibility, high shallow compressibility
M3	0.28	<i>hemipelagic</i>	10	1	0.87	S	no	6.12	Porosity-permeability relationship from Eq. 6.5
M4	0.28	<i>silty clay</i>	10	1	0.87	S	no	6.13	Porosity-permeability relationship from Eq. 6.6
M5	0.28	<i>1/10 of mud</i>	10	1	0.87	S	no	6.14	$k_z$ one order of magnitude lower than in Eq. 6.4
M6	0.28	mud	10	10	0.87	S	no	6.15	Newly deposited sediment less permeable than at the model surface
M7	0.28	mud	10	1	0.45	S	no	6.16	Weak internal frictional strength
M8	<i>Eq. 6.3</i>	<i>1/10 of mud</i>	10	10	0.87	S	no	6.17	combined model for maximum overpressure
M9	0.28	mud	100	1	0.87	S	no	6.18	permeability anisotropy=100
M10	0.28	mud	1000	1	0.87	S	no	6.19	permeability anisotropy=1000
M11	0.28	mud	10	1	0.87	S	no	6.20	<i>horizontal decrease in permeability</i>
M12	0.28	mud	1000	1	0.87	S	no	6.21	<i>horizontal decrease in permeability, permeability anisotropy=1000</i>
M13	0.28	mud	10	1	0.87	S	sand layer	6.22	<i>Model with sand layer</i>
M14	0.28	mud	10	1	0.87	L	sand layer	6.23	<i>sand layer with localised load distribution (Eq. 6.8)</i>
M15	0.28	mud	10	1	0.87	S	sand layer	6.24	<i>sand layer whose horizontal permeability decrease seawards</i>
M16	0.28	mud	10	1	0.87	L	sand layer	6.25	<i>See M15, with localised load distribution (Eq. 6.8)</i>

Table 6.3: Input parameters for all models shown in the following. A detailed description of the parameters and how they are changed throughout the different models is given in the text. *Column 1*: Name of the model as it is referred to in the text. *Column 2*: Logarithmic bulk modulus (or compressibility),  $\lambda$ . *Column 3*: Porosity-permeability relationship used in this model,  $k_z$ . *Column 4*: Permeability anisotropy,  $k_x/k_z$ . *Column 5*: Ratio of the vertical permeability at the model surface to the vertical permeability in the virtual layer,  $k_z/k_{vt}$ . *Column 6*: Slope of the critical state line,  $M$ . *Column 7*: Load distribution (S = smooth as in Eq. 6.7, L = localised as in Eq. 6.8). Italic prints indicate parameters that differ to those of the reference model whose parameters are given in Table 6.2. Parameters that are not listed in this table are identical to those used in the reference model and can also be found in Table 6.2.

### 6.2.11 Assumptions and limitations

Newly deposited sediment only provides a surface load in the models. Compaction and pore fluid generation within the newly deposited sediment would occur in nature, but are not simulated here. Consequently, the model is not capable of simulating failure within this interval of newly deposited sediment. The failure surface for large-volume landslides on low gradient seafloor is typically located around 100 m below seafloor (Hühnerbach et al., 2004, Fig. 6.1). Therefore failure is not commonly observed within the upper 100 m of the sediment column. The limitation is thus only critical if the thickness of deposited sediment exceeds 100 m, which is only the case when very long time scales or high deposition rates are involved.

The surface flow boundary condition considers seepage only, and does not allow fluid to drain from the virtual layer into the modelled sediment body. However, downward fluid flow is not expected. Pore pressure at the new seafloor is hydrostatic (zero excess pore pressure) and fluid will consequently flow upwards and towards the new seafloor.

All models are calculated using small strain theory to reduce computational costs, which is known to overestimate excess pore pressures (Gibson et al., 1981; Schiffman et al., 1984). This can be crucial for geotechnical design analyses. The aim of this study, however, is to investigate fundamental processes and sensitivities in a qualitative manner. Moreover, this systematic error affects all models equally so that the results of models obtained using small strain analysis can confidently be compared. For a detailed investigation on the discrepancies between small and finite strain analyses the reader is referred to chapter 4.

The model does not account for thermal expansion of water, dehydration of clays, and the cementation of pore space, although these processes can contribute to excess pore pressure generation. I justify neglecting these processes with the fact that the contribution of thermal expansion to excess pore pressure is about one order of magnitude less than that of mechanical compaction (Wangen, 2001). Clay dehydration (smectite to illite transformation) is typically observed at burial depth in excess of 2 km (Chamley, 1989). This is much deeper than the typical depth of the failure surface for most submarine landslides, which often is around 100 m sediment depth (Hühnerbach et al., 2004; Twichell et al., 2009). Wangen (2000) suggests that fluid expulsion due to cementation in lithified sediments causes overpressure build-up. Lithification in fine grained sediments is observed at burial depth of 2 to 3 km (Skempton, 1970), which is also too deep to be related to slope failure. There is, however, some evidence that early cementation in carbonates sets on at much shallower depth, providing unusual high stiffness to carbonate rich sediments (Westphal and Munnecke, 1997, Masson, personal communication). It has

not been investigated yet, whether this early cementation causes a closure in pore spaces and thereby increases pore pressure. However, the common observation that calcareous sediments maintain a higher porosity at a given pressure compared to other sediment types speaks against this (Bryant et al., 1981).

The standard FE method is not able to simulate strain softening behaviour, which has been reported for marine sediments (e.g. Kvalstad et al., 2005). Unless specific techniques are applied, softening behaviour leads to first order mesh dependence and therefore physically incorrect results. The current model is therefore not capable of modelling strain softening behaviour.

## 6.3 Results

To analyse the model results, I plot the stress paths of representative nodes and corresponding critical state lines in a plot of mean effective stress,  $p'$ , and deviatoric stress,  $q$ . This allows instability, or stress paths that indicate a decrease in stability due to overpressure generation, to be identified. The selected nodes are at depths of 50 m below the original undeformed seafloor along the entire slope. Node 1 is located at the crest of the slope ( $x = 10$  km), node 2 at the upper slope ( $x = 30$  km), node 3 at the mid-slope ( $x = 60$  km), node 4 at the lower slope ( $x = 80$  km), and node 5 at the toe of the slope ( $x = 110$  km). For models with a sand layer the selected nodes are initially located 40 m below the model surface. Their location corresponds to the upper boundary of the higher permeability sand layer. Stresses and flow velocities are interpolated from integration points to nodal values using the original shape functions. The stability of the slope over time is assessed by plotting the overpressure ratio (Eq. 6.10), vertical permeability and horizontal fluid flow velocity over time at these selected nodes. The spatial overpressure ratio distribution at the final state of the model is presented in 2D contour plots. Normalised velocity vectors indicate the direction of fluid flow.

### 6.3.1 Rapid versus slow sedimentation rates

The first numerical experiment addresses the differences of rapid and slow deposition on a slope. The model with rapid deposition stops converging after about 400,000 years, indicating the onset of failure. In contrast, the slow deposition model continuous without failure until the end of the analysis (2 million years). Failure is also expressed clearly in the stress paths of several of the selected nodes (Fig. 6.5). At the initial stages of loading (low  $p'$  and  $q$  values) all nodes follow a straight line; the normal compression line. At a certain pressure a first node starts to show behaviour typical of undrained loading. The node leaves the normal compression line as the effective stress decreases until the critical

state line is reached. Rising excess pore pressures cause the reduction in effective stress and the bend in the stress path.

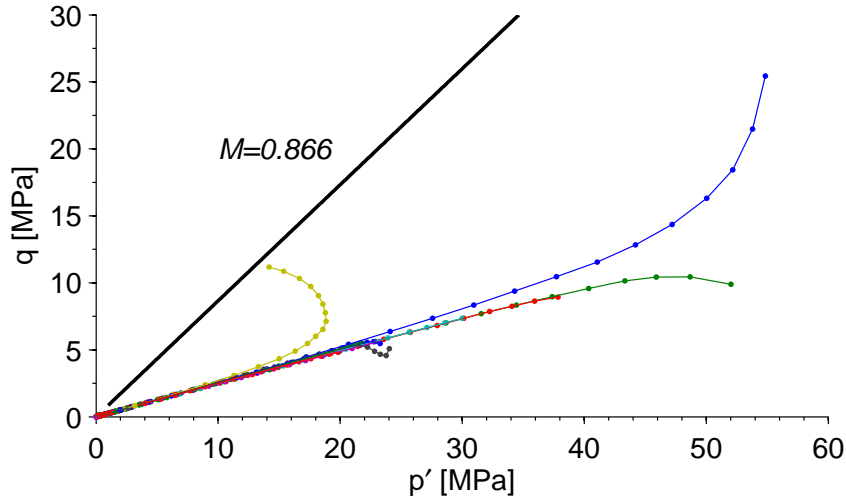


Figure 6.5: Stress paths of several nodes in a  $p'$ - $q$  plot for a model with rapid deposition. The nodes are located at a depth of 50 m below the initial seafloor at the crest of the slope ( $x = 10$  km, yellow), the upper slope ( $x = 30$  km, blue), the mid-slope ( $x = 60$  km, green), the lower slope ( $x = 80$  km, red), and at the toe of the slope ( $x = 110$  km, black). The black solid line represents the critical state line for material properties as given in Table 6.2.

High excess pore pressures are also responsible for the shallow overpressure ratio reaching up to 0.7 (Fig. 6.6a) in the model with rapid deposition. In contrast, the overpressure ratio does not exceed 0.005 at any time in the model with slow deposition. For both models the overpressure ratio at node 1 is highest compared to the other four selected nodes. Node 1 locates at the top of the slope where overburden is largest.

The vertical permeability of the five selected nodes decreases by more than one order of magnitude to  $k_z = 5 \cdot 10^{-11}$  m/s when the rate of loading is high (Fig. 6.6b). Under low loading rates the final vertical permeability is about  $2 \cdot 10^{-10}$  m/s. In both models the rate of permeability decrease is highest in the early stages of the model runs, and decreases as time progresses.

Fluid flows in positive  $x$ -direction (Fig. 6.6c). Flow velocities at the selected nodes plotted in Fig. 6.6c reach up to 0.6 mm/y in the initial stages in the model with rapid deposition. The velocities drop and level at about 0.1 mm/y as loading continues. This is most likely due to rapidly decreasing permeabilities, as the development of horizontal fluid velocity over time mirrors that of the vertical permeability (compare the left panels of Fig. 6.6b and Fig. 6.6c). When loading is slow, fluid flow in  $x$ -direction is much slower and does

not exceed 0.015 mm/y.

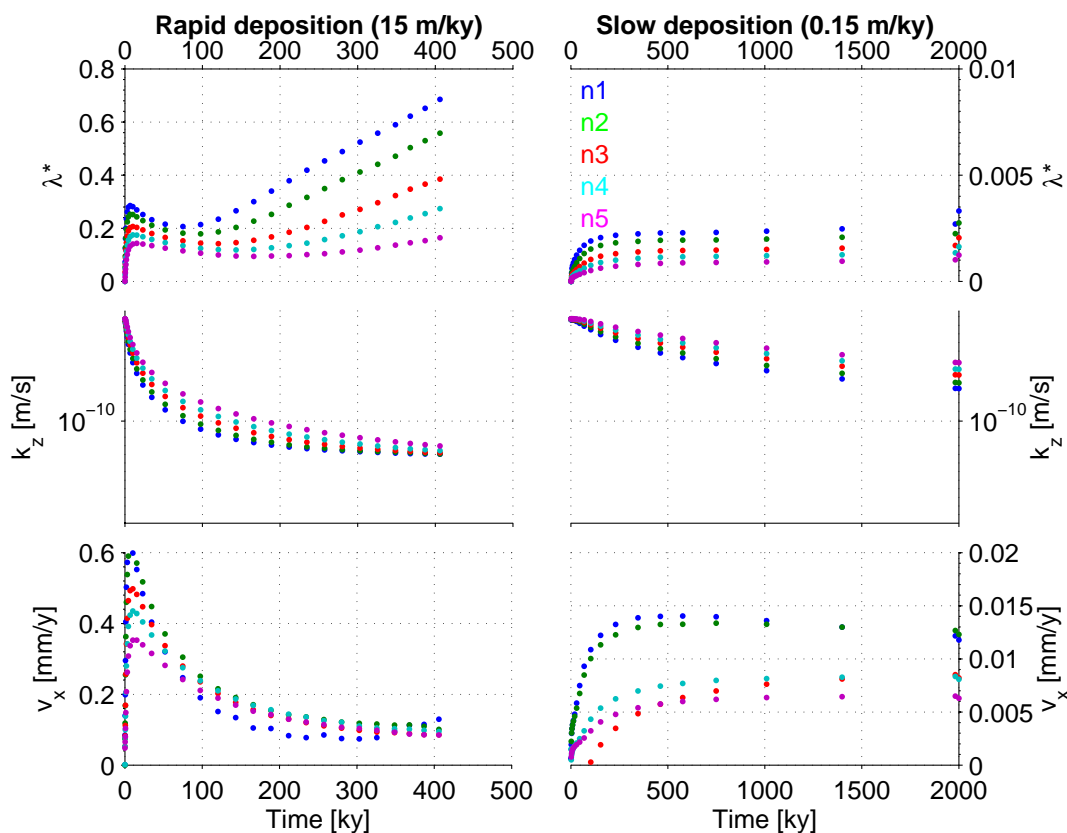


Figure 6.6: Temporal evolution of (a) overpressure ratio,  $\lambda^*$ , (b) vertical permeability,  $k_z$ , and (c) horizontal fluid flow velocity,  $v_x$ , at five selected nodes for a model with parameters given in Table 6.2. The locations of the selected nodes are explained in the caption of Fig. 6.5. The model is subjected to rapid deposition (left column) as well as slow deposition (right column). Note different scaling of y-axes.

Figs. 6.7 and 6.8 show the states of the models at the end of the last increment, i.e. just before failure of the model with rapid deposition, and at the end of the analysis for the model with slow deposition, respectively. Figs. 6.7a and 6.8a show the spatial distribution of the overpressure ratio as well as the direction of total fluid flow on the undeformed model geometry. The model with high sedimentation rates (Fig. 6.7a) has an overpressure ratio maximum of  $> 0.9$  at the upper slope at about 500 m below the original seafloor. The overpressure ratio decreases in all directions away from this maximum. Along the model's surface the highest  $\lambda^*$  value occurs at  $x=13$  km. Near surface fluid flow is predominantly upwards. However, below the  $\lambda^*$  maximum the fluid flows laterally towards the middle and lower slope. The transition of stable slope conditions to those of shear failure is progressive and initiates just seaward of the shelf edge. Failure is not confined to the crest of the slope, as the wide lateral extend of the high shear zone

suggests (Fig. 6.7b).

Under low deposition rates the overpressure ratio builds up to a maximum of 0.084 in the shelf area at a model depth of 900 m (Fig. 6.8a). This would correspond to a burial depth of about 1200 m after 2 million years of loading, ignoring vertical deformation and compaction of the freshly deposited sediment. The overpressure ratio decreases towards the bottom, the right side and towards the top. At the model surface the maximum overpressure ratio reaches 0.002. Along the surface the overpressure ratio decreases monotonically towards the toe of the slope, where its value is as low as 0.001. The direction of the total fluid flow represented by black normalised vectors is dominated by vertical upwards flow in the entire model. Shear strains occur all along the slope with highest shear at the model surface (Fig. 6.8b). However, no zone of localised high shear is obvious and maximum strains are everywhere below 10%.

A 2° slope subjected to rapid deposition ( $< 15$  m/ky) fails due to excess pore pressures. The same slope under slow deposition ( $< 0.15$  m/ky) is stable and does not show any indications of failure. The sediment mechanical properties used in these models, however, are average values. In the following, a range of extreme sediment mechanical properties that are likely to favour the retention of pore fluid (e.g. low permeability and high compressibility) are modelled in order to test their potential for overpressure generation.

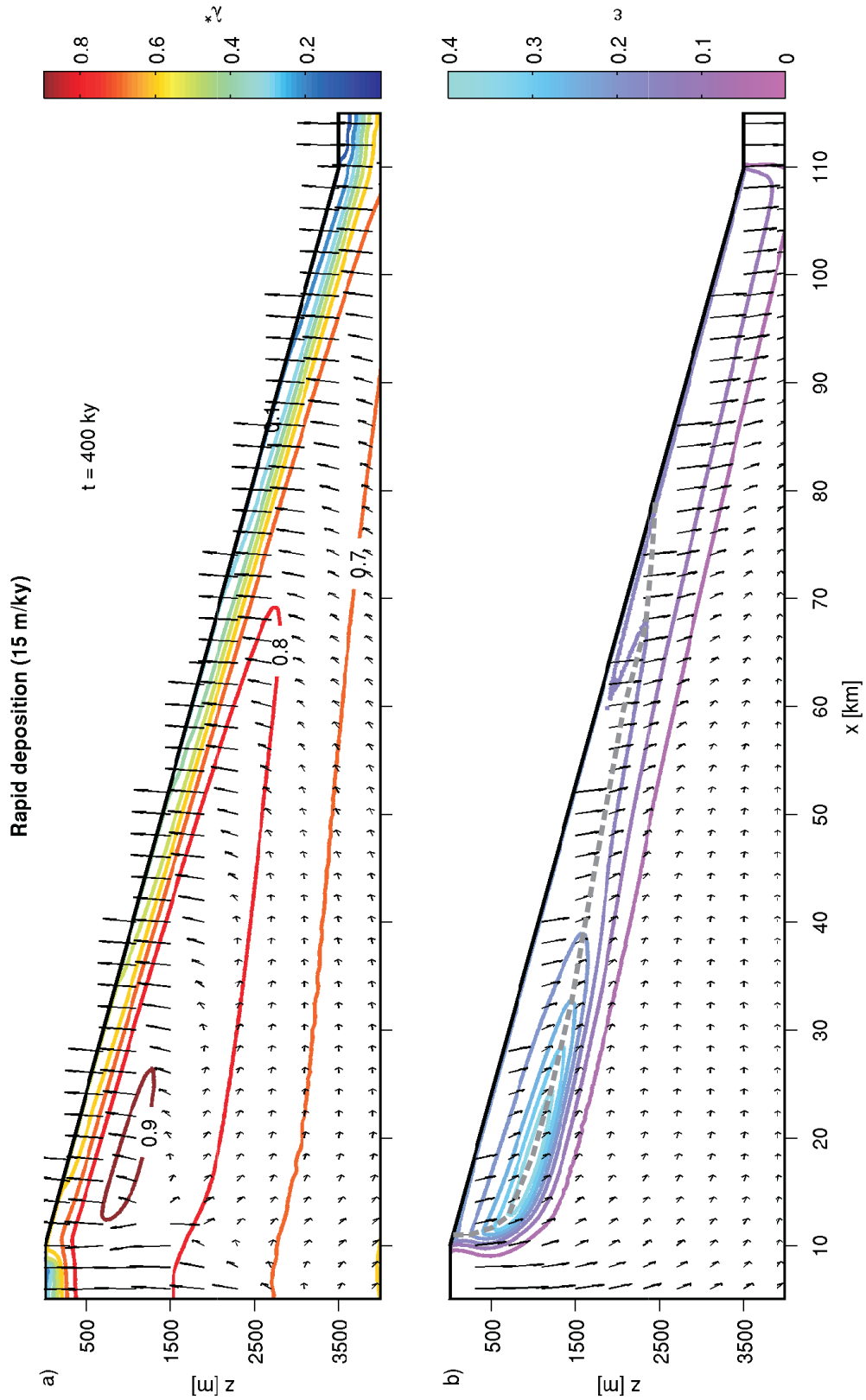


Figure 6.7: Final state of the model with rapid deposition: (a) shows overpressure ratio (contour lines) and the direction of fluid flow with normalised vectors, and (b) depicts shear strain contours and displacement vectors. All vectors are normalised, their apparent differences in length are an effect of vertical exaggeration of the model outline. The grey dashed line delineates the possible slip line.

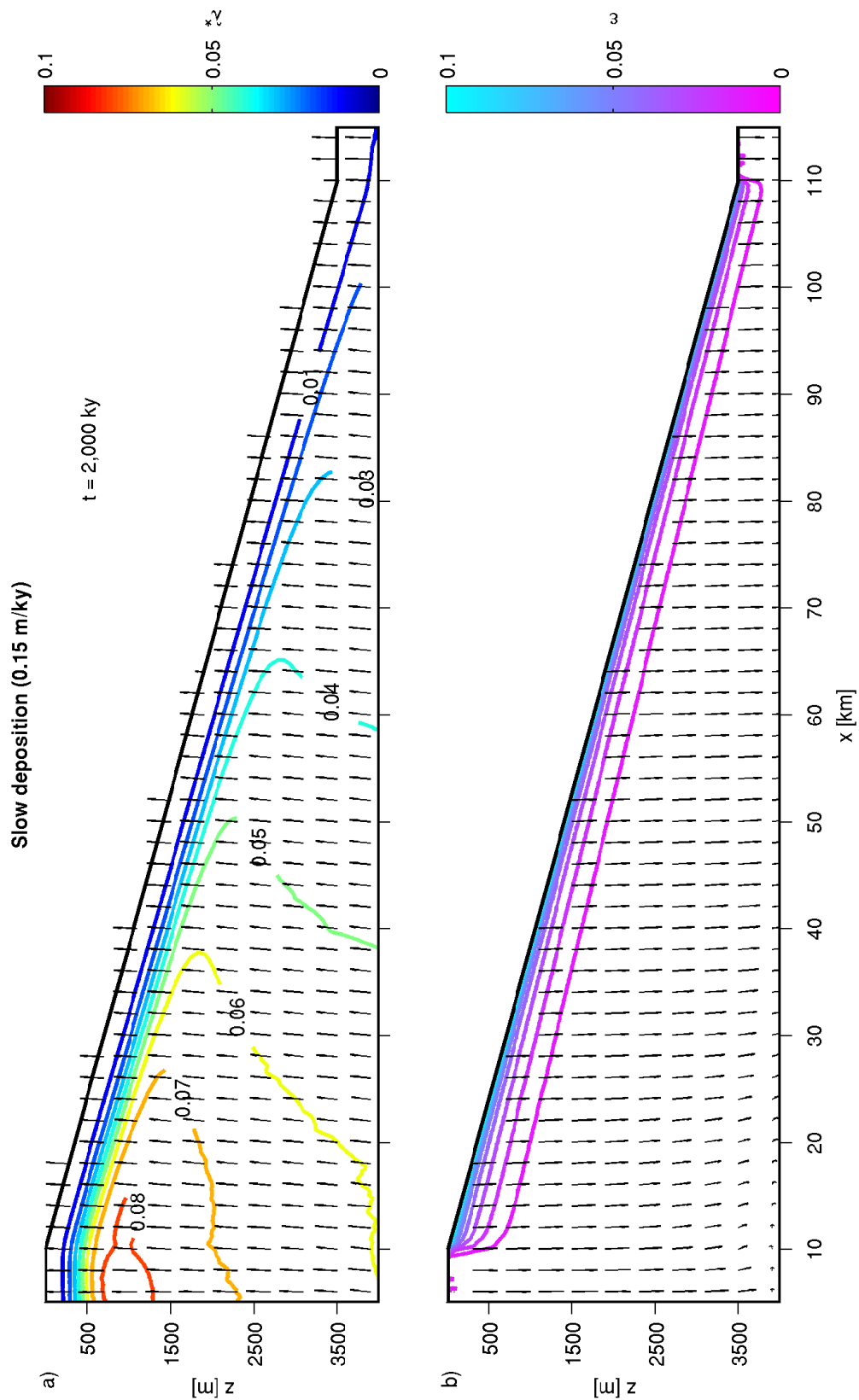


Figure 6.8: Final state of the model with slow deposition: (a) shows overpressure ratio (contour lines) and the direction of fluid flow with normalised vectors, and (b) depicts shear strain contours and displacement vectors. All vectors are normalised, their apparent differences in length are an effect of vertical exaggeration.

### 6.3.2 Consolidation properties tests (model runs M1 to M8)

To test the sensitivity of overpressure generation to consolidation properties, eight model runs are conducted (Table 6.3, M1-M8). All models are subjected to slow rates of sediment deposition with a smooth downslope decrease (load  $S$ ,  $< 0.15$  m/ky). The models differ in one (M1-M7) or several properties (M8) from the previous model (Table 6.2). In models M1 and M2 the compressibilities are different and M3 and M4 have different permeability-porosity relationships. Model M5 has lower absolute permeability magnitudes. The vertical permeability of the overlying virtual sediment is lower than the vertical permeability at the model surface in M6. The critical shear strength is lower in M7. Model M8 combines high compressibility from M1, low permeability as in M5 and low permeable overlying sediment as in M6, to test for maximal overpressure generation.

All models converge and run for 2 million years. Fig. 6.9 shows the stress paths of five exemplary nodes for all models, as well as the respective critical state lines. The stress paths for the selected nodes evolve along the normal compression lines and do not divert significantly from this line. As loading and consolidation progress the distance to the critical state line increases for all selected nodes. Hence, all models are stable and are nowhere close to failure at any time.

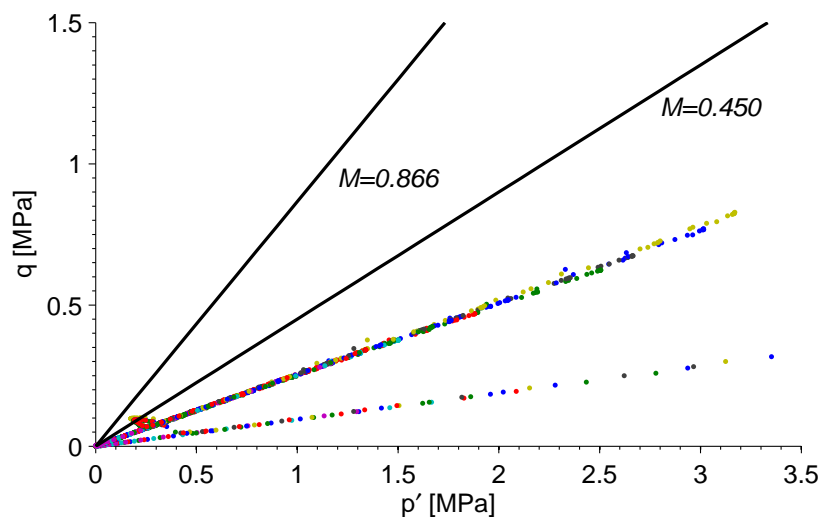


Figure 6.9: Stress paths of several nodes (refer to the caption of Fig. 6.5 for locations of the nodes) in a  $p'$ - $q$  plot for all models listed in Table 6.3. The black lines represent the corresponding critical state lines.

#### 6.3.2.1 Model M1

Model M1 is characterised by a comparatively high compressibility at low stresses, which decreases as stresses increase (Eq. 6.2, Fig. 6.10). The overpressure ratio increases steeply

in the first 100,000 years and flattens afterwards (Fig. 6.10a). It is highest at nodes at the landward side of the model, where load is largest (blue dots). However, the magnitude of  $\lambda^*$  is less than 0.5 % of the hydrostatic vertical effective stress, and therefore negligible. The permeability declines rapidly in the first 800,000 years (Fig. 6.10b). At the end of the analysis  $k_z$  has decreased by almost one order of magnitude and is lowest at the shelf edge (blue marker). Horizontal fluid flow velocities do not exceed 0.015 mm/y at the nodes shown in Fig. 6.10c. Initially, fluid flows in negative  $x$ -direction at two nodes, but flow soon changes direction and fluid flows in positive  $x$ -direction at all nodes. At the nodes that are located close to the landward side where overburden is highest, flow velocities decrease after reaching a maximum. This is most likely an effect of lower permeability compared to nodes that are located at the seaward side of the model (compare Fig. 6.10b).

After 2 million years of loading, a maximum in overpressure ratio locates below the shelf, where the load is highest (Fig. 6.10d). The maximum  $\lambda^*$  is less than 0.05 and situated at a depth of about 1000 m below the new seafloor. At the model surface the overpressure ratio is  $< 0.01$ . The predominant drainage direction is vertically upwards.

### 6.3.2.2 Model M2

As in M1, the compressibility decreases with depth. However, in M2 the compressibility at low stresses is extremely high (Eq. 6.3). The overpressure ratio is considerably higher than in M1 (Fig. 6.11a). The excess pore pressures reach up to 21 % of the hydrostatic vertical effective stress. The increase in  $\lambda^*$  over time has a concave up shape, indicating a higher rate of overpressure ratio increase from about 800,000 years onwards. Permeability decreases continuously and final values are about one order of magnitude smaller than before loading (Fig. 6.11b). The horizontal fluid flow in the four nodes at the right side of the model resembles that of M1 and has a similar velocity. The blue node near the crest of the slope, however, is an exception. Flow velocities are positive until about 800,000 years, subsequently turn negative and reach -0.036 mm/y. This indicates a zone of particularly high excess pore pressure between the blue and the green node near the top of the slope, which starts building up from 300,000 years onwards.

This particular zone is also reflected in the overpressure ratio field at the end of the analysis (Fig. 6.11d). A maximum of  $\lambda^* = 0.22$  occurs at  $x = 14$  km at the model surface. Including the newly deposited sediment, the model surface at this location would correspond to a burial depth of approximately 280 m. Interestingly, the location of the overpressure ratio maximum does not agree with the location of the maximum load. The overpressure ratio is considerably smaller upslope (left) of this maximum, where overburden is highest. A possible explanation for this apparent contradiction is higher shear strain on the slope than on the flat shelf. Shearing causes a volume loss

and hence an increase in excess pore pressure. The rate at which volume is lost at the surface is particularly fast in this model due to extremely high compressibility at shallow depth. The overpressure ratio is about 0.05 in all other areas of this model. The flow direction vectors change from left-upward directed flow to right-upward directed flow at the location of the  $\lambda^*$  maximum, as a result of higher pore pressures at the upper slope than at the shelf.

### 6.3.2.3 Model M3

The porosity-permeability relationship in M3 is that of hemipelagic clay as suggested by Binh et al. (2009). The initial permeability is lower than that of the previous models (Fig. 6.12b). Nevertheless, the rate of permeability decrease is less steep, so that final permeabilities are similar to those of the previous models. Magnitudes and development of overpressure ratio and horizontal fluid flow over time are similar to M1. At the end of the analysis the overpressure ratio is highest at 1000 m depth below the shelf ( $\lambda^* = 0.08$ ).

### 6.3.2.4 Model M4

In this model the porosity-permeability relationship is that of silty clay (Binh et al., 2009). Initial as well as final permeabilities at the selected nodes are lower than those of the previously shown model (Fig. 6.13b). The overpressure ratio over time is about twice as high as in M1, but the excess pore pressure is not higher than about 1% of the hydrostatic vertical effective stress at any time (Fig. 6.13a). Flow velocities are similar to those in M1 and M3. The overpressure ratio field at the end of the analysis also resembles that of M1 and M3 with maximum values just under 0.09.

### 6.3.2.5 Model M5

This model has the same porosity-permeability relationship as the original model, but all values are one magnitude lower. The temporal evolution at the selected nodes as well as the spatial patterns of the overpressure ratio (Fig. 6.14a,d) are identical to that of models with higher permeability (e.g. M1, M3, M4). However, the absolute values of  $\lambda^*$  are slightly higher. The  $\lambda^*$  maximum at the end of the analysis at 1000 m depth is 0.2 in M5, as opposed to  $\lambda^* = 0.08$  in M1, M3 and M4. Horizontal fluid velocity is lower than in previous models (Fig. 6.14c). The main direction of drainage is vertically upwards, although in the deepest part the fluid tends to flow sideways (Fig. 6.14d). This is possibly a result of extremely low vertical permeabilities near the lower boundary of the model. Lateral permeability is an order of magnitude higher.

### 6.3.2.6 Model M6

In model run M6 the newly deposited sediment is assigned a permeability that is one order of magnitude lower than that of the sediment at the model surface. The newly deposited sediment thus acts like a 'cap' to vertical upwards fluid flow. The overpressure ratio continuously increases as time progresses (Fig. 6.15a), but does not exceed 0.015. The decrease in permeability over time (Fig. 6.15b) as well as the horizontal fluid flow pattern at the selected nodes (Fig. 6.15c) resemble those of previous models M1, M3, M4 and M5. The last increment of the analysis is an exception as the horizontal velocity increases abruptly at all nodes except the node at the shelf edge. The overpressure ratio field after the final time step shows the typical maximum at 1000 m depth below the shelf, which has already been observed in models M1 and M3-M5. Compared to these models,  $\lambda^*$  near the surface is slightly higher here.

### 6.3.2.7 Model M7

Even if the critical friction angle is as low as  $15^\circ$ , the slope is stable. Model run M7 shows the lowest overpressure ratio of all models (Fig. 6.16a). Permeability decreases comparatively slowly (Fig. 6.16b) and horizontal flow is as slow as 0.008 mm/y (Fig. 6.16c). M7 differs from all previously shown models in that the overpressure ratio becomes higher with increasing depth (Fig. 6.16d) and decreases seawards.

### 6.3.2.8 Model M8

This model combines those consolidation properties that generated the most significant overpressure ratios: high compressibility as in M2, low permeability as in M5 and a less permeable sediment 'cap' as in M6. Not surprisingly, the overpressure ratio is higher than in any previous model with slow deposition. The  $\lambda^*$  development over time is of concave down shape with an initial steep increase in the first  $\sim 300,000$  years (Fig. 6.17a). Horizontal velocity at the selected nodes shows a similar pattern to that of M2. Flow velocity in node 1 (blue marker) reaches a maximum at about 250,000 years after the onset of loading and then decreases rapidly, with a tendency to turn into negative flow if the model were run beyond the 2 million year limit (Fig. 6.17c). The maximum overpressure ratio at the end of the analysis is 0.43. Its location, just seaward of the shelf break, is identical to that observed in model run M2. The direction of fluid flow near the shallow overpressure maximum is also in agreement with M2. At greater depth horizontal flow dominates, similar to the flow in model run M5 with low permeability.

### 6.3.2.9 Summary and interpretation

There are no indications for instability due to excess pore pressure in any of the M1-M8 models. All models are based on a slope that is initially in hydrostatic conditions. This is not necessarily the case, and the modelling results may therefore underestimate the overpressure ratio. The corresponding initial overpressure ratio from Table 6.1 at about 10 m below the original seafloor is, however, negligible ( $< 0.003$ ).

Model runs M2 and M8 are exceptional, as they are the only models with significantly elevated shallow overpressure ratios (Figs. 6.11a,d and 6.17a,d). The excess pore pressure reaches 22 % and 43 % of the vertical effective stress if pore pressures were hydrostatic. A common feature of both models is the high compressibility of the uppermost sediment (Table 6.3). This suggests that compressibility is the key factor for generating shallow ( $< 300$  mbsf) overpressure.

If permeability is low, maximum overpressure tends to develop at burial depths of about 1000 m. This is deeper than the depth at which failure planes are observed typically in nature (100 m; Hühnerbach et al., 2004). The sediment's permeability is therefore of secondary importance for slope stability.

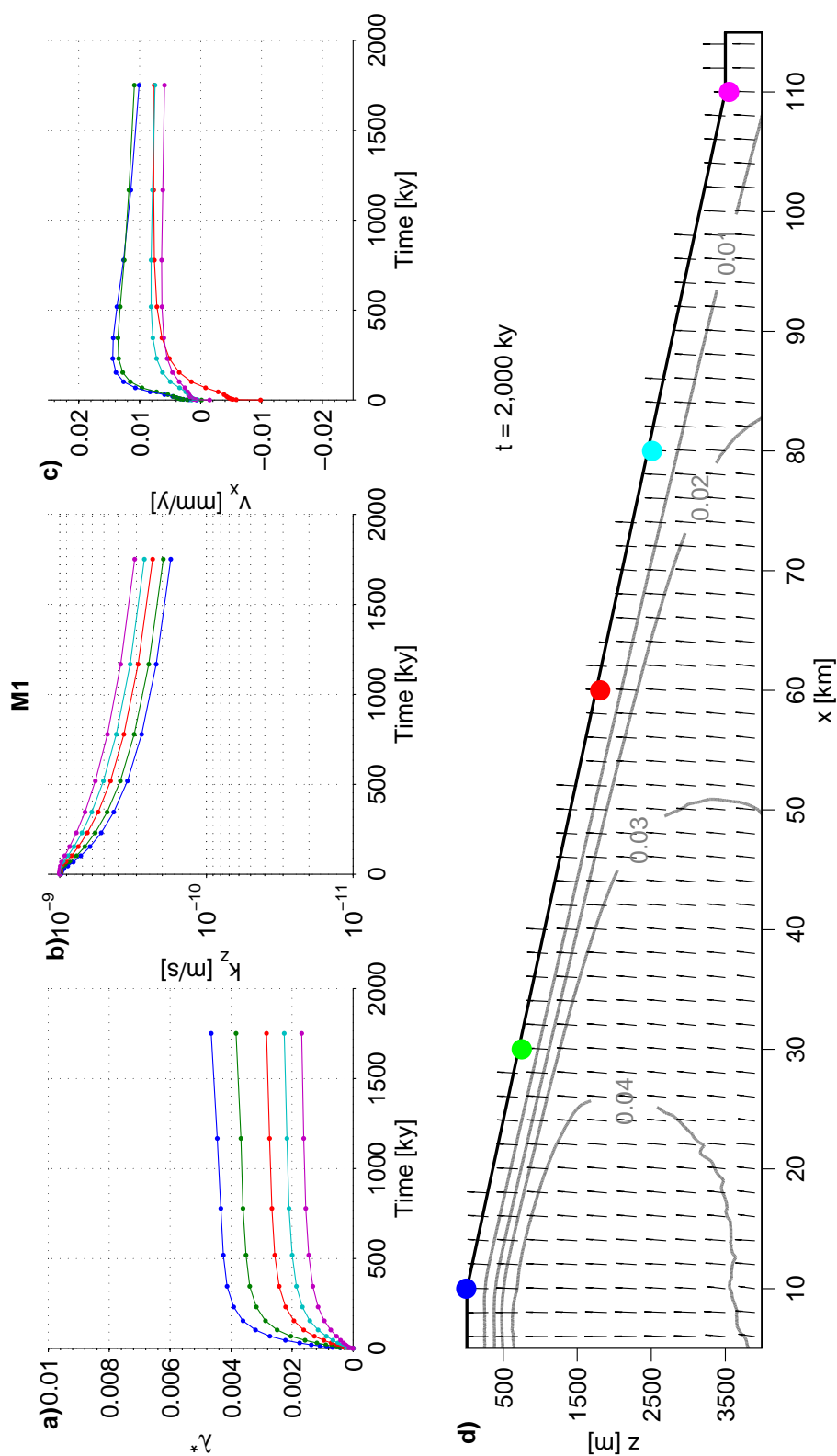


Figure 6.10: FE solutions for model run M1 with depth-dependent compressibility after Long et al. (2011). Temporal evolution of five nodes along the slope for a) overpressure ratio  $\lambda^*$ , b) vertical permeability  $k_z$  and c) horizontal fluid flow velocity  $v_x$ . The contour lines in d) depict the final overpressure ratio field after 2 million years and the black arrows show the direction of fluid flow (normalised vectors). Model outline is vertically exaggerated.

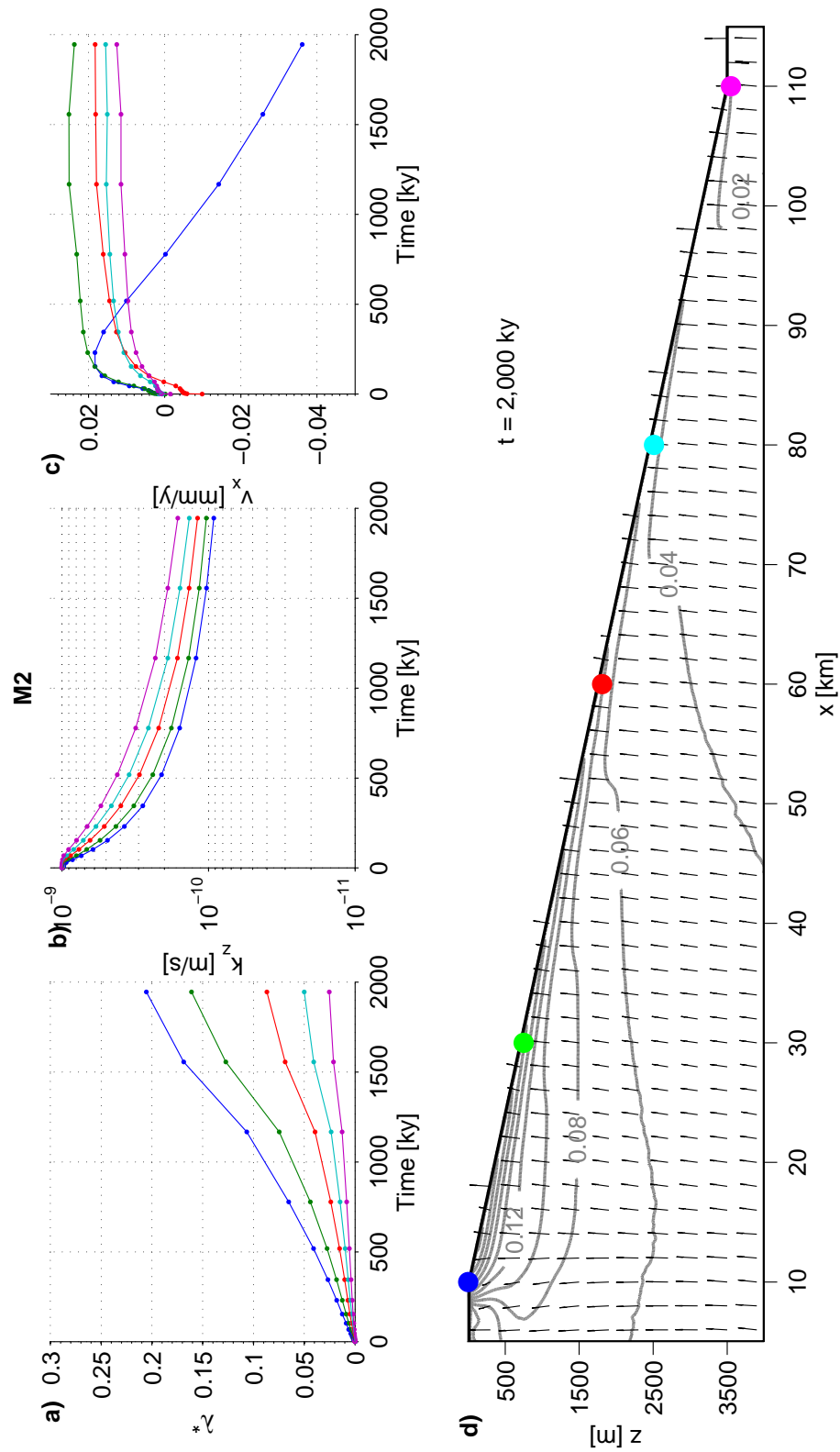


Figure 6.11: FE solution for model run M2 with depth-dependent compressibility and extremely high shallow compressibility. Notation is identical to Fig. 6.10.

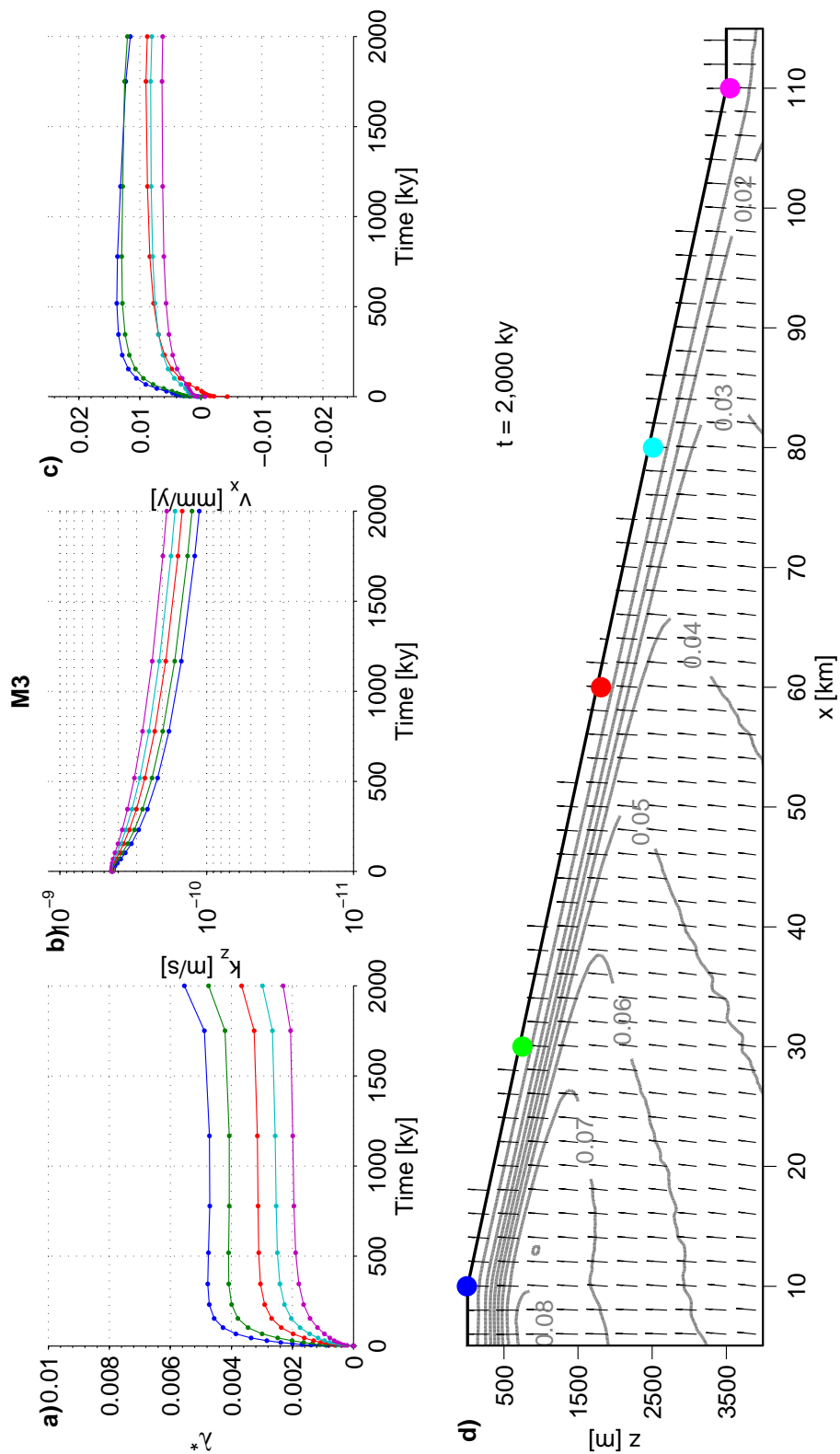


Figure 6.12: FE solution for model run M3 with a porosity-permeability relationship for hemipelagic sediment. Notation is identical to Fig. 6.10.

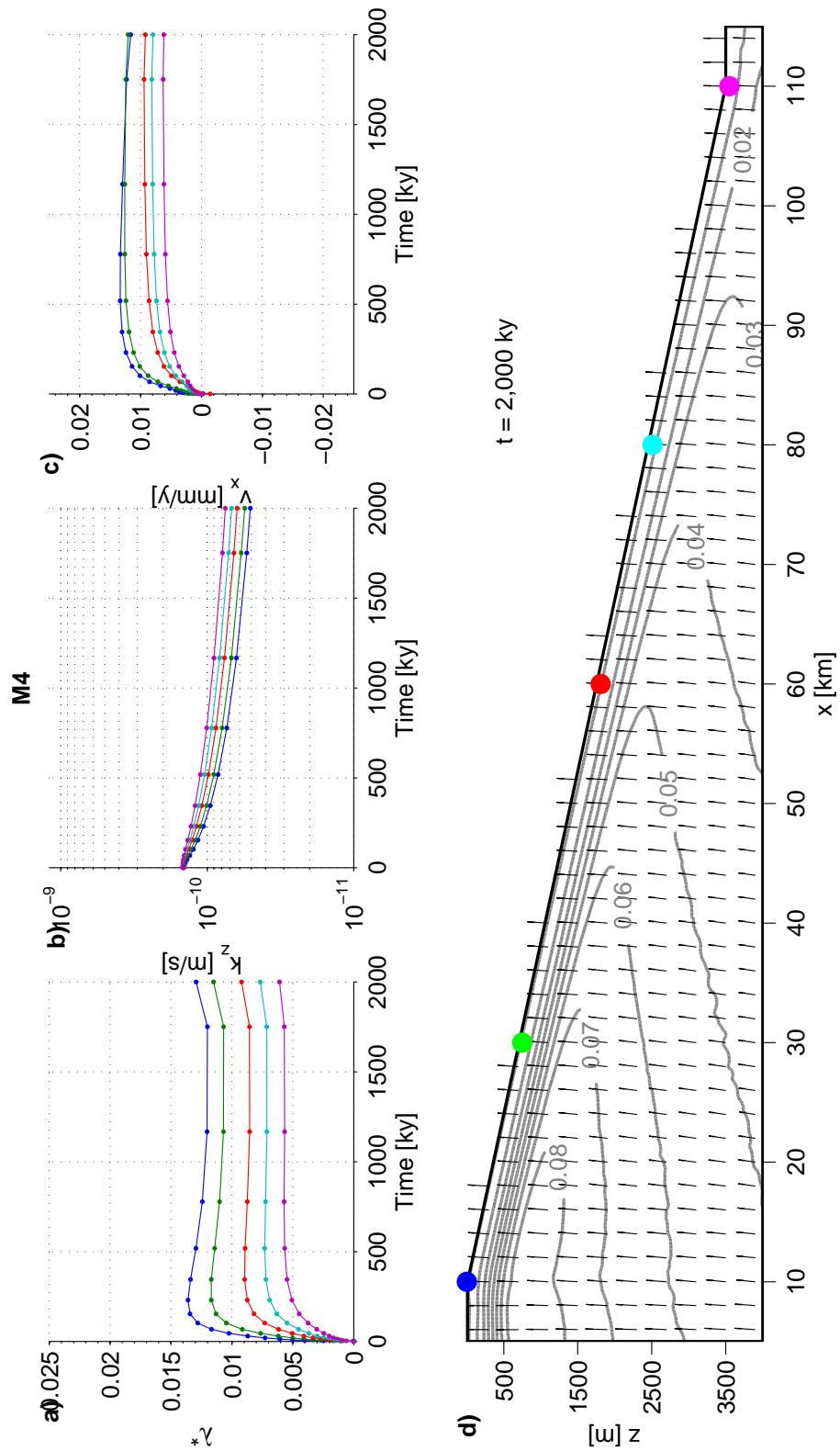


Figure 6.13: FE solution for model run M4 with a porosity-permeability relationship for silty clay. Notation is identical to Fig. 6.10.

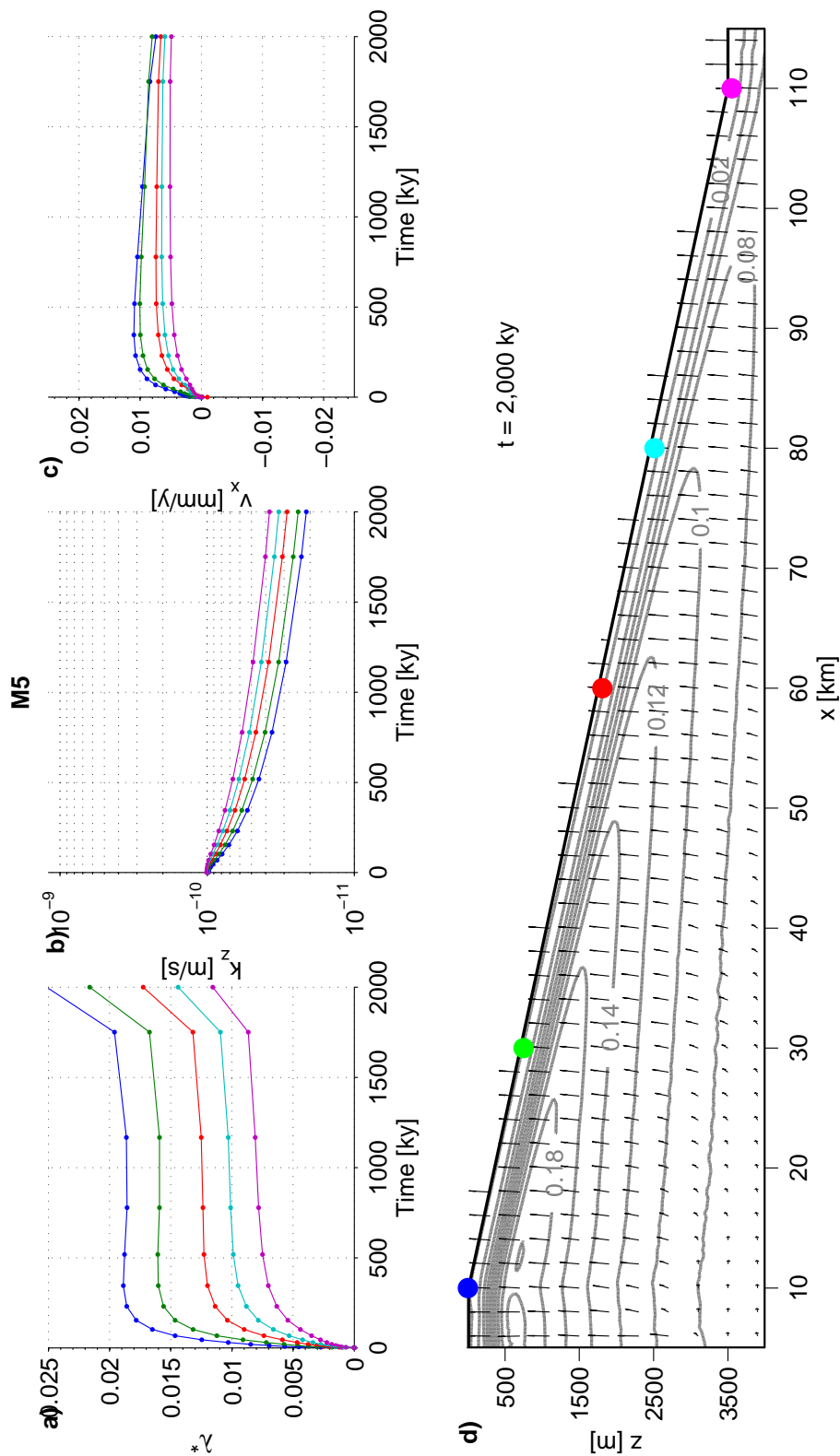


Figure 6.14: FE solution for model run M5 with a permeability that is  $1/10_{th}$  that of the reference model in Figs. 6.6 and 6.8. Notation is identical to Fig. 6.10.

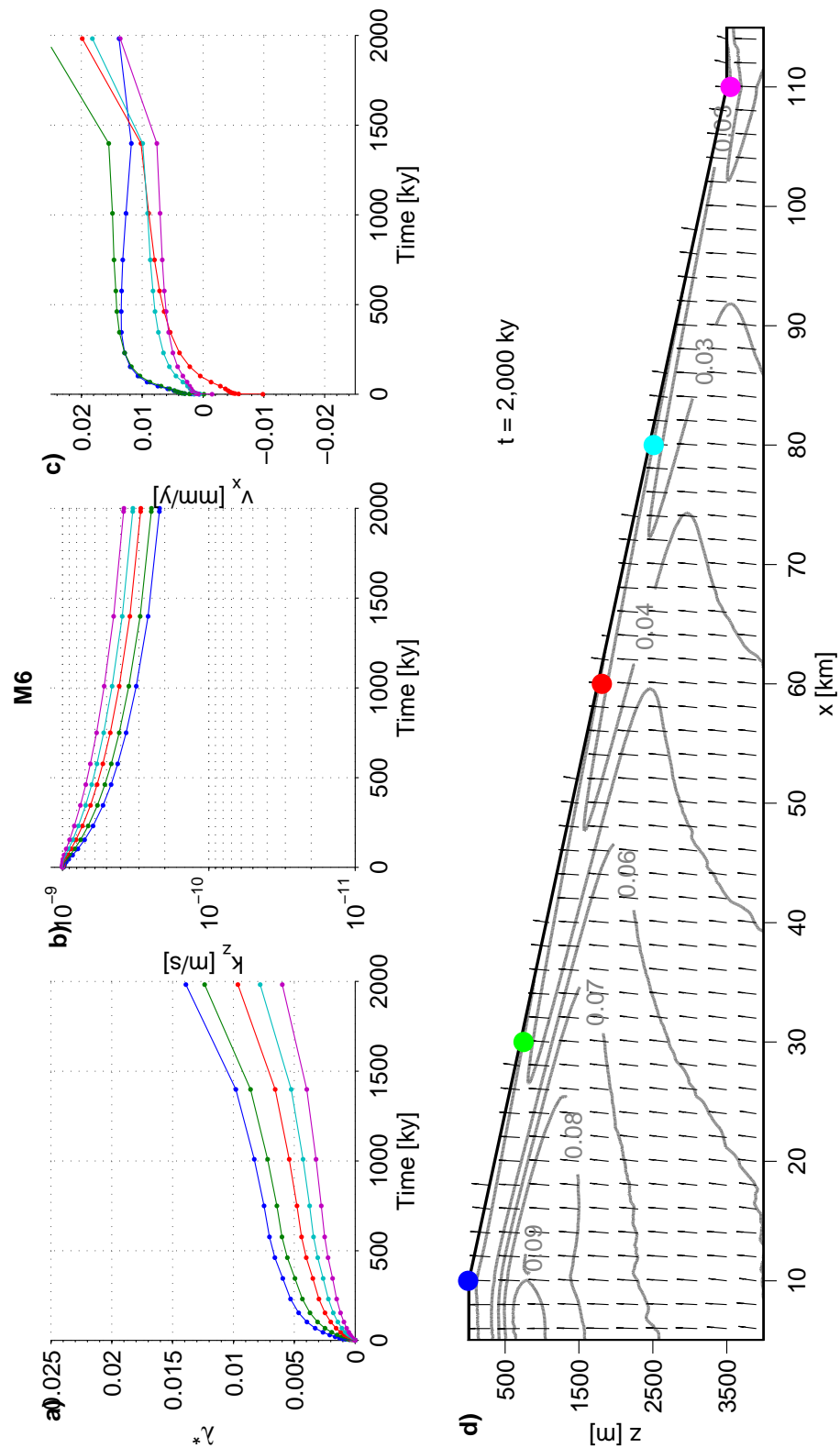


Figure 6.15: FE solution for model run M6 in which the newly deposited sediment has a lower permeability than the sediment at the model surface. Notation is identical to Fig. 6.10.

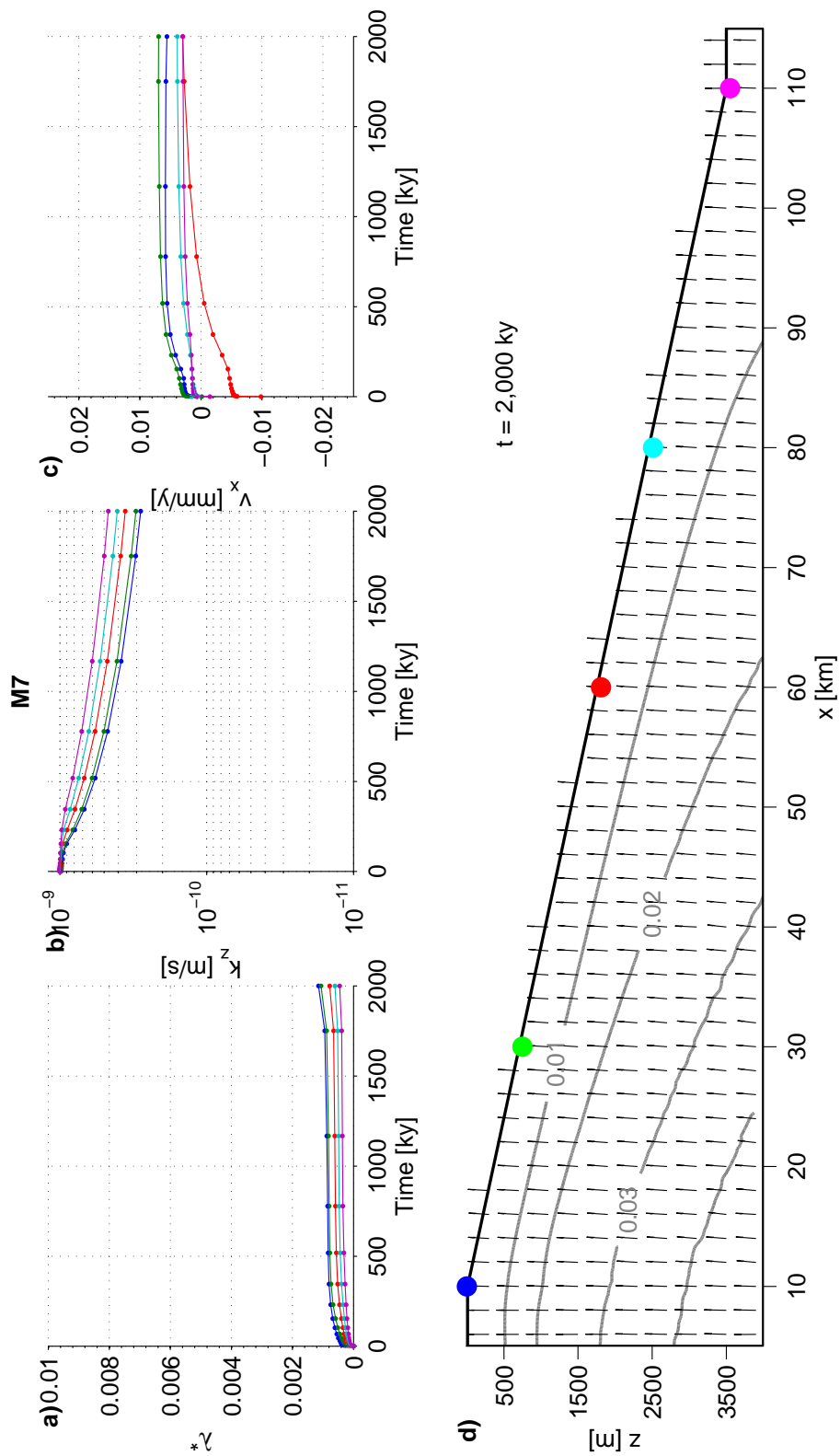


Figure 6.16: FE solution for model run M7 with a low angle of critical friction ( $\phi'_{crit} = 15^\circ$ ). Notation is identical to Fig. 6.10.

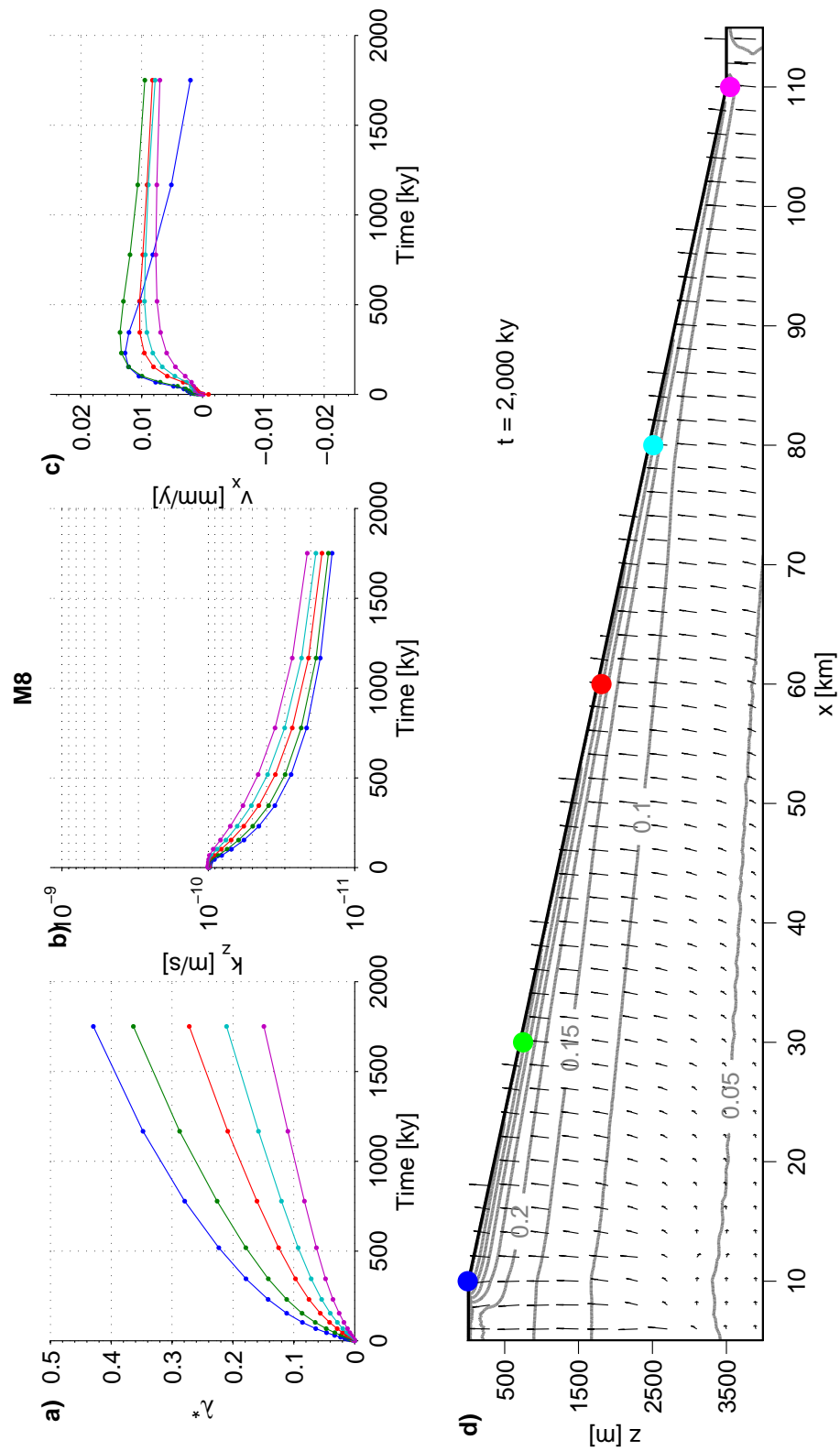


Figure 6.17: FE solution for model run M8 with an extremely high compressibility, low permeability and a less permeable newly deposited sediment. Notation is identical to Fig. 6.10.

### 6.3.3 Lateral flow tests (model runs M9-M16)

I now investigate whether lateral flow can contribute to instability at continental slopes with low sedimentation rates. I present the results for homogeneous models with permeability anisotropy (M9, M10), horizontal permeability decrease (M11), horizontal permeability decrease combined with strong anisotropy (M12), as well as models that include a layer of higher permeability (M13-M16). The permeability of the higher permeability layer is uniform along the slope (M13, M14), or decreases towards the toe of the slope (M15, M16). The higher exponential load  $L$  (Fig. 6.2b) is applied in model runs M14 and M16. All models converge and run for 2 million years. None of the models shows indication for instability (Fig. 6.9).

#### 6.3.3.1 Model M9

The sediment's horizontal permeability is two orders of magnitude higher than its vertical permeability in model run M9. The overpressure ratio near the model surface is extremely low and therefore negligible everywhere in the model over the modelled time period ( $< 0.002$ , Fig. 6.18a). Permeability decreases by almost one order of magnitude (Fig. 6.18b). Horizontal flow velocity at the selected nodes is highest on the upper slope ( $x=30$  km, green marker) but does not exceed  $0.15$  mm/y (Fig. 6.18c). Flow velocities at the shelf edge (blue markers) decrease during the analysis. This can be attributed to a more rapid decrease in permeability where overburden is high. An overpressure ratio maximum of just under  $0.06$  develops at a depth of about  $1000$  m, which decreases towards all sides (Fig. 6.18d). This maximum locates at  $x=15$  km and is slightly offset from the area of highest overburden ( $0-10$  km). Shallow overpressure is  $< 0.01$ . Fluid flow has a stronger lateral component than in any of the previous models.

#### 6.3.3.2 Model M10

This model has an extremely high anisotropy ratio of  $1000$ . It exhibits similar patterns to M9 in the temporal evolution of  $\lambda^*$ ,  $k_z$  and  $v_x$  (Fig. 6.19a,b,c). However, the overpressure ratio is smaller ( $\lambda^* < 0.04$ ) and horizontal flow velocities are considerably higher, reaching up to  $0.6$  mm/y. The overpressure maximum locates at the same depth as in M9, but slightly further to the right at  $x=20$  km. It is lower in this model ( $\lambda^* < 0.04$ ) compared to M9 ( $\lambda^* < 0.06$ ). The direction of drainage is almost purely horizontal (Fig. 6.19d).

#### 6.3.3.3 Model M11

In model run M11 the permeability decreases with increasing distance from the shelf as well as with depth. This means that the permeability is lowest at the toe of the slope

(magenta marker, Fig. 6.20b). The low permeability at this node explains the highest overpressure ratio (Fig. 6.20a). The velocity pattern for the selected nodes of M11 is identical to M9, but about one order of magnitude smaller (Fig. 6.20c). This can be explained by the ten times higher permeability anisotropy ratio in M9. Although both models have the same vertical permeability, the horizontal permeability in M11 is one order of magnitude lower than in M9.  $\lambda^*$  increases to just over 0.07 at  $x=15$  km and a depth of 1000 m below the model surface. Vertical upwards drainage is dominant along the modelled sediment body.

#### 6.3.3.4 Model M12

Model M12 combines the lateral permeability decrease as in M11 with high permeability anisotropy as in M10. The overpressure ratio over time remains low ( $\lambda^* < 0.003$ , Fig. 6.21a). Horizontal flow velocities (Fig. 6.21c) resemble those of M10, as both models have permeability anisotropy ratios of 1000. After 2 million years of loading two  $\lambda^*$  maxima can be observed (Fig. 6.21d). Both maxima occur at depths of 1500 m below the seafloor, and have a  $\lambda^*$  magnitude of just above 0.035. They are located at the upper slope ( $x=30$  km) and the lower slope ( $x=105$  km). Fluid flow is largely horizontal.

#### 6.3.3.5 Model M13

M13-M16 are models with a sand layer acting as an aquifer. In M13, the overpressure ratio at selected nodes is small ( $\lambda^* < 0.03$ , Fig. 6.22a). Horizontal flow is comparatively fast in the sand layer (cross markers,  $\sim 0.3$  mm/y) and continuously increases as time progresses, especially at nodes where overburden is highest (Fig. 6.22c). Flow velocities in the surrounding clay are smaller (circle markers). An overpressure maximum of  $\lambda^* = 0.055$  occurs at a sub-seafloor depth of 1000 m at  $x=5$  km (Fig. 6.22d). Overall, flow is vertically upwards. The flow direction within the aquifer is largely horizontal but vectors in the graphic display are too coarse to give flow direction within the aquifer.

#### 6.3.3.6 Model M14

The load applied to this model is localised at the shelf with a sharp seawards decay (load L, Fig. 6.2a). High overpressure ratios are limited to areas close to the shelf (Fig. 6.23a). The permeability decrease is particularly low in areas of low overburden (Fig. 6.23b). Horizontal flow velocities and directions are similar to M13. However, in contrast to M13, velocity at the shelf edge decreases over time here (Fig. 6.23c). The location of the overpressure maximum agrees with that in M13 but is slightly higher ( $\lambda^* = 0.06$ ).

### **6.3.3.7 Model M15**

The permeability within the aquifer decreases with increasing distances from the shelf in this model. The magnitude, temporal and spatial distribution of  $\lambda^*$  and  $v_x$  (Fig. 6.24) are very similar to those in M13.

### **6.3.3.8 Model M16**

The set up and properties of model M16 are identical to M15. The difference is that here, the more localised load L is applied. Nevertheless, the results hardly differ from those obtained from M14.

### **6.3.3.9 Summary and interpretation**

All models are stable and excess pore pressure is always below 10 % of the hydrostatic vertical effective stress. Overall, overpressure ratios are smaller in models with a high permeability layer (M13-M16) than in models without such a layer. The results suggest that lateral fluid flow redistributes excess pore pressure away from the area of high overburden. As a consequence, the slope becomes more stable. The pressure shift from areas of high overburden into areas of low overburden is not strong enough to significantly affect the stability of the slope anywhere in the model.

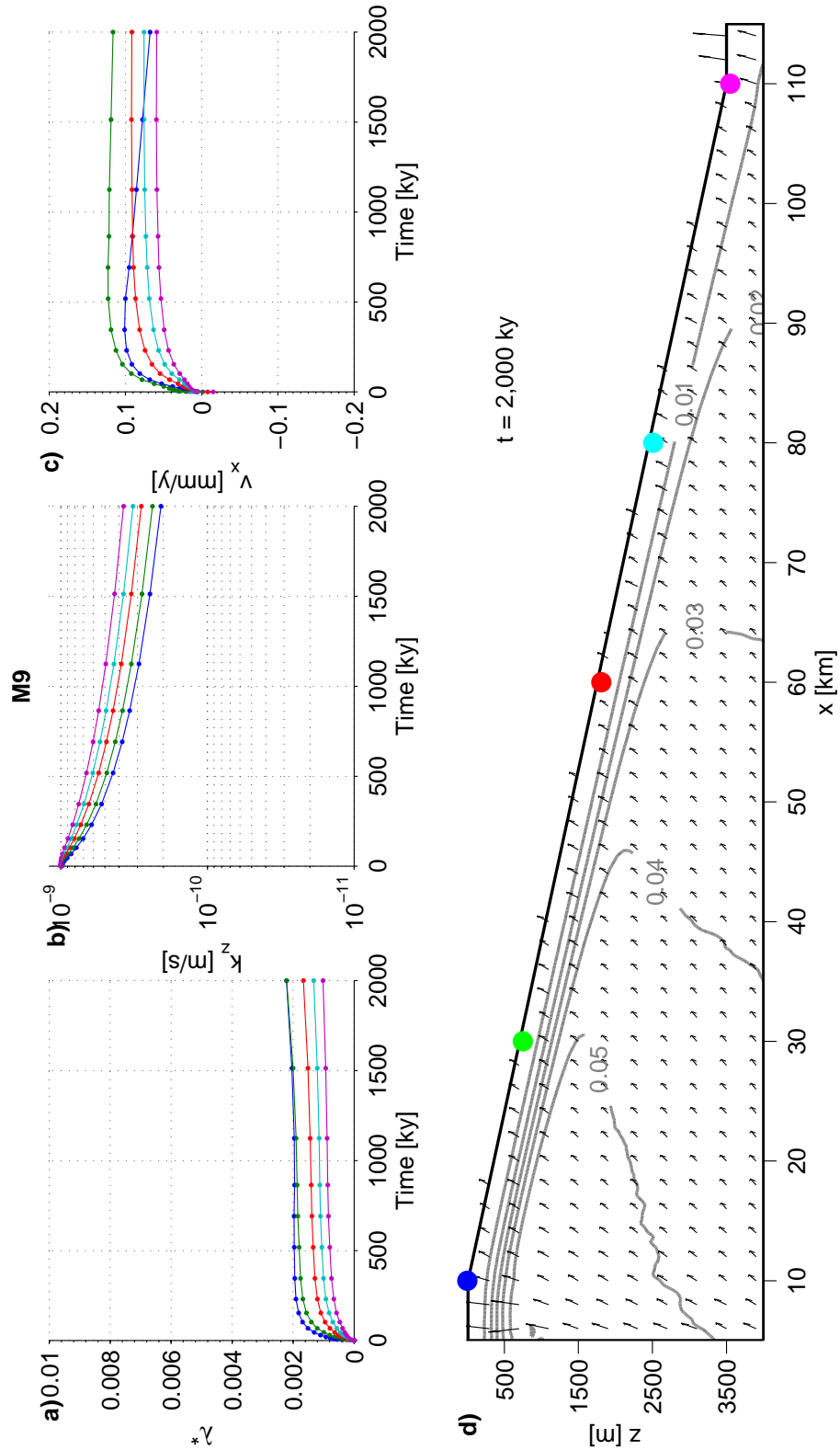


Figure 6.18: FE solutions for model run M9 with a permeability anisotropy ratio of 100. Temporal evolution of five nodes along the slope for a) overpressure ratio  $\lambda^*$ , b) vertical permeability  $k_z$  and c) horizontal fluid flow velocity  $v_x$ . The contour lines in d) depict the final overpressure ratio field after 2 million years and the black arrows show the direction of fluid flow. Flow vectors are normalised, however, due to vertical exaggeration the length of the horizontal vectors is reduced.



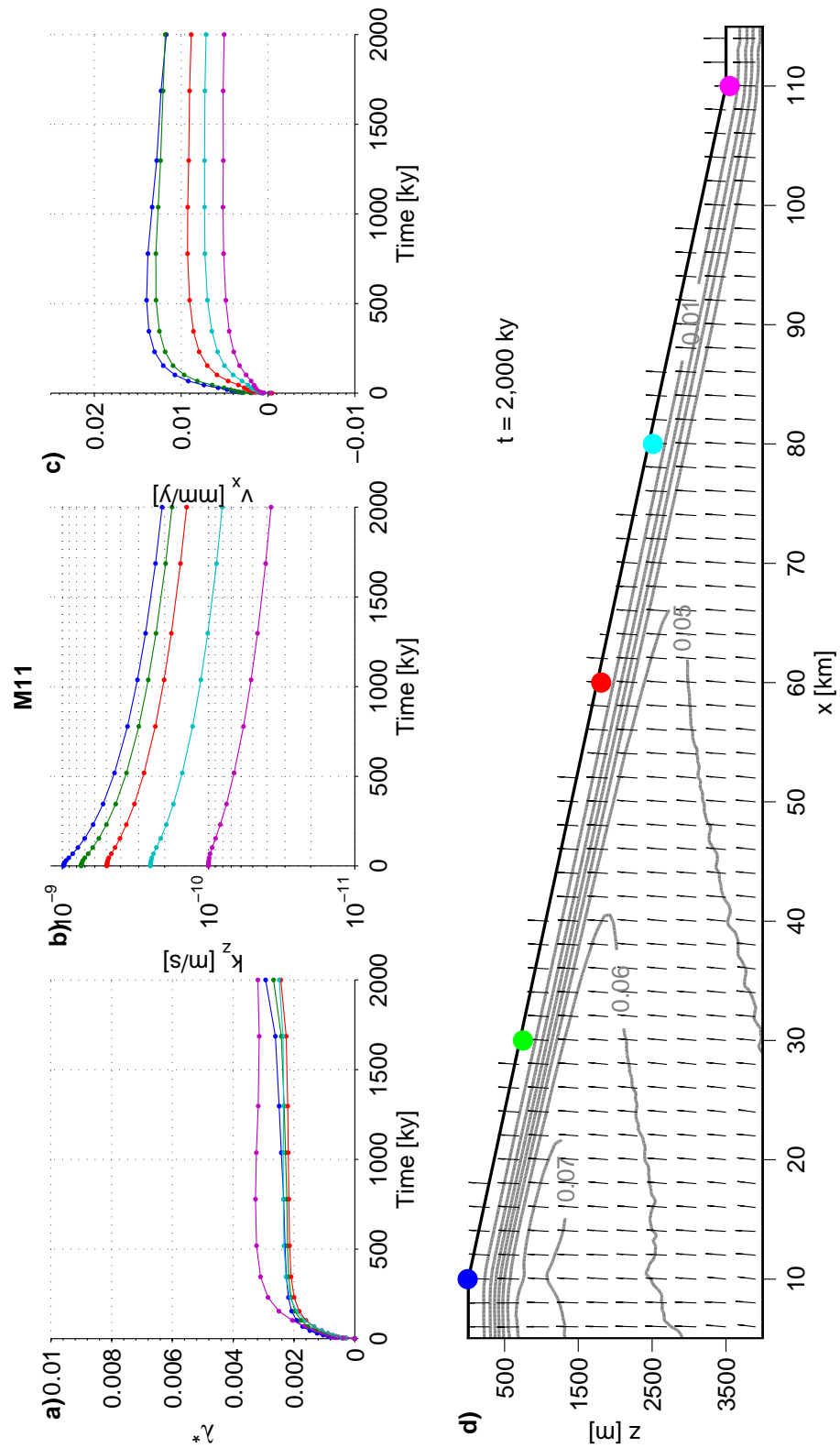


Figure 6.20: FE solution for model run M11 with horizontal permeability decrease. Notation is identical to Fig. 6.18.

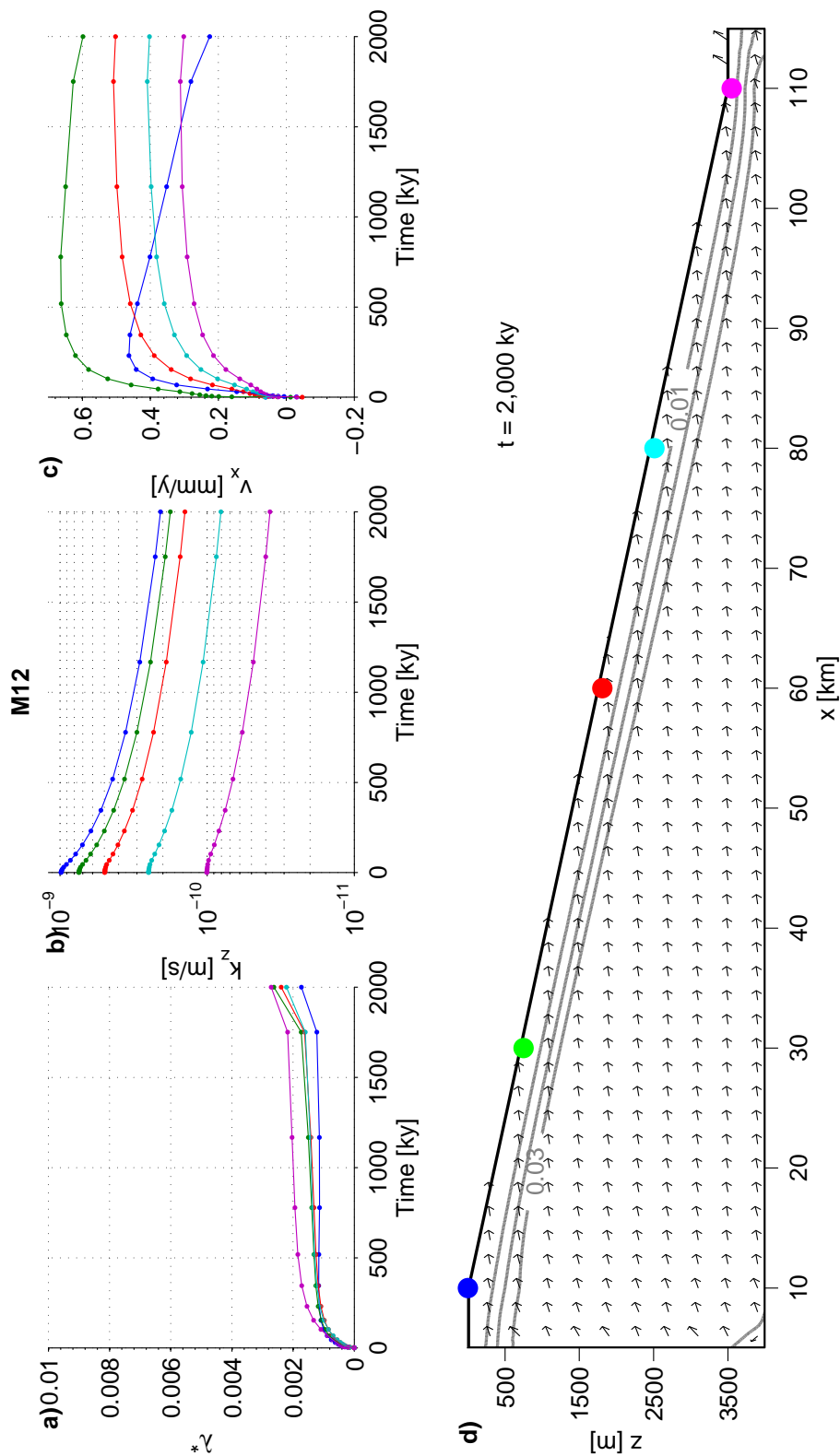


Figure 6.21: FE solution for model run M12 horizontal permeability decrease and permeability anisotropy of 1000. Notation is identical to Fig. 6.18.

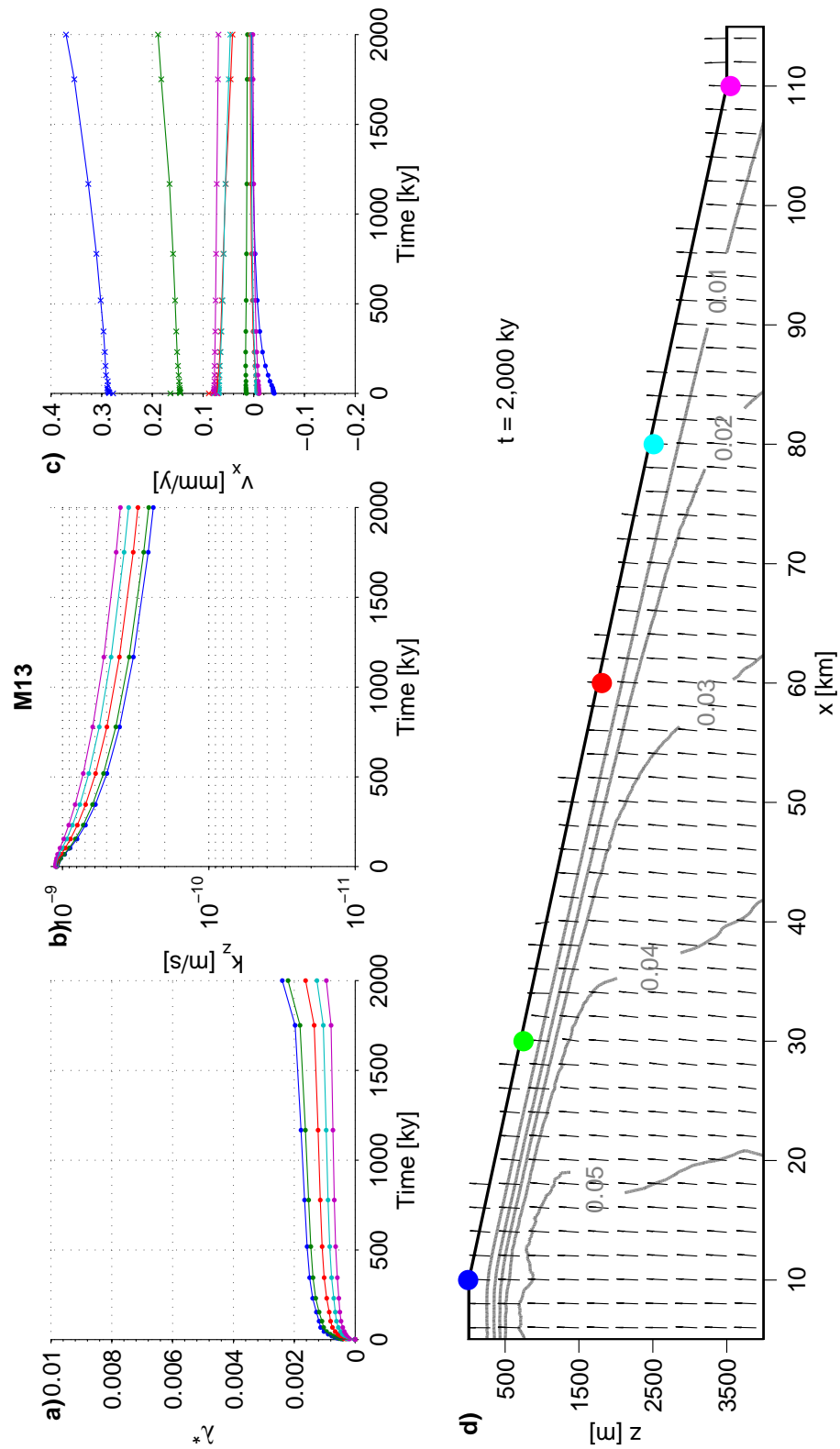


Figure 6.22: FE solution for model run M13 with a sand layer. Notation is identical to Fig. 6.18.

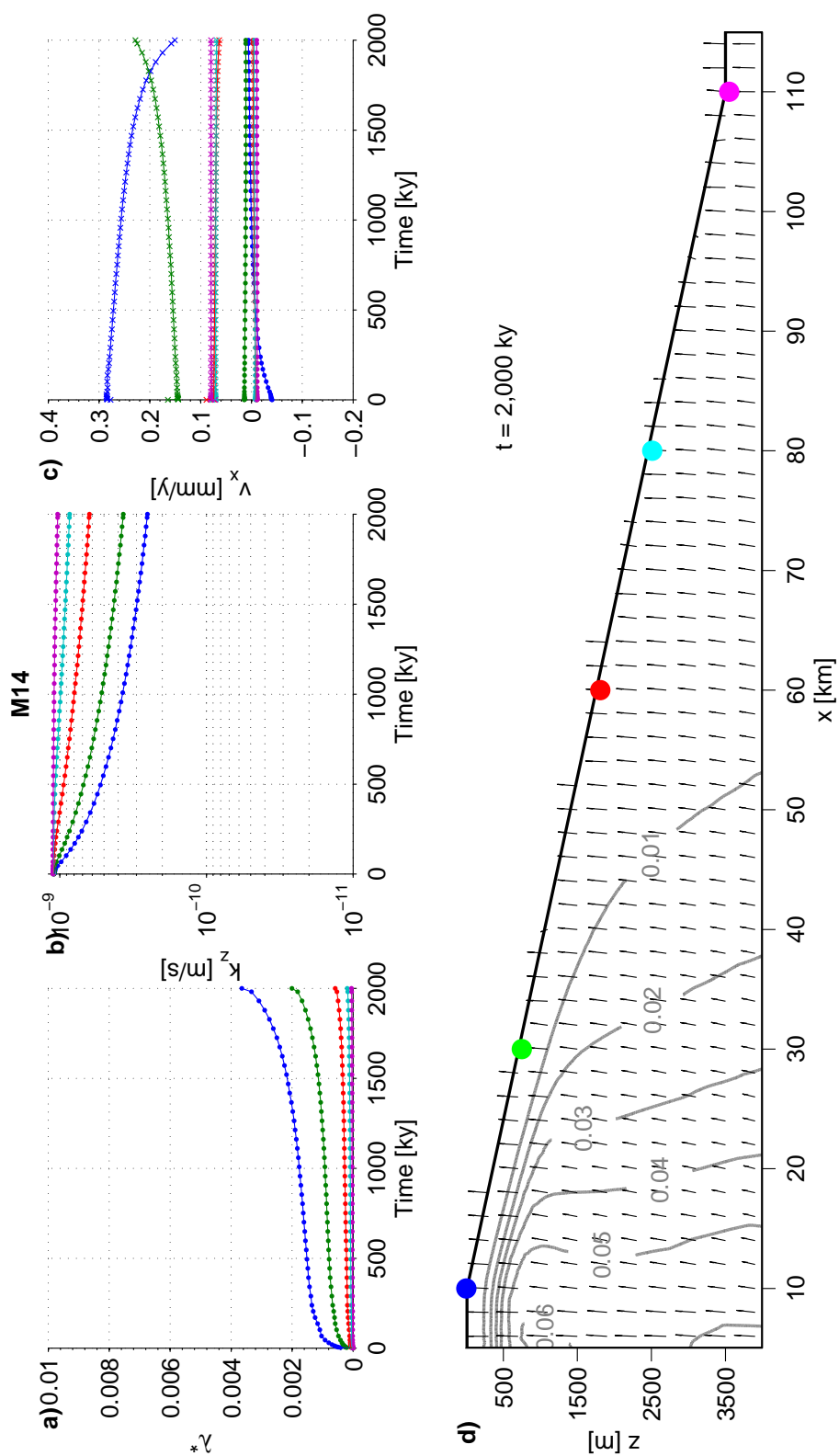


Figure 6.23: FE solution for model run M14 with sand layer loaded by localised load distribution L. Notation is identical to Fig. 6.18.

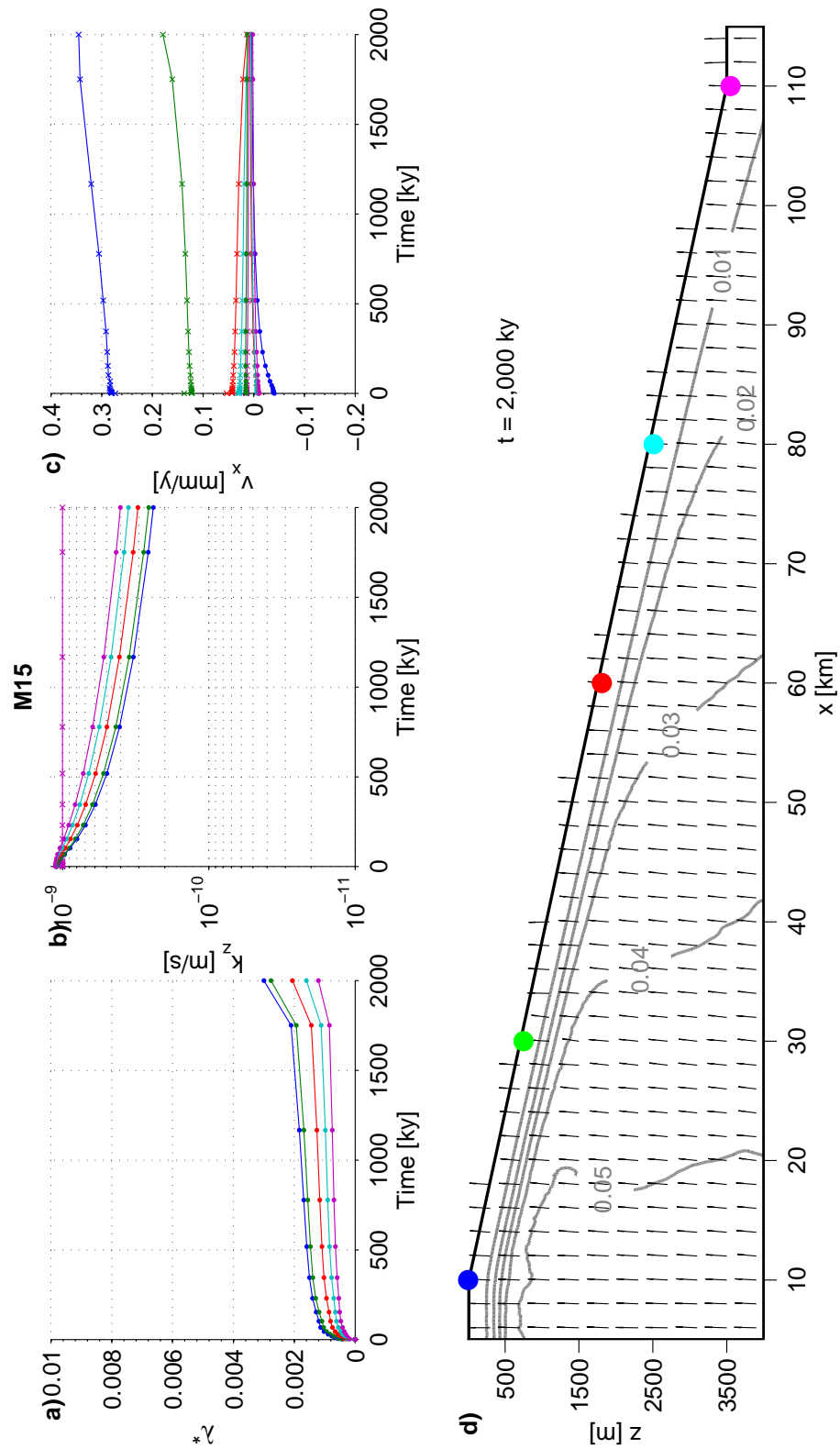


Figure 6.24: FE solution for model run M15 with a sand layer whose permeability decreases seawards. Notation is identical to Fig. 6.18.

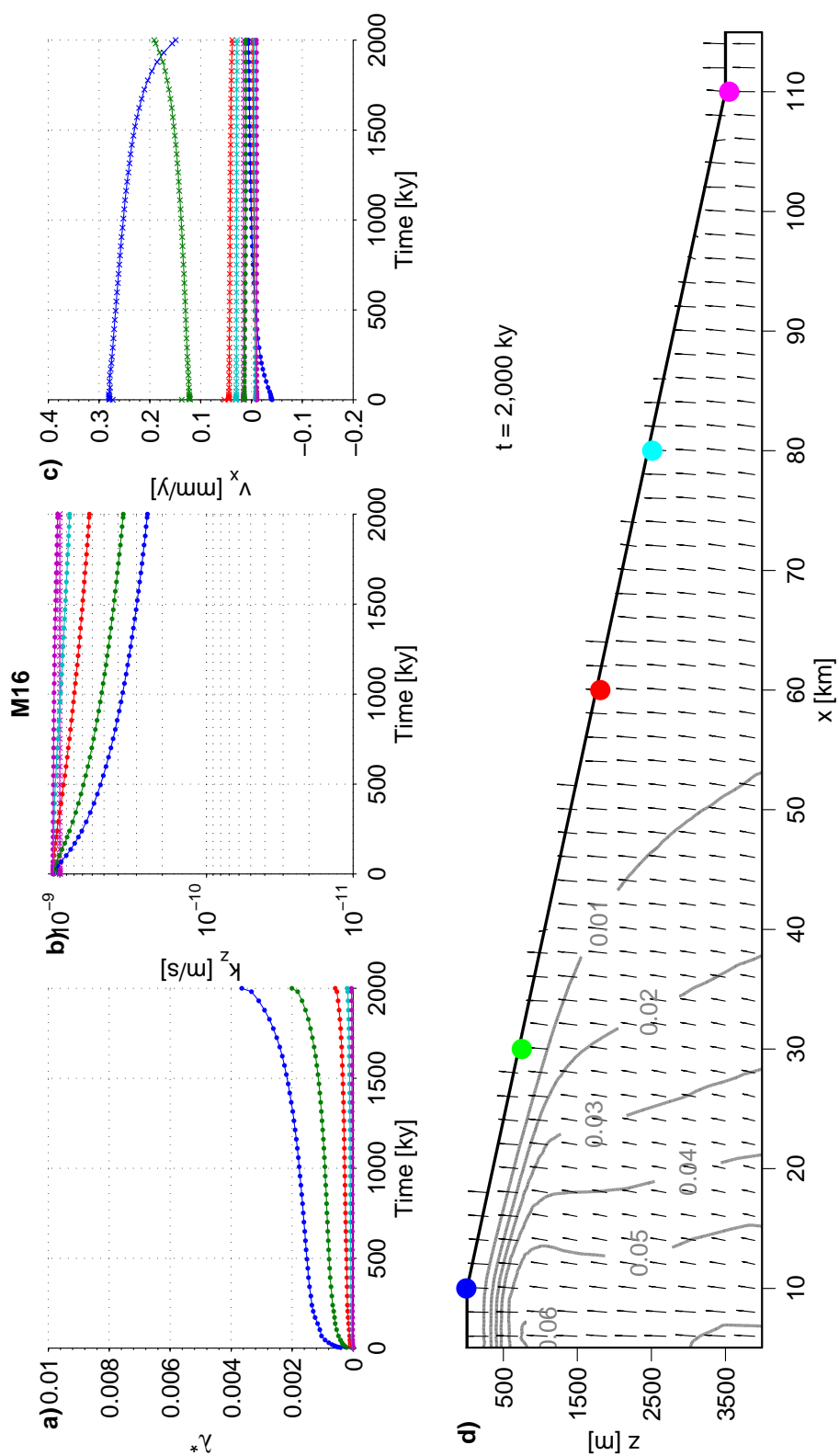


Figure 6.25: FE solution for model run M16 with a sand layer whose permeability decreases seawards and which is loaded by load distribution load  $L$ . Notation is identical to Fig. 6.18.

## 6.4 Discussion

Pore pressures in excess of hydrostatic have been measured by drilling at a number of continental margins (e.g. Kvalstad et al., 2005; Flemings et al., 2008). Laboratory experiments and modelling have shown that consolidation of soft marine sediments during burial can generate excess pore pressures when certain preconditions, such as high sedimentation rates, are fulfilled (Binh et al., 2009; Schneider et al., 2009). Rapid ( $\sim 30$  m/ky) and prolonged (several thousand years) sediment deposition from river discharges or ice streams can generate sufficiently high overpressure ratios to directly cause failure of nearly flat slopes, or weaken the slope to an extent that a moderate earthquake can cause failure (Stigall and Dugan, 2010). Slope failure may also occur as a result of focused lateral fluid flow from areas of high overburden into areas low overburden (Dugan and Flemings, 2000; Flemings et al., 2002). This contribution shows that high excess pore pressures are very difficult to generate in areas of slower (0.15 m/ky) sediment accumulation, such as offshore north-west Africa, even when high permeability layers are present that encourage lateral flow of pore fluid.

The parametric study also shows that only a very high compressibility causes significant overpressure ratios at shallow depths. However, the  $\lambda$  value necessary to cause significant overpressure,  $\lambda = 0.88$ , is at the absolute maximum end of measured compressibility ranges. Such high compressibility has only been reported from two deep sea locations; the Gulf of Guinea (Hattab and Favre, 2010), and the Peru-Chile continental margin (Busch and Keller, 1982). The geological setting of the two regions is remarkably similar. Both margins experience only little terrestrial sediment input. The main sediment source are local zones of high biological productivity due to coastal upwelling (Busch and Keller, 1982; Altenbach et al., 2003, and references therein). Sedimentation rates in the upwelling area at the Peru-Chile margin range between 0.17-1.4 m/ky (Busch and Keller, 1982) and are about 0.3 m/ky in the Gulf of Guinea (Pastouret et al., 1979). The samples on which such high compressibilities were measured are highly plastic clays with abundant organic matter (6-12%) and shell fragments. Busch and Keller (1982) as well as numerous other authors (e.g. Pusch, 1973; Keller, 1982; Booth and Dahl, 1985; Bennett et al., 1985) suggest a close relationship between organic matter and geotechnical properties. Compressibility, for example, is found to increase with increasing organic content. Sediments underlying highly productive coastal waters are particularly rich in organic matter, but the presence of such organic matter rich clays is not limited to specific geological settings (Premuzic et al., 1982). It is therefore possible, that such high compressibilities are more prevalent than reflected in the literature.

The modelling results predict lateral fluid flow with velocities up to 0.6 mm/y. This lateral flow helps to stabilise the slope in areas of high overburden by providing effective drainage towards areas of low overburden. However, the lateral fluid and pressure transfer is not high enough to affect stability in these areas of lower overburden, as it has been predicted for example at the New Jersey continental slope (Dugan and Flemings, 2000, 2002). Beside the different technical approaches between the model used here and the one used by Dugan and Flemings (2000), the main differences are the relief and geometry of the aquifer, as well as the rate and shape of loading. The authors simulated a horizontal aquifer of 100 m thickness, buried by sedimentation rates of 1.2 m/ky (decreasing downslope). The aquifer terminates abruptly at the downslope end causing a sharp vertical interface between high and low permeability, which is where their model predicts failure. The aquifer in the model used here has a thickness of 20 m and parallels the seafloor (Fig. 6.4). It is continuous with a gradual decrease in permeability. The particular aquifer geometry, the differences in mechanical properties across the material interfaces, and the mechanical behaviour of the materials themselves, are all factors that could explain the different modelling results. The loading parameters are also important as they induce lateral pore pressure gradients, which cause fluid to flow not only vertically up but also horizontally. A high sedimentation rate that decreases abruptly over short distances will cause higher gradients and faster flow than a slow sedimentation rate that slowly decreases over large distances. Overall, pore pressure transfer due to lateral fluid flow does not appear to be a universal failure mechanism, especially not for slopes with low sedimentation rates.

#### **6.4.1 Why do shallow angle slopes in slow deposition areas fail? What is the missing link?**

Although the models predict that low angle slopes with low sedimentation rates, such as the north-west African margin, are stable, these margins have experienced large-scale slope failures (Wynn et al., 2000; Krastel et al., 2012). Their slab-like morphology is broadly similar to failures attributed to high excess pore pressures due to rapid deposition, as in the Gulf of Mexico and off the Norwegian margin (Masson et al., 2010). This observation, along with the fact that slope angles are very low, suggests that excess pore pressures must have also been high at continental slopes with slow sediment deposition. The results show that such high pore pressures are not caused by sedimentation alone and that other pore pressure generating mechanisms must be active. Below, I discuss whether these mechanisms could be sudden events, such as gas hydrate dissociation or earthquakes. Alternatively, I suggest an as yet untested hypothesis that stress controlled sediment behaviour can lead to overpressurisation.

#### 6.4.1.1 Gas hydrates

It has been suggested that the dissociation of gas hydrates could produce excess pore pressures in a number of ways including rapid removal of cement or the formation of gas bubbles (Henriet and Mienert, 1998). However, gas hydrates are stable in sediments at water depths greater than about 300 m (Kvenvolden, 1993). Many head scars of large submarine slides at open continental slopes are located at water depths of about 2000 m (Hühnerbach et al., 2004; Twichell et al., 2009), well below a potential zone of hydrate dissociation, including climate induced shifts. Therefore, gas hydrate dissociation does not appear to be the missing link in explaining high excess pore pressures.

#### 6.4.1.2 Earthquakes

Seismic forces alone are usually not high enough to cause large slope failures on low submarine gradients (Wright and Rathje, 2003; Leynaud et al., 2004), so that a certain degree of preconditioning of the slope is important. Cyclic loading due to earthquakes can increase the strength of the sediment due to rearrangement of particles and creation of drainage paths (Boulanger and Truman, 1996; Boulanger et al., 1998). This cyclic strength may explain the relatively infrequent occurrence of landslides due to earthquakes on land (Leroueil, 2001). However, seismic shaking can cause an increase in pore pressure during or after the earthquake, and thus provides an additional excess pore pressure source. Earthquakes therefore have the potential to act as triggers for submarine landslides (Biscontin et al., 2004). Stigall and Dugan (2010) calculate that an earthquake of magnitude 5 or higher is necessary to cause slope failure in the Gulf of Mexico, where high and persistent sedimentation rates ( $\sim 30$  m/ky) produced overpressure ratios ( $\lambda^*$ ) of  $\sim 0.7$ . An earthquake with a magnitude  $> 7$  was necessary to cause the Storegga Slide, in addition to overpressure ratios of 0.3 to 0.6 that were generated initially by high sedimentation rates (5 to 36 m/ky) (Kvalstad et al., 2005). Consequently, a slope preconditioned by much slower sedimentation requires an even stronger earthquake to cause failure.

#### 6.4.2 The role of compressibility

In this section I suggest a process that may provide the as yet missing link in explaining why low angle slopes fail at continental slopes with low sediment input. This process is potentially global and is not limited by regional constraints or specific settings. I also propose a possible reason for why this process has not been revealed yet.

The modelling results suggest that compressibility is the key factor for the stability of low angle slopes with slow deposition rates. Compressibility controls not only the magnitude of excess pore pressures, but also the location and depth at which maximum excess pore pressures develop. High compressibility causes a rapid porosity decrease as stress increases. Such a rapid volume loss generates large amounts of excess pore fluid, the drainage of which is hampered by a simultaneous rapid decrease in permeability. Compressibility is a negative logarithmic function of porosity. The greatest volume loss thus occurs at high porosities, i.e. causing overpressure build-up in the shallow sediment. The modelling results also show that even the maximum compressibility values given in the literature do not generate sufficient excess pore pressure to cause failure. Even higher compressibilities would be needed. In the following I discuss how "destructuring" of sediment microstructure may provide such high compressibilities.

Burland (1990) showed that the mechanical properties of an intact (or natural) soil differ from its reconstituted (or remoulded) properties due to the influence of soil structure. Such structure is a combination of a specific arrangement of the soil component particles (fabric) and the nature of interparticle contacts (bonding). Structure allows the soil to exist at higher porosities at a given stress than structureless soil. However, volumetric or shear strains cause a breakdown of fabric and bonding (Leroueil et al., 1979). Marine sediments are likely to reach these critical strains during compaction due to burial. This process of destructuring causes a gradual loss of the sediment's structure-permitted porosity, which is characterised by high compressibility. Fig. 6.26 illustrates the effect of structure and destructuring during compaction. If the sediment is of low permeability, the excess pore fluid caused by this rapid volume loss cannot drain, and excess pore pressures develop. Destructuring and the resulting excess pore pressures have been considered as a potential cause for failure of low angle slopes on land (e.g. Calabresi and Rampello, 1987). Typical stresses at which bonds and fabric start to break can be less than 100 kPa or up to several 1000 kPa, depending on soil types (Burland, 1990). More specifically, for one marine sediment sample Hattab and Favre (2010) report the destructuring phase to be active between 90-300 kPa. This would correspond to roughly 30-100 m below seafloor and agrees with the depth at which submarine slope failure is typically observed.

The porosity loss in such sediments could be significant and provide another source of excess pore pressure. The net rate of volume loss is related to the initial degree of structure (Burland, 1990). However, measuring and quantifying the degree of structuring of a soil is problematic. Sampling for geotechnical analyses can be challenging even on land (Clayton et al., 1995). Most deep sea sediment samples used for consolidation tests are recovered using standard sediment corers with typical barrel diameters of <10 cm. This is problematic as partial remoulding of the sample occurs during penetration of the

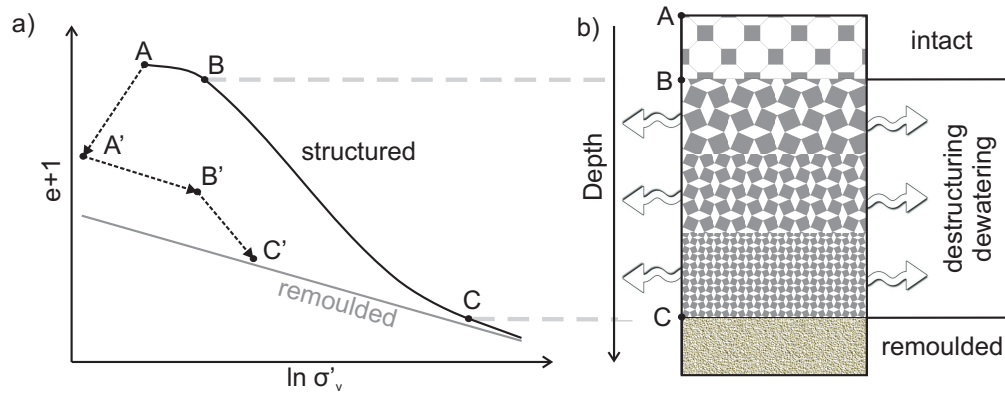


Figure 6.26: (a) Conceptual compaction lines for non-structured or remoulded sediment (grey line), partly structured (dashed black line) and highly structured sediment (solid black line). Point A corresponds to the natural porosity of a structured sediment at a given burial stress. The structural framework allows the sediment to maintain a higher porosity than the remoulded sediment. As natural burial proceeds and pressure increases, the structure breaks gradually between B and C. This destructuring process is characterised by a steep slope (large  $\lambda$ ). The slope of the compaction line,  $\lambda$ , decreases when the structure-permitted porosity is lost at C. Subsequent compaction equals that of the remoulded sediment. If a structured sediment sample with natural porosity corresponding to A is retrieved using a standard sampling device, the sample loses a large part of the structure (A-A'). Laboratory consolidation tests measure compaction from A' to C'. The resulting compressibility is significantly lower than for the natural sediment (A-C). (b) A cartoon of the destructuring process analogue in the sediment with increasing burial depth.

device into the sediment, let alone during handling on deck (Locat and Lee, 2002). What is measured eventually in the laboratory is a partially or fully remoulded sample that has lost its potential structural framework (Fig. 6.26). As a remoulded sample has lost all or large parts of its structure, its compressibility will be significantly lower. Hence, it is possible that compressibility is underestimated in consolidation tests using marine sediment samples recovered by standard procedures.

Although measurement of structure in marine sediments is complicated there is some evidence of strong bonding and fabric. A common characteristic of marine sediments is their high overconsolidation ratios in the absence of signs of erosion (e.g. Richards and Hamilton, 1967; Bryant et al., 1974; Busch and Keller, 1982; Keller, 1982; Baltzer et al., 1994; Hattab and Favre, 2010). A high overconsolidation ratio indicates that the sediment is capable of sustaining pressures greater than the overburden pressure at their original depth in the seabed. Such an "apparent overconsolidation" is often attributed to structural bonding.

There are a number of reasons that could favour a high degree of structuring in marine sediments. Sediment builds up its structural framework by various depositional and post-depositional processes such as ageing, bonding, or thixotrophy (Clayton et al., 1992). Long time scales and slow deposition rates are likely to favour the development of such bonding (Skempton, 1970). Sediments at continental margins with slow deposition may therefore be highly structured.

Crushing of microfossils during compaction is a process with similar effects on excess pore pressure generation as destructuring of clay. Microfossil rich sediments do not consolidate to as low porosities as other marine clays due to microfossil shells acting as a structural component (Hamilton, 1976; Keller, 1982; Tanaka and Locat, 1999). At some point during burial these shells cannot withstand the pressure and collapse, providing a high compressibility, sudden loss in volume and consequently excess pore pressure (Valent et al., 1982). Indeed, the increase in microfossil content of a sediment correlates to an increase in compressibility (Shiwakoti et al., 2002; Hong et al., 2006). Moreover, the expulsion of intraparticle water stored in hollow shells and skeletal pores due to their breakage could provide an additional pressure source (Demars, 1982; Keller, 1982; Hong et al., 2006).

## 6.5 Conclusion

The importance of excess pore pressures in the failure of submarine slopes with low gradients is evident. Finite Element modelling of a 2° slope shows that the slope is stable when slow sediment deposition is the only pressure source. The magnitude of excess pore pressure generated by consolidation and focused fluid flow is comparatively small for common consolidation properties. Therefore, some other mechanism must exist for producing large overpressurisation ratios. The modelling suggests that high compressibility is the key factor for shallow overpressure generation and, hence, slope stability. Based on this finding I propose that the gradual breakage of particularly strong interparticle bonds can cause very large sediment compressibility and may explain why large submarine landslides occur on nearly flat slopes. However, laboratory experiments on high quality sediment samples are needed to confirm this specific property of marine sediments.

## Chapter 7

### Conclusions and future perspectives

This thesis addresses the processes and mechanisms that could cause large submarine landslides on low ( $<2^\circ$ ) gradients at open continental slopes. Such landslides, that can reach volumes of several thousands of cubic kilometres, are one of the main process for moving sediment in the ocean. In some cases there is strong evidence that they have generated far travelled tsunamis (Tappin et al., 2001; Bondevik et al., 2005a). Consequently, there is a need to understand what causes large submarine landslides at open continental slopes in order to enable a thorough evaluation of the geohazard of a particular region as well as for potential mitigation efforts.

Submarine landslides of this type are extremely difficult to observe directly. This means that they (and their hazards) are relatively poorly understood (Masson et al., 2010). Indeed, in order to understand the frequency of landslides and how that may change in the future, we need a better understanding of their preconditioning and triggers. Because landslides at open continental slopes occur on remarkably low gradients of  $<2^\circ$ , it is difficult to explain how failure occurs. Significantly elevated pore pressures are most likely involved to overcome the sediment's shearing resistance at such low gradients (Hampton et al., 1996). There are a number of hypotheses for how submarine landslides are triggered and what could cause high excess pore pressures. However, these hypotheses may apply to some landslides, but often fail to explain the characteristics of others. For instance in the case of the Storegga Slide with a headwall at water depths around 300 m, gas hydrate dissociation could have triggered parts of the failure (Mienert et al., 2005). But gas hydrates cannot be the trigger for landslides with headwalls at water depth greater than 1000 m, such as most slides at the north-west African and US east coast continental margins (Twichell et al., 2009; Krastel et al., 2012), due to high pressures at these depths (Reagan and Moridis, 2008). Although the suggested failure mechanisms are contentious, some mechanisms, such as rapid deposition or earthquakes, have repeatedly been used by default to explain landslides at low gradient slopes. Before being confidently used to explain submarine landslides, however, these hypotheses need more rigorous testing - as done in this thesis.

Changes in global climate such as transitions between ice- and greenhouse worlds produce changes in environmental conditions, for example sea level or sedimentation rates. It has been suggested that such changes could affect slope stability, and are reflected in the frequency and timing of past submarine landslides (Maslin et al., 2004; Owen et al., 2007; Lee, 2009). However, these previous studies have not taken into account uncertainty intervals or used quantitative statistical analyses, as done in this thesis. Understanding the relationship between the timing of submarine landslides and climate change is of major significance for the evaluation of future geohazards, and could help to test and narrow down the number of hypotheses that are suggested to explain submarine slope failure. Whether changes in climate affected continental slope stability globally is tested in chapter 2 of this thesis by comparing the timing of past landslides to sea level as well as to local sedimentation rates. A correlation to other climate-related changes, such as local sea level, bottom water temperatures or seismicity, were not in the scope of the thesis but could be undertaken in the future.

One of the most widely held views for what causes failure of open continental slopes is excess pore pressure due to rapid sedimentation (Locat et al., 2009; Masson et al., 2010; Stigall and Dugan, 2010). However, slope failure also occurs where sedimentation rates are comparatively low (Lee, 2009). If excess pore pressures due to rapid sedimentation is a universal mechanism that could cause failure globally, it should also hold in areas with low sedimentation rates. Whether slow sedimentation and/or lateral fluid flow cause sufficient excess pore pressure to initiate failure at low gradients was assessed in the second part of the thesis (chapters 5 and 6).

### 7.1 Does climate affect continental slope stability?

A data base of ages of large submarine landslides worldwide was established to test for a potential link between climate and landslide frequency. The data base contains only landslides for which reliable age determination is available, and uncertainty intervals were assigned to the individual age estimates. The temporal distribution of landslides was compared to global sea level and local sedimentation rates, both of which are influenced by climate.

The comparison to a global sea level curve suggested that landslides may have occurred almost randomly over various climatic intervals. Thus, if there is a link to global climate it is too weak to be significant in the most comprehensive data base available to date. This conclusion contrasts with those of previous studies on the timing of landslides, which suggest an increased landslide occurrence during periods of glaciation and/or during glacial to interglacial transitions (Maslin et al., 2004; Owen et al., 2007; Lee, 2009;

Leynaud et al., 2009). None of these studies included age uncertainty intervals or such a strict control on the quality of the methodology used to determine individual landslide ages, as done in this thesis. The conclusions of these previous studies were based on qualitative analysis of histograms, the results of which strongly depend on the bin size. Certain bin sizes can skew visual perception and give a misleading picture. It is therefore important to do a more rigorous statistical analysis, such as applied in this thesis. For these reasons the conclusions based on the analysis conducted within this thesis may be more reliable.

A subdivision into sets of different depositional environments (glacial margins, river fan systems or low sediment input margins) confirms the absence of significant frequency peaks, with the exception of river fan systems. Although not statistically significant, most landslides occurred during rising sea level at river-fed continental margins. This could be related to high discharge rates and consequently large sediment input that dominated most river systems during glacials (Covault and Graham, 2010).

Not only in river fan systems but also in other depositional environments a comparison of the timing of large landslides and sedimentation rates showed that landslides can occur with a delay of several thousands of years after sedimentation rates were highest. Previous to this thesis, such a delay has been shown locally for example for the Storegga Slide (Leynaud et al., 2007), but never in a global data set for numerous locations. This finding is somewhat surprising as a slope subjected to high sedimentation rates is generally assumed less stable compared to one subjected to low sedimentation rates, because in the latter case excess pore fluid has more time to dissipate (Gibson, 1958). This suggests that an impact of peak sedimentation rates on slope failure, such as through generating excess pore pressure, is indirect. Some transient process, which could be the flow of pore fluid in the sediment, must be responsible for such a delay.

Although the data base is the most comprehensive of its kind to date, it has only a limited number of 62 samples. A bias towards younger ages, which is due to limited core penetration in many places, restricts the statistical analysis to an even smaller subset of unbiased data. Moreover, for about half of the landslides, the uncertainties within the dates are too great to attribute the landslide to a particular sea level stand. As local and global sea level can be different, it would be more accurate to compare landslide frequency to local sea levels. However, local sea level curves were not always available so that a global curve was used. Similarly, sedimentation rate estimates are not always available from ideal locations and can also involve large uncertainties as well, which were not quantified. It is important to be aware of these limitations when interpreting the results. However, these limitations also reflect the large uncertainties that are involved with our current understanding of large submarine landslides at open continental slopes.

## 7.2 Is slope failure triggered by rapid sedimentation, and how can failure occur in areas of slow sedimentation?

Rapid sedimentation, high compressibility and low permeability favour the build-up of excess pore pressure during sediment consolidation which could cause slope instability. Submarine landslides occur regardless of sedimentation rate, also in locations where sedimentation rates are low (several cm/ky), such as the north-west African margin. The hydromechanical properties of the sediment in this location must be extreme to generate enough excess pore pressure to cause failure. To test if underconsolidation is a more general failure mechanism, and therefore also occurs in areas of slow sedimentation, a Finite Element model was created. The transient model simulated consolidation of sediment with a range of extreme hydromechanical properties on a 2° continental slope. Sediment loading is asymmetric with highest deposition rates at the shelf edge that decrease exponentially downslope. The sediment body is either homogeneous without abrupt material interfaces or includes an aquifer.

Previous slope modelling supported by in situ pore pressure measurements suggests that rapid (peaking at  $\sim 30$  m/ka) and prolonged (several thousand years) sediment deposition from river discharges or ice streams can generate sufficiently high overpressure ratios to make a continental slope unstable. Slope failure is induced either directly in the area of high deposition (Leynaud et al., 2007; Stigall and Dugan, 2010), or away from it as a result of lateral fluid flow (Dugan and Flemings, 2000, 2002). The modelling in this thesis, however, predicts that continental slopes subjected to comparatively low sedimentation rates, such as the north-west African margin, are stable, even when values for permeability and compressibility are extreme. The simulations also indicate that lateral drainage rather stabilises the slope, even if sediment deposition is localised and lateral fluid flow to areas of less overburden is facilitated by the presence of an aquifer. I was able to identify compressibility as the key factor for the stability of continental slopes if sedimentation rates are low. This is new, as previous studies highlighted permeability and/or sedimentation rate as the most important parameters (Hampton et al., 1996; Masson et al., 2006; Leynaud et al., 2007; Flemings et al., 2008). High compressibility could lead to reasonably high overpressures if the model is run for millions of years.

The modelling results indicate that (i) sedimentation as the only pressure source is not sufficient to cause failure at continental slopes with low sediment input and (ii) excess pore pressure generation due to sediment deposition is not a universal failure mechanism. Although the modelling predicts these slopes to be stable, continental slopes where sedimentation rates are low (several cm/ky, such as the north-west African, US east coast, Brazilian and south-east Australian margins) have experienced numerous large submarine landslides (McAdoo et al., 2000; Wynn et al., 2000; Kowsmann et al., 2002; Chaytor

et al., 2009; Twichell et al., 2009; Boyd et al., 2010; Krastel et al., 2012). These models therefore miss some key process that can generate high excess pore pressures. The modelling results also indicate that extreme values for compressibility can potentially precondition a slope to fail. Can compressibility be high enough to precondition a slope to fail when sedimentation rates are low? A mechanical effect known as destructuring could provide high values of compressibility, and potentially be capable of producing high pressures. Destructuring refers to a gradual breakage of particularly strong interparticle bonds (structure) that can result in very high compressibility at certain pressures. This process has the potential to be a global preconditioning factor, as structured sediment is not limited to a particular geological setting or depositional regime. However, unless this hypothesis is tested and quantified by means of combined field evidence and numerical modelling, uncertainties remain large.

An important shortcoming of the model is its inability to detect failure within newly deposited sediment. With respect to the expected failure depth of submarine landslides (~100 m, Hühnerbach et al., 2004; Twichell et al., 2009), this means that the model can only be run until the newly deposited sediment reaches a thickness of approximately 100 m. In the case of slow sedimentation rates this corresponds to about 2 million years, which turned out to be long enough to identify excess pore pressure patterns in most modelled scenarios. If longer time scales or faster sedimentation rates are to be modelled in the future, a growing mesh approach is more suitable. Modelling strain softening requires specific constitutive models and was therefore not addressed in this thesis, although strain softening behaviour has been reported for some deep sea sediments (e.g. Kvalstad et al., 2005).

### **7.3 How could future studies be directed in order to constrain remaining uncertainties and improve understanding?**

The findings of this thesis improve the understanding of initiation mechanisms of submarine landslides, through revisiting the effect of climate change on slope stability, which has previously been considered as important, and by excluding excess pore pressure generation due to rapid sedimentation or complex fluid flow patterns as a universal failure mechanism. Moreover, compressibility was identified to be a key parameter for slope stability. These all are valuable information for any future research efforts towards an understanding of what causes large submarine landslides. However, there are still very large uncertainties, which makes the geohazard assessment for submarine landslides more difficult than for other natural hazards. More research is needed to reduce uncertainties

and improve understanding.

There is a need for a greater number of well dated landslides with a focus on the precision of data, rather than the number of examples. This would allow a more robust statistical test of links between landslide occurrence and climate-related factors such as sea level or sedimentation rates. To determine whether sea level preconditions slopes to fail an unbiased data set that covers one full sea level cycle is necessary. In addition to a global data base of the type shown in this thesis, detailed regional studies based on long-term recurrence rates of landslides and local sea levels could provide information on how different geological settings respond to climate forcing. This knowledge could help to prevent signals being obscured in an analysis of a global data set. A promising strategy for obtaining long-term records of large submarine landslides in a particular region is to drill through abyssal plain sequences (Weaver et al., 2000). Large submarine landslides tend to produce turbidity currents that deposit on the abyssal plain. Such turbidite records therefore represent an archive of major landslides that occurred at a variety of locations on the adjacent continental slopes. An additional advantage of these deposits is that turbidites are relatively thin compared to the displaced landslide mass near the headwall, allowing recovery of a large number of turbidites.

In order to further improve our understanding of what causes landslides, it is important to address the as yet hidden process(es) that could cause high excess pore pressures in continental slopes with low sediment input. A potential mechanism suggested above and based on the findings of this thesis is destructuring. If not sediment deposition, could the breaking of interparticle bonds (destructuring) cause high enough excess pore pressure to fail a low gradient slope? Implementing destructuring in the numerical model used in this thesis allows a first evaluation of its potential for causing slope failure. The degree of initial structure that has to be destructured in order to cause failure of a low angle slope can be determined. Whether the required degree of structure can be found in marine sediments needs to be assessed by geotechnical testing of sediment samples. This is problematic as standard sediment sampling either by gravity or drill cores severely disturbs the intact sediment (e.g. Locat and Lee, 2002; Lunne and Long, 2006). In order to minimise sample disturbance and preserve structure specific sampling tools are required. Advanced coring devices such as the STACOR gravity corer or the Ocean Drilling Program Advance Piston Corer yield high quality sediment cores, but suffer from a number of drawbacks, for instance the time consuming deployment, so that they are rarely used for scientific purposes (Skinner and McCave, 2003). Lunne and Long (2006) came up with detailed recommendations for the design of a cost and time efficient sampler that minimises disturbance, but the device is yet to build.

The results of this thesis not only indicate that failure mechanisms that have previously been considered important may not be universal. They also pinpoint the large uncertainties in our current understanding of the occurrence, timing and frequency of large submarine landslides at open continental slopes. An integrated approach that combines numerical modelling, geological and geophysical field data as well as geotechnical testing is a promising way forward to constrain remaining uncertainties and improve understanding.



## Bibliography

- ABAQUS (2009). ABAQUS manuals, version 6.5, ABAQUS Inc.
- Altenbach, A. V., Lutze, G. F., Schiebel, R., and Schönfeld, J. (2003). Impact of interrelated and interdependent ecological controls on benthic foraminifera: an example from the Gulf of Guinea. *Palaeogeography, Palaeoclimatology, Palaeoecology*, 197(3-4):213–238.
- Antobreh, A. A. and Krastel, S. (2007). Mauritania Slide Complex: morphology, seismic characterisation and process of formation. *International Journal of Earth Science*, 96:451–472.
- Audet, D. M. and Fowler, A. C. (1992). A mathematical model for compaction in sedimentary basins. *Geophysical Journal International*, 110(3):577–590.
- Baas, J. H. and Best, J. L. (2002). Turbulence modulation in clay-rich sediment-laden flows and some implications for sediment deposition. *Journal of Sedimentary Research*, 72(3):336–340.
- Baas, J. H., Mienert, J., Abrantes, F., and Prins, M. A. (1997). Late Quaternary sedimentation on the Portuguese continental margin: climate-related processes and products. *Paleogeography, Paleoclimatology, Paleoecology*, 130:1–23.
- Balsam, W. (1981). Late Quaternary sedimentation in the western north Atlantic: stratigraphy and paleoceanography. *Palaeogeography, Palaeoclimatology, Palaeoecology*, 35(0):215 – 240.
- Baltzer, A., Cochonat, P., and Piper, D. J. (1994). In situ geotechnical characterization of sediments on the Nova Scotian Slope, eastern Canadian continental margin. *Marine Geology*, 120(3-4):291 – 308.
- Baraza, J., Ercilla, G., and Lee, H. J. (1992). Geotechnical properties and preliminary assessment of sediment stability on the continental slope of the northwestern Alboran Sea. *Geo-Marine Letters*, 12:150–156. 10.1007/BF02084926.
- Bartetzko, A. and Kopf, A. (2007). The relationship of undrained shear strength and porosity with depth in shallow (< 50 m) marine sediments. *Sedimentary Geology*, 196(1-4):235–249.

- Baudet, B. A. and Ho, E. W. L. (2004). On the behaviour of deep-ocean sediments. *Geotechnique*, 54(9):571–580.
- Bayer, U. and Wetzels, A. (1989). Compactional behavior of fine-grained sediments: examples from Deep Sea Drilling Project cores. *Geologische Rundschau*, 78:807–819. 10.1007/BF01829324.
- Bea, R. (1971). How sea floor slides affect offshore structures. *Oil and Gas Journal*, 69(48):88–92.
- Bennett, R. H., Fischer, K. M., Lavoie, D. L., Bryant, W. R., and Rezak, R. (1989). Porometry and fabric of marine clay and carbonate sediments: Determinants of permeability. *Marine Geology*, 89:127–152.
- Bennett, R. H., Lehman, L., Hulbert, M. H., Harvey, G. R., Bush, S. A., Forde, E. B., Crews, P., and Sawyer, W. B. (1985). Interrelationships of organic carbon and submarine sediment geotechnical properties. *Marine Geotechnology*, 6(1):61–98.
- Berger, W. H. (1972). Deep sea carbonates: Dissolution facies and age-depth constancy. *Nature*, 236(5347):392–395.
- Berger, W. H. and Wefer, G. (1991). Productivity of the glacial ocean: Discussion of the iron hypothesis. *Limnology and Oceanography*, 36(8):1899–1918.
- Bethke, C. and Corbet, T. (1988). Linear and nonlinear solutions for one-dimensional compaction flow in sedimentary basins. *Water Resources Research*, 24:461–467.
- Binh, N. T. T., Tokunaga, T., Nakamura, T., Kozumi, K., Nakajuma, M., Kubota, M., Kameya, H., and Taniue, M. (2009). Physical properties of the shallow sediments in late Pleistocene formations, Ursa Basin, Gulf of Mexico, and their implications for generation and preservation of shallow overpressures. *Marine and Petroleum Geology*, 26:474–486.
- Biscontin, G., Pestana, J. M., and Nadim, F. (2004). Seismic triggering of submarine slides in soft cohesive soil deposits. *Marine Geology*, 203:341–354.
- Bondevik, S., Lovholt, F., Harbitz, C., Mangerud, J., Dawson, A., and Svendsen, J. I. (2005a). The storegga slide tsunami-comparing field observations with numerical simulations. *Marine and Petroleum Geology*, 22(1-2):195–208.
- Bondevik, S., Mangerud, J., Dawson, S., Dawson, A., and Lohne, O. (2005b). Evidence for three North Sea tsunamis at the Shetland Islands between 8000 and 1500 years ago. *Quaternary Science Reviews*, 24(14-15):1757–1775.
- Bondevik, S., Svendsen, J. I., and Mangerud, J. (1997). Tsunami sedimentary facies deposited by the Storegga tsunami in shallow marine basins and coastal lakes, western Norway. *Sedimentology*, 44(6):1115–1131.

- Booth, J. S. and Dahl, A. G. (1985). A note on the relationships between organic matter and some geotechnical properties of a marine sediment. *Marine Geotechnology*, 6(3):281–289.
- Booth, J. S. and O’Leary, D. W. (1991). A statistical overview of mass movement characteristics on the North American atlantic outer continental margin. *Marine Geotechnology*, 10(1-2):1–18.
- Boulanger, E., Konrad, J. M., Locat, J., and Lee, H. J. (1998). *EOS, Abstract*, volume 79, chapter Cyclic behavior of Eel River sediments: a possible explanation for the paucity of submarine landslide features, page 254. American Geophysical Union San Francisco.
- Boulanger, R. W. and Truman, S. P. (1996). Void redistribution in sand under post-earthquake loading. *Canadian Geotechnical Journal*, 33(5):829–834.
- Bourget, J., Zaragosi, S., Ellouz-Zimmermann, N., Mouchot, N., Garlan, T., Schneider, J.-L., Lanfumey, V., and Lallemand, S. (2011). Turbidite system architecture and sedimentary processes along topographically complex slopes: the Makran convergent margin. *Sedimentology*, 58:376–406.
- Bouriak, S., Vanneste, M., and Saoutkine, A. (2000). Inferred gas hydrates and clay diapirs near the Storegga Slide on the southern edge of the Vøring Plateau, offshore Norway. *Marine Geology*, 163:125–148.
- Boutt, D. F., Saffer, D., Doan, M.-L., Lin, W., Ito, T., Kano, Y., Flemings, P., McNeill, L. C., Byrne, T., Hayman, N. W., and Moe, K. T. (2012). Scale dependence of in-situ permeability measurements in the Nankai accretionary prism: The role of fractures. *Geophysical Research Letters*, 39.
- Boyd, R., Keene, J., Hubble, T., Gardner, J., Glenn, K., Ruming, K., and Exon, N. (2010). Southeast Australia: A Cenozoic continental margin dominated by mass transport. In Mosher, D. C., Moscardelli, L., Baxter, C. D., Urgeles, R., Shipp, R. C., Chaytor, J. D., and Lee, H. J., editors, *Submarine Mass Movements and Their Consequences*, volume 28 of *Advances in Natural and Technological Hazards Research*, pages 491–502. Springer Netherlands.
- Brandes, H. G. (2010). Geotechnical characteristics of deep-sea sediments from the North Atlantic and North Pacific oceans. *Ocean Engineering*, 38(7):835–848.
- Bredehoeft, J. D. and Hanshaw, B. B. (1968). On the maintenance of anomalous fluid pressures: I. Thick sedimentary sequences. *Geological Society of America Bulletin*, 79:1097–1106.
- Bryant, W. R., Bennett, R. H., and Katherman, C. E. (1981). *The Oceanic Lithosphere, The Sea*, volume 7, chapter Shear strength, consolidation, porosity, and permeability of oceanic sediments, pages 1555–1616. Wiley, New York.

- Bryant, W. R., Delflache, A. P., and Trabant, P. K. (1974). *Deep-Sea Sediments*, chapter Consolidation of marine clays and carbonates, pages 209–244. Plenum, New York.
- Bryn, P., Berg, K., Forsberg, C. F., Solheim, A., and Kvalstad, T. J. (2005). Explaining the Storegga Slide. *Marine and Petroleum Geology*, 22(1-2):11–19.
- Bugge, T., Belderson, R. H., and Kenyon, N. H. (1988). The Storegga Slide. *Philosophical Transactions of the Royal Society*, 325:357–388.
- Bull, S., Cartwright, J., and Huuse, M. (2009). A subsurface evacuation model for submarine slope failure. *Basin Research*, 21:433–443.
- Bungum, H., Lindholm, C., and Faleide, J. (2005). Postglacial seismicity offshore mid-Norway with emphasis on spatio-temporal-magnitudinal variations. *Marine and Petroleum Geology*, 22(1-2):137–148.
- Burland, J. B. (1990). On the compressibility and shear strength of natural clays. *Geotechnique*, 40(3):329–378.
- Busch, W. H. and Keller, G. H. (1982). Consolidation characteristics of sediments from the Peru-Chile continental margin and implications for past sediment instability. *Marine Geology*, 45(1-2):17 – 39.
- Butterfield, R. (1979). A natural compression law for soils (an advance on e-logp'). *Geotechnique*, 29(4):469–480.
- Butterfield, R. (2011). An improved model of soil response to load, unload and re-load cycles in an oedometer. *Soils and foundations*, 51(2):253–263.
- Calabresi, G. and Rampello, S. (1987). Swelling of overconsolidated clays in excavations. In *European Conference on Soil mechanics and Foundation Engineering*.
- Canals, M., Lastras, G., Urgeles, R., Casamor, J. L., Mienert, J., Cattaneo, A., Batist, M. D., Hafidason, H., Imbo, Y., Laberg, J. S., Locat, J., Long, D., Longva, O., Masson, D. G., Sultan, N., Trincardi, F., and Bryn, P. (2004). Slope failure dynamics and impacts from seafloor and shallow sub-seafloor geophysical data: case studies from the COSTA project. *Marine Geology*, 213:9–72.
- Castelltort, S. and VanDenDriessche, J. (2003). How plausible are high-frequency sediment supply-driven cycles in the stratigraphic record? *Sedimentary Geology*, 157(1-2):3–13.
- Chamley, H. (1989). *Clay sedimentology*. Springer Berlin.
- Chaytor, J. D., ten Brink, U. S., Solow, A. R., and Andrews, B. D. (2009). Size distribution of submarine landslides along the U.S. Atlantic margin. *Marine Geology*, 264:16–27.

- Clark, P. U., Dyke, A. S., Shakun, J. D., Carlson, A. E., Clark, J., Wohlfarth, B., Mitrovica, J. X., Hostetler, S. W., and McCabe, A. M. (2009). The Last Glacial Maximum. *Science*, 325:710–714.
- Clarke, S., Hubble, T., Airey, D., Yu, P., Boyd, R., Keene, J., Exon, N., and Gardner, J. (2012). Submarine landslides on the upper Southeast Australian passive continental margin - preliminary findings. In Yamada, Y., Kawamura, K., Ikehara, K., Ogawa, Y., Urgeles, R., Mosher, D., Chaytor, J., and Strasser, M., editors, *Submarine Mass Movements and Their Consequences*, volume 31 of *Advances in Natural and Technological Hazards Research*, pages 55–66. Springer Netherlands.
- Clayton, C. R. I., Hight, D. W., and Hopper, R. J. (1992). Progressive destructuration of Bothkennar clay: implications for sampling and reconsolidation procedures. *Geotechnique*, 42(2):219–239.
- Clayton, C. R. I., Matthews, M. C., and Simons, N. E. (1995). *Site investigation: A handbook for engineers*. Blackwell Science.
- Coleman, J. M. and Prior, D. B. (1988). Mass wasting on continental margins. *Annual Reviews of Earth and Planetary Science*, 16:101–119.
- Covault, J. A. and Graham, S. A. (2010). Submarine fans at all sea-level stands: Tectonomorphologic and climatic controls on terrigenous sediment delivery to the deep sea. *Geology*, 38(10):939–942.
- Dahlgren, K. and Vorren, T. O. (2003). Sedimentary environment and glacial history during the last 40 ka of the Vøring continental margin, mid-Norway. *Marine Geology*, 193(1-2):93–127.
- Davies, R. J. and Clarke, A. L. (2010). Methane recycling between hydrate and critically pressured stratigraphic traps, offshore Mauritania. *Geology*, 38:963–966.
- Dawson, A., Bondevik, S., and Teller, J. T. (2011). Relative timing of the Storegga submarine slide, methane release, and climate change during the 8.2 ka cold event. *The Holocene*, 21(7):1167–1171.
- Day-Stirrat, R. J., Dutton, S. P., Milliken, K. L., Loucks, R. G., Aplin, A. C., Hillier, S., and van der Pluijm, B. A. (2010). Fabric anisotropy induced by primary depositional variations in the silt: clay ratio in two fine-grained slope fan complexes: Texas Gulf Coast and northern North Sea. *Sedimentary Geology*, 226(1-4):42–53.
- DeFoor, W., Person, M., Larsen, H. C., Lizarralde, D., Cohen, D., and Dugan, B. (2011). Ice sheet-derived submarine groundwater discharge on Greenland’s continental shelf. *Water Resources Research*, 47.
- Demars, K. R. (1982). Unique engineering properties and compression behavior of deep-sea calcareous sediments. In Demars, K. R. and Chaney, R. C., editors, *Geotechnical properties, behavior and performance of calcareous soils*.

- Denniellou, B., Jallet, L., Sultan, N., Jouet, G., Giresse, P., Voisset, M., and Berne, S. (2009). Post-glacial persistence of turbiditic activity within the Rhone deep-sea turbidite system (Gulf of Lions, Western Mediterranean): Linking the outer shelf and the basin sedimentary records. *Marine Geology*, 257:65–86.
- Dowdeswell, J. A. and Elverhøi, A. (2002). The timing of initiation of fast-flowing ice streams during a glacial cycle inferred from glacimarine sedimentation. *Marine Geology*, 188(1-2):3–14.
- Doyle, L. J., Pilkey, O. H., and Woo, C. C. (1979). Sedimentation on the Eastern United States Continental Slope. *Society of the Economic Paleontologists and Mineralogists*, 27:119–129.
- Ducassou, E., Capotondi, L., Murat, A., Bernasconi, S. M., Mulder, T., Gonthier, E., Migeon, S., Duprat, J., Giraudeau, J., and Mascle, J. (2007). Multiproxy Late Quaternary stratigraphy of the Nile deep-sea turbidite system - Towards a chronology of deep-sea terrigenous systems. *Sedimentary Geology*, 200:1–13.
- Ducassou, E., Migeon, S., Mulder, T., Murat, A., Capotondi, L., Bernasconi, S. M., and Mascle, J. (2009). Evolution of the Nile deep-sea turbidite system during the Late Quaternary: influence of climate change on fan sedimentation. *Sedimentology*, 56:2061–2090.
- Dugan, B. (2008). Fluid flow in the Keathley Canyon 151 Mini-Basin, northern Gulf of Mexico. *Marine and Petroleum Geology*, 25(9):919 – 923.
- Dugan, B. (2012). A review of overpressure, flow focusing, and slope failure. In Yamada, Y., Kawamura, K., Ikehara, K., Ogawa, Y., Urgeles, R., Mosher, D., Chaytor, J., and Strasser, M., editors, *Submarine Mass Movements and Their Consequences*, volume 31 of *Advances in Natural and Technological Hazards Research*, pages 267–276. Springer Netherlands.
- Dugan, B. and Flemings, P. B. (2000). Overpressure and fluid flow in the New Jersey continental slope: Implications for slope failure and cold seeps. *Science*, 289:288–291.
- Dugan, B. and Flemings, P. B. (2002). Fluid flow and stability of the US continental slope offshore New Jersey from the Pleistocene to the present. *Geofluids*, 2:137–146.
- Dugan, B. and Germaine, J. T. (2008). Near-seafloor overpressure in the deepwater Mississippi Canyon, northern Gulf of Mexico. *Geophysical Research Letters*, 35.
- Duncan, J. M. (1996). State of the art: Limit equilibrium and finite-element analysis of slopes. *Journal of Geotechnical Engineering*, 122(7):577–596.
- Duncan, J. M. and Wright, S. G. (2005). *Soil strength and slope stability*.

- Elmore, R. D., Pilkey, O. H., Cleary, W. J., and Curran, H. A. (1979). Black Shell turbidite, Hatteras Abyssal Plain, western Atlantic Ocean. *Geological Society of America Bulletin*, 90:1165–1176.
- Elverhøi, A., Harbitz, C. B., Dimakis, P., Mohrig, D., Marr, J., and Parker, G. (2000). On the dynamics of subaqueous debris flows. *Oceanography*, 13(3):109–117.
- Evans, D., Harrison, Z., Shannon, P. M., Laberg, J. S., Nielsen, T., Ayers, S., Holmes, R., Houlst, R. J., Lindberg, B., Haflidason, H., Long, D., Kuijpers, A., Andersen, E. S., and Bryn, P. (2005). Paleoslides and other mass failures of Pliocene to Pleistocene age along the Atlantic continental margin of NW Europe. *Marine and Petroleum Geology*, 22:1131–1148.
- Fine, I., Rabinovich, A., Bornhold, B., Thomson, R., and Kulikov, E. (2005). The Grand Banks landslide-generated tsunami of November 18, 1929: preliminary analysis and numerical modeling. *Marine Geology*, 215(1-2):45–57.
- Flemings, P., Behrmann, J., John, C., and Expedition 308 Scientists (2006). Gulf of Mexico Hydrogeology. *Proceedings of the Ocean Drilling Program, Scientific Results, Expedition 308*, 308.
- Flemings, P. B., John, C., and Behrmann, J. H. (2012). Expedition 308 synthesis: Overpressure, consolidation and slope stability on the continental slope of the Gulf of Mexico. *Proceedings of the International Ocean Drilling Program, Scientific Results*, 308.
- Flemings, P. B., Long, H., Dugan, B., Germaine, J. T., John, C. M., Behrmann, J. H., Sawyer, D. E., and IODP Expedition 308 Scientists (2008). Erratum to "Pore pressure penetrometers document high overpressure near the seafloor where multiple submarine landslides have occurred on the continental slope, offshore Louisiana, Gulf of Mexico". *Earth and Planetary Science Letters*, 274:269–283.
- Flemings, P. B., Stump, B. B., Finkbeiner, T., and Zoback, M. (2002). Flow focusing in overpressured sandstones: Theory, observations, and applications. *American Journal of Science*, 302(10):827–855.
- Förster, A., Ellis, R., Henrich, R., Krastel, S., and Kopf, A. J. (2010). Geotechnical characterisation and strain analyses of sediment in the Mauritania Slide Complex, NW-Africa. *Marine and Petroleum Geology*, 27(6):1175–1189.
- Frey-Martinez, J., Cartwright, J., and Hall, B. (2005). 3D seismic interpretation of slump complexes: examples from the continental margin of Israel. *Basin Research*, 17:83–108.
- Fryer, G., Watts, P., and Pratson, L. (2004). Source of the great tsunami of 1 April 1946: a landslide in the upper Aleutian forearc. *Marine Geology*, 203(3-4):201–218.

- Garziglia, S., Migeon, S., Ducassou, E., Loncke, L., and Mascle, J. (2008). Mass-transport deposits on the Rosetta province (NW Nile deep-sea turbidite system, Egyptian margin): Characteristics, distribution and potential causal processes. *Marine Geology*, 250:180–198.
- Gee, M., Gawthorpe, R., and Friedmann, J. (2005). Giant striations at the base of a submarine landslide. *Marine Geology*, 214(1-3):287–294.
- Gens, A. and Potts, D. (1988). Critical state models in computational geomechanics. *Engineering Computations*, 5(3):178–197.
- Georgiopoulou, A., Masson, D. G., Wynn, R. B., and Krastel, S. (2010). Sahara Slide: Age, initiation, and processes of a giant submarine slide. *Geochemistry Geophysics Geosystems*, 11(7).
- Georgiopoulou, A., Wynn, R. B., Masson, D. G., and Frenz, M. (2009). Linked turbidite-debrite resulting from recent Sahara Slide headwall reactivation. *Marine and Petroleum Geology*, 26:2021–2031.
- Gibson, R. E. (1958). The progress of consolidation in a clay layer increasing in thickness with time. *Geotechnique*, 8(2):171–182.
- Gibson, R. E., England, G. L., and Hussey, M. J. L. (1967). The theory of one-dimensional consolidation of saturated clays. I. Finite non-linear consolidation of thin homogeneous layers. *Geotechnique*, 17:261–273.
- Gibson, R. E., Schiffman, R. L., and Cargill, K. W. (1981). The theory of one-dimensional consolidation of saturated clays. II. Finite nonlinear consolidation of thick homogeneous layers. *Canadian Geotechnical Journal*, 18(2):280–293.
- Gracia, E., Vizcaino, A., Escutia, C., Asioli, A., Rodes, A., Pallas, R., Garcia-Orellana, J., Lebreiro, S. M., and Goldfinger, C. (2010). Holocene earthquake record offshore Portugal (SW Iberia): testing turbidite paleoseismology in a slow-convergence margin. *Quaternary Science Reviews*, 29:1156–1172.
- Grantz, A., Philips, R. L., Mullen, M. W., Starratt, S. W., Jones, G. A., Naidu, A. S., and Finney, B. P. (1996). Character, paleoenvironment, rate of accumulation, and evidence for seismic triggering of Holocene turbidites, Canada Abyssal Plain, Arctic Ocean. *Marine Geology*, 133:51–73.
- Griffiths, D. V. and Lane, P. A. (1999). Slope stability analysis by finite elements. *Geotechnique*, 49(3):387–403.
- Grinsted, A., Moore, J. C., and Jevrejeva, S. (2010). Reconstructing sea level from paleo and projected temperatures 200 to 2100 ad. *Climate Dynamics*, 34:461–472.

- Gröger, M., Henrich, R., and Bickert, T. (2003). Glacial-interglacial variability in lower North Atlantic deep water: inference from silt grain-size analysis and carbonate preservation in the western equatorial Atlantic. *Marine Geology*, 201(4):321 – 332.
- Hafliðason, H., Lien, R., Sejrup, H. P., Forsberg, C. F., and Bryn, P. (2005). The dating and morphometry of the Storegga Slide. *Marine and Petroleum Geology*, 22:123–136.
- Hafliðason, H., Sejrup, H. P., Nygard, A., Mienert, J., Bryn, P., Lien, R., Forsberg, C. F., Berg, K., and Masson, D. (2004). The Storegga Slide: architecture, geometry and slide development. *Marine Geology*, 213:201–234.
- Hamilton, E. L. (1976). Variations of density and porosity with depth in deep-sea sediments. *Journal of Sedimentary Petrology*, 46(2):280–300.
- Hampton, M. A., Lee, H. J., and Locat, J. (1996). Submarine landslides. *Reviews of Geophysics*, 34:33–59.
- Harbitz, C., Lovholt, F., Pedersen, G., Glimsdal, S., and Masson, D. (2006). Mechanisms of tsunami generation by submarine landslides - a short review. *Norwegian Journal of Geology*, 86:255–264.
- Hattab, M. and Favre, J.-L. (2010). Analysis of the experimental compressibility of deep water marine sediments from the Gulf of Guinea. *Marine and Petroleum Geology*, 27(2):486 – 499.
- Henrich, R., Cherubini, Y., and Meggers, H. (2010). Climate and sea level induced turbidite activity in a canyon system offshore the hyperarid Western Sahara (Mauritania): The Timiris Canyon. *Marine Geology*, 275(1-4):178–198.
- Henrich, R., Hanebuth, T. J. J., Krastel, S., Neubert, N., and Wynn, R. B. (2008). Architecture and sediment dynamics of the Mauritania Slide Complex. *Marine and Petroleum Geology*, 25(1):17–33.
- Henriet, J. P. and Mienert, J. (1998). Gas Hydrates: the Gent debates. Outlook on research horizons and strategies. *Geological Society, London, Special Publications*, 137:1–8.
- Hjelstuen, B. O., Sejrup, H. P., Hafliðason, H., Nygard, A., Berstad, I. M., and Knorr, G. (2004). Late Quaternary seismic stratigraphy and geological development of the south Vøring margin, Norwegian Sea. *Quaternary Science Reviews*, 23:1847–1865.
- Hong, Z., Tateishi, Y., and Han, J. (2006). Experimental study of macro- and microbehavior of natural diatomite. *Journal of Geotechnical and Geoenvironmental Engineering*, 132:603–610.
- Hornbach, M. J., Lavier, L. L., and Ruppel, C. D. (2007). Triggering mechanism and tsunamogenic potential of the Cape Fear Slide complex, U.S. Atlantic margin. *Geochemistry Geophysics Geosystems*, 8(12).

- Hühnerbach, V., Masson, D. G., and partners of the COSTA-Project (2004). Landslides in the North Atlantic and its adjacent seas: an analysis of their morphology, setting and behaviour. *Marine Geology*, 213:343–362.
- Hunt, J. E. (2012). *Determining the provenance, recurrence, magnitudes and failure mechanisms of submarine landslides from the Moroccan Margin and Canary Islands using distal turbidite records*. PhD thesis, Faculty of Natural and Environmental Sciences, School of Ocean and Earth Sciences, University of Southampton.
- Hunt, J. E., Wynn, R. B., Masson, D. G., Talling, P. J., and Teagle, D. A. H. (2011). Sedimentological and geochemical evidence for multistage failure of volcanic island landslides: A case study from Icod landslide on north Tenerife, Canary Islands. *Geochem. Geophys. Geosyst.*, 12:Q12007–.
- Huppertz, T. J. and Piper, D. J. W. (2009). The influence of shelf-crossing glaciation on continental slope sedimentation, Flemish Pass, eastern Canadian continental margin. *Marine Geology*, 26:67–85.
- Hustoft, S., Dugan, B., and Mienert, J. (2009). Effects of rapid sedimentation of developing the Nyegga pockmark field: Constraints from hydrological modeling and 3-D seismic data, offshore mid-Norway. *Geochemistry Geophysics Geosystems*, 10(6).
- Hutson, W. H. (1980). Bioturbation of deep-sea sediments: Oxygen isotopes and stratigraphic uncertainty. *Geology*, 8:127–130.
- Imbrie, J., Hays, J. D., Martinson, D. G., McIntyre, A., Mix, A. C., Morley, J. J., Pisias, N. G., Prell, W. L., and Shackleton, N. J. (1984). The orbital theory of Pleistocene climate : support from a revised chronology of the marine  $\delta^{18}\text{O}$  record. In Berger, A., Imbrie, J., Hays, J., Kukla, G., and Saltzman, B., editors, *Milankovitch and Climate: Understanding the Response to Astronomical Forcing*, page 269.
- Iverson, R. M. (1997). The physics of debris flows. *Reviews of Geophysics*, 35(3):245–296.
- Jasko, T. (1984). The first find: estimation of the precision of range zone boundaries. *Computers & Geosciences*, 10(1):133–136.
- Jenkins, C. J. and Keene, J. B. (1992). Submarine slope failures of the southeast Australian continental slope: a thinly sedimented margin. *Deep-Sea Research*, 39(2):121–136.
- Jorstad, F. (1968). Waves generated by landslides in Norwegian fjords and lakes. *Norwegian Geotechnical Institute Publ.*
- Karig, D. E. and Hou, G. (1992). High-stress consolidation experiments and their geological implications. *Journal of Geophysical Research*, 97(B1):289–300.

- Kawamura, K. and Ogawa, Y. (2004). Progressive change of pelagic clay microstructure during burial process: examples from piston cores and ODP cores. *Marine Geology*, 207(1-4):131–144.
- Kayen, R. E. and Lee, H. J. (1991). Pleistocene slope instability of gas hydrate-laden sediment on the Beaufort sea margin. *Marine Geotechnology*, 10(1-2):125–141.
- Keller, G. H. (1982). Organic matter and the geotechnical properties of submarine sediments. *Geo-Marine Letters*, 2:191–198.
- King, E., Haffidason, H., Sejrup, H., and Løvlie, R. (1998). Glacigenic debris flows on the North Sea Trough Mouth Fan during ice stream maxima. *Marine Geology*, 152(1-3):217 – 246.
- Knutz, P., Jones, E., Austin, W., and van Weering, T. (2002). Glacimarine slope sedimentation, contourite drifts and bottom current pathways on the Barra Fan, UK North Atlantic margin. *Marine Geology*, 188(1-2):129 – 146.
- Kokusho, T. and Kojima, T. (2002). Mechanism for postliquefaction water film generation in layered sand. *Journal of Geotechnical and Geoenvironmental Engineering*, 128(2):129–137.
- Kolla, V. and Perlmutter, M. A. (1993). Timing of turbidite sedimentation on the Mississippi Fan. *AAPG Bulletin*, 77(7):1129–1141.
- Kopf, A., Kasten, S., and Bles, J. (2010). Geochemical evidence for groundwater-charging of slope sediments: The Nice airport 1979 landslide and tsunami revisited. In Mosher, D. C., Shipp, R. C., Moscardelli, L., Chaytor, J. D., Baxter, C. D. P., Lee, H. J., and Urgeles, R., editors, *Submarine Mass Movements and Their Consequences*, volume 31 of *Advances in Natural and Technological Hazards Research*, pages 203–214. Springer Netherlands.
- Korup, O., Clague, J. J., Hermanns, R. L., Hewitt, K., Strom, A. L., and Weidinger, J. T. (2007). Giant landslides, topography, and erosion. *Earth and Planetary Science Letters*, 261(3-4):578 – 589.
- Kowsmann, R. O., Machado, L. C. R., Viana, A. R., Almeida, W., and Vicalvi, M. A. (2002). Controls on mass-wasting in deep water of the Campos Basin. In *Offshore Technology Conference*.
- Krastel, S., Wynn, R. B., Georgiopoulou, A., Geersen, J., Henrich, R., Meyer, M., and Schwenk, T. (2012). Large-scale mass wasting on the Northwest African Continental Margin: Some general Implications for mass wasting on passive continental margins. In Yamada, Y., Kawamura, K., Ikehara, K., Ogawa, Y., Urgeles, R., Mosher, D., Chaytor, J., and Strasser, M., editors, *Submarine Mass Movements and Their Consequences*, volume 31 of *Advances in Natural and Technological Hazards Research*, pages 189–199. Springer Netherlands.

- Kroon, D., Shimmiel, G., Austin, W. E. N., Derrick, S., Knutz, P., and Shimmiel, T. (2000). Century- to millennial-scale sedimentological-geochemical records of glacial-Holocene sediment variations from the Barra Fan (NE Atlantic). *Journal of the Geological Society, London*, 157:643–653.
- Kvalstad, T. J., Andresen, L., Forsberg, C. F., Berg, K., Bryn, P., and Wangen, M. (2005). The Storegga Slide: evaluation of triggering sources and slide mechanics. *Marine and Petroleum Geology*, 22:245–256.
- Kvenvolden, K. A. (1993). Gas hydrates-geological perspective and global change. *Reviews of Geophysics*, 31(2):173–187.
- Laberg, J., Vorren, T., Kenyon, N., and Ivanov, M. (2006). Frequency and triggering mechanisms of submarine landslides of the North Norwegian continental margin. *Norwegian Journal of Geology*, 86:155–161.
- Laberg, J., Vorren, T., Mienert, J., Bryn, P., and Lien, R. (2002a). The Trænadjupet Slide: a large slope failure affecting the continental margin of Norway 4,000 years ago. *Geo-Marine Letters*, 22:19–24. 10.1007/s00367-002-0092-z.
- Laberg, J. S. and Camerlenghi, A. (2008). The significance of contourites for submarine slope stability. In *Developments in Sedimentology*, volume 60, pages 537–556.
- Laberg, J. S., Dahlgren, T., Vorren, T. O., Haffidason, H., and Bryn, P. (2001). Seismic analyses of Cenozoic contourite drift development in the Northern Norwegian Sea. *Marine Geophysical Researches*, 22:401–416.
- Laberg, J. S., Vorren, T. O., Mienert, J., Evans, D., Lindberg, B., Ottesen, D., Kenyon, N. H., and Henriksen, S. (2002b). Late Quaternary paleoenvironment and chronology in the Trænadjupet Slide area offshore Norway. *Marine Geology*, 188:35–60.
- Laberg, J. S., Vorren, T. O., Mienert, J., Haffidason, H., Bryn, P., and Lien, R. (2003). Preconditions leading to the Holocene Trænadjupet Slide offshore Norway. In Locat, J., Mienert, J., and Boisvert, L., editors, *Submarine Mass Movements and Their Consequences*, volume 19 of *Advances in Natural and Technological Hazards Research*, pages 247–254. Springer Netherlands.
- Lambe, T. W. and Whitman, R. V. (1979). *Soil mechanics*. Wiley, New York.
- Lassey, K. R., Manning, M. R., Sparks, R. J., and Wallace, G. (1990). Radiocarbon in the sub-tropical convergence east of Tasmania- an interim report. Technical report, DSIR Physical Sciences.
- Lastras, G., Canals, M., Hughes-Clarke, J. E., Moreno, A., Batist, M. D., Masson, D. G., and Cochonat, P. (2002). Seafloor imagery from the BIG'95 debris flow, western Mediterranean. *Geology*, 30(10):871–874.

- Lastras, G., Canals, M., Urgeles, R., and Batist, M. D. (2004). Characterisation of the recent BIG'95 debris flow deposit on the Ebro margin, Western Mediterranean Sea, after a variety of seismic reflection data. *Marine Geology*, 213:235–255.
- Lebreiro, S. M., Voelker, A. H. L., Vizcaino, A., Abrantes, F. G., Alt-Epping, U., Jung, S., Thouveny, N., and Gracia, E. (2009). Sediment instability on the Portuguese continental margin under abrupt glacial climate changes (last 60 kyr). *Quaternary Science Reviews*, 28:3211–3223.
- Lee, H., Chun, S., Yoon, S., and Kim, S. (1993). Slope stability and geotechnical properties of sediment of the southern margin of Ulleung Basin, East Sea (Sea of Japan). *Marine Geology*, 110(1-2):31 – 45.
- Lee, H. J. (2009). Timing and occurrence of large submarine landslides on the Atlantic Ocean Margin. *Marine Geology*, 264:53–64.
- Lee, H. J., Chough, S. K., and Yoon, S. H. (1996). Slope-stability change from late Pleistocene to Holocene in the Ulleung Basin, East Sea (Japan Sea). *Sedimentary Geology*, 104:39–51.
- Lee, H. J., Ryan, H., Haeussler, P. J., Kayen, R. E., Hampton, M. A., Locat, J., Suleimani, E., and Alexander, C. R. (2007). Reassessment of seismically induced, tsunamigenic submarine slope failures in Port Valdez, Alaska, USA. In Lykousis, V and Sakellariou, D and Locat, J, editor, *Submarine Mass Movements and Their Consequences*, volume 27 of *Advances in Natural and Technological Hazards Research*, pages 357–365. Springer Berlin.
- Lee, S. H., Bahk, J. J., Kim, H. J., Lee, K. E., Jou, H. T., and Suk, B. C. (2010). Changes in the frequency, scale, and failing areas of latest Quaternary (<29.4 cal. ka B.P.) slope failures along the SW Ulleung Basin, East Sea (Japan Sea), inferred from depositional characters of densely dated turbidite successions. *Geo-Marine Letters*, 30:133–142.
- Leroueil, S. (2001). Natural slopes and cuts: movement and failure mechanisms. *Geotechnique*, 51(3):197–243.
- Leroueil, S., Roy, M., LaRochelle, P., Brucey, F., and Tavenas, F. A. (1979). Behaviour of destructured natural clays. *Journal of the Geotechnical Engineering Division*, 105(6):759–778.
- Leynaud, D., Mienert, J., and Nadim, F. (2004). Slope stability assessment of the Helland Hansen area offshore the mid-Norwegian margin. *Marine Geology*, 213(1-4):457–480.
- Leynaud, D., Mienert, J., and Vanneste, M. (2009). Submarine mass movements on glaciated and non-glaciated European continental margins: A review of triggering mechanisms and preconditions to failure. *Marine and Petroleum Geology*, 26:618–632.

- Leynaud, D., Sultan, N., and Mienert, J. (2007). The role of sedimentation rate and permeability in the slope stability of the formerly glaciated Norwegian continental margin: the Storegga Slide model. *Landslides*, 4:297–309.
- Lindberg, B., Laberg, J. S., and Vorren, T. O. (2004). The Nyk Slide - morphology, progression, and age of a partly buried submarine slide offshore northern Norway. *Marine Geology*, 213:277–289.
- Lisiecki, L. E. and Raymo, M. E. (2005). A Pliocene-Pleistocene stack of 57 globally distributed benthic  $\delta^{18}O$  records. *Paleoceanography*, 20(1):PA1003–1010.
- Liu, X. and Flemings, P. B. (2009). Dynamic response of oceanic hydrates to sea level drop. *Geophysical Research Letters*, 36.
- Locat, J., Lee, H., ten Brink, U. S., Twichell, D., Geist, E., and Sansoucy, M. (2009). Geomorphology, stability and mobility of the Currituck slide. *Marine Geology*, 264(1-2):28–40.
- Locat, J. and Lee, H. J. (2002). Submarine landslides: advances and challenges. *Canadian Geotechnical Journal*, 39:193–212.
- Long, H., Flemings, P., Germaine, J., and Saffer, D. (2011). Consolidation and overpressure near the seafloor in the Ursa Basin, deepwater Gulf of Mexico. *Earth and Planetary Science Letters*, 305(1-2):11 – 20.
- Long, H., Flemings, P., Germaine, J., Saffer, D., and Dugan, B. (2008). Data report: consolidation characteristics of sediments from IODP Expedition 308, Ursa Basin, Gulf of Mexico. In *Proceedings of the Ocean Drilling Program, Scientific Results*, volume 308, page 2.
- Lunne, T. and Long, M. (2006). Review of long seabed samplers and criteria for new sampler design. *Marine Geology*, 226(1-2):145–165.
- Maltman, H. J. and Bolton, A. (2003). How sediments become mobilised. *Geological Society, London, Special Publications*, 216:9–20.
- Martinson, D. G., Pisias, N. G., Hays, J. D., Imbrie, J., Theodore C Moore, J., and Shackleton, N. (1987). Age dating and the orbital theory of the ice ages: development of a high-resolution 0 to 300,000-year chronostratigraphy. *Quaternary Research*, 27:1–29.
- Maslin, M., Mikkelsen, N., Vilela, C., and Haq, B. (1998). Sea-level- and gas-hydrate-controlled catastrophic sediment failures of the Amazon Fan. *Geology*, 26(12):1107–1110.
- Maslin, M., Owen, M., Betts, R., Day, S., Dunkley Jones, T., and Ridgwell, A. (2010). Gas hydrates: past and future geohazard? *Philosophical Transactions of the Royal Society*, 368(1919):2369–2393.

- Maslin, M., Owen, M., Day, S., and Long, D. (2004). Linking continental-slope failures and climate change: Testing the clathrate gun hypothesis. *Geology*, 32:53–56.
- Maslin, M., Vilela, C., Mikkelsen, N., and Grootes, P. (2005). Causes of catastrophic sediment failures of the Amazon Fan. *Quaternary Science Reviews*, 24:2180–2193.
- Masson, D., Watts, A., Gee, M., Urgeles, R., Mitchell, N., Bas, T. L., and Canals, M. (2002). Slope failures on the flanks of the western Canary Islands. *Earth-Science Reviews*, 57(1-2):1 – 35.
- Masson, D. G., Arzola, R. G., Wynn, R. B., Hunt, J. E., and Weaver, P. P. E. (2011). Seismic triggering of landslides and turbidity currents offshore Portugal. *Geochemistry Geophysics Geosystems*, 12(12).
- Masson, D. G., Harbitz, C. B., Wynn, R. B., Pedersen, G., and Løvholt, F. (2006). Submarine landslides: processes, triggers and hazard prediction. *Philosophical Transactions of the Royal Society*, 364:2009–2039.
- Masson, D. G., Wynn, R. B., and Talling, P. J. (2010). Large landslides on passive continental margins: Processes, hypotheses and outstanding questions. In Mosher, D. C., Shipp, R. C., Moscardelli, L., Chaytor, J. D., Baxter, C. D. P., Lee, H. J., and Urgeles, R., editors, *Submarine Mass Movements and Their Consequences*, volume 28 of *Advances in Natural and Technological Hazards Research*, pages 153–165. Springer Netherlands.
- McAdoo, B. G., Pratson, L. F., and Orange, D. L. (2000). Submarine landslide geomorphology, US continental slope. *Marine Geology*, 169:103–136.
- McCave, I. N., Manighetti, B., and Robinson, S. G. (1995). Sortable silt and fine sediment size/composition slicing: Parameters for paleocurrent speed and paleoceanography. *Paleoceanography*, 10:593–610.
- Meehl, G. A., Covey, C., Delworth, T., Latif, M., McAvaney, B., Mitchell, J. F. B., Stouffer, R. J., and Taylor, K. E. (2007). The WCRP CMIP3 multimodel dataset: A new era in climate change research. *Bulletin of the American Meteorological Society*, 88:1383.
- Mei, C. (1985). Gravity effects in consolidation of layer of soft soil. *Journal of Engineering Mechanics*, 111(8):1038–1047.
- Métiver, F. and Gaudemer, Y. (1999). Stability of output fluxes of large rivers in South and East Asia during the last 2 million years: implications on floodplain processes. *Basin Research*, 11(4):293–303.
- Mienert, J., Vanneste, M., Bünz, S., Andreassen, K., Hafidason, H., and Sejrup, H. P. (2005). Ocean warming and gas hydrate stability on the mid-Norwegian margin at the Storegga Slide. *Marine and Petroleum Geology*, 22(1-2):233–244.

- Mikkelsen, N., Maslin, M., Giraudeau, J., and Showers, W. (1997). Biostratigraphy and sedimentation rates of the Amazon Fan. In Flood, R., Piper, D., Klaus, A., and Peterson, L., editors, *Proceedings of the Ocean Drilling Program, Scientific Results*, volume 155.
- Milliman, J. D. and Syvitski, J. P. M. (1992). Geomorphic/tectonic control of sediment discharge to the ocean: The importance of small mountaineous rivers. *The Journal of Geology*, 100:525–544.
- Milne, G. A., Davis, J. L., Mitrovica, J. X., Scherneck, H. G., Johansson, J. M., Vermeer, M., and Koivula, H. (2001). Space-geodetic constraints on glacial isostatic adjustment in Fennoscandia. *Science*, 291:2381–2385.
- Mohrig, D., Ellis, C., Parker, G., Whipple, K. X., and Hondzo, M. (1998). Hydroplaning of subaqueous debris flows. *Geological Society of America Bulletin*, 110(3):387–394.
- Mohrig, D. and Marr, J. G. (2003). Constraining the efficiency of turbidity current generation from submarine debris flows and slides using laboratory experiments. *Marine and Petroleum Geology*, 20:883–899.
- Mörner, N. (1979). The Fennoscandian uplift and late cenozoic geodynamics: geological evidence. *GeoJournal*, 3(3):287–318.
- Mulder, T. and Alexander, J. (2001). The physical character of subaqueous sedimentary density flows and their deposits. *Sedimentology*, 48(2):269–299.
- Mulder, T. and Moran, K. (1995). Relationship among submarine instabilities, sea level variations, and the presence of an ice sheet on the continental shelf: An example from the Verrill Canyon Area, Scotian Shelf. *Paleoceanography*, 10(1):137–154.
- Nadim, F. (2012). Risk assessment for earthquake-induced submarine slides. In Yamada, Y., Kawamura, K., Ikehara, K., Ogawa, Y., Urgeles, R., Mosher, D., Chaytor, J., and Strasser, M., editors, *Submarine Mass Movements and Their Consequences*, volume 31 of *Advances in Natural and Technological Hazards Research*, pages 15–27. Springer Netherlands.
- Nelson, C. H. (1990). Estimated post-Messinian sediment supply and sedimentation rates on the Ebro continental margin, Spain. *Marine Geology*, 95:395–418.
- Nittrouer, C. A. (2007). *Continental margin sedimentation - from sediment transport to sequence stratigraphy*. Wiley-Blackwell.
- Norem, H., Locat, J., and Schieldrop, B. (1990). Approach to the physics and the modeling of submarine flowslides. *Marine Geotechnology*, 9(2):93–111.
- ÓCofaigh, C., Dowdeswell, J. A., and Grobe, H. (2001). Holocene glacimarine sedimentation, inner Scoresby Sund, East Greenland: the influence of fast-flowing ice-sheet outlet glaciers. *Marine Geology*, 175(1-4):103 – 129.

- Okal, E., Plafker, G., Synolakis, C., and Borrero, J. (2003). Near-field survey of the 1946 Aleutian Tsunami on Unimak and Sanak Islands. *Bulletin of the Seismological Society of America*, 93(3):1226–1234.
- O’Leary, D. W. (1991). Structures and morphology of submarine slab slides: clues to origin and behavior. *Marine Geotechnology*, 10:53–69.
- Osborne, M. J. and Swarbrick, R. E. (1997). Mechanisms for generating overpressure in sedimentary basins; a reevaluation. *AAPG Bulletin*, 81(6):1023–1041.
- Owen, M., Day, S., and Long, D. (2010). Investigations on the Peach 4 Debrite, a late Pleistocene mass movement on the Northwest British Continental Margin. In Mosher, D. C., Shipp, R. C., Moscardelli, L., Chaytor, J. D., Baxter, C. D. P., Lee, H. J., and Urgeles., R., editors, *Submarine Mass Movements and Their Consequences*, volume 28 of *Advances in Natural and Technological Hazards Research*, pages 301–311. Springer Netherlands.
- Owen, M., Day, S., and Maslin, M. (2007). Late Pleistocene submarine mass movements: occurrence and causes. *Quaternary Science Reviews*, 26:958–978.
- Pachur, H. J. and Kröpelin, S. (1987). Wadi Howar: Paleoclimatic evidence from an extinct river system in the southeastern Sahara. *Science*, 237(4812):298–300.
- Pastouret, L., Chamley, H., Delibrias, G., Duplessy, J.-C., and Thiede, J. (1979). Late Quaternary climatic changes in Western Tropical Africa deduced from deep-sea sedimentation off Niger Delta. *Oceanologica Acta*, 1(2):217–232.
- Paull, C. K., Buelow, W. J., III, W. U., and Borowski, W. S. (1996). Increased continental-margin slumping frequency during sea-level lowstands above gas hydrate-bearing sediments. *Geology*, 24:143–136.
- Pearce, T. J. and Jarvis, I. (1992). Composition and provenance of turbidite sands: Late Quaternary, Madeira Abyssal Plain. *Marine Geology*, 109:21–51.
- Piper, D. J. and Normark, W. R. (2009). Processes that initiate turbidity currents and their influence on turbidites: A marine geology perspective. *Journal of Sedimentary Research*, 79(6):347–362.
- Piper, D. J. W. and Aksu, A. E. (1987). The source and origin of the 1929 Grand Banks turbidity current inferred from sediment budgets. *Geo-Marine Letters*, 7(4):177–182.
- Piper, D. J. W., Mosher, D. C., Gauley, B. J., Jenner, K., and Campbell, D. C. (2003). The chronology and recurrence of submarine mass movements on the continental slope off southeastern Canada. In Locat, J., Mienert, J., and Boisvert, L., editors, *Submarine Mass Movements and Their Consequences*, volume 19 of *Advances in Natural and Technological Hazards Research*, pages 299–306. Springer Netherlands.

- Posamentier, H. W., Allen, G. P., James, D. P., and Tesson, M. (1992). Forced regressions in a sequence stratigraphic framework; concepts, examples, and exploration significance. *AAPG Bulletin*, 76(11):1687–1709.
- Potts, D. M. and Zdravkovic, L. (2001). *Finite Element analysis in geotechnical engineering. Theory*. Thomas Telford.
- Poulos, H. G. (1988). *Marine Geotechnics*. Unwin Hyman, London.
- Powrie, W. (2002). *Soil Mechanics*. Spon, London.
- Prell, W. L., Imbrie, J., Martinson, D. G., Morley, J. J., Pisias, N. G., Shackleton, N. J., and Streeter, H. F. (1986). Graphic correlation of oxygen isotope stratigraphy application to the Late Quaternary. *Paleoceanography*, 1(2):137–162.
- Premuzic, E. T., Benkovitz, C. M., Gaffney, J. S., and Walsh, J. J. (1982). The nature and distribution of organic matter in the surface sediments of world oceans and seas. *Organic Geochemistry*, 4(2):63 – 77.
- Prins, M. A., Postma, G., and Weltje, G. J. (2000). Controls on terrigenous sediment supply to the Arabian Sea during the late Quaternary: the Makran continental slope. *Marine Geology*, 169:351–371.
- Prior, D. B. and Coleman, J. M. (1982). *Marine slides and other mass movements*, chapter Active slides and flows in underconsolidated marine sediments on the slopes of the Mississippi delta, pages 21–49. Plenum, New York.
- Pusch, R. (1973). Influence of salinity and organic matter on the formation of clay microstructures. In *International Symposium on Soil Structure*.
- Rahmstorf, S. (2002). Ocean circulation and climate during the past 120,000 years. *Nature*, 419:207–214.
- Raymo, M. E. and Mitrovica, J. X. (2012). Collapse of polar ice sheets during the stage 11 interglacial. *Nature*, 483:453–456.
- Reagan, M. T. and Moridis, G. J. (2008). Dynamic response of oceanic hydrate deposits to ocean temperature change. *Journal of Geophysical Research*, 113.
- Reeder, M. S., Rothwell, R. G., and Stow, D. A. V. (2000). Influence of sea level and basin physiography on emplacement of the late Pleistocene Heradotus Basin Megaturbidite, SE Mediterranean Sea. *Marine and Petroleum Geology*, 17:199–218.
- Reeder, M. S., Stow, D. A. V., and Rothwell, R. G. (2002). Late Quaternary turbidite input into the east Mediterranean basin: new radiocarbon constraints on climate and sea-level control. *Geological Society Special Publications*, 191:267–278.
- Reid, R. P., Carey, S. N., and Ross, D. R. (1996). Late Quaternary sedimentation in the Lesser Antilles island arc. *Geological Society of America Bulletin*, 108(1):78–100.

- Reimer, P. J., Baillie, M. G. L., Bard, E., Bayliss, A., Beck, J. W., Blackwell, P. G., Ramsey, C. B., Buck, C. E., Burr, G. S., Edwards, R. L., Friedrich, M., Grootes, P. M., Guilderson, T. P., Hajdas, I., Heaton, T. J., Hogg, A. G., Hughen, K. A., Kaiser, K. F., Kromer, B., McCormac, F. G., Manning, S. W., Reimer, R. W., Richards, D. A., Southon, J. R., Talamo, S., Turney, C. S. M., van der Plicht, J., and Weyhenmeyer, C. E. (2009). Intcal09 and Marine09 radiocarbon age calibration curves, 0-50,000 years cal BP. *Radiocarbon*, 51(4):1111–1150.
- Revel, M., Cremer, M., Grousset, F. E., and Labeyrie, L. (1996). Grain-size and Sr Nd isotopes as tracer of paleo-bottom current strength, Northeast Atlantic Ocean. *Marine Geology*, 131(3-4):233–249.
- Richards, A. F. and Hamilton, E. L. (1967). *Investigations of deep-sea sediment cores, III. Consolidation*. University of Illinois Press, Chicago.
- Rørvik, K. L., Laberg, J. S., Hald, M., Ravna, E. K., and Vorren, T. O. (2010). Behavior of the northwestern part of the Fennoscandian Ice Sheet during the Last Glacial Maximum - a response to external forcing. *Quaternary Science Reviews*, 29:2224–2237.
- Roscoe, K. H. and Burland, J. B. (1968). *Engineering plasticity*, chapter On the generalised stress-strain behaviour of 'wet' clay, pages 535–609. Cambridge University Press.
- Rothwell, R., Thomson, J., and G.Kähler (1998). Low-sea-level emplacement of very large Late Pleistocene 'megaturbidite' in the western Mediterranean Sea. *Nature*, 392:377–380.
- Rothwell, R. G., Reeder, M. S., Anastasakis, G., Stow, D. A. V., Thomson, J., and Kähler, G. (2000). Low sea-level stand emplacement of megaturbidites in the western and eastern Mediterranean Sea. *Sedimentary Geology*, 135:75–88.
- Rowe, P. W. (1965). The calculation of the consolidation rates of laminated, varved or layered clays, with particular reference to sand drains. *Geotechnique*, 14(4):321–340.
- Rowe, P. W. (1968). The influence of geological features of clay deposits on the design and performance of sand drains. In *Institution of Civil Engineers UK*.
- Ruddiman, W., Sarnthein, M., and Expedition 108 Scientists (1988). Expedition 108. *Proceedings of the Ocean Drilling Program, Scientific Results, Expedition 108*.
- Sadler, P. M. (2004). Quantitative biostratigraphy - achieving finer resolution in global correlation. *Annual Reviews of Earth and Planetary Science*, 32:187–213.
- Sager, W. W., Lee, C. S., Macdonald, I. R., and Schroeder, W. W. (1999). High-frequency near-bottom acoustic reflection signatures of hydrocarbon seeps on the Northern Gulf of Mexico continental slope. *Geo-Marine Letters*, 18:267–276.

- Sarnthein, M., Thiede, J., Pflaumann, U., Erlenkeuser, U., and Fütterer, D. (1982). *Geology of the Northwest African continental margin*, chapter Atmospheric and oceanic circulation patterns off Northwest Africa during the past 25 million years, pages 545–604. Berlin: Springer Verlag.
- Schiffman, R. (1982). The consolidation of soft marine sediments. *Geo-Marine Letters*, 2:199–203.
- Schiffman, R. L., Pane, V., and Gibson, R. E. (1984). The theory of one-dimensional consolidation of clays. iv. an overview of nonlinear finite strain sedimentation and consolidation. In *Proceedings of the Symposium on Sedimentation-Consolidation Models: Prediction and Validation*.
- Schneider, J., Flemings, P. B., Dugan, B., Long, H., and Germaine, J. T. (2009). Overpressure and consolidation near the seafloor of Brazos-Trinity Basin IV, northwest deepwater Gulf of Mexico. *Journal of Geophysical Research*, 114.
- Shackleton, N. J. and Opdyke, N. D. (1973). Oxygen isotope and paleomagnetic stratigraphy of Equatorial Pacific core V28-238: Oxygen isotope temperatures and ice volumes on a  $10^5$  year and  $10^6$  year scale. *Quaternary Research*, 3:39–55.
- Shiwakoti, D. R., Tanaka, H., Tanaka, M., and Locat, J. (2002). Influences of diatom microfossils on engineering properties of soils. *Journal of the Japanese Geotechnical Society of Soils and Foundations*, 42(3):1–17.
- Skempton, A. W. (1970). The consolidation of clays by gravitational compaction. *Quarterly Journal of the Geological Society of London*, 125:373–411.
- Skinner, L. and McCave, I. (2003). Analysis and modelling of gravity- and piston coring based on soil mechanics. *Marine Geology*, 199(1-2):181–204.
- Smith, J. E. (1971). The dynamics of shale compaction and evolution of pore-fluid pressures. *Mathematical Geology*, 3:239–263. 10.1007/BF02045794.
- Sterling, G. and Strohbeck, E. (1973). The failure of the South Pass 70" B" platform. In *Offshore Technology Conference*.
- Stigall, J. and Dugan, B. (2010). Overpressure and earthquake initiated slope failure in the Ursa region, northern Gulf of Mexico. *Journal of Geophysical Research*, 115(B04101).
- Su, C., Tseng, J., Hsu, H., Chiang, C., Yu, H., Lin, S., and Liu, J. (2012). Records of submarine natural hazards off SW Taiwan. *Geological Society, London, Special Publications*, 361(1):41–60.
- Sumner, E., Siti, M., McNeill, L. C., Talling, P. J., Wynn, R., Henstock, T., Djajadihardja, Y., and Permana, H. (2010). Testing the validity of using turbidites as an

- earthquake proxy on the Sumatran margin. In *American Geophysical Union, Fall Meeting 2010*.
- Suter, J. R. and Berryhill, H. L. (1985). Late Quaternary shelf-margin deltas, Northwest Gulf of Mexico. *AAPG Bulletin*, 69(1):77–91.
- Swan, A. R. H. and Sandilands, M. (1995). *Introduction to geological data analysis*. Blackwell Science Ltd.
- Talling, P. J., Wynn, R. B., Masson, D. G., Frenz, M., Cronin, B. T., Schiebel, R., Akhmetzhanov, A. M., Dallmeier-Tiessen, S., Benetti, S., Weaver, P. P. E., Georgiopoulou, A., Zühlsdorff, C., and Amy, L. A. (2007). Onset of submarine debris flow deposition far from original giant landslide. *Nature*, 450:541–544.
- Tanaka, H. and Locat, J. (1999). A microstructural investigation of Osaka Bay clay: the impact of microfossils on its mechanical behaviour. *Canadian Geotechnical Journal*, 36(3):493–508.
- Tappin, D. R. (2010). Submarine mass failures as tsunami sources: their climate control. *Philosophical Transactions of the Royal Society*, 368:2417–2434.
- Tappin, D. R., Watts, P., McMurtry, G. M., Lafoy, Y., and Matsumoto, T. (2001). The Sissano, Papua New Guinea tsunami of July 1998 - offshore evidence on the source mechanism. *Marine Geology*, 175:1–23.
- ten Brink, U. S., Lee, H. J., Geist, E. L., and Twichell, D. (2009). Assessment of tsunami hazard to the US East Coast using relationships between submarine landslides and earthquakes. *Marine Geology*, 264(1-2):65–73.
- Terzaghi, K. and Peck, R. B. (1948). *Soil mechanics in engineering practice*. John Wiley, New York.
- Thomson, J. and Weaver, P. P. E. (1994). An AMS radiocarbon method to determine the emplacement time of recent deep-sea turbidites. *Sedimentary Geology*, 89:1–7.
- Toucanne, S., Zaragosi, S., Bourillet, J.-F., Dennielou, B., Jorry, S. J., Jouet, G., and Cremer, M. (2012). External controls on turbidite sedimentation on the glacially-influenced Armorican margin (Bay of Biscay, western European margin). *Marine Geology*, 303-306:137–153.
- Trofimovs, J., Fisher, J. K., Macdonald, H. A., Talling, P. J., Sparks, R. S. J., Hart, M. B., Smart, C. W., Boudon, G., Deplus, C., Komorowski, J.-C., LeFriant, A., Moreton, S. G., and Leng, M. L. (2010). Evidence for carbonate platform failure during rapid sea-level rise; ca 14 000 year old bioclastic flow deposit in the Lesser Antilles. *Sedimentology*, 57:735–759.

- Twichell, D. C., Chaytor, J. D., ten Brink, U. S., and Buczkowski, B. (2009). Morphology of late Quarternary submarine landslides along the U.S. Atlantic continental margin. *Marine Geology*, 264:4–15.
- Urlaub, M., Zervos, A., Talling, P. J., Masson, D. G., and Clayton, C. I. (2012). How do 2° slopes fail in areas of slow sedimentation? A sensitivity study on the influence of accumulation rate and permeability on submarine slope stability. In Yamada, Y., Kawamura, K., Ikehara, K., Ogawa, Y., Urgeles, R., Mosher, D., Chaytor, J., and Strasser, M., editors, *Submarine Mass Movements and Their Consequences*, volume 31 of *Advances in Natural and Technological Hazards Research*, pages 277–287. Springer Netherlands.
- USGS (2004). Fact sheet: Landslide types and processes.
- Valent, P. J., Altschaeffl, A. G., and Lee, H. J. (1982). Geotechnical properties of two caclareous oozes. In Demars, K. R. and Chaney, R. C., editors, *Geotechnical properties, behavior and performance of calcareous soils*.
- Vanneste, M., Mienert, J., and Bünz, S. (2006). The Hinlopen Slide: A giant, submarine slope failure on the northern Svalbard margin, Arctic Ocean. *Earth and Planetary Science Letters*, 245:373–388.
- Velde, B. (1996). Compaction trends of clay-rich deep sea sediments. *Marine Geology*, 133:193–201.
- Voight, B., Friant, A., Boudon, G., Deplus, C., Komorowski, J.-C., Lebas, E., Sparks, R. S. J., Talling, P., and Trofimovs, J. (2012). Undrained sediment loading key to long-runout submarine mass movements: Evidence from the Caribbean Volcanic Arc. In Yamada, Y., Kawamura, K., Ikehara, K., Ogawa, Y., Urgeles, R., Mosher, D., Chaytor, J., and Strasser, M., editors, *Submarine Mass Movements and Their Consequences*, volume 31 of *Advances in Natural and Technological Hazards Research*, pages 417–428. Springer Netherlands.
- Voight, B., Janda, R. J., and Glicken, H. (1985). Nature and mechanics of the Mount St. Helens rockslide-avalanche of 18 May 1980. In *The 26th U.S. Symposium on Rock Mechanics*. American Rock Mechanics Association.
- Völker, D., Scholz, F., and Geersen, J. (2011). Analysis of submarine landsliding in the rupture area of the 27 February 2010 Maule earthquake, Central Chile. *Marine Geology*, 288:79–89.
- Volpi, V., Camerlenghi, A., Hillenbrand, C.-D., Rebesco, M., and Ivaldi, R. (2003). Effects of biogenic silica on sediment compaction and slope stability on the Pacific margin of the Antarctic Peninsula. *Basin Research*, 15(3):339–363.

- Vorren, T. O., Laberg, J. S., Blaume, F., Dowdeswell, J. A., Kenyon, N. H., Mienert, J., Rumohr, J., and Werner, F. (1998). The Norwegian-Greenland sea continental margins: Morphology and late Quaternary sedimentary processes and environment. *Quaternary Science Reviews*, 17(1-3):173–302.
- Waelbroeck, C., Labeyrie, L., Michel, E., Duplessy, J., McManus, J., Lambeck, K., Balbon, E., and Labracherie, M. (2002). Sea-level and deep water temperature changes derived from benthic foraminifera isotopic records. *Quaternary Science Reviews*, 21(1-3):295 – 305.
- Walker, J. R. and Massingill, J. V. (1970). Slump features on the Mississippi Fan, Northeastern Gulf of Mexico. *Geological Society of America Bulletin*, 81:3101–3108.
- Wangen, M. (1992). Pressure and temperature evolution in sedimentary basins. *Geophysical Journal International*, 110(3):601–613.
- Wangen, M. (1997). A simple model of pressure build-up caused by porosity reduction during burial. *Geophysical Journal International*, 130(3):757–764.
- Wangen, M. (2000). Generation of overpressure by cementation of pore space in sedimentary rocks. *Geophysical Journal International*, 143(3):608–620.
- Wangen, M. (2001). A quantitative comparison of some mechanisms generating overpressure in sedimentary basins. *Tectonophysics*, 334(3-4):211 – 234.
- Weaver, P. P. E. (1994). Determination of turbidity current erosional characteristics from reworked coccolith assemblages, Canary Basin, north-east Atlantic. *Sedimentology*, 41:1025–1038.
- Weaver, P. P. E. and Kuijpers, A. (1983). Climatic control of turbiditic deposition on the Madeira Abyssal Plain. *Nature*, 306:360–363.
- Weaver, P. P. E., Wynn, R. B., Kenyon, N. H., and Evans, J. (2000). Continental margin sedimentation, with special reference to the north-east Atlantic margin. *Sedimentology*, 47:239–256.
- Westphal, H. and Munnecke, A. (1997). Mechanical compaction versus early cementation in fine-grained limestones: differentiation by the preservation of organic microfossils. *Sedimentary Geology*, 112(1-2):33 – 42.
- Wien, K., Kölling, M., and Schulz, H. D. (2007). Age models for the Cape Blanc Debris Flow and the Mauritania Slide Complex in the Atlantic Ocean off NW Africa. *Quaternary Science Reviews*, 26:2258–2573.
- Wilson, C. K., Long, D., and Bulat, J. (2004). The morphology, setting and processes of the Afen Slide. *Marine Geology*, 213(1-4):149–167.

- Winkelmann, D., Geissler, W., Schneider, J., and Stein, R. (2008). Dynamics and timing of the Hinlopen/Yermak Megaslide north of Spitsbergen, Arctic Ocean. *Marine Geology*, 250(1-2):34–50.
- Wright, S. G. and Rathje, E. M. (2003). Triggering mechanisms of slope instability and their relationship to earthquake and tsunamis. *Pure and Applied Geophysics*, 160:1865–1877.
- Wynn, R. B., Masson, D. G., Stow, D. A. V., and Weaver, P. P. E. (2000). The Northwest African slope apron: a modern analogue for deep-water systems with complex seafloor topography. *Marine and Petroleum Geology*, 17:253–265.
- Wynn, R. B., Weaver, P. P. E., Masson, D. G., and Stow, D. A. V. (2002). Turbidite depositional architecture across three interconnected deep-water basins on the northwest African margin. *Sedimentology*, 49:669–695.
- Yang, Y. and Aplin, A. C. (2010). A permeability-porosity relationship for mudstones. *Marine and Petroleum Geology*, 27:1692–1697.
- Yardley, G. and Swarbrick, R. (2000). Lateral transfer: a source of additional overpressure? *Marine and Petroleum Geology*, 17(4):523 – 537.
- Zienkiewicz, O. C. and Taylor, R. L. (1989). *The Finite Element Method*. McGraw-Hill.